Ollscoil na hÉireann - The National University of Ireland

Improved analysis of measured MHD activity and the use of Toroidicity induced Alfvén Eigenmodes to constrain current density profile reconstruction in the ASDEX Upgrade tokamak.

Karl D. Sassenberg

Roinn na Fisice

Coláiste na hOllscoile, Corcaigh

Department of Physics

University College Cork

Supervisor: Dr. Patrick J. Mc Carthy

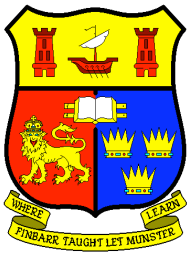

Thesis submitted for the Degree of Doctor of Philosophy to the

National University of Ireland

June 2009

Contents

Abstract

In a tokamak plasma, knowledge of the thermal and hot particle populations, and their dynamics are essential for controlled operation. The plasma pressure and current gradients can provide the energy required to trigger various MHD instabilities that will then act to degrade control and performance. Therefore studying the activity of MHD instabilities within the plasma will reveal considerable information about the thermal and hot particle populations.

A readily excitable and sensitive class of MHD instabilities in a tokamak plasma are Toroidicity induced Alfvén Eigenmodes **TAE**s. This follows firstly from the sensitivity of the gap frequency of a TAE $f_{gap} = \frac{V_A}{2qR_0}$ ($V_A = \frac{B_0}{\sqrt{\mu_0 \rho}}$ is the Alfvén velocity) to B_0, the magnetic field strength, ρ, the mass density profile, q, the safety factor and the major radius R_0. Secondly, TAEs have the ability to extract energy from resonant fast ions through Inverse Landau Damping, and thirdly, the existence of these modes in the weakly damped Toroidicity induced gaps in the Alfvén spectrum. As these modes grow, they alter the orbits of resonant fast ions, leading to the premature loss and a redistribution of a significant proportion of these fast ions, thus reducing the self-heating efficiency and potentially resulting in damage of plasma facing components.

At ASDEX Upgrade fast ions can be introduced into the plasma using Neutral Beam Injection (NBI), or ions already present can be accelerated to energies of 1MeV and higher by Ion Cyclotron Resonance Heating (ICRH). The analysis of the effects TAEs have on these ICRH accelerated fast ions will be used to infer the effects of TAEs on α-particles in a thermonuclear reactor. This is of paramount importance to ITER[74] and any future fusion devices, because α-particles are envisioned to be the main source of energy used to sustain a burning plasma. To address this issue a simple formula for volume averaged β_{fast} in ICRH only plasmas is proposed. With this formula it is possible to further study operating regimes in which TAEs are unstable.

The goal of this research was to characterise TAEs at ASDEX Upgrade and to demonstrate that TAEs could be used to passively diagnose the plasma equilibrium. To achieve this the following milestones had to be reached, the compilation of a characterisation of most typically observed fast ion driven TAEs, to provide a comparison of observations with expectations derived from established theory, to demonstrate that fast ion driven TAEs could provide good quality q-profile information in order to improve equilibrium reconstructions, to demonstrate that ICRF beatwaves can drive the same TAEs

described in the compiled characterisation, and to demonstrate that like the fast ion driven TAEs ICRF beatwave driven TAEs can also provide q-profile information.

In the course of compiling this characterisation several new results were demonstrated. These include: the even character of these TAEs, ICRF power threshold versus density of TAEs, the effect of magnetic shear on a TAE's frequency and stability, measurements of fast ion drive, damping rate and growth rate of TAEs, and the use of TAEs in validating fast ion pressure profiles.

Once these TAEs were identified, it was found that they could provide either individual points of q-profile information, or a single *group* point of q-profile information. The amount of information that could be extracted was seen to depend on the ability of diagnostics; based on microwave reflectometry, electron cyclotron emissions, and soft X-Ray emissions; to localise individual TAEs.

Using the knowledge of TAEs gleaned from the characterisation, experiments were designed to demonstrate that ICRF beatwave could destabilise these same TAEs. After which the characterisation provided a frame of reference enabling the identification of ICRF excited modes as the TAEs typically excited by fast ions. Q-profile information was extracted from these TAEs using the techniques developed to process fast ion excited TAEs, and was subsequently used to improve equilibrium reconstructions.

Achieving these milestones demonstrated that techniques developed to drive TAEs with ICRF beatwaves provides the basis for a new q-profile diagnostic, which complements existing diagnostics.

Acknowledgements

This work was supervised by Dr. P. J. McCarthy, Dr. M. Maraschek and Prof. H. Zohm. I would like to acknowledge their support, guidance, and hard work which made this thesis possible. For this I will always very grateful. This research was undertaken as part of the Plasma Physics Group at UCC and also as a member of the ASDEX Upgrade Experimental Group at the Max-Planck-Institut für Plasmaphysik (IPP), Garching bei Muenchen, Germany.

I would like to give my particular thanks to the many colleagues that helped me over the years. To Dr. P .J. Mc Carthy for his insights into the CLISTE code and plasma physics, facilitating my research secondments to IPP, and support throughout by research. I am indebted to Dr. M. Maraschek for his support, insights, fruitful discussions, knowledge of experimental operation, endless enthusiasm and representation on my behalf. To Dr. V. Igochine for assisting me with the CASTOR_FLOW code and answering all my question with clarity and good nature. Dr. P. Lauber for facilitating very fruitful discussions. To Dr. E. Strumberger for instructing me in the use of the CASTOR_FLOW and HELENA codes. Prof. S. Günter's experience, knowledge of TAEs, and contributions to the design of the beatwave experiments was very important and greatly appreciated. To Dr. M. García-Muñoz for all our discussions on a wide variety of topics, but mainly for his knowledge of fast ion dynamics and fast ion losses. The wide range of ICRH and ICRF beatwave experiments achieved would not have been possible without the expertise and efforts of Dr. W. Bobkov and the ICRF group at ASDEX Upgrade. Thanks also to Mr. P. Martin and Dr. W. Schneider for all their help with the CLISTE code. I would also like to thank the members of the ASDEX Upgrade team who made the experimental discharges possible and all those responsible for the development and maintenance of the various codes used for the purposes of this work. Furthermore I would like to thank the Head of the Physics department at UCC, Prof. John McInerney.

To the friends I have made at IPP and UCC over the years, thanks for all the support, friendship and all the good times. With special thanks to A. Flaws.

To my family, my mother, Irene, my late father Dieter, and my sisters, Nicola and Lucinda. Your love and support made a long journey from my first days to now very enjoyable and enriching. I will endeavour to make you all proud, now and into the future, and of course return all that you have given me with interest.

This work was supported by a research agreement between: the Max-Planck-Institut für Plasmaphysik (IPP), Garching bei Muenchen, Germany; University College Cork (UCC), Ireland; and EURATOM. I would like to especially thank EURATOM and IPP for their financial support, and IPP and UCC for their administrative and logistical support.

Chapter 1

Introduction

1.1 What is Nuclear Fusion?

Nuclear Fusion is the name given to the process of two nuclei combining to form a heavier nucleus. Once the heavier nucleus is formed, it can be either stable, or unstable and break apart. If it is an exothermic reaction, then energy is released. The amount of energy released $E = \Delta mc^2$, is equal to the difference in mass between the total mass of the reactants and the total mass of the products. In order to harness this process to produce energy on earth, a candidate reaction must release more energy than is required to sustain the reaction, once initiated. The most promising candidate reactions that achieve this goal are represented by the equations 1.1-1.4.

$$D + T = {}^4\mathrm{He} + n + 17.6\ \mathrm{MeV} \tag{1.1}$$

$$D + {}^3\mathrm{He} = {}^4\mathrm{He} + p + 18.4\ \mathrm{MeV} \tag{1.2}$$

$$D + D = n + {}^3\mathrm{He} + 3.27\ \mathrm{MeV} \tag{1.3}$$

$$D + D = p + T + 4.032\ \mathrm{MeV} \tag{1.4}$$

Of these, the most attractive reaction is the Deuterium-Tritium reaction, equation 1.1, for the following reasons. Each DT-reaction releases a tremendous amount of energy, the scattering cross section is much larger than for the other candidate reactions, including those involving Helium, and the maximal value of the scattering cross section occurs at a lower energy than all other candidates reactions (figure 1.1). In fact the D-T fusion reaction has the largest gain of all nuclear reactions, including those involving either Helium or the Weak-interaction.

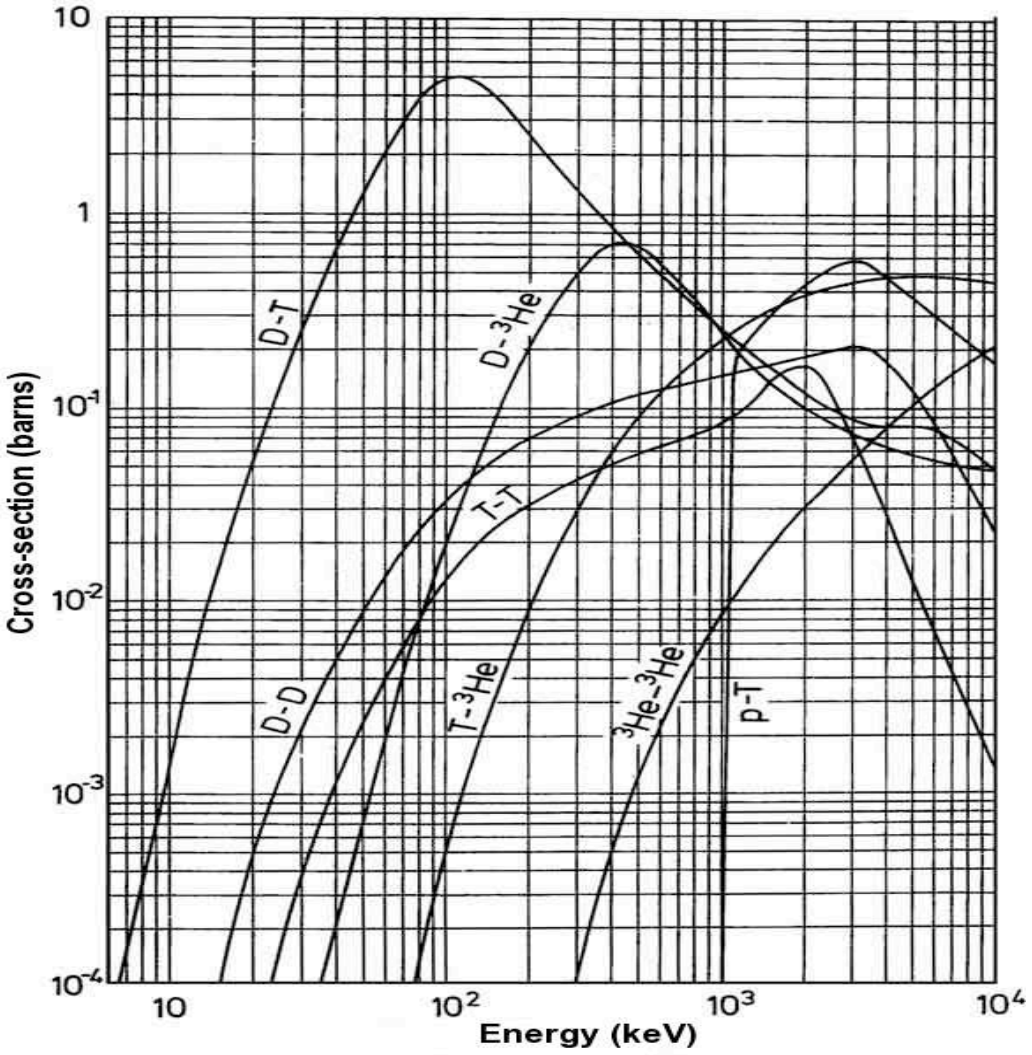

Figure 1.1: Scattering cross sections for candidate fusion reactions as a function of relative energies of the reactants.(1 barn = $10^{-28}m^2$)

1.2 Why pursue Nuclear Fusion?

When commercial nuclear Fusion power stations become available, the world will benefit from a clean virtually limitless source of energy. Currently, the world demand for power is being satisfied by fossil fuels, renewable energy resources and nuclear fission power stations. Of these, fossil fuels have a short remaining lifetime, a detrimental effect on the environment and as supply diminishes, costs will soar (table 1.1). Renewable energy sources on the other hand, are in theory endless and clean, but expectations and some implementations are often short-sighted. While renewable energy sources are a

vital component of any future energy strategy, they can not possibly meet the needs of a world with an ever increasing demand for energy. Nuclear power promises a solution to the world's energy demand with high energy output and extremely large fuel reserves. Across the world nuclear fission power plants are supplying energy to power businesses and homes. On the surface it would appear that a solution has been found, but lessons from history have made it painfully clear that this method of releasing nuclear power must be respected and dealt with responsibly. So, nuclear fission is currently only able to deliver on half of its initial promise. The problem stems from its two prominent drawbacks, the possibility of a dangerous run-away chain reaction, and the proportionality of long half-life radioactive waste production to energy output. In contrast, a nuclear fusion reactor will power down if confinement is

Resources	GJ	Life-Time
Coal	10^{14}	300 years
Oil	1.2×10^{13}	40 years
Natural Gas	1.4×10^{13}	50 years
^{235}U (fission reactors)	10^{13}	30 years
^{238}U and ^{232}Th (breeder reactors)	10^{16}	30000 years
Lithium (D-T fusion reactors):		
Land	10^{16}	30000 years
Oceans	10^{19}	$3 \cdot 10^{7}$ years
Present world annual primary energy consumption	3×10^{11}	

Table 1.1: Forecasted World Energy Resources. Energy and Life-Time data are estimates and depend strongly on the prices of the mentioned resources[10].

lost, radioactive waste produced has a short half-life and the amount of waste is inversely proportional to the lifetime of reactor vessel materials. Therefore, any drawbacks pale in comparison, while providing a plentiful and potentially endless source of energy.

1.3 Achieving Nuclear Fusion

The most promising method of producing energy is thermonuclear fusion, which requires the D-T fuel mixture to be heated to a sufficiently high temperature, such that the velocities of the reactants are large enough to overcome Coulomb repulsion and generate fusion reactions. In this process, the optimum temperature (10keV)[1] is lower than the corresponding energy at which the maximum scattering cross section occurs (100keV). This is made possible because the required reactions between ions in the high energy tail of the Maxwellian distribution of ions in the plasma. In order to start a self-sustaining and positive net energy producing D-T plasma through fusion born α-particle heating alone, the plasma first needs to be heated by external means to a temperature in the range $10-20keV$, while simultaneously satisfying the inequality [10]:

$$\hat{n}\hat{T}\tau_E > 5\times 10^{21} m^{-3} s\ keV. \tag{1.5}$$

Here $\hat{n}$ and $\hat{T}$ are the peak ion density and temperature in the plasma and τ_E (equation 1.6) is the energy confinement time. Once these conditions are satisfied the plasma is said to be *ignited* (or *burning*). In achieving this the required heating will be completely supplied by the α-particles, $P_H = P_H^{\alpha}$. Using the energy balance: $dW/dt = P_H - W/\tau_E$, where W is the total energy stored in the plasma, τ_E is defined as the time required for W to drop to by a factor of e^{-1} after heating has been removed ($P_H = 0$). Under stationary conditions $dW/dt = 0$, which allows one to solve for τ_E as follows

$$\tau_E = \frac{W}{P_H}. \tag{1.6}$$

At these temperatures the fuel is completely ionised and because they carry a charge these ions will gyrate around magnetic field lines. This means that the plasma can be confined within a magnetic cage.

A Tokamak, from the Russian acronym, TOroidalnaya KAmera MAgnitnymi Katushkami, which means "toroidal chamber with magnetic coils" is a device which confines a toroidal plasma using magnetic fields, see figure 1.2. In practice the magnetic field is the sum of a toroidal field created by a set of toroidal symmetric super-conducting coils and a poloidal field. The poloidal field is produced by a toroidal current induced in the plasma by a transformer, with the plasma itself acting as the secondary winding of the transformer. The combination of toroidal and poloidal magnetic fields results in field

[1] Following the convention accepted in Fusion, temperatures are written in eV. Thus, in place of conventional kT^0 (where k is Boltzmann's constant and T^0 is in degrees Kelvin) we write T(eV), so that $T^0 = T(joules)/1.381\cdot 10^{-23}$, where $T(joules) = T(eV)\cdot 1.602\cdot 10^{-19}$.

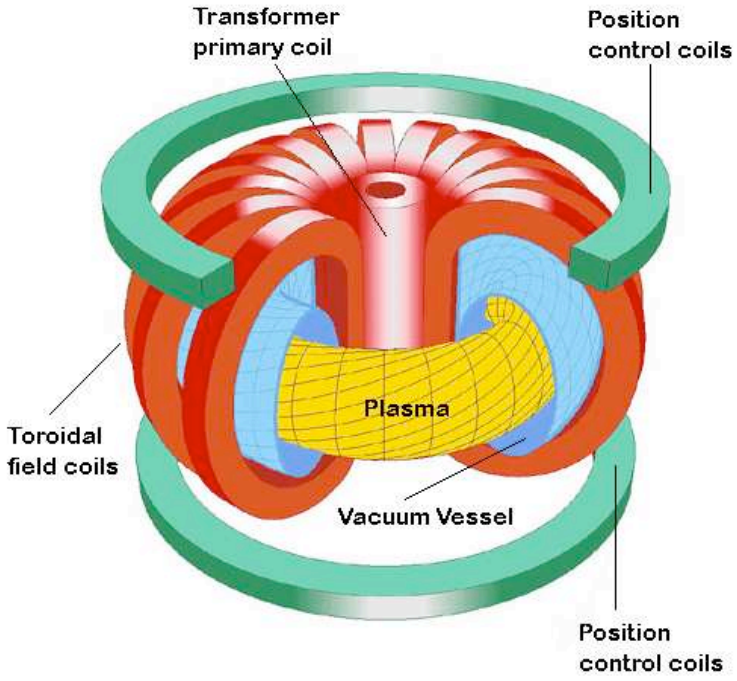

Figure 1.2: Graphic representations of tokamak fusion reactor.

lines following a helical trajectory around the torus.

The Axial Symmetric Divertor EXperiment (ASDEX) Upgrade is a tokamak based thermonuclear fusion experiment at the Max-Planck-Institut für Plasma Physik in Garching bei München, Germany. Table 1.2 presents important machine parameters and heating capabilities of ASDEX Upgrade.

There is an alternative concept utilising magnetic confinement, upon which a thermonuclear fusion reactor could be based. This is the Stellarator, so named because is produces energy like the sun, a stellar body. In a stellarator the magnetic fields are defined completely by super-conducting coils outside of the plasma making a plasma current unnecessary. This removes the cost and complexity of current drive systems and avoids machine stresses during current disruptions and pulsed operation. However, the complexity of the super-conducting coils' non-planar geometry and resulting magnetic field line structure make engineering and theory very complicated. Historically the Stellarator was the first device conceived to achieve thermonuclear fusion, whereas the TOKAMAK design was later

Table 1.2: Main Parameters of ASDEX Upgrade

Major plasma radius	R_0	1.65m
Minor plasma radius	a	0.5m
Plasma height	b	0.85m
Triangularity	δ	≤ 0.5
Plasma current	I_p	$\leq 1.4MA$
Toroidal magnetic field at the magnetic axis	B_0	$\leq 3.1T$
Current flat top duration	t_D	10s
Installed auxiliary heating power	P_H	28MW
Neutral beam heating 60keV		10MW
Neutral beam heating 100keV		10MW
Ion cyclotron heating 30-40MHz		8MW
Electron cyclotron heating 30-90MHz		2MW

devised to address these issues.

The next stage from current day tokamaks is the building of the International Thermonuclear Experimental Reactor - ITER. It is through the co-operation of many of this worlds nations that this historic experiment is currently being constructed and once complete, the world's nations will be one step closer to a clean long-term energy supply.

1.4 Thesis Outline

In a tokamak plasma, knowledge of the thermal and hot particle populations, and their dynamics are essential for controlled operation and stability against MHD phenomena. A readily excitable and sensitive class of MHD instability are weakly damped Toroidicity induced Alfvén Eigenmodes (**TAE**s). This follows firstly from: the sensitivity of the gap frequency of a TAE, the magnetic field strength B, the mass density profile ρ, and the safety factor profile q. Secondly TAEs have the ability to extract energy from resonant fast ions through Inverse Landau Damping, and thirdly the existence of these modes in the weakly damped Toroidicity induced gaps in the Alfvén spectrum. As these modes grow, they alter the orbits of resonant fast ions leading to the premature loss and a redistribution of a significant

proportion of these fast ions, thereby reducing heating efficiency and potentially resulting in damage to plasma facing components. Therefore a good understanding of characteristics of TAEs and stability is required to minimise these effects.

At ASDEX Upgrade fast ions can be introduced into the plasma using Neutral Beam Injection (NBI), or ions already present can be accelerated to energies of 1MeV and higher by Ion Cyclotron Resonance Heating (ICRH). In order to quantify what effect TAEs destabilised by fast α-particles could be expected to cause, TAEs excited by ICRH-generated fast ions and ICRH beatwaves were studied. This is of special interest to ITER and any future fusion devices, as α-particles are the dominant fast ion species and the main source of energy to maintain a burning plasma.

Chapter 2 will begin with a description of motion of charged particles in a magnetic field followed by an introduction to Ideal Magnetohydrodynamics, a single fluid model for perfectly conducting plasmas. This will then be used to describe the plasma equilibrium, plasma waves, and perturbation of the equilibrium by instabilities. The remaining sections of this chapter will cover plasma diagnostics, the reconstruction of the equilibrium current density and pressure profiles at ASDEX Upgrade, the methods by which fast ions are generated in ASDEX Upgrade, and the behaviour of fast ions (supra-thermal ion). In chapter 3 the theory and effects of TAEs and other important plasma instabilities, such as the sawtooth and Fishbone instabilities and neo-classical tearing modes, are introduced. The experimental scenarios in which TAEs were studied are presented in chapter 4. Chapters 5 and 6 represent a characterisation of TAEs at ASDEX Upgrade destabilised using ion cyclotron resonance heating (ICRH) and ICRH beatwaves. Chapter 7 demonstrates how TAEs can be used to improve equilibrium current density and pressure profiles. This will be followed by conclusions, an outlook, and appendices.

Chapter 2

Theoretical Background

2.1 Motion of Charged Particles in Electromagnetic Fields

The Lorentz force experienced by a charged particle moving in an electromagnetic field binds it tightly to the magnetic field line. In magnetically confined tokamak fusion plasmas the Lorentz force must be strong enough to dominate all other forces, so as to hinder particle transport perpendicular to the magnetic field. There are two important features of the Tokamak design which make it a viable candidate for a fusion reactor. The first feature is that its toroidal geometry removes end losses experienced by linear devices with magnetic mirrors, leading to an increased energy confinement time over such devices. Secondly, the helical nature of the magnetic field counteracts vertical particle drifts arising from the curvature and gradient in the toroidal component of the magnetic field. This in turn eliminates the $\vec{E} \times \vec{B}$ induced outward drift of the entire plasma, which would result from the charge separation caused by such vertical particle drifts[9].

In a fully ionised plasma, charged particles rarely experience large angle deflections through Coulomb collisions, instead the particle's orbit is deflected many times by small interactions[10][15].

Motion in a constant magnetic Field

The motion of a particle of mass m, carrying a charge q, moving with a velocity $\vec{v}$ in a constant magnetic field $\vec{B}$ is defined by the following equation,

$$m\dot{\vec{v}} = q(\vec{v} \times \vec{B}) \tag{2.1}$$

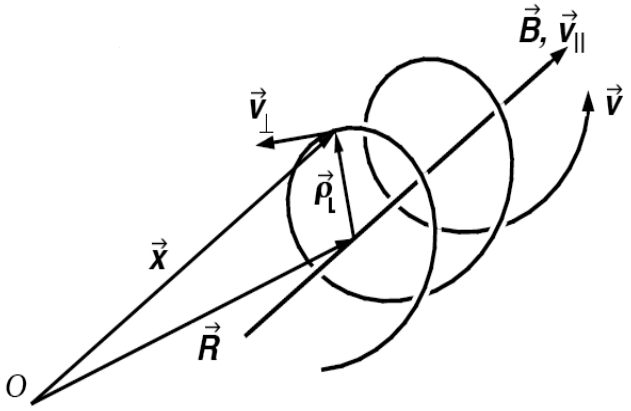

Figure 2.1: Definition of guiding centre co-ordinates.

This is the Lorentz force. Since the Lorentz force is always perpendicular to the particle's velocity, its direction can change but not its magnitude and so, neglecting the slow rate of energy loss due to cyclotron radiation, the particle's kinetic energy remains unchanged. Decomposing the particle velocity $\vec{v} = \vec{v}_{\|} + \vec{v}_{\perp}$ in to components parallel and perpendicular to the magnetic field as seen figure 2.1 and substituting it into equation 2.1, reveals that the perpendicular motion alone interacts with the magnetic field leading to a circular motion perpendicular to $\vec{B}$

$$m\dot{\vec{v}}_{\|} = 0 \tag{2.2}$$

$$m\dot{\vec{v}}_{\perp} = q(\vec{v}_{\perp} \times \vec{B}). \tag{2.3}$$

The centrifugal force $mv_{\perp}^2/\rho_L$ balances the Lorentz force $qv_{\perp}B$ at the radius $\rho_L = \frac{mv_{\perp}}{|q|B}$ called the Larmor radius. This circular motion has an associated frequency $\omega_c = |q|B/m$ called the cyclotron frequency. In figure 2.1 the position vector of the particle $\vec{x} = \vec{R} + \vec{\rho}_L$ is separated into two components, the vector $\vec{R}$ along the magnetic field, known as the position of the "guiding centre" and the position vector $\vec{\rho}_L = -m\vec{v} \times \vec{B}/(qB^2)$ of the particle in its orbit of gyration.

The gyrating particle has an associated magnetic moment μ defined as the product of the current I times the area A surrounded by the current. This leads to the value of $\mu = IA = (q\omega_c/[2\pi])(\pi\rho_L^2) = mv_{\perp}^2/2B$. Tokamak plasmas are normally diamagnetic, with gyro-orbits of ions and electrons being such as to reduce the applied magnetic field, however situations can occur where paramagnetic behaviour can occur[9]. This occurs even though ions gyrate in the opposite sense to electrons, as each carries a net

charge opposite to the other. Thus the product of their their motion and charge result in currents flowing in the same direction, which in turn produces parallel magnetic fields, that can be shown to be oriented in the direction opposite to the external magnetic field by the application of the Biot-Savart law.

In Tokamak experiments, the magnetic field strength is chosen, such that the Lorentz force dominates all other forces, and that the gyro-radius ρ_L and gyro-period of the particle motion about the field lines are the shortest length and time scales. This means that the particle's trajectory is well described by the motion of the guiding centre.

Particle motion in a constant magnetic field due to an additional force $\vec{F}$

If an additional force $\vec{F}$ acts on the charged particle then the equation of motion becomes

$$m\dot{\vec{v}} = q(\vec{v}\times\vec{B}) + \vec{F}. \tag{2.4}$$

The motion of the particle under the influence of $\vec{F}$ can be separated from the gyrating motion if the position of particle's guiding centre is considered alone. The velocity of the guiding centre $\vec{v}_g$ is found by differentiating $\vec{R}$:

$$\vec{v}_g = \dot{\vec{R}} = \dot{\vec{x}} - \dot{\vec{\rho}}_L \tag{2.5}$$

$$= \vec{v} + \frac{m}{qB^2}\dot{\vec{v}}\times\vec{B} \tag{2.6}$$

$$= \vec{v} + \frac{1}{qB^2}(q(\vec{v}\times\vec{B}) + \vec{F})\times\vec{B}. \tag{2.7}$$

Since $(\vec{v}\times\vec{B})\times\vec{B} = -\vec{v}_\perp B^2$ and $\vec{v}_\parallel = \vec{v} - \vec{v}_\perp$, we find that

$$\vec{v}_g = \vec{v}_\parallel + \frac{1}{qB^2}\vec{F}\times\vec{B}. \tag{2.8}$$

From this one can see that a force perpendicular to $\vec{B}$ leads to a drift of the particle orbit, perpendicular to both $\vec{F}$ and $\vec{B}$. A force parallel to $\vec{B}$ accelerates the particle along the magnetic line, but does not lead to a perpendicular drift. Therefore an arbitrary force $\vec{F} = \vec{F}_\perp + \vec{F}_\parallel$ results in the following drift perpendicular and acceleration parallel, to $\vec{B}$:

$$\vec{v}_g = \frac{1}{qB^2}\vec{F}_\perp\times\vec{B} \tag{2.9}$$

$$\dot{\vec{v}}_{g,\parallel} = \frac{\vec{F}_\parallel}{m}. \tag{2.10}$$

The $\vec{E} \times \vec{B}$ drift

If a charged particle is acted upon by a constant electric field, then resulting force it experiences is $\vec{F} = q\vec{E}$. This force, provided it is not parallel to $\vec{B}$, causes the particle orbits to drift. The drift velocity which arises is

$$\vec{v}_{E\times B} = \frac{1}{B^2}\vec{E} \times \vec{B}. \tag{2.11}$$

Since this drift velocity is independent of the particle's charge and mass, the ions and electrons experience a drift in the same direction. This leads to a net flow of particles, but not a current.

The Polarisation drift

In a spatially constant time dependent electric field $\vec{E}(t)$ a particle experiences an force perpendicular to $\vec{B}$. This force can be taken as being equivalent to

$$\vec{F}_p = \frac{m}{B^2}\frac{d\vec{E}}{dt} \times \vec{B}. \tag{2.12}$$

Through this force the particle orbits drift with the velocity

$$\vec{v}_p = -\frac{m}{qB^2}\left(\frac{d\vec{E}}{dt}\right)_\perp = -\frac{sgn(q)}{\omega_c B}\left(\frac{d\vec{E}}{dt}\right)_\perp \tag{2.13}$$

where $sgn(q)$ is the sign of the electrical charge q, which is -1 for electrons and +1 for ions. The resulting drift velocity is in opposite directions for ions and electrons because of the dependency on the particle charge q. However it is much larger for ions as the ion mass is considerably larger than the electron mass. If the individual particle density is denoted by n_i then the total current density arising from the particle drift for all particle species i is $\vec{j}_p = \sum_i n_i q_i \vec{v}_{pi}$. Using the formula for $\vec{v}_p$ the total polarisation current density is

$$\vec{j}_p = \frac{\rho_m}{B^2}\frac{d\vec{E}}{dt}, \tag{2.14}$$

where $\rho_m = \sum_i n_i m_i$ is the total mass density.

The Curvature drift

If magnetic field with a non zero curvature varies relatively little spatially along one gyration of the particle, then equation 2.8 can be used to analyse the resulting drift motion. The corresponding

force felt by a particle is $\vec{F}_c = mv_\parallel^2 \vec{R}_c / R_c^2$, where $\vec{R}_c$ is the curvature radius vector. The drift velocity associated with this curvature force is

$$\vec{v}_c = -\frac{mv_\parallel^2}{qB^2 R_c^2} \vec{R}_c \times \vec{B}. \tag{2.15}$$

Due to the dependence of this drift velocity on both the mass and charge of the particle, this drift will be of different magnitude and sign for ions and electrons.

The $\vec{\nabla}B$ drift

The transverse gradient of the magnetic field is the source of an additional particle drift. This arises because the particle's orbit has a smaller radius of curvature in the region containing a stronger magnetic field. This force however is not constant and therefore can not be treated using equation 2.8 directly. To understand the effect transverse gradient has on a particle, we will consider the averaged effect of $\vec{\nabla}B$ on the particle's gyration orbit instead. This amounts to the force

$$\vec{F}_{\nabla B} = -\mu \vec{\nabla} B \tag{2.16}$$

averaged over the gyration orbit. This force is constant with respect to the particle and can be analysed using equation 2.8. This gives a drift velocity

$$\vec{v}_{\nabla B} = -\frac{1}{qB^2} \left\langle \mu \vec{\nabla} B \right\rangle \times \vec{B}. \tag{2.17}$$

This force also leads to different drifts for different particle species.

The $\vec{\nabla}p$ drift

In a magnetically confined conducting fluid, the kinetic pressure gradient must be balanced exactly by the Lorentz force per unit volume, this is represented by the force balance equation for a conducting fluid $\vec{\nabla}p = \vec{j} \times \vec{B}$ (equation 2.44). If one takes each particle species to be a separate fluid, then the force balance must hold for each species individually. This amounts to $\vec{\nabla}p_i = \vec{j}_i \times \vec{B}$ for each fluid, composed solely of particle of species i, where $\vec{j}_i = n_i q_i v_i$. Taking the cross product of the force per ion $\vec{\nabla}p_i/(n_i)$ with $\vec{B}$ gives an equation for a drift velocity of each fluid perpendicular to the magnetic field.

$$\vec{v}_{di} = -\frac{\vec{\nabla}p_i \times \vec{B}}{n_i q_i B^2} \tag{2.18}$$

This $\vec{v}_{di}$ is known as the diamagnetic drift velocity and is in the opposite directions for ions and electrons.

Anomalous transport

In a tokamak plasma the collisional transport of particles and energy is called neo-classical transport[1]. However, in practice the experimental confinement times are much shorter than that predicted by neo-classical theory. This is due to transport mechanisms not accounted for in the theory, and is called anomalous transport. It is thought that this *extra* transport is caused by turbulence due to plasma instabilities, which allows energy and particles to escape more rapidly. This could occur as a result of perturbations causing either changes in the nested magnetic field structure or transport across the magnetic field, or both. This can either be small around the same size as the Larmor radius, called micro-instabilities or large global modes called Magnetohydrodynamic (MHD) instabilities.

Adiabatic invariants

When a charged particle performs a periodic motion the action integral $I = \oint PdQ$ taken over one period is a constant of the motion. Here P is the generalised momentum and Q is the corresponding coordinate. For changes in the system which are slow compared to the characteristic time of the periodic motion, I remains constant and is called an Adiabatic Invariant.

The first adiabatic invariant is the magnetic moment μ associated with a gyrating particles orbit[11][10]. Here the periodic motion is the Larmor gyration, where $P = mv_\perp \rho_L$ is the angular momentum and $dQ = d\phi$ is the change in the corresponding angle ϕ. From this we find that $I = \oint PdQ = \oint mv_\perp \rho_L d\phi = 2\pi\rho_L mv_\perp = 4\pi\frac{m}{q}\mu$. Now since I is a constant, μ must remain constant, once the charge q does not change.

If the particle has a larger periodic motion than the gyration about the magnetic field lines, an invariant of that motion $J = \oint v_\parallel \, dl$ over that larger periodic orbit can be defined. If there is no electric field present then the total energy $W = \frac{1}{2}m(v_\parallel^2 + v_\perp^2)$ of the particle remains constant. Re-expressing the equation for W, using the magnetic moment μ, we arrive at an equation for $v_\parallel$ in terms of the constants of the motion and the magnetic field:

$$v_\parallel = \left(\frac{2}{m}(W - \mu B)\right)^{\frac{1}{2}}. \tag{2.19}$$

An example of such a motion is a charged particle between caught between two magnetic mirrors.

If the periodic motion involved in J has drifts associated with it, these drift velocities v_d can themselves lead to larger scale periodic motion. A third adiabatic invariant $K = \oint v_d \, dl$ can be

associated with this periodic motion.

Particle trapping in a magnetic field

As the guiding centre of a charged particle enters a region of larger magnetic field strength, it experiences a parallel deceleration

$$m\dot{\vec{v}}_{\|} = -\mu\vec{\nabla}_{\|}B \tag{2.20}$$

and if B is large enough it will be reflected. Taking the constancy of μ and energy conservation in the absence of an electric field as given, in equation 2.19, $v_{\|}$ decreases as B increases and finally reaches zero at $B = B_{max}$. Therefore the criterion for particle trapping ($v_{\|} = 0$) is

$$W \leq \mu B_{max}. \tag{2.21}$$

Particle orbits in a Tokamak

In a tokamak with a large inverse aspect ratio, the maximum of the magnetic field strength B_{max} is at the separatrix on the high field side of the torus, where $R = R_{min}(separatrix)$ (see figure 2.2) and decays radially away from the centre with increasing R. As a particle travels along a magnetic field line it will experience a periodic mirror force as is travels around the tokamak toroidally. If the magnetic moment and energy of this particle are such that $W > \mu B_{max}$ it will not be reflected, and will continue encircling the torus (figure 2.2a). These are referred to as circulating or passing particles. On the other hand, if $W < \mu B_{max}$ then the particle will be reflected at the turning point where $B = B_{tp} = \frac{W}{\mu}$ (figure 2.2b). This particle is then trapped between these two turning points and will execute a periodic motion along the field line. Due to the non-uniformity of the magnetic field all particle guiding centre orbits are subject to a drift $v_d = \frac{m(v_{\|}^2 + \frac{1}{2}v_{\perp}^2)}{qRB_{\phi}}$ away from the magnetic flux surface upon which the magnetic field line they would gyrate about lies in the absence of the drift. Here B_{ϕ} is the toroidal magnetic field strength. This modified orbit is called the guiding centre drift orbit.

For a passing particle, the guiding centre drift orbit has the form[10]

$$(R - R_0 - \frac{v_d}{\omega})^2 + z^2 = constant \tag{2.22}$$

in the poloidal plane, where ω is the poloidal rotation frequency of the particle, z is the vertical coordinate and R_0 is the centre of the flux surface along the major radius. This shows that passing particle

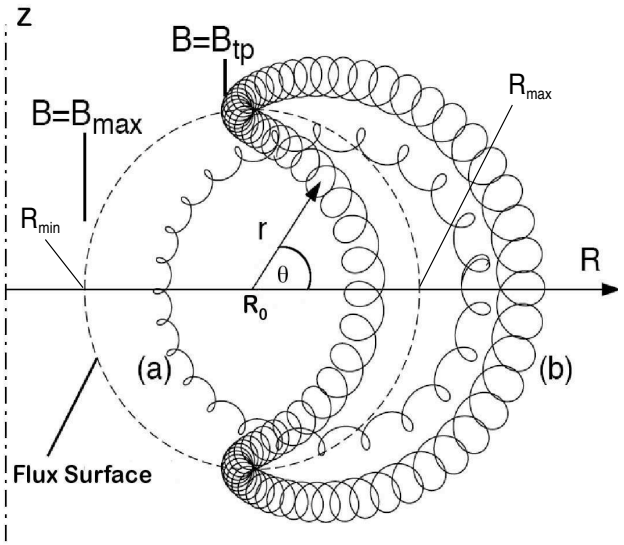

Figure 2.2: The projection of a circulating a) and trapped b) particle orbit onto the poloidal plane in a tokamak, where R is the distance from the vertical axis.

orbits are circular surfaces displaced from the magnetic flux surface by a distance $d = \frac{v_d}{\omega}$, see figure 2.2 (a).

Taking $R = R_0 + r\,cos\theta$ (see figure 2.2) the parallel gradient of the magnetic field line $\frac{dB}{ds}$ can be calculated using the equation for the magnetic field in a circular plasma

$$B = B_0 \frac{R_0}{R} = \frac{B_0}{1 + (r/R_0 cos\theta)} \tag{2.23}$$

where s is the curve length along the field line. Assuming $\theta = v_{\|0}/v_{\perp 0} \ll 1$ (deeply trapped particles), where $v_{\|0}$ and $v_{\perp 0}$ are the initial parallel and perpendicular velocities, and large aspect ratio $r/R_0 \ll 1$, one gets the following equation

$$\frac{dB}{ds} = \frac{rB_0}{R_0} \frac{d(\theta^2/2)}{ds} \tag{2.24}$$

for the parallel gradient. When equation 2.20 is written in terms of s, it becomes

$$\frac{d^2 s}{dt^2} = -\mu \frac{dB}{ds}. \tag{2.25}$$

Now combining the equation of a magnetic field line

$$r d\theta/ds = B_\theta/B \tag{2.26}$$

with equation 2.25, one arrives at the following equation

$$\frac{d^2s}{dt^2} = -\omega_b^2 s \tag{2.27}$$

where $\omega_b = \frac{v_{\perp} R_0 B_\theta}{r B_0} \left(\frac{r}{2R_0}\right)^{1/2}$ is the bounce frequency and B_θ is the poloidal magnetic field strength. This gives equation of motion along the field line $s = s_b \sin\omega_b t$. Solving the field line equation for θ, one sees that $\theta = (B_\theta / rB)s \propto s$. Therefore $\theta = \theta_b \sin\omega_b t$. Using the bounce condition $\frac{B_{tp}}{B_{min}} = 1 + \frac{r}{R_0}\frac{\theta_b^2}{2} = 1 + \left(\frac{v_{\parallel 0}}{v_{\perp 0}}\right)^2$ [10], one arrives at the expression

$$\theta_b = \frac{v_{\parallel 0}}{v_{\perp 0}} \left(\frac{2R_0}{r}\right)^{1/2} \tag{2.28}$$

with $B_{min} = B_0 R_0/(R_0 + r)$. For $v_\parallel \ll v_\perp$, the drift velocity becomes $v_d = \frac{1}{2} m v_\perp^2 / qRB_\phi$ and in this case the equation of the drift surface is

$$(r - r_0)^2 = \left(\frac{\theta_b v_d}{\omega_b}\right)^2 \left(1 - \left(\frac{\theta}{\theta_b}\right)^2\right) \tag{2.29}$$

where $\Delta r = \frac{\theta_b v_d}{\omega_b}$ is the half width of the orbit. In figure 2.2 (b) these orbits have the shape of a banana, and are hence referred to as banana orbits.

In the analysis of trapped particle orbits, it was always assumed that the deviation from the flux surface was small. However particles such as fusion born $\alpha - particles$ can have Larmor radii of the order of tens of centimetres, leading to much broader orbits. These orbits are called potato orbits.

2.2 The Ideal MagnetoHydroDynamic (MHD) model

Ideal MagnetoHydroDynamics (MHD) is a single fluid description of a plasma[10][12]. To formulate a single fluid description, it is first necessary to define the mass density, fluid velocity and current density as follows:

$$\rho = m_i n_i + m_e n_e \simeq m_i n_i \tag{2.30}$$

$$\vec{v} = \frac{1}{\rho}(m_i n_i \vec{v}_i + m_e n_e \vec{v}_e) \simeq \vec{v}_i \tag{2.31}$$

$$\vec{J} = e(Z n_i \vec{v}_i - n_e \vec{v}_e) \tag{2.32}$$

where n_i and n_e are the ion and electron number densities, m_i and m_e are the ion and electron masses, $\vec{v}_i$ and $\vec{v}_e$ are the ion and electron fluid velocities and Z is the ion atomic number. To attain the smallest closed set of fluid equations to combine with Maxwell's equations in order to describe the plasma,

it is necessary to assume that all particle motion is adiabatic. Combining this with the additional assumptions that the plasma is perfectly conducting, and electron inertia and the displacement current are negligible, gives rise the following set of equations that are the 'Ideal MHD' model.

$$\frac{\partial \rho}{\partial t} + \vec{\nabla} \cdot (\rho \vec{v}) = 0 \quad \text{(Mass conservation)} \tag{2.33}$$

$$\rho \frac{\partial \vec{v}}{\partial t} + \rho \vec{v} \cdot \vec{\nabla} \vec{v} + \vec{\nabla} p - \vec{J} \times \vec{B} = 0 \quad \text{(Momentum balance)} \tag{2.34}$$

$$\frac{\partial p}{\partial t} + \vec{v} \cdot \vec{\nabla} p + \gamma p \vec{\nabla} \cdot \vec{v} = 0 \quad \text{(Adiabatic equation of state)} \tag{2.35}$$

$$\vec{E} + \vec{v} \times \vec{B} = 0 \quad \text{(Ohm's Law)} \tag{2.36}$$

$$\vec{\nabla} \cdot \vec{B} = 0 \quad \text{(No magnetic mono-poles)} \tag{2.37}$$

$$\vec{\nabla} \times \vec{B} - \mu_0 \vec{J} = 0 \quad \text{(Ampère's Law)} \tag{2.38}$$

$$\frac{\partial \vec{B}}{\partial t} + \vec{\nabla} \times \vec{E} = 0 \quad \text{(Faraday's Law)} \tag{2.39}$$

Here $p = p_i + p_e$ is the sum of the ion and electron plasma pressures and $\gamma = 5/3$ is the adiabatic index. The electric and magnetic field, $\vec{E}$ and $\vec{B}$, that appear in these expressions consist of the externally applied fields and the averaged internal fields arising from the long-range particle interactions.

In order to account for electrical resistance, only a small modification to the above system of equations is necessary to recover the 'Resistive MHD' model. The necessary changes are to replace $\vec{E} + \vec{v} \times \vec{B} = 0$ with $\vec{E} + \vec{v} \times \vec{B} = \eta \vec{J}$ and

$$\frac{\partial p}{\partial t} = -\vec{v} \cdot \vec{\nabla} p - \gamma p \vec{\nabla} \cdot \vec{v} \tag{2.40}$$

with

$$\frac{d}{dt} \left(\frac{p}{\gamma - 1} \right) = -\frac{\gamma}{\gamma - 1} p \vec{\nabla} \cdot \vec{v} - \eta J^2 \tag{2.41}$$

where η is the plasma resistivity. To represent an incompressible fluid $\vec{\nabla} \cdot \vec{v}$ must be set to zero.

2.3 The Plasma Equilibrium

2.3.1 The Grad-Shrafranov Equation (GSE)

In the plasma rest frame for a steady-state (or slowly evolving) plasma, one sets $\vec{v} = 0$ and takes $\frac{d}{dt} = 0$ in the system of equations 2.33 - 2.39 to get [10][14]

$$\vec{\nabla} \cdot \vec{B} = 0, \tag{2.42}$$

$$\vec{J} \times \vec{B} = \mu_0{}^{-1} (\vec{\nabla} \times \vec{B}) \times \vec{B} = \vec{\nabla} p. \tag{2.43}$$

The basic condition for equilibrium is that the force on the plasma be zero at all points in the plasma. This means that the Lorentz force density, $\vec{J} \times \vec{B}$, will balance the force density due to the plasma pressure, p,

$$\vec{J} \times \vec{B} = \vec{\nabla} p. \tag{2.44}$$

From equation 2.44 it follows that $\vec{B} \cdot \vec{\nabla} p = 0$. This implies that there is no difference in pressure along the magnetic field lines and the magnetic surfaces are also surfaces of constant pressure. In addition equation 2.44 gives $\vec{J} \cdot \vec{\nabla} p = 0$, so the current lines also lie in surfaces of constant pressure.

For a given toroidal magnetic surface consider the *cut surfaces* S_{pol}, spanning the toroid, and the poloidal cross-section of the toroid S_{tor} shown in figure 2.3. Through any cross-section of the toroid, S_{tor}, the *toroidal flux* is

$$\Psi_{tor} = \int_{S_{tor}} \vec{B} \cdot \vec{dS} \tag{2.45}$$

while through any cut surface spanning the hole in the toroid, S_{pol} the *poloidal flux* is

$$\Psi_{pol} = \int_{S_{pol}} \vec{B} \cdot \vec{dS}. \tag{2.46}$$

Using $\vec{\nabla} \cdot \vec{B} = 0$ and Gauss' theorem, it can be shown that the flux is the same for all surfaces spanning the same contour. Furthermore, there is no flux through the toroidal magnetic surface since $\vec{B}$ is everywhere tangent to it. Therefore, the flux is the same through any topologically equivalent contour on the flux surface. A *surface quantity* is any variable that is uniform over a magnetic surface. It follows that both Ψ_{tor} and Ψ_{pol} are surface quantities.

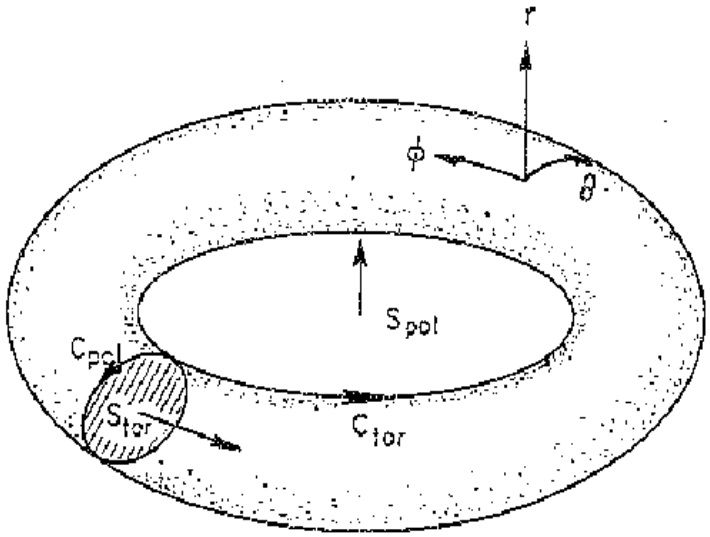

Figure 2.3: Toroidal flux surface showing cut surfaces and contours.

Axisymmetric equilibrium. In the case of axisymmetry ($\frac{\partial}{\partial\phi} = 0$) in cylindrical co-ordinates (R, ϕ, z), the equilibrium equation (2.44) reduces to a scalar partial differential equation[14].

Firstly, one can write the total magnetic field as $\vec{B} = \vec{B}_\phi + \vec{B}_\theta$ where $\vec{B}_\phi = (0, B_\phi, 0)$ and $\vec{B}_\theta = (B_R, 0, B_Z)$. Note all three components are functions of R, z only. Writing $\vec{B}_\theta = \nabla \times \vec{A}$ one finds that

$$\vec{B}_\theta = \left(-\frac{\partial A_\phi}{\partial Z}, \frac{\partial A_R}{\partial Z} - \frac{\partial A_Z}{\partial R}, \frac{1}{R}\frac{\partial R A_\phi}{\partial R} \right). \tag{2.47}$$

The only constraint on A_R and A_Z is that the ϕ component of $\vec{B}_\theta$ vanish. Here the simplest solution is to set $A_R = A_Z = 0$. With this we can define $\vec{B}$ as $\vec{B} = \vec{\nabla} \times (A_\phi \hat{\phi}) + B_\phi \hat{\phi}$. To express A_ϕ in terms of the poloidal flux enclosed by a magnetic surface, one uses Stokes' theorem with the contour C_{pol} (a circle of radius R) as follows:

$$\begin{aligned} \Psi_{pol} &= \int_{S_{pol}} \vec{B} \cdot \vec{dS} \\ &= \int_{S_{pol}} \left(\vec{\nabla} \times (A_\phi \hat{\phi}) \right) \cdot \vec{dS} + \int_{S_{pol}} B_\phi \hat{\phi} \cdot \vec{dS} \\ &= \oint_{C_{pol}} A_\phi \hat{\phi} \cdot \vec{dl} \; + \; 0 \\ &= 2\pi R A_\phi. \end{aligned} \tag{2.48}$$

Defining a stream function $\Psi \equiv \Psi_{pol}/2\pi$, one now finds (note $\vec{\nabla}\phi = \frac{1}{R}\hat{\phi}$) that $\vec{B}$ can be expressed as

$$\begin{aligned}\vec{B} &= \vec{\nabla} \times (\Psi\vec{\nabla}\phi) + B_\phi\hat{\phi}, \\ &= \vec{\nabla}\Psi \times \vec{\nabla}\phi + B_\phi\hat{\phi}, \\ &= -\frac{1}{R}\frac{\partial\Psi}{\partial Z}\vec{R} + \frac{1}{R}\frac{\partial\Psi}{\partial R}\hat{Z} + B_\phi\hat{\phi}.\end{aligned} \tag{2.49}$$

Since $\Psi \propto \Psi_{pol}$, it is a surface quantity, and it may be used to uniquely label the flux surfaces. Thus any surface quantity can also be regarded as a *flux function*. Using equation 2.49, the current density $\vec{J} = {\mu_0}^{-1}\vec{\nabla} \times \vec{B}$ can be expressed in the form

$$\begin{aligned}\mu_0\vec{J} &= \vec{\nabla} \times \vec{B}_\theta + \vec{\nabla} \times \vec{B}_\phi \\ &= \left(-\frac{1}{R}\frac{\partial^2\Psi}{\partial Z^2} - \frac{\partial}{\partial R}\frac{1}{R}\frac{\partial\Psi}{\partial R}\right)\hat{\phi} + \vec{\nabla} \times (B_\phi R\vec{\nabla}\phi) \\ &= -\frac{1}{R}\Delta^*\Psi\,\hat{\phi} + \vec{\nabla}(RB_\phi) \times \vec{\nabla}\phi\end{aligned} \tag{2.50}$$

where Δ^* is a special operator defined by

$$\Delta^*\Psi \equiv R\frac{\partial}{\partial R}\frac{1}{R}\frac{\partial\Psi}{\partial R} + \frac{\partial^2\Psi}{\partial Z^2}. \tag{2.51}$$

The choice of the latter symbol is due to its similarity to the Laplacian in cylindrical co-ordinates.

From $\vec{B}\cdot\vec{\nabla}p = \vec{B}\cdot(\vec{J}\times\vec{B}) = 0$ it follows that the pressure is a surface quantity, such that $p = p(\Psi)$. Substitution of equations 2.49 and 2.50 into the force balance equation $\vec{\nabla}p = \vec{J} \times \vec{B}$ yields (note in the following cross product expansion $\vec{\nabla}(RB_\phi)\cdot\hat{\phi} = 0$ by axisymmetry)

$$\begin{aligned}\mu_0 p'(\Psi)\vec{\nabla}\Psi &= \left(-\frac{1}{R}\Delta^*\Psi\,\hat{\phi} + \vec{\nabla}(RB_\phi) \times \vec{\nabla}\phi\right) \times \left(\vec{\nabla}\Psi \times \vec{\nabla}\phi + B_\phi\hat{\phi}\right) \\ &= -\frac{1}{R^2}\Delta^*\Psi\vec{\nabla}\Psi\; - \frac{B_\phi}{R}\vec{\nabla}(RB_\phi).\end{aligned} \tag{2.52}$$

For this equation to hold everywhere, one must have $\vec{\nabla}(RB_\phi) \parallel \vec{\nabla}\Psi$. Thus RB_ϕ must be a function of Ψ, say $F(\Psi)$, and therefore a surface quantity.

Since $\vec{J}\cdot\vec{\nabla}p = 0$, current density field lines must also lie on magnetic surfaces. Hence the poloidal current $I_{pol} = \int_{S_{pol}} \vec{J}\cdot\vec{dS}$ must also be a flux function. We see this by substituting for $\vec{J}$ using equation

2.50 yielding

$$\begin{aligned}\mu_0 I_{pol} &= \int_{S_{pol}} \vec{\nabla}\times\vec{B}\cdot\vec{dS} \\ &= \int_{S_{pol}} -\frac{1}{R}\Delta^*\Psi\hat{\phi}\cdot\vec{dS} + \int_{S_{pol}} \left(\vec{\nabla}\times(B_\phi R\vec{\nabla}\phi)\right)\cdot\vec{dS} \\ &= 0 + \oint_{C_{pol}} B_\phi\hat{\phi}\cdot\vec{dl} \\ &= 2\pi R B_\phi.\end{aligned} \tag{2.53}$$

Thus $RB_\phi \equiv F(\Psi) = \mu_0 I_{pol}/2\pi$ is proportional to the poloidal current. Then by rearranging equation 2.52, one obtains

$$-\Delta^*\Psi = \mu_0 R^2\, p'(\Psi) + FF'(\Psi), \tag{2.54}$$

where p and F are arbitrary functions of Ψ alone. Equation 2.54 is commonly known as the Grad-Shafranov equation (GSE). Equation 2.50 can now be expressed as

$$\begin{aligned}\mu_0\vec{J} &= -\frac{1}{R}\Delta^*\Psi\hat{\phi} + F'(\Psi)\vec{\nabla}\Psi\times\vec{\nabla}\phi \\ &= -\frac{1}{R}\Delta^*\Psi\hat{\phi} - \frac{F'}{R}\frac{\partial\Psi}{\partial Z}\hat{R} + \frac{F'}{R}\frac{\partial\Psi}{\partial R}\hat{Z} \\ &\equiv \mu_0\vec{J}_\phi + \mu_0\vec{J}_\theta,\end{aligned} \tag{2.55}$$

so that one may write the Grad-Shafranov equation in a more compact form, namely,

$$-\Delta^*\Psi = \mu_0 R\vec{J}_\phi. \tag{2.56}$$

2.3.2 The Safety factor q and plasma β

As was previously discussed, the magnetic topology in a tokamak is set of nested toroidal flux surfaces each uniquely identified by the poloidal flux function Ψ, while field lines follow helical paths as they go around the torus on their associated magnetic surface.

The q value of a field line is defined as the ratio of the toroidal angle $\Delta\phi$ swept out by a field line as it makes one complete poloidal revolution of the torus, namely,

$$q = \frac{\Delta\phi}{2\pi}. \tag{2.57}$$

Using the equation of field line, equation 2.26, one can calculate q in terms of the toroidal and poloidal magnetic fields, which is

$$q = \frac{1}{2\pi}\oint \frac{1}{R}\frac{B_\phi}{B_\theta} ds, \tag{2.58}$$

where ds is the distance moved in the poloidal direction while moving through a toroidal angle angle $d\phi$[10]. The magnetic surfaces with a rational q value are important for MHD stability. If an MHD instability has the form $e^{i(m\theta - n\phi)}$, where m and n are integers corresponding to the poloidal and toroidal modes numbers respectively, the stabilising effect of line bending is minimised on the magnetic surfaces for which the magnetic field helix matches that of the mode, or equivalently $q = \frac{m}{n}$.

The local plasma β is the ratio of the plasma energy density to the magnetic field energy and is defined as follows,

$$\beta = \frac{p}{\left(\frac{B^2}{2\mu_0}\right)}. \tag{2.59}$$

Here p is the total plasma pressure and B is the magnetic field strength.

2.3.3 Reconstructing Experimental Equilibria - the CLISTE Code

The Grad-Shafranov equation is a weakly non-linear elliptic PDE which is solved by specifying the functions $p = p(\Psi)$ and $F = F(\Psi)$, together with boundary conditions or externally imposed constraints on Ψ, and then inverting equation 2.54 to determine $\Psi = \Psi(R,z)$.

CLISTE[1] is an acronym for CompLete Interpretive Suite for Tokamak Equilibria. The CLISTE code[49] finds a numerical solution to the Grad-Shafranov equation 2.54 for a given set of poloidal field coil currents and limiter structures by varying the free parameters in the parameterisation of the $p'(\Psi)$ and $FF'(\Psi)$ source profiles which define the toroidal current density profile J_ϕ so as to obtain a best fit in the least squares sense to a set of experimental measurements. These measurements can include external magnetic data, Motional Stark Effect (MSE) diagnostic data[17], kinetic data[18], q-profile information from Soft X-Ray (SXR) measurements, and other diagnostic data. The free parameters are varied such that the penalty or *cost function* (the squared modulus of the vector of weighted differences between the set of experimental measurements and those predicted by the equilibrium code) of the solution is minimised. The two source profiles in 2.54 are constructed by a linear superposition of basis functions, either cubic splines or polynomials, the magnitudes of which constitute the set of free parameters to be fitted. Among the features of the code are the inclusion of scrape-off layer (SOL) currents in the equilibrium calculations under the assumption that $\vec{j} \times \vec{B} = \vec{\nabla} p$ also holds in the SOL.

[1] klish-teh, Gaelic for clever.

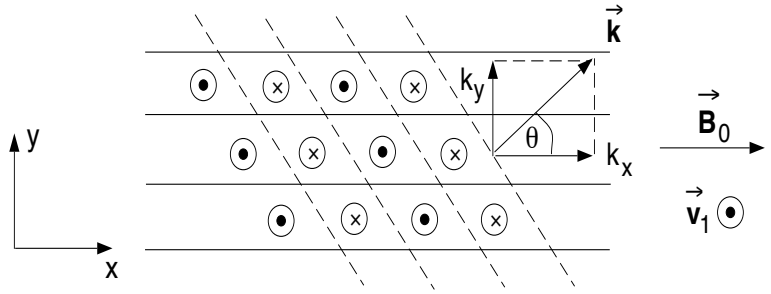

Figure 2.4: Velocity oscillations $\vec{v}$ of shear Alfvén waves from ideal MHD in the plane perpendicular to $\vec{B}_0$ and $\vec{k}$.

The current density is truncated where the open field lines intersect material structures. In addition, return currents through these structures are neglected.

The code proceeds by utilising an algorithm, which is similar to that used in the EFIT[20] code, that is restricted to source profiles which are linear in the free parameters. For more information see the Appendix and [73].

The CLISTE code does not directly use the MHD mode's positions, rather it takes the diameter of the corresponding flux surface $d_{mid} = R_{max} - R_{min}$, where $R_{max} > 0$ and $R_{min} > 0$ are the maximum and minimum radii of the flux surface in the magnetic mid-plane $Z = Z_{mag}$ (see [73], and figure 2.2).

2.4 Alfvén Waves in Ideal MHD

The simplest example of an Alfvén wave occurs when the wave vector is parallel to the magnetic field. The curvature of the bent field lines gives rise to a restoring magnetic tension (force density) $\vec{B} \cdot \vec{\nabla}\vec{B}/\mu_0$ in the opposite direction to the plasma displacement. The inertia is provided by the mass density which is dominated by the ions. In order to describe the general Alfvén wave[12], we will assume a uniform magnetic field and choose a coordinate system with the x-axis along the magnetic field and the wave vector $\vec{k}$ in the x-y plane.

In this choice of coordinate, if we choose the wave displacement to be entirely along the z direction, the solution will be that of the Shear Alfvén wave. The configuration described above is presented in figure 2.4. After linearising the MHD equations 2.33-2.39 and taking the perturbed quantities to vary as $e^{i(-\omega t + k_x x + k_y y)}$ (plane wave solutions), we end up with a set of equations which define our wave.

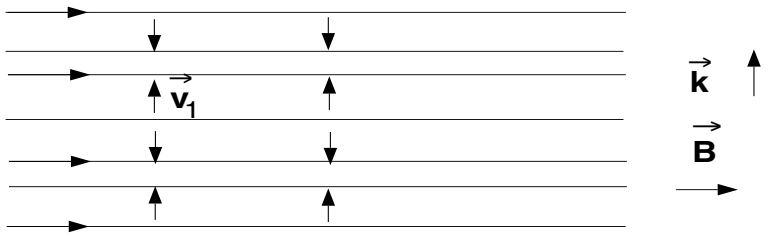

Figure 2.5: Velocity oscillations Magnetosonic waves from ideal MHD in the plane containing $\vec{B}_0$ and $\vec{k}$.

These equations are as follows:

$$\rho\frac{\partial\vec{v}}{\partial t} = \vec{J}\times\vec{B} \quad \rightarrow \quad -\rho i\omega v_{z1} = -J_{y1}B_0 \tag{2.60}$$

$$\vec{J} = \vec{\nabla}\times\vec{B}/\mu_0 \quad \rightarrow \quad J_{y1} = -ik_xB_{z1} \tag{2.61}$$

$$\frac{\partial\vec{B}}{\partial t} = -\vec{\nabla}\times\vec{E} \quad \rightarrow \quad -i\omega B_{z1} = -ik_xE_{y1} + ik_yE_{x1} \tag{2.62}$$

$$\vec{E} = -\vec{v}\times\vec{B} \quad \rightarrow \quad E_{x1} = 0, E_{y1} = -v_{z1}B_0. \tag{2.63}$$

In these equations, equilibrium quantities have the subscript 0, whereas perturbations are labelled with a 1. Solving these set of equations we find the dispersion relation of the wave to be

$$\omega^2 = k_x^2V_A^2, \tag{2.64}$$

where $V_A = \frac{B_0}{\sqrt{\mu_0\rho}}$ is the Alfvén velocity.

If we now choose the wave displacement to be in the x-y plane, the solution we will find will be that of Magnetosonic waves. These waves are governed by the same set of equations as the Shear Alfvén wave with the addition of the adiabatic equation for the plasma pressure. These equations with their linearised forms are:

$$\rho\frac{\partial\vec{v}}{\partial t} = \vec{J}\times\vec{B} \quad \rightarrow \quad -\rho_0 i\omega v_{x1} = -ik_xp_1,\ -\rho_0 i\omega v_{y1} = J_{z1}B_0 - ik_yp_1 \tag{2.65}$$

$$\vec{J} = \vec{\nabla}\times\vec{B}/\mu_0 \quad \rightarrow \quad J_{y1} = i(k_xB_{y1} - k_yB_{x1})/\mu_0 \tag{2.66}$$

$$\frac{\partial\vec{B}}{\partial t} = -\vec{\nabla}\times\vec{E} \quad \rightarrow \quad -i\omega B_{x1} = -ik_yE_{z1},\ -i\omega B_{y1} = -ik_xE_{z1} \tag{2.67}$$

$$\vec{E} = -\vec{v}\times\vec{B} \quad \rightarrow \quad E_{z1} = -v_{y1}B_0 \tag{2.68}$$

$$\frac{\partial p}{\partial t} = -\gamma p\vec{\nabla}\cdot\vec{v} \quad \rightarrow \quad -i\omega p_1 = \gamma p_0 i(k_xv_{x1} + k_yv_{y1}). \tag{2.69}$$

Solving this system of equations, we find the dispersion relation for magnetosonic waves to be

$$(\rho\omega^2 - k_x^2\gamma p)\left(\rho\omega^2 - k_y^2\gamma p - k^2\frac{B_0^2}{\mu_0}\right) = k_x^2k_y^2\gamma^2p^2. \tag{2.70}$$

If we define θ to be the angle between $\vec{k}$ and $\vec{B}_0$, equation 2.70 can be rewritten as

$$\frac{\omega^2}{k^2} = \frac{1}{2}\left[C_s^2 + V_A^2 \pm ((C_s^2 + V_A^2)^2 - 4C_s^2 V_A^2 cos^2\theta)^{1/2}\right], \tag{2.71}$$

where $C_s = \sqrt{\frac{\gamma p}{\rho}}$ is the speed of sound. The wave in equation 2.71 with the positive sign is called the fast magnetosonic wave and the one with the negative sign is the slow magnetosonic wave.

For $\theta = 0$, or equivalently $\vec{k} \parallel \vec{B}$, the fast and slow waves become the shear Alfvén ($\frac{\omega}{k} = V_A$) and sound waves ($\frac{\omega}{k} = C_s$) respectively. If $\vec{k} \perp \vec{B}$ (or $\theta = \frac{\pi}{2}$), the fast wave ($\frac{\omega^2}{k^2} = V_A^2 + C_s^2$) becomes a compressional wave in which both the magnetic field and plasma are compressed. Whereas, the slow wave no longer exists ($\omega = 0$). The fast Alfvén wave under these conditions is shown in figure 2.5.

2.5 Characteristics of MHD instabilities

MHD instabilities play two different roles in fusion experiments. On the one hand, they have a negative influence by limiting the accessible operating regime and restricting the fusion output and minimum power plant size. On the other hand, these instabilities can be used to achieve quasi-stationary discharge conditions and diagnose the plasma.

An MHD instability is characterised by its poloidal and toroidal mode numbers m and n, mode frequency f, net growth rate γ, and the radial structure of the eigenfunction $\vec{\xi}_0$. This leads to the general form of an MHD instability's eigenfunction

$$\vec{\xi} = \vec{\xi}_0(r) e^{i(m\theta + n\phi - 2\pi f t)} e^{\gamma t}. \tag{2.72}$$

The poloidal and toroidal mode numbers determine the helicity of the instability. The difference between the growth and decay rate of the instability are represented together by the net growth rate. The displacement function depends on the type of the instability and varies across the plasma radius.

To demonstrate different forms of MHD instabilities, the field perturbation due to a tearing mode and an ideal kink mode are shown in figure 2.6 together with the radial component of the displacement eigenfunctions. As a result of the finite resistivity of the plasma, the tearing mode causes field lines in the vicinity of the resonant surface to break and reconnect, leading to the formation of magnetic islands in the plasma. An example of its eigenfunction in figure 2.6a shows the change in sign of the eigenfunction which causes the field line tearing. Figure 2.7 shows an example of an m=3 magnetic island structure in the poloidal plane as a result of field line tearing and reconnection. Typically tearing

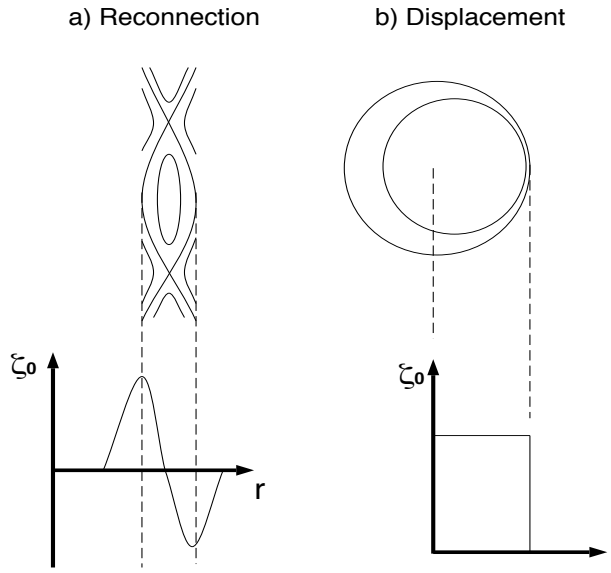

Figure 2.6: a) Magnetic field line breaking and reconnection, and b) a displacement of the magnetic surface.

modes are current driven, however in a high-β plasma an additional pressure driven effect occurs, see section 3.2.3. On the other hand, the internal kink (m=1,n=1) mode is characterised by a rigid shift of the plasma inside the q=1 surface without forming an island. In this case the eigenfunction is a step function. It is the change in sign of the eigenfunction which characterises the mode as a resistive instability, in contrast to an ideal instability which has no sign change in its eigenfunction. Another important difference between these two types of instability is their driving forces and corresponding growth times. These two modes represent typical resistive (tearing mode) and ideal (kink mode) types of MHD activity.

2.6 Plasma Diagnostics

A wide range of diagnostics are used in plasma physics to measure temperature, density, current profile related information and other plasma parameters. Some of these measurements can give information pertaining to plasma instabilities. This work relies most on measurements from: magnetic pickup mirnov coils, soft X-Ray cameras (SXR), electron cyclotron emissions (ECE), microwave reflectometry, Motional Stark Effect (MSE) and the Fast Ion loss detector (FILD). These diagnostics are all in operation in the ASDEX Upgrade tokamak.

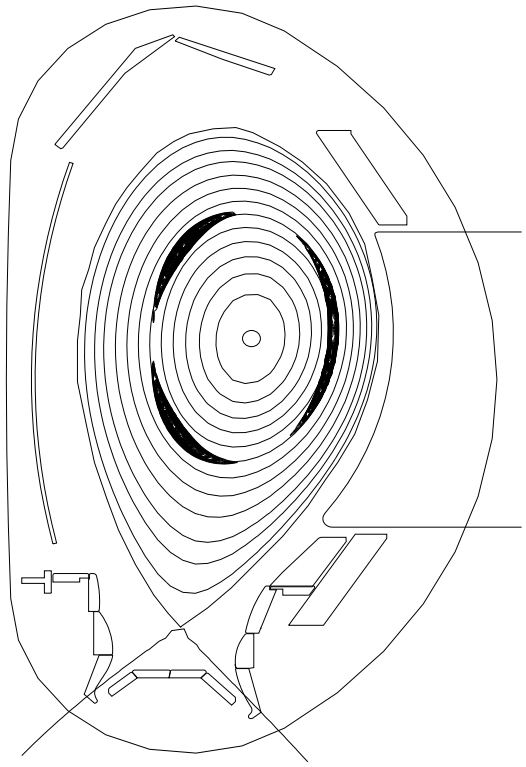

Figure 2.7: m=3 magnetic island structure in the poloidal plane.

2.6.1 Mirnov coils

In ASDEX upgrade magnetic perturbation are measured by a set of 32 poloidal and 10 toroidal mirnov coils with a sampling rate of 2MHz, which measure $\dot{B}_\theta$[2]. In addition there is a set of poloidal and toroidally arranged high frequency ballooning coils which measure $\dot{B}_R$ also with 2MHz sampling. Using these coils, plasma perturbations can be measured at the plasma edge, even if their amplitude is small. This is possible because the coils detect the time derivative of $\vec{B}$ which is equal to $2\pi f B$.

By taking measurements at different toroidal and poloidal locations the magnetic structure of a magnetic perturbation (m,n) can be determined as well as their amplitude, frequency, and growth rate. These quantities are most commonly determined at ASDEX Upgrade using these mirnov coils. The location of these coils toroidally and poloidally are shown in figure 2.8.

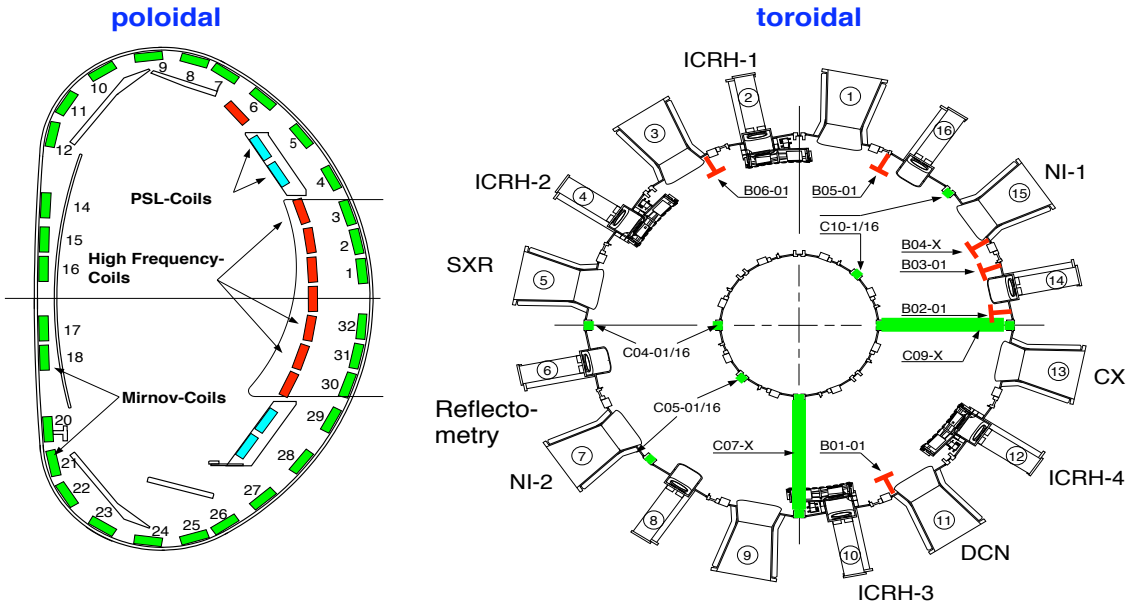

Figure 2.8: Mirnov coil positions as seen in poloidal and toroidal cross sections of ASDEX Upgrade. The green markers represent the toroidal and poloidal standard mirnov coils, the red markers represent the high frequency ballooning coils and the blue markers represent the Passive stabilisation Loop coils (PSL). In the toroidal cross section the location of other diagnostics and heating systems are also shown.

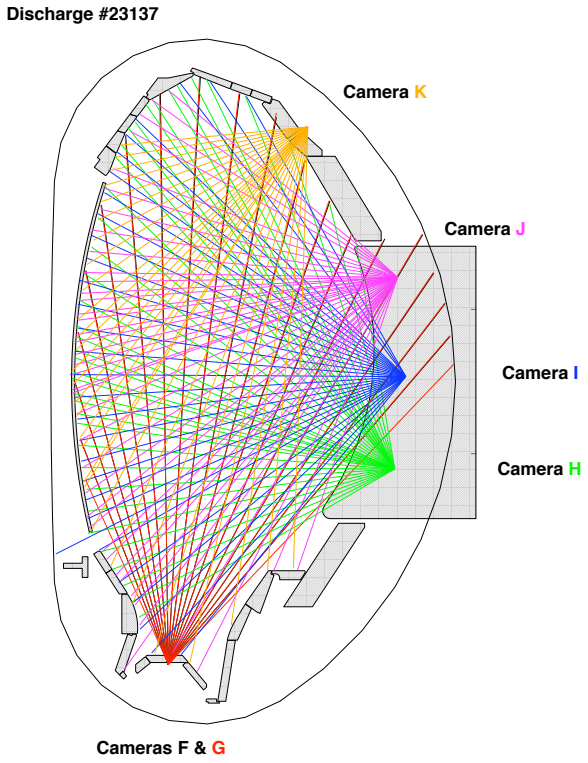

Figure 2.9: The positions and sight lines of the Soft X-Ray cameras K, J, I, H, G & F on ASDEX Upgrade.

2.6.2 Soft X-Ray - SXR

The soft X-ray radiation (SXR)[2] emitted by the plasma is a very good tool to study MHD instabilities in the plasma core[3]. ASDEX Upgrade is equipped with six pinhole SXR cameras with a total of 179 chords[4]. These lines of sight cover the entire plasma volume. Figure 2.9 shows the positions of the SXR cameras K, J, I, H, G, F and their sight-lines. The sight-lines of cameras F and G are seen to overlap in this figure. This diagnostic provides information about a mode's poloidal number m and frequency, and can be used in a tomographic reconstruction of the plasma[79][6][7]. All camera data is sampled with a 2MHz sampling rate allowing very high frequency events to be studied.

2.6.3 Electron Cyclotron Emissions - ECE

As was shown in a previous section, charged particles gyrate around magnetic field lines. As a consequence of this motion they emit radiation at the cyclotron resonance frequency $f_c = \frac{qB}{2\pi m}$, where q is the

[2]The radiation is between 100eV and 10keV.

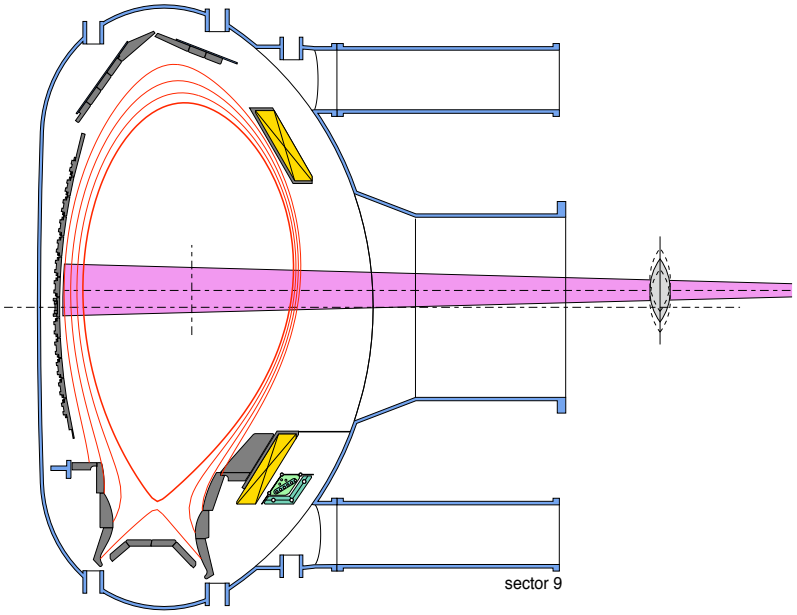

Figure 2.10: The position and alignment of the ECE diagnostic on ASDEX Upgrade.

charge of the particle, B is the magnetic field strength and m is the mass of the particle. This radiation emitted by plasma electrons can be used to determine the electron temperature of the plasma with very high spatial and temporal resolution[8].

Under tokamak conditions, the plasma is optically thick for all frequencies resonant inside the the plasma and practically all of the radiation is absorbed by the cyclotron resonance in a single pass of the wave through the plasma. Under these conditions the plasma emits radiation as if it were a black-body and the radiation intensity is related to the electron temperature[10]. In a tokamak the major field component is the toroidal magnetic field and it depends on the major radius R ($B_\phi \propto 1/R$). Since the magnetic field is inhomogeneous, the frequency resolution of electron emission measurements translates into a spatial resolution and outputs radial profiles of T_e along one line of sight. At ASDEX Upgrade several detectors are installed each capable of observing different frequency bands. These lines of sight are shown in figure 2.10.

2.6.4 Motional Stark Effect - MSE

A well established method on tokamaks is to exploit the motional linear stark effect in order to measure the pitch angle of the magnetic field. This is then used to constrain q-profile reconstructions. Injected neutral atoms of deuterium or hydrogen are excited by interactions with plasma particles leading to the

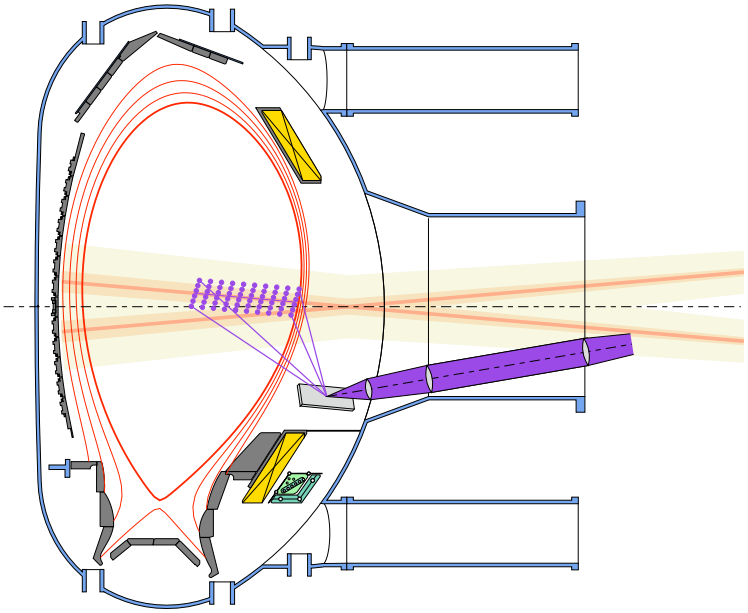

Figure 2.11: Position of the Motional linear Stark effect diagnostic on ASDEX Upgrade, and location of the intersection of the injected beam ions and the viewing optics.

emission of Balmer-α radiation. During the injection, atoms with velocity $\vec{v}$ see in their rest frame an electric field $\vec{E}_L = \vec{v} \times \vec{B}$. This field splits the spectral lines into π and σ components. This splitting is considerably larger than Zeeman splitting by the magnetic field[10]. From this splitting, the pitch angle of magnetic field can be determined from the linearly polarised σ components. The intersection of the atom beam and viewing optics gives the spatial resolution of the diagnostic. The experimental arrangement is shown in figure 2.11. The MSE diagnostic on ASDEX Upgrade has 10 spatial channels covering the plasma radius between $\rho_{toroidal} = 0.04$ and $\rho_{toroidal} = 0.8$. The CLISTE code is capable of using this vital information from the plasma core and beyond, to constrain q-profile reconstructions[16][17].

2.6.5 Reflectometry

Reflectometry is an efficient method for measuring the electron density profile and density fluctuations. This method involves launching microwave radiation of a particular frequency f into the plasma along the density gradient. The microwaves are then reflected at the layer where the electron density equals a critical value. Phase changes in the reflected radiation are measured by mixing this radiation with a reference beam in the detector. The relative positions of the different density layers in the plasma are

determined by taking measurements using a range of probing frequencies. Alternatively, the movements of a single density layer are measured by holding the source frequency constant while measuring the phase output of the reflectometer. In figure 2.12 the positions of the antennae on the low and high field side in ASDEX Upgrade are shown.

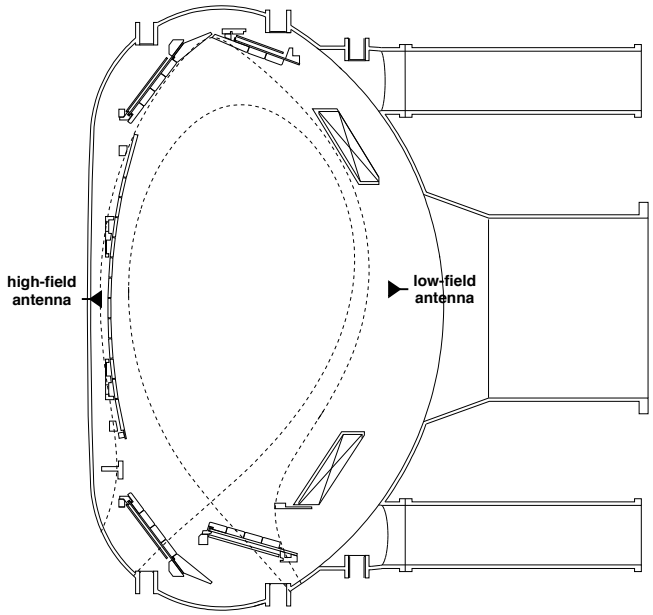

Figure 2.12: The position of the reflectometry antennae on the low and high field side of the ASDEX Upgrade tokamak.

At ASDEX upgrade the reflectometry signal is sampled at a frequency of 2MHz, and given that the diagnostic is very sensitive to the smallest density fluctuations, it is an ideal diagnostic to study low amplitude high frequency MHD and plasma fluctuations.

2.6.6 Fast Ion Loss Detector - FILD

The fast ion loss detector (FILD) acts as a magnetic spectrometer dispersing fast ions onto a scintillator plate with the strike point depending on their gyroradius (or equivalently energy), and pitch angle ($\arccos(v_{\parallel}/v_{\perp})$). Here m, $v_{\parallel}$ and $v_{\perp}$ are the mass, and velocity parallel and perpendicular to the magnetic field of the ion respectively.

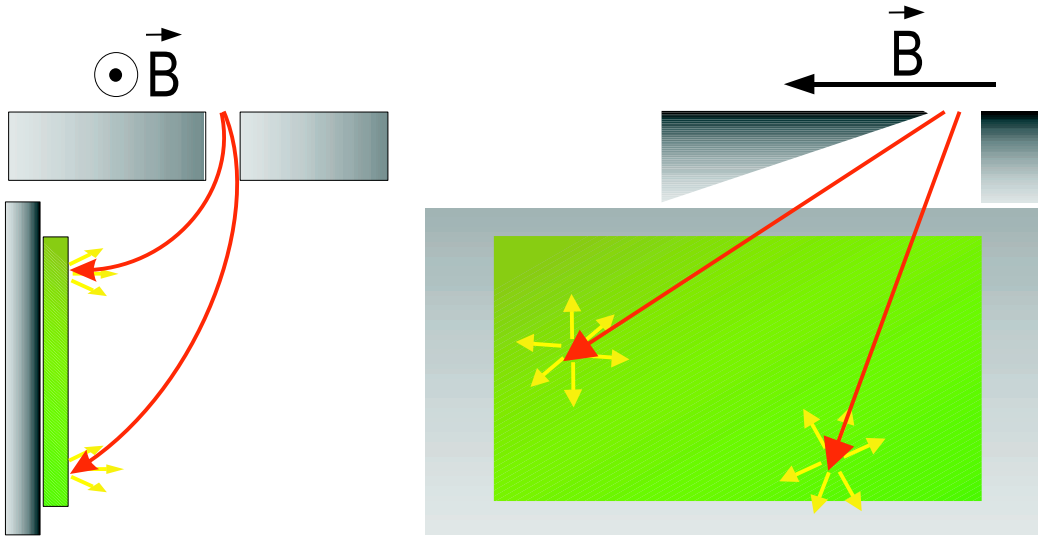

Figure 2.13: A schematic view of the top and side of the collimator operation principle, including two fast ion orbits. The gyroradius (energy) of the ion determines how far from the aperture it will strike the scintillator plate (left hand side). The pitch angle determines where the ions will strike the scintillator plate along the orthogonal dimension (right hand side).

The gyroradius of the ion orbit determines how far the from the aperture the ion will strike the scintillator plate. The pitch angle determines where the ion will strike along the orthogonal dimension of the scintillator plate. The chosen geometry of the detector enables the detection of ions with gyroradii of up to 120mm and pitch angles between 87^o (deeply trapped ions) and 30^o (passing ions). The collimator principle upon which the detector is based is shown in figure 2.13.

At ASDEX Upgrade, the scintillator material used in the FILD has three very important features: efficiency, temperature stability and a very short decay time ($< 1\mu s$). This enables the investigation of fast ion losses due to high frequency MHD phenomena. The position and diagnostic setup at ASDEX Upgrade is shown in figure 2.14.

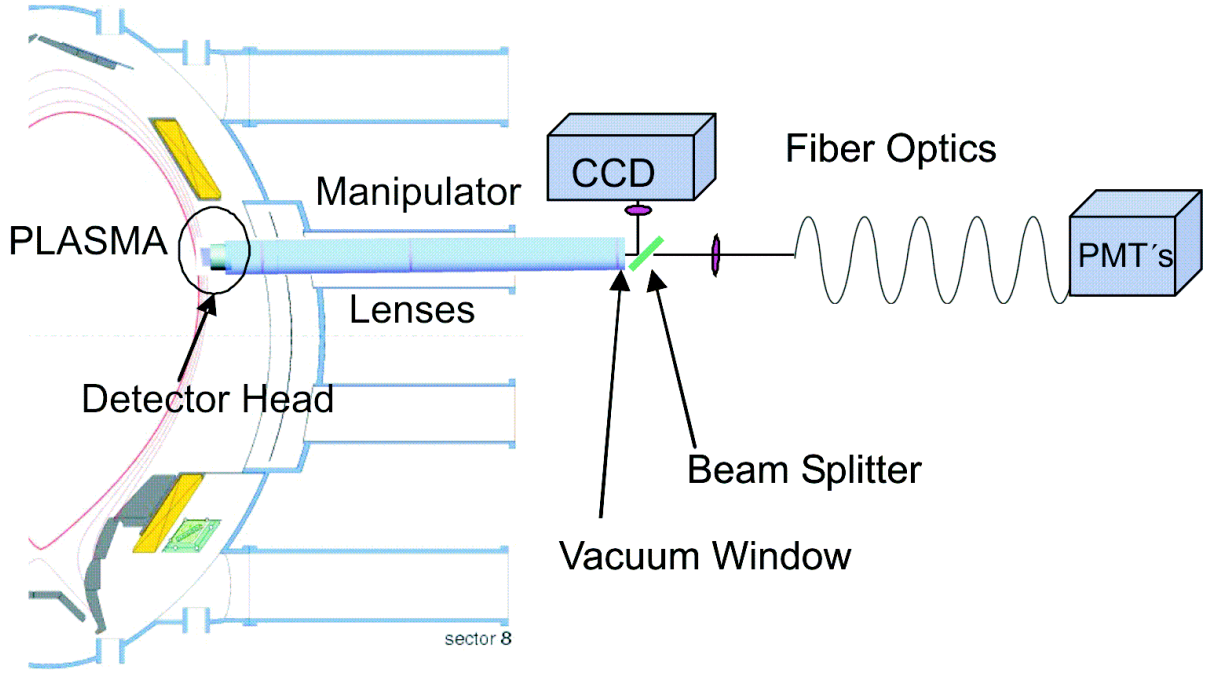

Figure 2.14: An overview of the fast ion loss diagnostic with a cross section of ASDEX Upgrade including the detector head, lens relay, CCD camera, optical fibres and photo multiplier tubes (PMTs).

2.7 Fast ions at ASDEX Upgrade

At ASDEX Upgrade fast ions can be introduced into the plasma using Neutral Beam Injection (NBI), or ions already present can be accelerated to energies of 1MeV and higher by Ion Cyclotron Resonance Heating (ICRH) (the Electron Cyclotron Resonance Heating (ECRH) accelerates plasma electrons to very high energies in a similar manner to ICRH)[10]. These accelerated ions then slow down through coulomb collisions with the background plasma, transferring this energy to the plasma and thereby heating it. The positions of each of these heating systems around the ASDEX Upgrade tokamak are shown in figure 2.15.

2.7.1 ICRF Accelerated Ions - ICRH

The ICRH system at ASDEX Upgrade consists of two antenna-generator groups each containing two antennae and two generators. These antenna-generator sets can provide waves in the frequency range $\omega \in [30, 40]$MHz with a maximum deliverable power of 8MW. This range allows for the matching to the

fundamental ion cyclotron resonance for Hydrogen ions in ASDEX Upgrade, which will be discussed in the following pages.

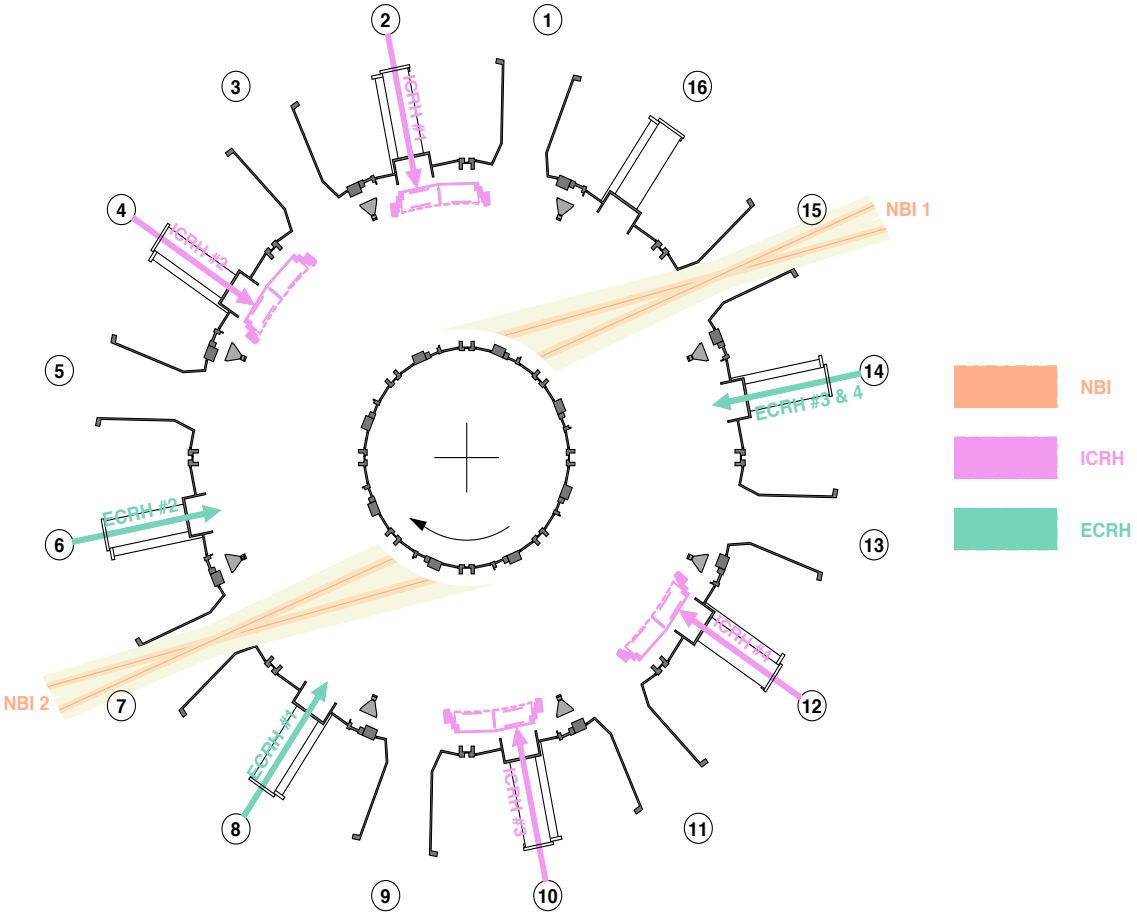

Figure 2.15: Ion Cyclotron Resonance Heating (ICRH), Electron Cyclotron Resonance Heating (ECRH) and Neutral Beam Injection (NBI) systems at ASDEX Upgrade.

An antenna contains parallel conducting loops, or straps, each carrying an RF current. A schematic view of an ICRF antenna is shown in figure 2.16. Depending on the relative phase $\Delta\phi$ between the RF current flowing in each strap, either plasma heating ($\Delta\phi = \pi$) or current drive ($\Delta\phi = \frac{\pi}{2}$) will occur. The corresponding configurations are shown in figure 2.17 along with the expected toroidal mode number vacuum spectrum of the launched waves. Here the toroidal mode number $n_\phi = R_0 k$, where k is the magnitude of the wave vector.

An ion will strongly absorb energy from the wave if a significant proportion of the wave's energy resides in the electric field component rotating in the same direction and frequency as the ion gyro-

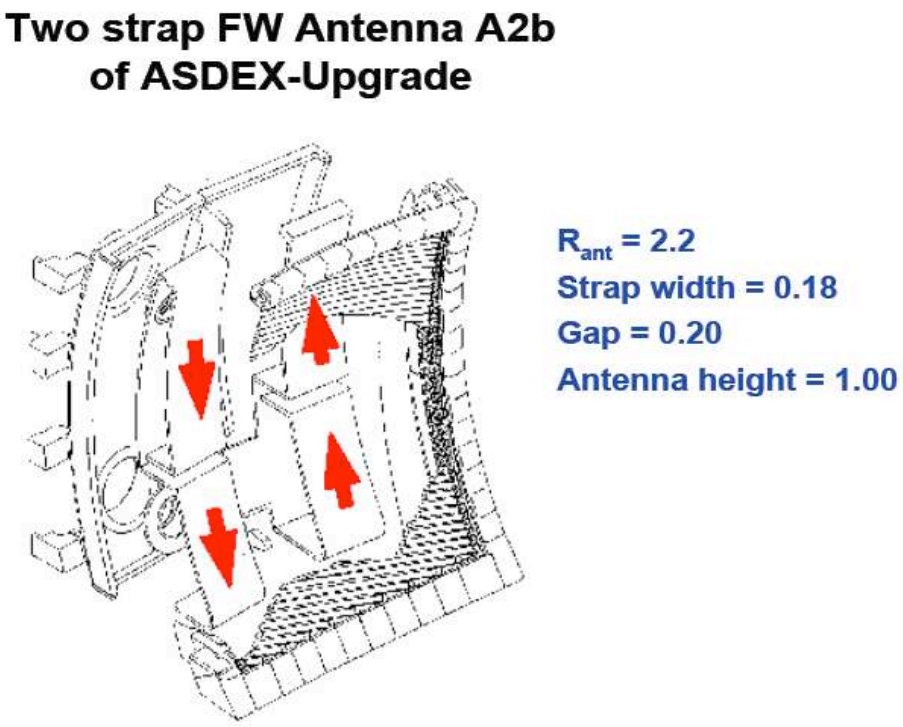

Figure 2.16: Schematic view of the ICRF Antennae used at ASDEX Upgrade for plasma heating and current drive. The arrows indicate the flow of RF current in the antenna straps.

frequency or one of its harmonics, namely

$$\omega - k_{\|} v_{\|} \simeq l|\omega_c|. \tag{2.73}$$

Here $v_{\|}$ is the component of the ion's velocity parallel to the magnetic field, ω_{ci} is the ion cyclotron frequency, ω is the angular frequency of the wave, $k_{\|}$ is the parallel component of the wave vector, and l is an integer. Since the toroidal magnetic field has a $1/R$ dependance, the ion cyclotron resonance is localised at a value of R for which the wave frequency ω satisfies $\omega = \omega_{ci}(R)$. The resonance width is subject to Doppler broadening, resulting, in most practical applications, in a width small compared to the minor plasma radius[10].

The Hydrogen Minority Heating Scheme. Usually in a plasma, the damping at the fundamental resonance is small due to the unfavourable polarisation which is determined by the bulk Deuterium plasma. The maximum therefore has its maximum at the 2^{nd} harmonic and decreases at higher harmonics. However if the plasma consists of another species with different Z/A and a low concentration, such as

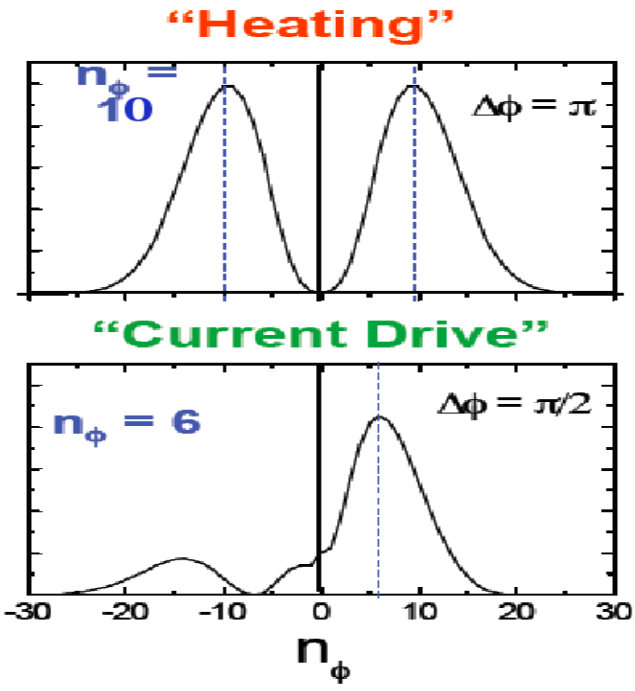

Figure 2.17: Vacuum ICRF antenna toroidal mode number spectrum for plasma heating and current drive scenarios. These calculation were performed by F. Meo with the FELICE code in a slab-geometry.

Hydrogen, absorption can be very strong. This occurs because in the vicinity of hydrogen resonance a considerable fraction of the wave power is left circularly polarised as determined by the deuterium majority. This scheme is called minority heating[10]. However if the hydrogen concentration is too high, the beneficial effect of the wave polarisation in the vicinity of the hydrogen resonance and damping decrease.

When switched on, ICRH will accelerate a passing bulk ion in the direction perpendicular to its motion, potentially changing it from a passing ion to a trapped one. Over several bounce times the ICRH will cause the tips of the ions banana orbit to move outwards to the edge of the ICRF resonance layer[38]. The ICRH system will continue to accelerate an ion as long as the ion stays in resonance. This has the effect that fast ions are continuously swept outwards across the plasma radius.

2.7.2 Injected Fast Ions - NBI

The NBI system is capable of injecting neutral Hydrogen or Deuterium atoms in to plasma[10]. This has the effect of heating the plasma as the neutral are ionised and slow down, or driving an additional current

in the plasma. A secondary effect is an increase in the relevant species' density. At ASDEX Upgrade there are two injectors each producing up to four ion beams. The first injector (NBI1) accelerates ions through a 55kV and 60kV potential difference for hydrogen and deuterium atoms respectively. In contrast, the second injector (NBI2) uses a 70kV and 100kV potential difference to accelerate hydrogen and deuterium atoms respectively. The maximum deliverable power is 14MW for hydrogen and 20MW for deuterium. The location of each injector is shown in figure 2.15. The beams Q1-Q4 in each injector are aligned on the torus such that the delivered beams are either nearly perpendicular or tangential to the plasma. This means that different beams will, in addition to heating, have different deposition profiles in the plasma. Furthermore tangentially aligned beams can drive a current in the plasma, see table 2.1. Under normal operation these beams are injected in the same direction as the plasma current, this is called co-current injection. If counter-current injection is desired then the magnetic field and current are reversed to achieve this.

Source # : Injector NBI1	Classification	Source # : Injector NBI2	Classification
Q1	radial	Q5	tangential
Q2	tangential	Q6	current drive
Q3	tangential	Q7	current drive
Q4	radial	Q8	tangential

Table 2.1: NBI beam classification for injectors 1 & 2 at ASDEX Upgrade.

2.8 ICRF Beatwaves

An ICRF beatwave is formed in the plasma as a result of non-linear coupling between two ICRF waves at slightly different frequencies f_1 and f_2 and wave vectors $\vec{k}_1$ and $\vec{k}_2$. There are several mechanisms that can give rise to this coupling. The non-linearity can be due to a coupling between current oscillations in ideal MHD, or a global ICRH field beating as a result of the overlap of both resonances. In non-ideal MHD, the non-linear coupling can also take place between density oscillations associated with ion Bernstein waves. Pondermotive effects on particle orbits can also be at the basis of the low frequency beatwave generation. Finally, at the plasma edge, surface effects and antenna sheath rectification effects could play an important role in generating a source term at the ICRH wave difference frequency[21].

All these processes can either lead to a classical three-wave process, involving the two ICRH waves and an Alfvén eigenmode, or to the creation of an oscillating source at the difference frequency. Here we consider the former case, where energy and momentum laws give

$$f_1 - f_2 = \Delta f_{IC} = f_{bw} \tag{2.74}$$

$$\vec{k}_{\|1} - \vec{k}_{\|2} = \vec{\Delta k}_{\|IC} = \vec{k}_{bw}. \tag{2.75}$$

In the latter case only the frequency relation holds. The maximum theoretical efficiency of the conversion of high frequency wave energy into the beatwave energy is

$$\eta_{max} = max(P_{bw}/P_{ICRH}) = f_{bw}/f_{ICRH}, \tag{2.76}$$

Using beatwave frequency of $\simeq 200kHz$ and an ICRH frequency $\simeq 35MHz$, equality 2.76 gives an upper bound on the wave conversion efficiency of 1%.

The ICRF beatwaves can drive MHD instabilities if the beatwave's frequency f_{bw} and wave vector $\vec{k}_{bw}$ matches an instabilities lab frame frequency $f_{lab}^{instability}$ and wave vector $\vec{k}^{instability}$. Thus the necessary conditions for the ICRF beatwave excitation of MHD instabilities can be summarised as follows:

$$f_{bw} = f_{lab}^{instability} \tag{2.77}$$

$$\vec{k}_{bw} = \vec{k}^{instability} \tag{2.78}$$

Using the toroidal mode number vacuum spectrum of waves launched during plasma heating shown in figure 2.17, one can make a naive approximation of the corresponding beatwave spectrum. In this approximation the spectrum is taken to be composed of the all possible differences $n_{\phi bw} = \Delta n_{\phi 1} - \Delta n_{\phi 2}$. For each possible pair $(n_{\phi 1}, n_{\phi 2})$ one estimates the amplitude of beatwave from the maximum amplitude of its envelope. The wave pairs are added as follows: $A_1 cos\left(\frac{n_{\phi 1}}{R_0}x\right) + A_2 cos\left(\frac{n_{\phi 2}}{R_0}x\right)$. The amplitudes of wave with the same $\Delta n_\phi = n_{\phi 1} - n_{\phi 2}$ are then added together to get the final spectrum. An example of such an ICRF beatwave toroidal mode number spectrum so calculated is shown in the bottom image in figure 2.18. The largest amplitudes in the resulting spectrum occur for $-10 \leq n_{\phi bw} \leq 10$. Most commonly observed MHD instabilities have toroidal numbers in this range. Therefore if this approximation is reasonable then the resulting beatwaves can be used to drive MHD instabilities with matching toroidal mode numbers.

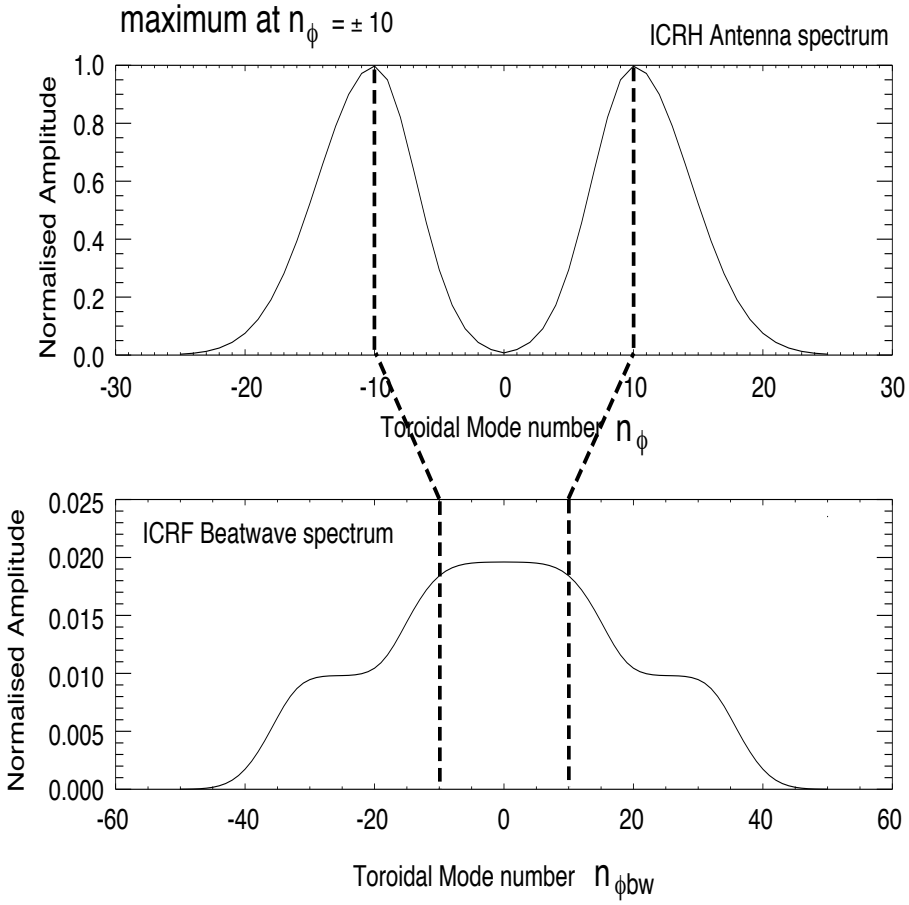

Figure 2.18: A double Gaussian approximation to the input antenna spectra (top). Simple approximation of a possible ICRF beatwave toroidal mode number spectrum (bottom).

Experimentally one can perturb the plasma with a fixed frequency beatwave, or a sweeping frequency beatwave by holding one ICRH frequency constant while sweeping the other. The former is useful when one wants to study the effect of the beatwave for different plasma parameters, and the latter is used when stationary conditions or a passive scan are required.

2.9 An expression for volume averaged β_{fast} in ICRH only plasmas

At ASDEX Upgrade it was shown that a valuable expression, in terms of simple observables, for β_{fast} resulting from NBI could be derived[24]. Following on from this one naturally asks if a similar expression could be found for ICRH. It turns out that an expression, in terms of simple observables, for the volume averaged β_{fast} in ICRH only plasmas can be derived rather than a local quantity. This occurs as a result of ions travelling radially during their orbits. For brevity a variable within angle brackets $\langle\ \rangle$ denotes an averaging over the plasma volume.

To derive an expression for $\langle\beta_{fast}\rangle$, one must first calculate the steady state value of W_{fast}. To do this it is assumed that the effective heating power $P_{eff} = P_{ICRH} - P_{losses}$ equals the rate at which the fast ion population is losing energy via slowing down off electrons. This is demonstrated by the following equation[27]

$$\frac{dW_{fast}}{dt} = P_{eff} - \frac{W_{fast}}{\langle\tau_{sd}\rangle} = 0 \tag{2.79}$$

Here τ_{sd} is the energy slowing down time of ICRF-accelerated hydrogen ions off electrons[3]

$$\tau_{sd} = 6.2\times10^{14}\frac{T_e^{\frac{3}{2}}}{n_e ln\Lambda} \tag{2.80}$$

In (2.80), $ln\Lambda \simeq 15.2 - \frac{1}{2}ln(n_e/10^{20}) + 0.14\ ln\ T_e \simeq 15.2$ is the coulomb logarithm for electron-ion collisions ($T_e \gtrsim 10eV$)[4], and it is assumed that $v_{th,e} \ll v_{fi}$ where $v_{th,e}$ and v_{fi} are the thermal electron and fast ion velocities respectively. Here $n_e(m^{-3})$ is the electron number density, T_e(eV) is the electron temperature. In section 5.6 the applicability of the previous assumption will be discussed in further detail. The resulting steady state solution of equation 2.79 is

$$W_{fast} = \langle\tau_{sd}\rangle P_{eff} \tag{2.81}$$

[3]The value of 6.2×10^{14} is for n_e in m^{-3} instead of cm^{-3} as in [61].

[4]The value of 0.14 is for T_e in eV instead of keV as used in [10]

where $W_{fast} = \frac{3}{2}\langle n_f T_f \rangle V$, $\langle \beta_{fast} \rangle = \frac{\langle n_f T_f \rangle}{B_0^2/2\mu_0}$, $B_0(T)$ is the toroidal magnetic field on the magnetic axis, n_f and T_f are the fast ion density and temperature, and $V(m^3)$ is the plasma volume. Using these equations, $\langle \beta_{fast} \rangle$ can be expressed in terms of W_{fast} from which we arrive at the final equation for $\langle \beta_{fast} \rangle$ in terms of simple observables

$$\langle \beta_{fast} \rangle = \frac{4\mu_0 \langle \tau_{sd} \rangle P_{eff}}{3B_0^2 V}. \tag{2.82}$$

2.10 Codes used in the analysis of TAEs

The **CASTOR_FLOW** code is an extended and completely revised version of the CASTOR (Resistive Complex Alfvén Spectrum for Toroidal plasmas) code[29][28]. It computes the entire spectrum of normal-modes in resistive MHD for axisymmetric equilibria and full eigenfunctions of unstable modes. There is a deficiency in CASTOR_FLOW, in that is does not accurately compute contributions from continuum damping at the plasma edge to the total damping of the mode and it does not consider kinetic effects. To overcome this the LIGKA code must be used.

The **LIGKA** (Linear Gyrokinetic Shear Alfvén Physics) code is required to calculate the damping of TAEs for comparison with those seen at ASDEX Upgrade. LIGKA is a new linear gyrokinetic MHD code which has been developed at ASDEX Upgrade[30] based on the theoretical gyrokinetic MHD model by Qin[31]. This code not only allows for growing and damped eigenvalues, but also for a change in mode-structure of the magnetic perturbation due to energetic particles to be simulated. Integration over the unperturbed particle orbits is performed with the drift-kinetic **HAGIS** (Hamiltonian Guiding centre System) code[32], which accurately describes the particles' trajectories. Additionally, given a TAE and an initial fast ion population, HAGIS can be used to identify the existing resonance conditions between TAEs and fast ion population and to simulate the influence that each has on the other.

The **TORIC** code solves the finite Larmor radius wave equations in the ion cyclotron range of frequencies in arbitrary axisymmetric toroidal geometry. The model used, based on the finite Larmor radius approximation, describes the compressional and torsional Alfvén waves and ion Bernstein waves excited by linear mode conversion. Within this work, TORIC has provided supra-thermal hydrogen perpendicular pressure and β profiles[33].

The ICRF modelling code **PION** [34][35] calculates the evolution of ICRF power deposition and

velocity distribution functions of the resonant ions in a self-consistent way. It uses simplified models: 1) The deposition model is constructed to approximate results from the full wave code LION (ray tracing to capture features of strong damping scenarios + parameterisation of LION results for representing the power absorbed in multi-passes of the waves). 2) 1D Fokker-Planck modelling for pitch-angle-averaged distribution functions of the resonant ions using finite differences, assuming classical collisional slowing down of fast ions. 3) Finite orbit widths taken into account by assuming that fast ions are trapped with turning points close to resonance layer and averaging collision coefficients in the collision operator over orbits.

Chapter 3

MHD Instabilities

3.1 Toroidicity Induced Alfvén Eigenmodes (TAEs)

3.1.1 Introduction

In a magnetised plasma, cylindrical shear continuum Alfvén waves with a frequency $f^2 = k_{\|m}^2 V_A^2/4\pi^2$ can resonantly interact with ICRH-accelerated ions through Inverse Landau Damping[45]. Here V_A is the Alfvén velocity and it is defined as

$$V_A = \frac{B_0}{\sqrt{\mu_0 \rho_m}}. \tag{3.1}$$

Here $k_{\|m} = (n - m/q(r))/R_0$ is the parallel component of the wave vector in a plasma with a circular poloidal cross section, m and n are the poloidal and toroidal mode numbers respectively, r is the minor radial coordinate, R_0 is the major radius of the plasma, B_0 is the magnetic field strength on the magnetic axis, and ρ_m is the mass density. These modes are highly localised, and strongly damped by the continuum represented by the short dashed curves in figure 3.1.

In a tokamak toroidicity leads to a modification of the Alfvén continuum, which causes cylindrical shear Alfvén waves with the same toroidal mode number n and adjacent poloidal mode numbers (m,m+1) or equivalently $\Delta m = 1$ to couple, resulting in the formation of gaps in the shear cylindrical Alfvén spectrum at the point where these continua cross. It is within these gaps that the weakly damped TAEs can be excited. These gaps are collectively called the TAE-gap [45]. For a given $n \geq 2$ and safety factor profile q, the innermost gap or core gap will be located on the magnetic axis and corresponds to the coupling of the m=n-1 and m=n poloidal harmonics. Each subsequent gap is labelled with a non-

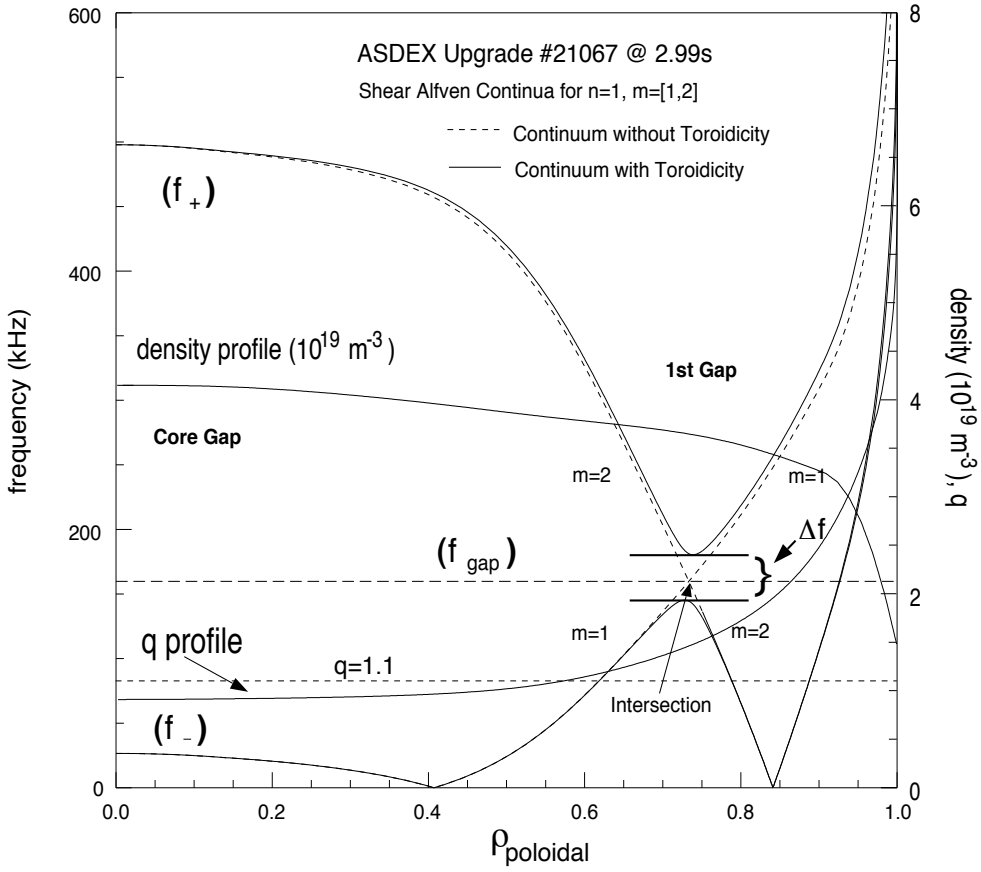

Figure 3.1: n=1 and m=(1,2) Alfvén continua. The short dashed curves represent the cylindrical continua and the solid curves $f\pm$ are the continua modified by toroidicity. The continua were calculated using the particle density and safety factor q profiles displayed in this figure. The vertical axis on the right hand side of the image is for the q-profile and electron density $n_e/10^{19}$. On the X-axis, $\rho_{poloidal}$ is the normalised poloidal flux radial coordinate of the plasma. The solid horizontal line represents the q=1.1 surface, which is the average value of q for the most typically observed TAEs, this will be used later in section 4.3.

negative integer i defined as the number of gaps radially between it and the magnetic axis not counting itself. For $n \geq 2$, the i^{th} gap is formed from the coupling of the two poloidal harmonics $m = n+i-1$ and $m = n+i$.

A TAE's eigenfunction has the fourier representation

$$\vec{\xi}(n,f) = e^{i(n\phi - 2\pi ft)} \sum_m \vec{\xi}_m(r) e^{-im\theta} + c.c \tag{3.2}$$

[46]. For each TAE the two poloidal harmonics m=n+i-1 and m=n+i that form the gap at r_{gap} determine the shape of the global mode structure and are referred to as the dominant poloidal harmonics [46]. A

unique frequency f_{gap} for a plasma with a circular plasma poloidal cross section,

$$f_{gap} = \frac{V_A(r_{gap})}{4\pi q(r_{gap})R_0} = \frac{B_0}{4\pi q(r_{gap})R_0\sqrt{\mu_0\rho_m(r_{gap})}} \propto \frac{1}{q(r_{gap})\sqrt{\rho_m(r_{gap})}} \tag{3.3}$$

is derived from the cylindrical shear wave dispersion relation and the intersection condition $k_{\|m} = -k_{\|m+1}$ for each gap, and hence each TAE. Additionally, the safety factor q at the position of the gap has the value $q(r_{gap}) = (m+1/2)/n$ [45]. In figure 3.1 an experimental Alfvén continuum for the (m,n)=(1,1) & (2,1) cylindrical shear Alfvén waves shows the toroidicity induced changes. The particle density and safety factor q profiles used in the calculations are also displayed in the figure. The structure of the modified continuum $f_{\pm}$ is given by the dispersion equation [45][48]:

$$f_{\pm} = \frac{k_{\|m}^2V_A^2 + k_{\|m+1}^2V_A^2 \pm \sqrt{(k_{\|m}^2V_A^2 - k_{\|m+1}^2V_A^2)^2 + 6\varepsilon x^2k_{\|}^2V_A^2k_{\|m+1}^2V_A^2}}{4\pi(1-(9\varepsilon^2x^2)/4)} \tag{3.4}$$

Here $x = r/a$ and $\varepsilon = a/R_0$ is the inverse aspect ratio, where a is the minor radius of the plasma. Using equation 3.4, the gap width Δf shown in figure 3.1 can be approximated as

$$\Delta f = f_+ - f_- \simeq 6\pi\varepsilon x_{gap}f_{gap}. \tag{3.5}$$

The gap frequency f_{gap} can be used as a 0^{th} approximation to the frequency of a TAE in the plasma rest frame, but the effect of magnetic shear has to be taken into account to recover the TAE's frequency fully. The effect of magnetic shear (the magnetic shear values used are calculated with the CLISTE equilibrium code[49])

$$s = \frac{r}{q}\frac{dq}{dr} \tag{3.6}$$

on the TAE's frequency is to move it away from the gap frequency f_{gap}. A geometry independent expression for magnetic shear can be found in reference [50]. By labeling the shear related frequency shift as $\Delta_s f$, the following equation shows how the frequency of a TAE in plasma's rest frame f_{TAE} is related to the gap frequency f_{gap},

$$f_{TAE} = f_{gap} + \Delta_s f. \tag{3.7}$$

The CASTOR_FLOW code[28][29] takes the effect of magnetic shear into account when it calculates the TAE's frequency f_{TAE} in the plasma's rest frame.

Two solutions exist simultaneously to a TAE's eigenmode problem, and depending on whether the mode frequency is close to the bottom or the top of the gap, the two dominant poloidal fourier

harmonics will have either the same or opposite signs respectively. This leads to a TAE being classified as either Even (same sign) or Odd (opposite sign)[51][52]. If the TAE is an even mode it will have a ballooning structure, otherwise it will have an anti-ballooning structure[52]. For low shear the Even-mode's frequency sits at the bottom of the gap, whereas the frequency of the Odd-mode sits at the top of the gap. As magnetic shear increases the frequencies of the even TAE and odd TAE move away from these points. Of these two modes the even TAE is the most frequently observed[52].

When TAEs from the i^{th} gap are observed, each is seen to have a distinct lab frame frequency. This distinction in frequency originates from the dispersion relations q-dependency, the radial separation between modes, magnetic shear, kinetic effects, and doppler shifts between the plasma rest frame and the lab frame. The doppler shift from the toroidal plasma rotation f_{tor} at the resonant surface of the TAE is a large part of the observed frequency shift, but is not sufficient to explain the difference between the frequencies of TAEs with consecutive toroidal mode numbers observed from the 1^{st} gap[53]. However, published results demonstrated that the ion diamagnetic frequency f_i^* [10] accounts for the remaining doppler shift[55]. We propose that the frequency of a TAE f_{TAE} in the plasma's rest frame should be calculated using the formula

$$f_{TAE} = f_{lab} - nf_{tor} + nq_{gap}f_i^*. \tag{3.8}$$

It is assumed that the shear and plasma rotation are the same for all TAEs observed from the 1^{st} gap because the resonant surfaces are radially very close to one another.

3.1.2 Sources of drive and damping for TAEs

The ICRH system introduces a strong anisotropy in the pitch angle ($\mu = arccos(v_{||}/v)$) distribution of trapped ions and an inhomogeneous radial distribution of fast ions, both which depend on the width and radial position of the particular ion cyclotron resonance. In order for fast ions to be resonant with a TAE, they must satisfy the following condition [70]

$$f_{TAE} \simeq f_{rot} + nf_d + kf_b, \tag{3.9}$$

where f_d is the drift precessional frequency of the fast ions, k is a non-negative integer, f_b is the bounce frequency of the trapped fast ions and f_{rot} is the rotation frequency of the plasma. Normally for ICRF accelerated fast ions, $f_b > f_d + f_{rot}$, and if $k > 0$ then the relevant contribution can be reduced to $f_{TAE} \simeq kf_b$. There exists a second potential resonance in expression (3.9) through the drift precessional

frequency f_d alone. However, due to the nature of ICRF heating, such resonances would not be expected without a sufficiently low f_{TAE}, and ions with sufficiently high parallel velocity, such as injected hydrogen atoms (NBI).

The net growth rate[45] for a TAE is defined in the following equation

$$\frac{\gamma}{f_{TAE}} \simeq \underbrace{\frac{9}{4}\beta_f \left(\frac{f_{*,f}}{f_{TAE}} - \frac{1}{2}\right) H\left(\frac{v_A}{v_f}\right)}_{driving\ term} - D, \tag{3.10}$$

where $\beta_f = \beta_f(0)e^{-\frac{r^2}{L_f^2}}$, $f_{*,f}$, and v_f are the fast ion beta, diamagnetic drift frequency and velocity, $H(y) = y(1+2y^2+2y^4)e^{-y^2}$, L_f is fast ion density gradient scale length, and D is the total damping experienced by the mode[45]. The fast ion diamagnetic drift frequency f_{*f}, represents the free energy available to the whole system through the gradients in the unperturbed fast ion distribution function. It is defined as

$$f_{*f} = -\frac{m}{2\pi r e_f B n_f}\frac{dp_f}{dr} \tag{3.11}$$

for a circular poloidal cross section [10]. Here m is the poloidal number for a resonant mode, p_f is the fast ion pressure, e_f is the charge of the fast ion species and n_f is the fast ion density.

An important deficiency in the driving term in equation 3.10 is the absence of finite ion orbit width effects. Finite orbit width effects lead to a modification of the driving term which is reflected in the growth rate dependence on n. Starting at low n the fast ion drive increases towards a maximum at moderate n values (n=3, 4 or 5 in ASDEX Upgrade, depending on the details of a particular discharge) and then decreases for larger values of n. For trapped ions, the values of n at which the drive reaches this maximum satisfy the expression $\Delta_b/\Delta_m \simeq 1$, where Δ_b is the width of the trapped fast ion's orbit and Δ_m is the width of the mode[57], and the requirement that the fast pressure gradient is such that the fast ion gives more energy to the mode than it takes on the return leg of its orbit.

The individual contributions to the total damping D are from: electron landau damping, continuum damping, radiative or Kinetic Alfvén Wave (**KAW**) damping, ion Landau damping, trapped electron collisional damping, and electron drift damping. Of these damping mechanisms the total contribution of electron and ion Landau damping, continuum damping, radiative damping and finite banana orbit width effects are calculated using the LIGKA code[30]. Continuum and radiative damping occur when, $f_{\pm} = f_{TAE}$ at a radial location in the plasma (or equivalently f_{TAE} intersects the continuum)

and $f_{\pm}(r_{gap}) \simeq f_{TAE}$ (f_{TAE} is close to but does not intersect the continuum $f_{\pm}$) respectively. Additionally a periodic stabilising effect due to the redistribution of fast ions by the sawtooth instability is observed[53]. The ordering of these terms depends predominantly on the poloidal mode number m[10][30].

Experimentally, a method exists to measure the total damping experienced by a stable TAE. This involves forcing an otherwise stable TAE to oscillate using an external antenna[54]. The TAE's resonance appears as complex pole in the transfer function H, between the antennas driving current and a particular diagnostic, for example mirnov coils[54]. The real part of the pole is equal to the growth rate of the TAE. In the absence of a drive source, the growth rate is equal to the total damping experienced by a TAE. However in the case of TAEs excited by resonant fast ions the situation is complicated by the non-linear processes which lead to the saturation of the mode's amplitude, and so damping rates can not be related in a simple fashion to measurements of the mode's spectral line widths. This being said when ICRH power is switched off during a discharge, effectively removing the fast ion drive, the measured TAE decay rate R_d is equal to the damping rate of the mode. This measurement will be a lower bound as a result of neglecting the finite slowing down time of the ICRH ions.

Driving TAEs using ICRF Beatwaves

Beatwaves formed in the plasma as a result of coupled ICRF waves, are capable of driving a TAE when the following conditions are met:

$$f_1 - f_2 = \Delta f_{bw} = f_{lab} \tag{3.12}$$

$$\vec{k}_{\|1} - \vec{k}_{\|2} = \vec{\Delta k} = \vec{k}_{\| \ TAE} \simeq 1/2 q_{TAE} R_0. \tag{3.13}$$

Here f_{lab} is the frequency of the TAE in the lab's frame. From the approximate beatwave toroidal mode number spectrum displayed in figure 2.18, the ICRH system at ASDEX Upgrade is capable of driving TAEs with a wide range of toroidal mode numbers. In fact, one would expect that those with $-10 \leq n \leq 10$ should receive the strongest drive, which is well suited to typical TAEs observed in ASDEX Upgrade as they are typically within this range.

3.1.3 Fast ion losses induced by TAEs

TAEs are capable of considerably changing the orbits of resonant fast ions from mode onset up until the fast ions leave the plasma. When switched on, ICRH will accelerate a passing bulk ion in the direction

perpendicular to its motion, potentially changing it from a passing ion to a trapped one. As a result of continuous perpendicular heating of an ion in a banana orbit the tips of the orbit move radially outwards to the edge of the ICRF resonance layer. Once there the ICRH system will continue to accelerate an ion as long as it stays resonant and as an ion gains energy its orbit will broaden[38]. This has the effect that fast ions are continuously swept from the core towards a TAE's resonance. Interactions between resonant trapped fast ions and a TAE can cause the orbit of the fast ion to drift outward over several bounce times until it is no longer fully contained within the last closed flux surface.

During typical discharges losses correlated with TAEs are recorded by the Fast ion Loss diagnostic (**FILD**), but these losses do not have a noticeable effect on performance (section 4.4). However losses could become noticeable, if f_{gap} were to be approximately constant across the entire plasma radius (a criterion not satisfied in the considered discharges), then the continuum damping would be effectively turned off, leading to the excitation of strong TAEs with different n all simultaneously capable of resonant interactions with the fast ion population. This could lead to considerable fast ions losses and potential damage to plasma facing components. A detailed discussion of the observed losses is given in section 5.2.

3.2 Other important instabilities

3.2.1 The Sawtooth Instability

Tokamak plasmas are subject to a periodic relaxation of the pressure profile in the core under a wide range of operating conditions. This appears as a sawtooth shaped oscillation of the temperature and density, although it is more prominent in the temperature. The cause of this is a breakdown of the confinement inside the q=1 flux surface leading to the release of a heat pulse to the outer part of the plasma and the loss of fast ions. An example of this process is shown in figure 3.2. In this figure one sees a rapid temperature drop in the plasma core ECE channels where the temperature is highest and an increase in temperature in the outer plasma beyond a certain radius. The location where temperature change is minimal is called the inversion radius and is high-lighted in red. This inversion radius is expected to be close radially to the radius of the q=1 flux surface, and is therefore often used as a simple approximation to the position of the q=1 flux surface.

There are several models which attempt to explain the sawtooth crash[10][4], however while each

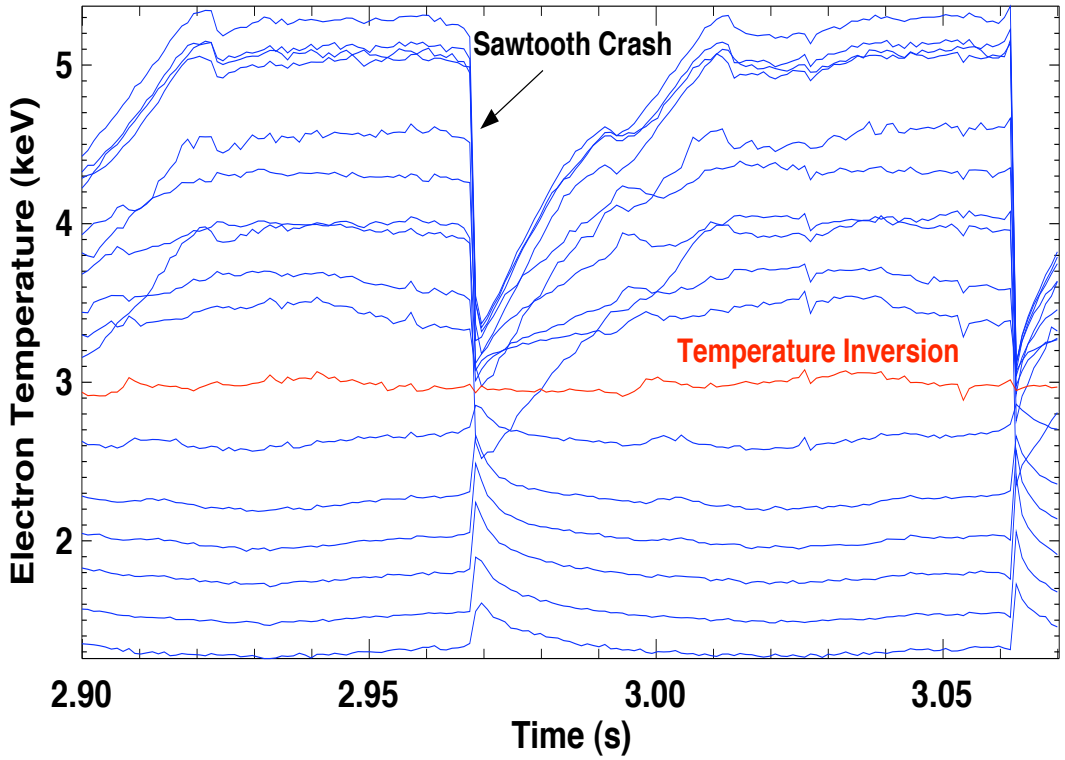

Figure 3.2: Discharge 20396 : Temperature crash seen across the plasma in ECE channels covering $0.0 \leq \rho_{poloidal} \leq 0.8$ *radially. The highest temperatures occur in the plasma core and decrease radially outwards. The red signal shows the signal with the minimum temperature perturbation and gives the position of the inversion radius at* $\rho_{poloidal} = 0.38$.

model can explain some features, none can explain all of them. Occasionally an (m=1,n=1) magnetic instability is seen prior to and right through the temperature crash. The crash is an extremely fast event lasting less than a millisecond after which the core plasma temperature recovers over several milliseconds. The sawtooth crash does have a beneficial effect, in that it removes impurities which accumulate in the plasma core and would otherwise cool it through radiation. This benefit increases the longer the inter-sawtooth period, as it allows the plasma to recover more fully in between crashes, however if the crashes are too frequent, then the plasma would remain at lower temperatures than would otherwise be possible.

3.2.2 The Fishbone Instability

Historically fishbones were the first fast ion driven MHD instability identified in a fusion plasma device[22] and therefore its origin, topology and behaviour are well known. It was found that under certain conditions, the injection of high energy neutral beams used to heat the plasma would excite this instability. The fishbone instability was believed to be an ideal instability with poloidal and toroidal mode numbers (m=1, n=1) localised to the q=1 flux surface, however in the recent past it was found to have a resistive character[23]. This instability derives its name from the fishbone-shaped bursts of magnetic activity seen in mirnov coils, see figure 3.3 (left hand side). The other defining feature is the rapid decrease in the frequency of each fishbone burst seen in a spectrogram of the mirnov coil data, see figure 3.3 (right hand side). The most severe effect of the fishbone instability is the ejection of the resonant fast ions driving the instability[24]. Two different models for the underlying destabilising mechanisms of the fishbone instability were proposed, and can be found in [25][26]. The first suggests that injected fast beam ions within the q=1 surface can kinetically destabilise an (m=1,n=1) kink mode and the resonance is between the parallel velocity of the mode and the trapped ions' toroidal precession velocity[10]. This theory predicts that the (m=1,n=1) fishbone mode will be excited if the pressure of the fast trapped ions is sufficiently high. The second model extends the first by including the effect of the finite ion diamagnetic frequency,

$$f_{*i} = \frac{1}{eBrn_i}\nabla p_i. \tag{3.14}$$

Here e is the electron charge, n_p is the ion density and ∇p_i is the is the radial ion pressure gradient of the bulk plasma.

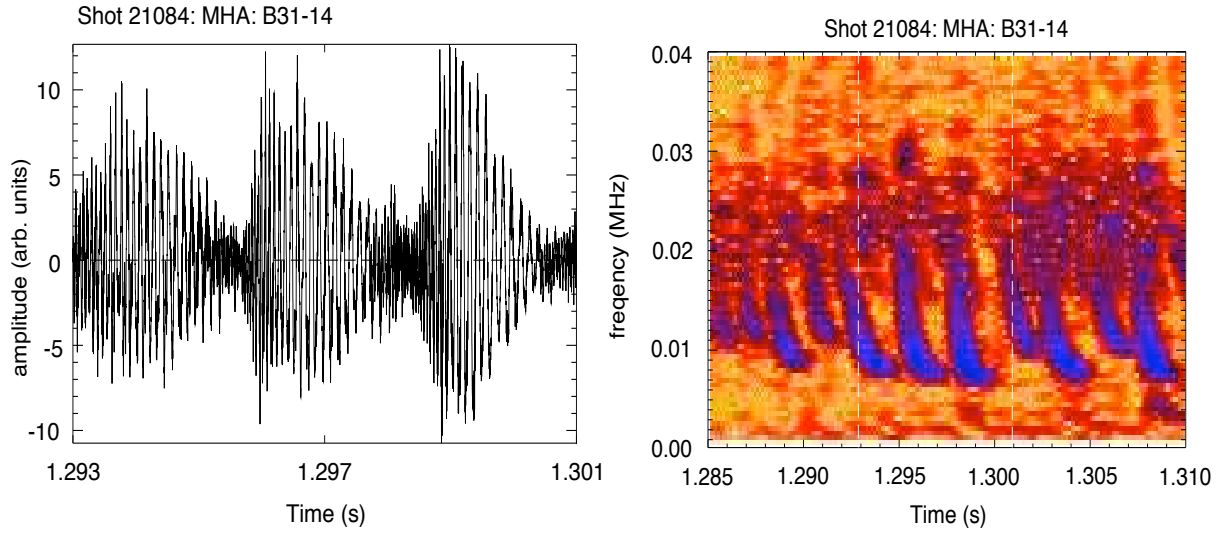

Figure 3.3: Discharge 21084 : (left) The Fishbone instability seen in raw mirnov coil data as a fishbone-shaped burst of magnetic activity, (right) Characteristic Fishbone rapid downward frequency sweep. The white vertical dashed lines identify the time window 1.293s-1.301s shown in the image on the left.

Kass et al. [24] have shown experimentally that the fishbone drive mechanism depends strongly on the trapped fraction of the fast particles at, and within, the q=1 flux surface, and that the fishbone instability occurs in ASDEX Upgrade only when the fast ion pressure exceeds a certain threshold. The initial mode frequency scales with the toroidal precession frequency of the trapped ions. The mode's structure is usually dominated by an (m=1,n=1) mode, but higher poloidal harmonics have also been observed. The fishbone instability is seen to rotate in the ion diamagnetic drift direction and to be enhanced on the low field side of the torus.

3.2.3 Neoclassical Tearing Modes (NTMs)

One of the main dissipative processes in a tokamak is related to the plasma resistivity. The presence of finite resistivity enables the reconnection of magnetic field lines broken by a tearing mode whose displacement function shown in figure 2.6a. This process leads to the formation of magnetic islands, the anatomy of a magnetic island is shown in figure 3.4. The centre of a magnetic island is called the O-point and the point where the field lines cross is called the X-point. The width of the island w is defined as the maximum distance radially within the last closed flux surface of the island. Typically a magnetic island is driven by a radial gradient of the equilibrium current profile. The most common types of

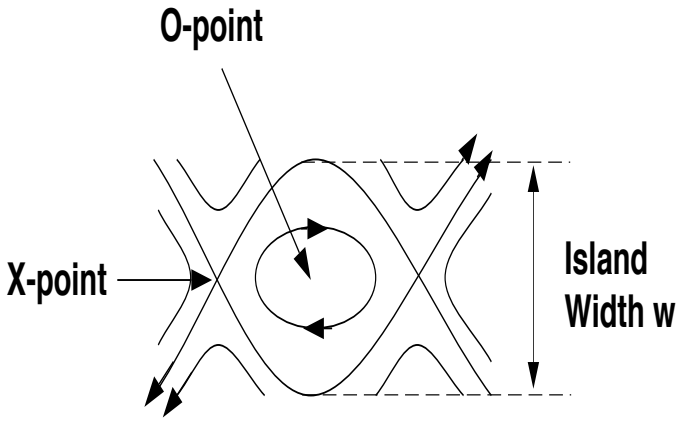

Figure 3.4: Magnetic Island due to field line reconnection of a perturbed magnetic field with the O-point, X-point and the island width w.

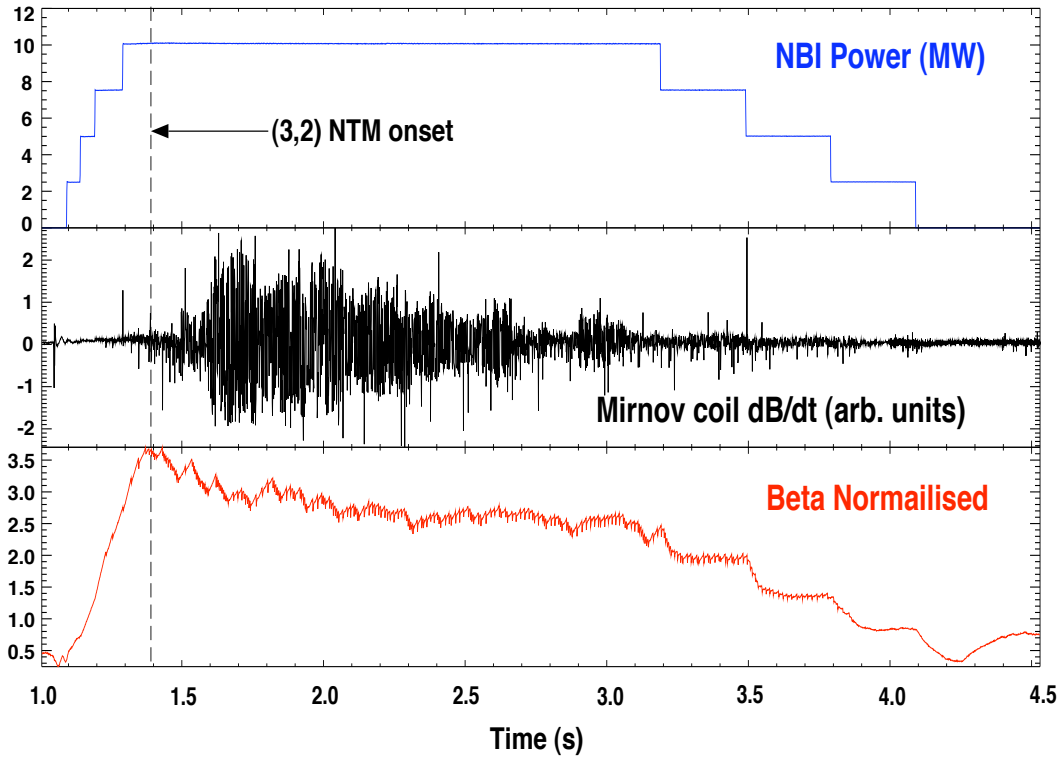

Figure 3.5: Discharge 20528 : (top) NBI power, (middle) mirnov coil signal dB/dt corresponding to a (3,2) NTM, (bottom) Normalised plasma β. The dashed vertical line marks the (3,2) NTM onset and subsequent decrease in the normalised plasma β.

resistive instabilities in a high β tokamak plasma are dominantly pressure driven Neoclassical Tearing Modes (NTMs)[36][40][37][39]. They degrade the plasma confinement through the enhancement of particle transport radially outwards. Figure 3.5 shows the reduction in plasma β as a result of the growth of an (m=3,n=2) NTM. In the case of these modes the magnetic reconnection leads to the formation of an initial so-called seed island flattening the pressure profile, which in turn deceases the local bootstrap current further driving the island to its saturated size[10]. The most common NTMs are those with poloidal and toroidal mode numbers (m=4,n=3), (m=3,n=2) and (m=2,n=1). An example of the 3-island structure formed by a (m=3,n=2) NTM is shown in figure 2.7.

Chapter 4

Experimental Scenarios

The following sections describe the discharge scenarios employed for the study of TAEs and their interaction with the fast ion population generated by ICRH with additional NBI.

4.1 ICRH discharge

Majority deuterium discharges were operated in a lower single null divertor configuration. The primary heating scheme used was hydrogen minority ICRH. In this environment the behaviour of typically observed $n = 2,..,7$ TAEs in response to variations in parameters such as toroidal magnetic field, particle density and plasma current were studied. The approach used to study the effects on TAE stability was to vary the relevant parameter smoothly. If stationary plasma conditions were required, a sequence of discharges with systematic variations in the relevant parameter was made.

Figure 4.1 shows the prototypical ICRH L-mode discharge upon which all other considered discharges were based. This discharge starts with an ohmic current ramp followed by an ICRH power increase, leading to a steady phase during which a sawtooth instability is excited indicating a $q_{min} \leq 1.0$. Two discharges are taken to be **similar**, if they have the same toroidal field, core line-integrated density, density peaking ("core line-integrated density"/"edge line-integrated density"), plasma current, heating and shape.

In all discharges analysed bulk parameters were within the following ranges, plasma current $[0.8, 1.0]$MA, toroidal magnetic field $[2.0, 2.5]$T, electron density n_e $[3.0, 7.0] \times 10^{19} m^{-3}$, total ICRH power $[4.0, 5.0]$MW, plasma elongation $\kappa \approx 1.6$, upper plasma triangularity $\delta^u \approx 0.0$ and lower plasma

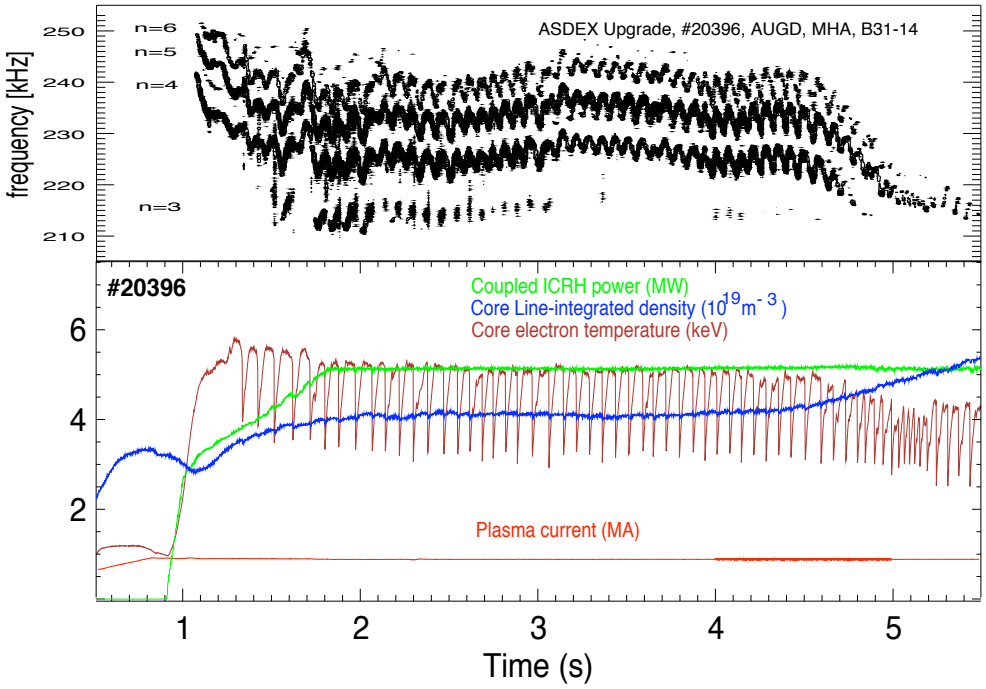

Figure 4.1: L-mode discharge with ICRH only : #20396 - parameter evolution and spectrogram(magnetic coil B31-14) displaying active TAEs. $\beta_N = 1.3$, $B_{tor} = -2.4T$, $q_{min} \leq 1.0$, $q_{95} \simeq 4.9$.

triangularity $\delta^l \approx 0.3$. During selected discharges radial (sources 3 & 8) NBI beams were used. This was to acquire MSE data for current profile reconstructions, and Charge Exchange data for rotation and ion temperature measurements. The operational ICRF frequencies used to provide central heating were 30.0MHz and 36.5MHz for a 2T and 2.5T magnetic field respectively.

Discharges with a small content of low-Z impurities after a fresh boronisation showed a transition to H-mode with ICRH alone, see figure 4.2. The transition to H-mode can be identified by a drop in the H_α signal directly followed by appearance of ELMS (Edge Localised modes)[42]. This provided the opportunity to compare TAEs observed in L-mode with those in H-mode.

4.2 Limiter Configuration experiments in L-mode

To complement the divertor discharges, a set of discharges were operated in a Limiter configuration (typically the n=4,5 TAEs are observed). An example of the difference between the magnetic flux surfaces for the limiter and divertor discharges is shown in figure 4.3. This provided the opportunity to

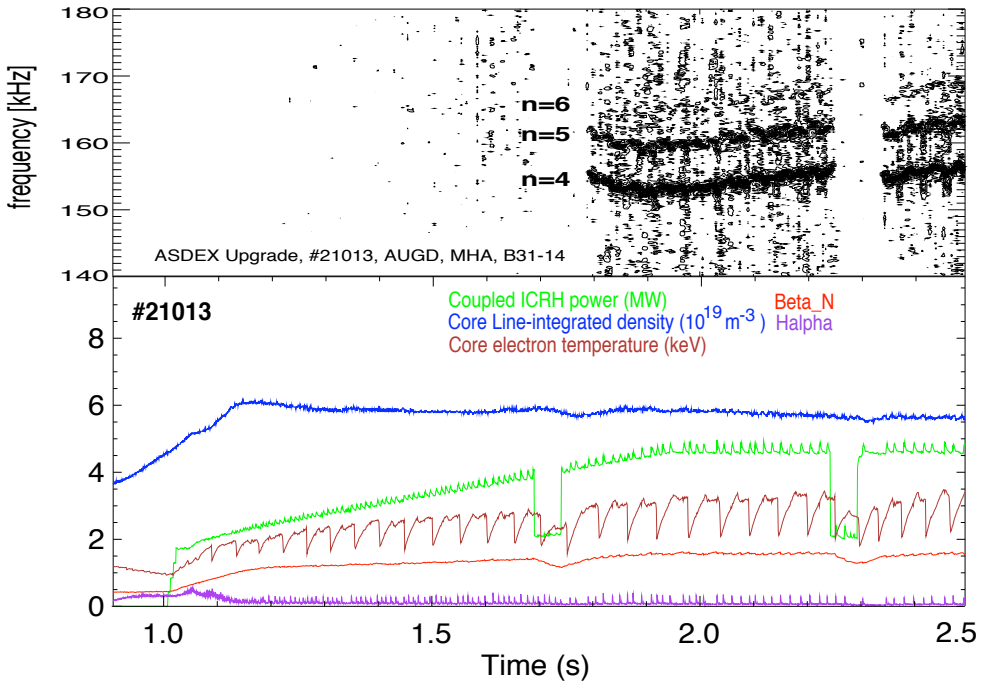

Figure 4.2: H-mode discharge with ICRH only : #21013 - parameter evolution and spectrogram(magnetic coil B31-14) displaying active TAEs. $I_p = 0.9MA$, $B_T = -2.0T$, $\beta_N \simeq 1.5$, $q_{min} \leq 1.0$, $q_{95} \simeq 4.0$. *The transition to H-mode occurs at* $t \simeq 1.1s$.

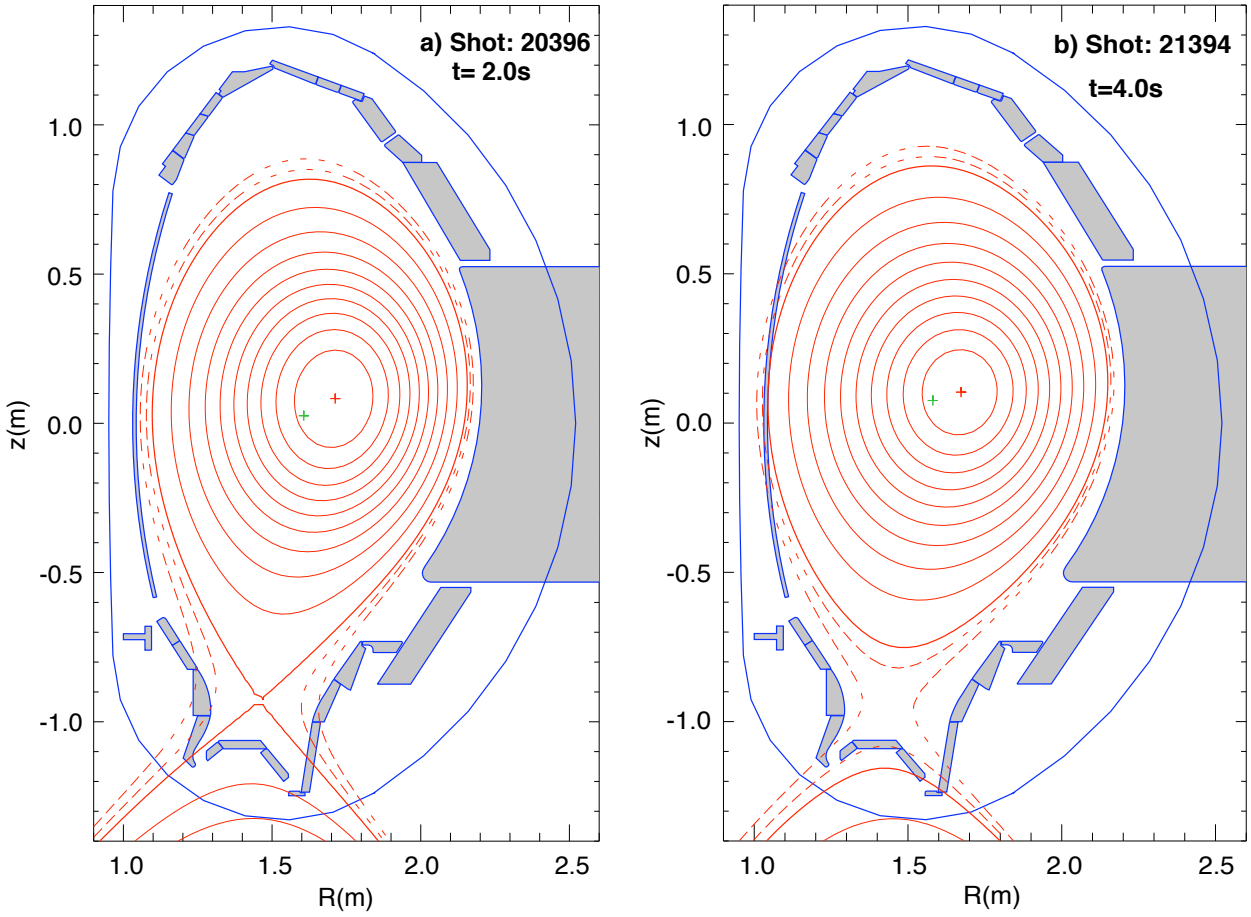

Figure 4.3: Flux surface topology in L-mode for (a) magnetic divertor and (b) a material limiter.

compare TAEs observed in different flux surface topologies.

4.3 ICRH discharge with tangential NBI

In order to mimic α-particles effects fast deuterium ions were injected during L-mode and H-modes discharges. The injected ions have a larger parallel energy, of the order of 100keV, than those accelerated by ICRH which increases an ion's energy preferentially in the perpendicular direction. These ICRH ions then undergo negligible pitch angle scattering off of electrons until much lower energies are reached, $\simeq$ 50keV. This allowed the effects of a change in confinement on the behaviour of TAEs to be studied. The starkest change in confinement occurs when the plasma undergoes the transition from L-mode to H-mode. This is of special interest to future experiments and reactors because they will oper-

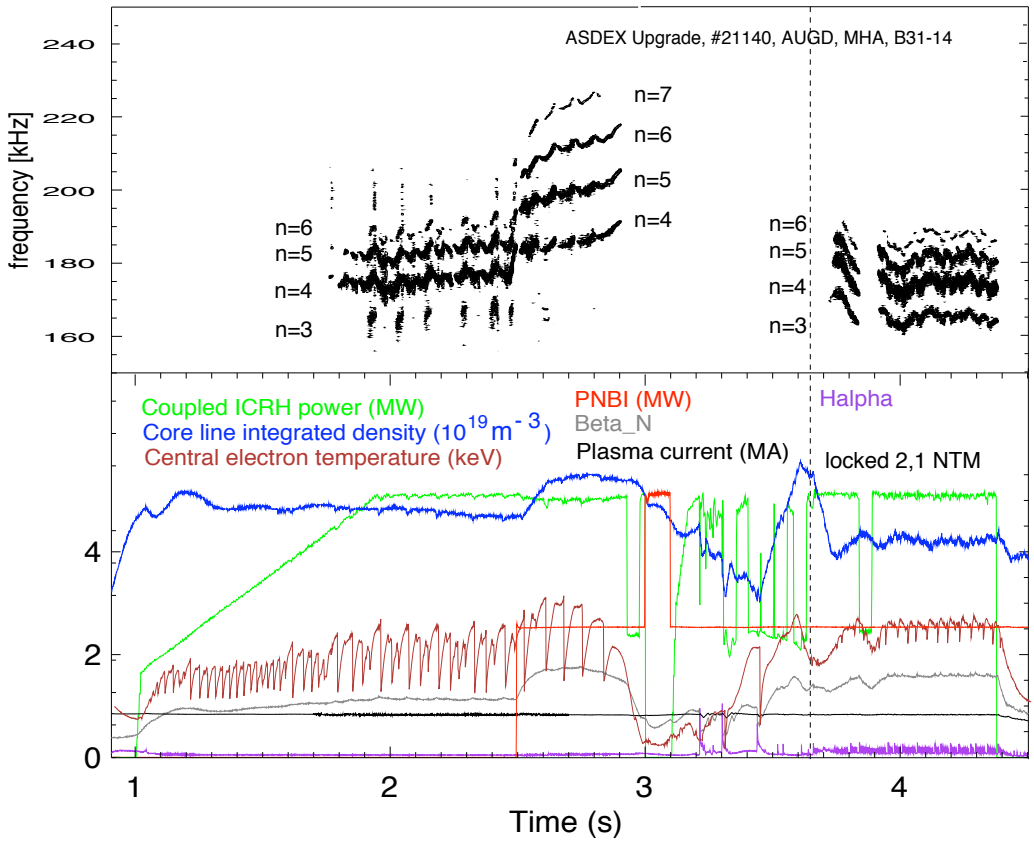

Figure 4.4: L/H-mode Discharge ICRH with additional NBI : #21140 - parameter evolution and spectrogram(magnetic coil B31-14) displaying active TAEs. $I_p = 0.9MA$, $B_T = -2.0T$, $q_{min} \leq 1.0$, $q_{95} \simeq 4.0$. *The dashed line indicates that a (m=2,n=1) NTM locks to the vessel at 3.65s which leads to a reduction of the plasma rotation, in addition to a brief mode locking from 3.21s-3.49s.*

ate in a H-mode scenario or improved variations. These discharges use the same start-up scenarios and plasma parameters as the ICRH discharges (figure 4.1); with a tangential NBI beam (#6) switching-on and remaining on for several seconds, once the current flat-top has been reached. An example of such a discharge in shown in figure 4.4.

Chapter 5

A Characterisation of TAEs at ASDEX Upgrade

At ASDEX Upgrade TAEs from the 1^{st} gap are most commonly observed and it is the analysis of these modes which is presented in the following sections. From this point onwards, the normalised poloidal flux coordinate

$$\rho_{poloidal} = \sqrt{\frac{\Psi_{mag} - \Psi}{\Psi_{mag} - \Psi_{edge}}}$$

where Ψ_{mag} and Ψ_{edge} are the poloidal flux values at the magnetic axis and plasma edge respectively, will be used exclusively as the radial coordinate.

In the discharges analysed, it was found that plasma density profile shape did not change during density ramps, through gas puffing, and consequently the density profile was simply multiplied by a factor. This led to an increase in core line integrated(CLI) electron density $\hat{n}_e$ by the same factor. Thus suggesting that $\hat{n}_e$ can be used in place of a local density measurement when one is specifically interested in the density changes.

5.1 Dependance of the frequency of TAEs on particle density and toroidal magnetic field

The frequency of individual TAEs are tracked during a density ramp and shown in figure 5.1. Using the excited modes' lab-frame frequencies and the corresponding toroidal mode numbers in a linear

extrapolation based on equation 3.8, the plasma rest frame frequency of these modes was calculated. If an excited mode is an Alfvén eigenmode, then its plasma rest frame frequency must be proportional to $\frac{B_\phi}{\sqrt{\hat{n}_e}}$. In figures 5.1 and 5.2 test signals proportional $1/\sqrt{\hat{n}_e}$ and B_ϕ respectively, and the corresponding frequency of individual TAEs in the plasma's rest frame are displayed. The close agreement between the plasma rest frame frequency and the test signals for a density and toroidal field ramp confirms that in each case these modes are Alfvén eigenmodes. The oscillation seen in the tracked frequencies is a result of density fluctuations caused by sawteeth.

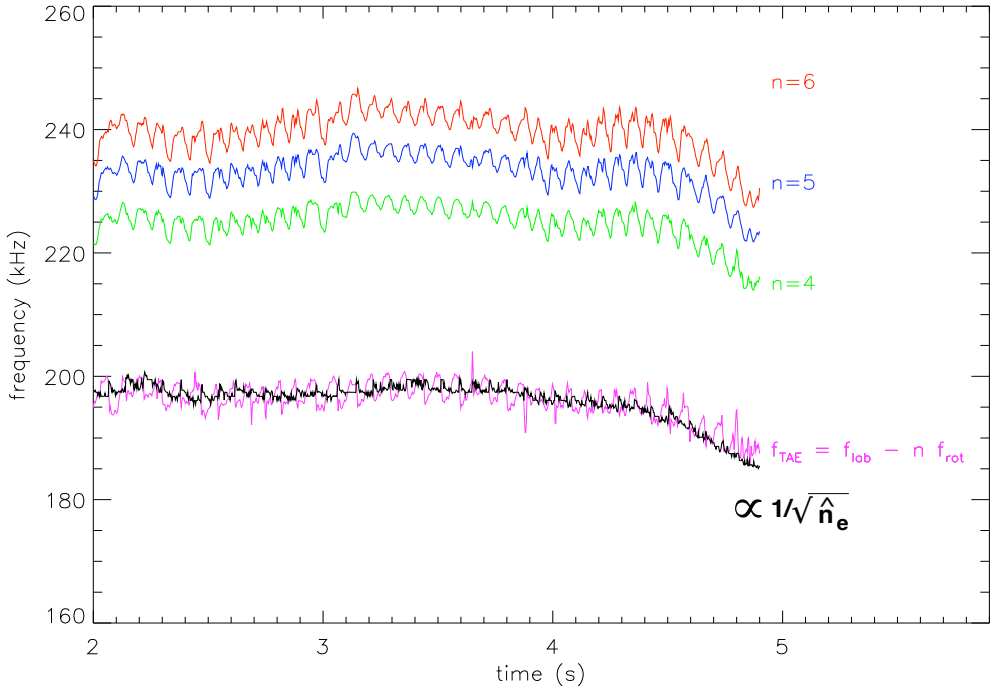

Figure 5.1: Discharge 20396 : dependance of the TAEs' frequencies on $1/\sqrt{\hat{n}_e}$.

5.2 Experimental spectra and eigenfunctions reconstructed from experimental data

The Alfvén continua and frequencies of the n=4,5,6 TAEs were calculated using the density profile and q profile (q-profile derived from an MHD-enhanced equilibrium, section 7.1.2) from discharge #21067 at 2.99s (see figure 3.1) and are presented in figure 5.3. The q-profile was derived from a current density profile reconstruction improved using MHD mode positions, and edge T_e and n_e data. The eigenfunction

calculation was performed using the CASTOR_FLOW code with 21 poloidal fourier harmonics and a radial range $0 \leq \rho_{poloidal} \leq 0.99$. The solid horizontal line in figure 5.3 represents the n=6 TAE plasma rest frame frequency in the 1^{st} gap calculated with CASTOR_FLOW. This line is seen to intersect the continuum at the edge at rho poloidal = 0.96 (see figure 5.3). For higher toroidal number the gaps are seen to shift radially inwards consistent with a monotonically increasing q-profile. For increasing toroidal number the core gap width decreases and in simulations is seen to vanish for $n \geq 8$.

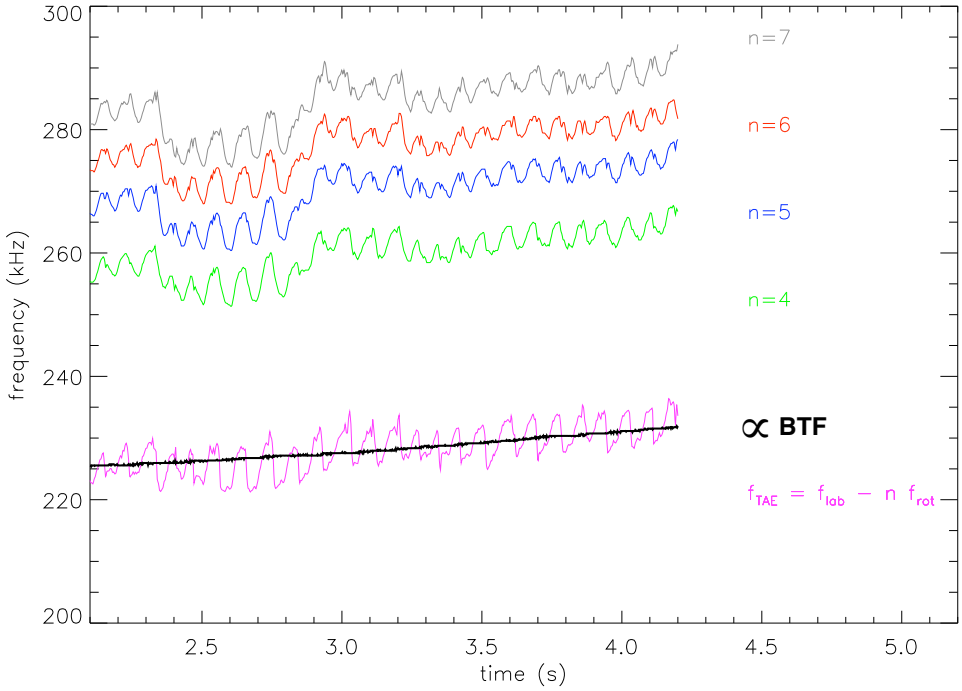

Figure 5.2: Discharge 20399 : dependance of the TAEs' frequencies on the Toroidal field (BTF) is seen, in addition to the influence of density fluctuations

In discharge #21067 at 2.99s the lab frame frequencies of the n=4,5,6 TAEs are 199kHz, 209kHz and 216kHz respectively. Using a linear extrapolation based equation 3.8, the plasma rest frame frequencies of the modes were found to be 165kHz, 166.5kHz and 165kHz respectively. The plasma rest frame frequencies calculated by CASTOR_FLOW for the n=4,5,6 TAEs were 158kHz, 160kHz and 163kHz respectively. The plasma rest frame frequencies from the extrapolation show good agreement with the corresponding frequencies calculated using CASTOR_FLOW. The modest difference between corresponding frequencies may be attributed to uncertainties in the mass density and safety factor profiles.

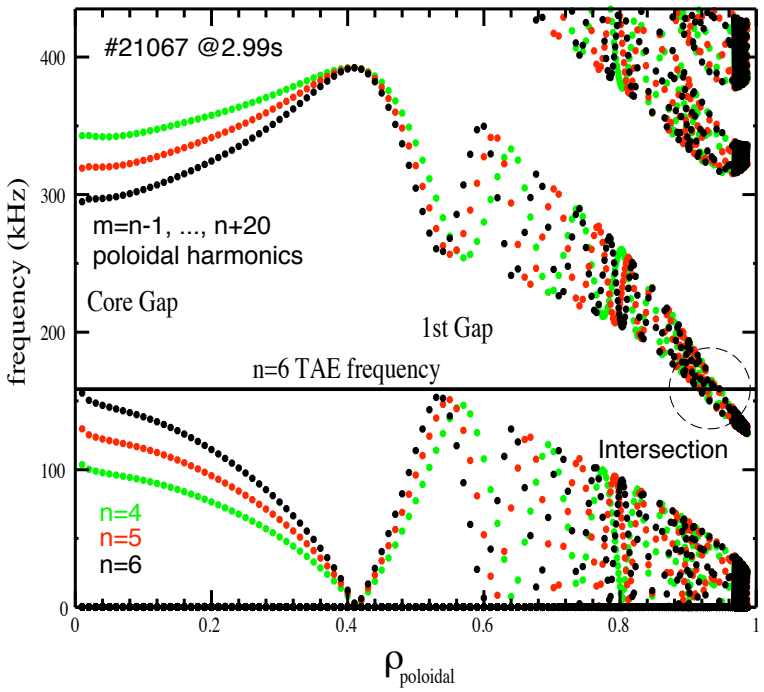

Figure 5.3: n=4,5,6 CASTOR_FLOW Alfvén continua for #21067 @ 2.99s. The horizontal line represents the n=6 TAE plasma rest frame frequency. The intersection of the horizontal line representing f_{TAE} and the Alfvén continuum at the plasma edge ($f_+ = f_{TAE}$) is highlighted by the circle.

A cross correlation analysis was performed between the mode's induced density fluctuations and magnetic perturbation field[63]. This produced the normalised amplitude distribution shown in figure 5.4b and phase shown in figure 5.4c of the n=4 TAE eigenfunction for discharge #21007 at 4.23s. These reconstructions were found to confirm important features of the corresponding eigenfunction calculated by CASTOR_FLOW. The salient features where reflectometry data confirms the eigenfunction structure calculated by CASTOR_FLOW are highlighted by vertical dashed lines in figure 5.4. The maximum of the correlation coefficient (figure 5.4b) from the reflectometry data coincides radially with the maxima of the two dominant poloidal harmonics in the CASTOR_FLOW eigenfunction at $\rho_{poloidal} \approx 0.6$ in figure 5.4a. Additionally, data from the ECE radiometer with 2MHz sampling in discharge #19162 2MHz ECE channel #11, show TAEs have a maximum amplitude at the same location as the maxima in the reflectometry and CASTOR_FLOW eigenfunctions.

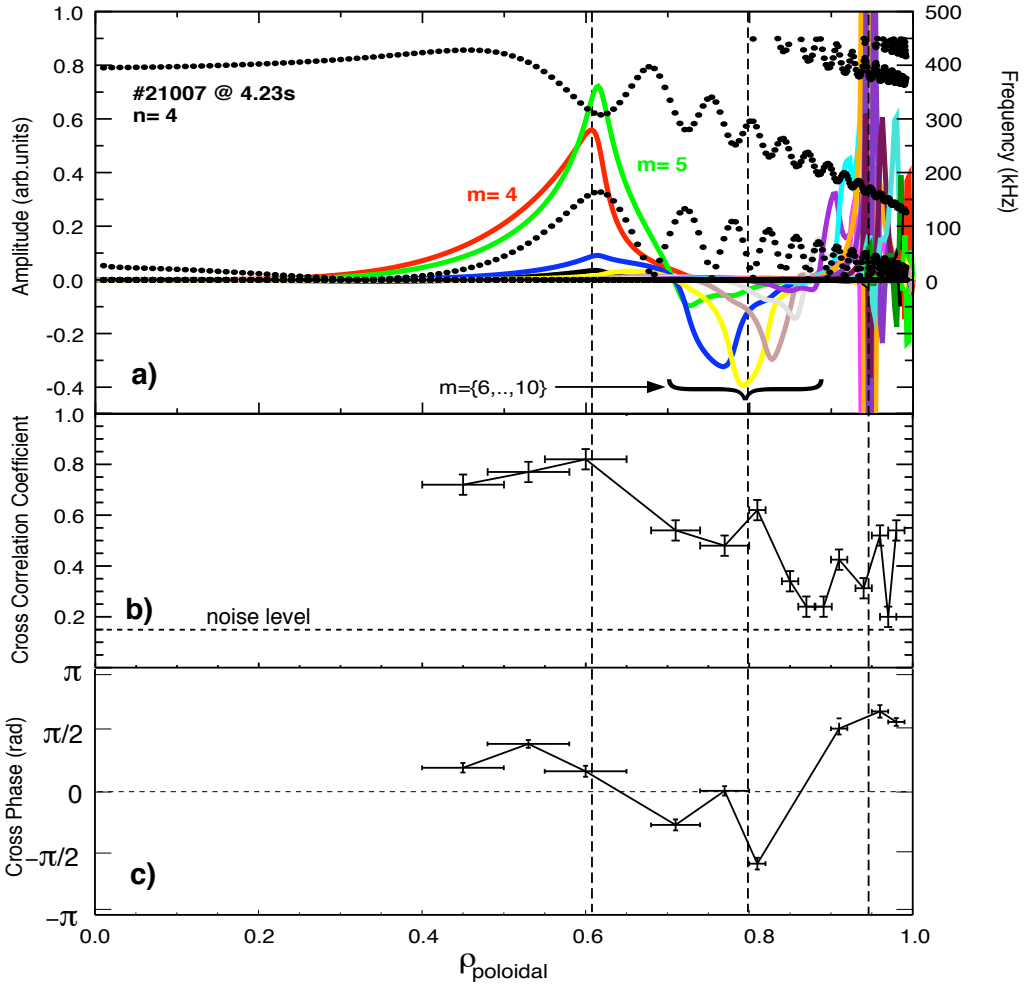

Figure 5.4: a) n=4 TAE eigenfunction's poloidal harmonics (solid curves) with corresponding Alfvén continuum for #21007 @ 4.23s n=4 Alfvén continuum - dotted curve from CASTOR_FLOW. b) Correlation coefficient and c) Cross phase values from a cross correlation analysis performed between the mode's induced density fluctuations and magnetic perturbation field[63]. The vertical dashed lines represent from left to right: the eigenfunction maximum, a sign change of the eigenfunction, the continuum intersection. In a) and b) the rapid oscillation in the curves at $\rho_{poloidal} = 0.95$ *represents the intersection of the frequency* f_{TAE} *with the continuum.*

The results of the cross phase analysis shows a large negative phase at $\rho_{poloidal} \approx 0.8$ in figure 5.4c at the position where the total eigenfunction is negative in figure 5.4a.

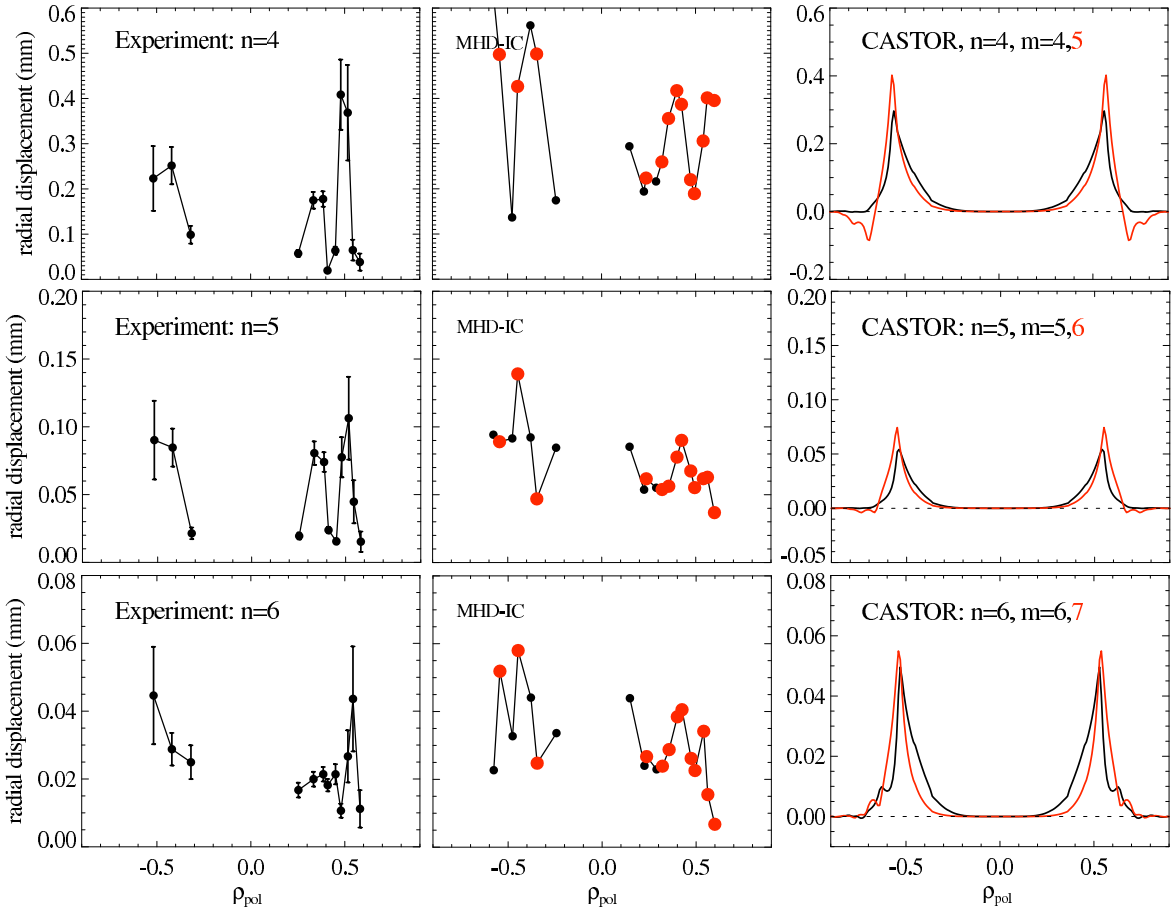

Figure 5.5: Discharge 21067 : n=4,5,6 TAEs' induced SXR fluctuations (left), SXR fluctuations reconstructed by the MHD_IC code using radial eigenfunctions predicted by the CASTOR_FLOW code (middle), and CASTOR_FLOW TAE radial eigenfunctions (right). The red discs in the middle figure represent the positions where actual SXR data was available.

The large radial extent of this eigenfunction demonstrates that these TAEs posses a global structure and that coupling to the outer gaps ($i \geq 2$) is not small.

Since Lithium beam and reflectometry diagnostics provide high quality edge density profiles, and the edge region of the q-profile is described accurately by edge magnetic measurements, CASTOR_FLOW can calculate the Alfvén continuum edge structure reliably. Therefore, we can trust that f_{TAE} intersects the continuum ($f_+ = f_{TAE}$) at the plasma edge. In this case the TAE gap is said to be closed. At $\rho_{poloidal} \approx 0.95$ in figures 5.4a & 5.4b the rapid oscillation of the curve represents this continuum intersection. Even though the continuum is closed at the edge, TAEs are unstable demonstrating

that continuum damping at the plasma edge is not so large that the total damping exceeds the drive.

The new 2MHz Soft X-ray diagnostic allowed Soft X-ray fluctuations induced by TAEs to be measured. These fluctuations are shown in the leftmost image in figure 5.5. These were compared with the SXR fluctuations simulated by the MHD_IC code, see the middle image in figure 5.5[66]. The simulated fluctuations were generated using radial eigenfunctions predicted by the CASTOR_FLOW code for discharge #21067 at 2.99s and are shown in the rightmost image in figure 5.5.

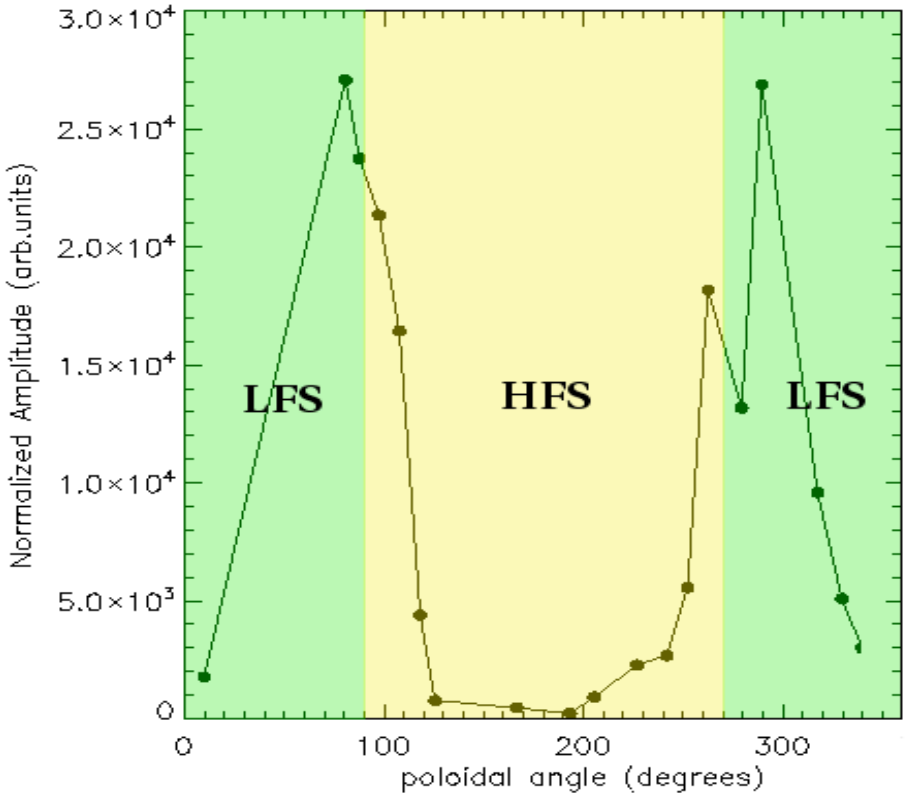

Figure 5.6: Poloidal amplitude distribution from a poloidal array of mirnov coils of the n=4 TAE in discharge #21067 at 2.99s corrected for the radial decay of the magnetic perturbation field. Here the TAE has a much lower amplitude on the high field side (HFS) than on the low field side (LFS).

In the Soft X-ray reconstructions, the fluctuation amplitudes induced by the TAEs are negligible for $\rho_{poloidal} > 0.55$. This agrees with the position of the 1^{st} gap in figure 5.3 and the maximum of the displacement reconstructed from reflectometry data. The maximum displacement of these modes is estimated to be 0.5mm for the n=4, 0.15mm for the n=5 and 0.06mm for the n=6 TAE[53][66].

In figure 5.3 one sees that the frequencies of the TAEs rest just above the lower continuum f_-, which indicates these are even modes. Therefore the eigenfunctions of two dominant poloidal harmonics of the TAE will have the same sign and the TAE will have a larger amplitude on the low-field-side of the the torus or a ballooning structure[46]. In figure 5.6 the n=4 TAE poloidal amplitude distribution measured by a poloidal array of mirnov coils is shown. This shows that the TAE has a larger amplitude on the low field side (LFS) of the torus between 0-90 and 270-360 degrees poloidally. This agrees with the expected behaviour and confirms it to be an even TAE. In figure 5.6 the amplitude measured for the given TAE from each mirnov coil had to be corrected for radial decay because all mirnov coils are not the same distance from the resonant flux surface. To do this it is assumed that the poloidal magnetic field of a TAE decays according to the following approximate formula (cylindrical vacuum approximation for $\lambda_{tor} \gg \lambda_{pol}$)[75]

$$B_{coil}^{edge} \sim B_{\theta}^{res} \left(\frac{r_{res}}{r_{coil}} \right)^{m+1}. \tag{5.1}$$

Here B_{coil}^{edge} is the poloidal magnetic field at the mirnov coil, B_{θ}^{res} is the value of the poloidal magnetic field at the resonant surface, r_{coil} is the distance from the mirnov coil to the magnetic axis, r_{res} is the distance from the resonant surface to the magnetic axis at the same poloidal angle and $m = nq_{gap}$.

5.3 Coupled ICRF power vs density and q_{95} at the onset of TAEs

When considering stability of TAEs, the ICRH power $P_{ICRH}^{onset}[MW]$ required to excite TAEs of a particular toroidal mode number n versus core line integrated (CLI) density $\hat{n}_e[10^{19}m^{-3}]$ reveals several facts about the fast ion drive and individual TAEs. An increase in density with other parameters held constant increases collisionality, thereby reducing the slowing-down time of the fast ion population, which in turn decreases β_f, leading to a reduction of the driving term in equation 3.10. Therefore one would expect the threshold, when TAEs appear, to increase with increasing density. In figures 5.7 (L-mode) and 5.9 (H-mode) this is demonstrated by the positive slope A_1 of the linear least squares fit $P_{ICRH}^{onset} = A_1\hat{n}_e + A_0$ to the data.

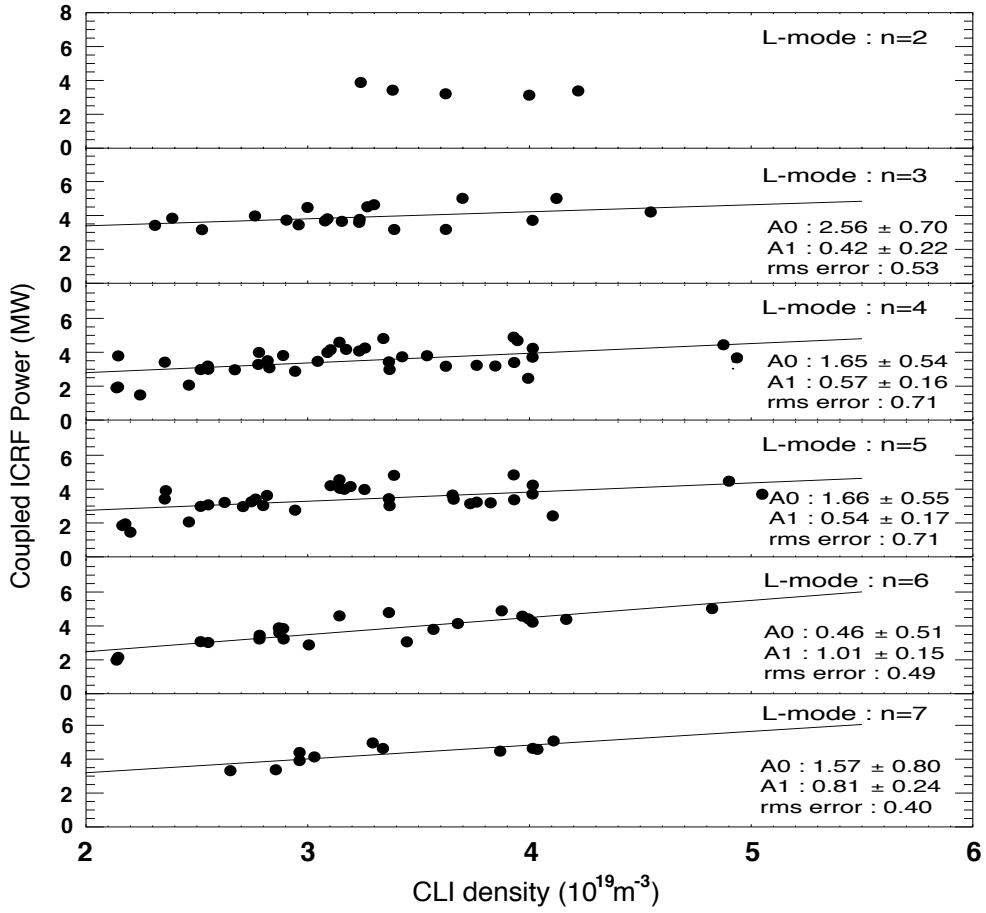

Figure 5.7: ICRF power threshold versus CLI density for TAEs during L-mode. Linear fit $P_{ICRH}^{onset} = A_1\hat{n}_e + A_0$ *performed on data. RMS-error and coefficients* A_0, A_1 *with the corresponding standard deviations are presented.*

The fitted slopes A_1 of the L-mode data set (figure 5.7) are plotted in figure 5.8, where the strength of the dependence of the threshold on density for individual TAEs suggests an overall increasing trend with increasing n (highlighted by the dashed line). The deviations from an increasing trend are not considered fatal as a result of the large uncertainties in the fitted slopes. If one considers finite orbit width effects[57] together with a density increase, then one could expect to observe an increasing trend in the strength of the threshold dependence on density for increasing n. This occurs as the fast ion drive is believed to be at its maximum at low to moderate n (n=3-5 for ASDEX Upgrade) and then decreases with increasing n, which would amplify the detrimental effect that an increase in density has on the fast ion β as n increases. In addition, differences in the shape of the Alfvén continuum observed for different n and changes resulting from an increase in density were also initially considered as a possible

explanation of the observed trend, however no conclusive pattern was identified which would support that idea. As a final remark the inclusion of H-mode data in figure 5.8 shows that in H-mode the strength of the density dependance for n=4 and n=5 TAEs are very close, similar to their counterparts in L-mode. This suggests that this particular feature is not a result of the quality of confinement but the effects of the finite orbit widths of the fast ions.

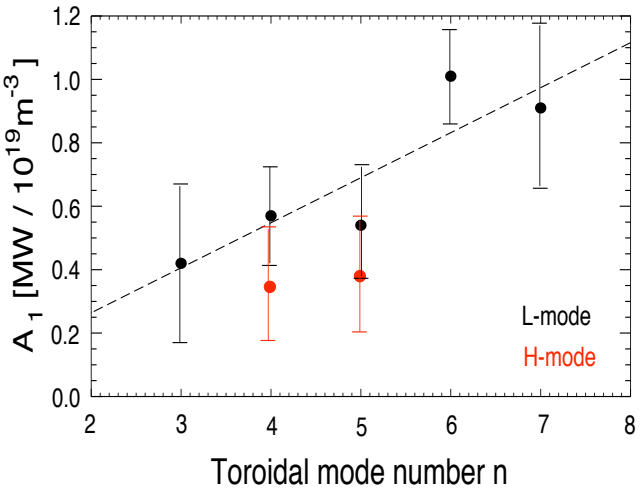

Figure 5.8: Fitted slopes A_1 shown in figures 5.7 and 5.9, from the linear fit of the ICRF power threshold versus CLI density for TAEs during L-mode and H-mode, versus toroidal mode number n. The dashed line is a visual guide to the increasing trend from moderate to high n.

The absolute coupled ICRF power required to overcome the threshold for TAEs was found to be independent of q_{95} (the q-vqlue of the flux surface which contains 95% of the total poloidal flux). However it was seen that if $q_{95} > 3.9$ (figure 5.10), an n=2 TAE was not observed while $n \geq 3$ TAEs were. In addition, discharges operated in limiter configuration showed no $n = 2$ TAE activity. In these discharges, the value of q_{95} remained above of 3.9. These results suggest that $q_{95} > 3.9$, and by extension that edge magnetic shear above a certain value, is the important stabilising factor for TAEs with $n < 3$ and not necessarily a separatrix. This position is supported by the work done by A. Jaun et al.[64], in which it was shown that a high value of q_{95} and by extension edge magnetic shear resulted in a localisation of the wave radial field, and increased continuum damping rates.

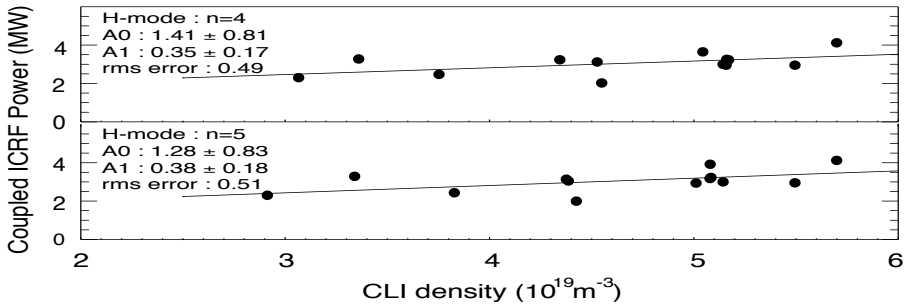

Figure 5.9: ICRF power threshold versus CLI density for TAEs during H-mode. Linear fit $P_{ICRH}^{onset} = A_1\hat{n}_e + A_0$ performed on data. RMS-error and coefficients A_0, A_1 with the corresponding standard deviations are presented.

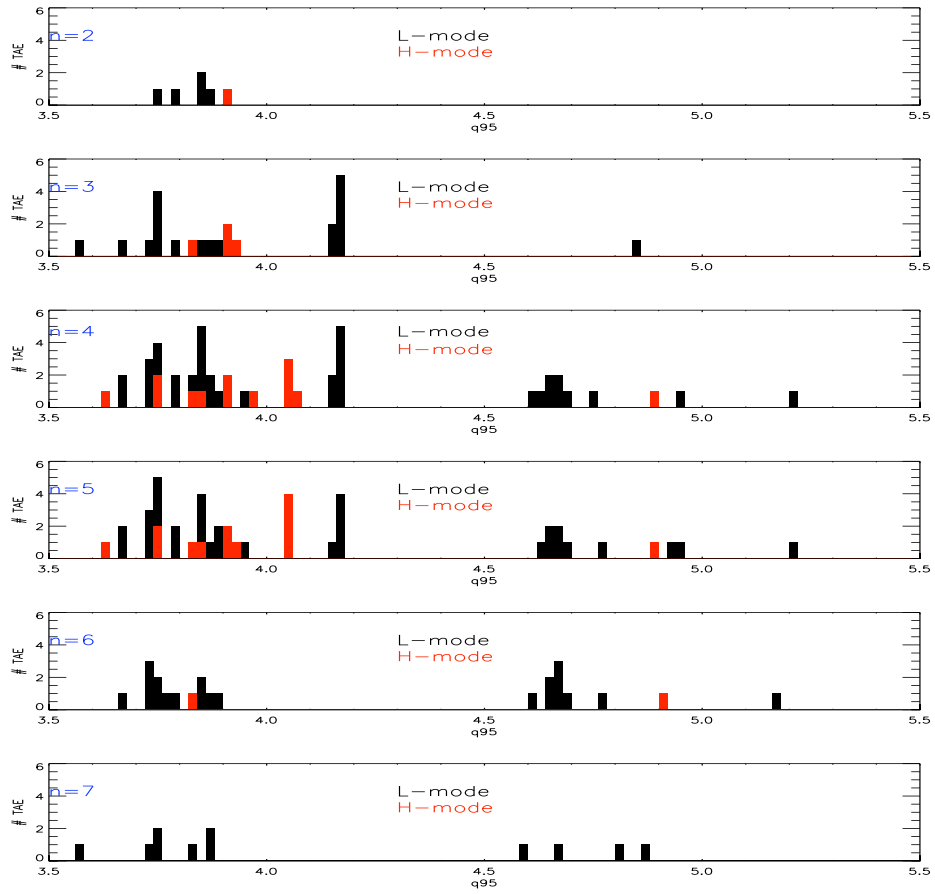

Figure 5.10: q_{95} values recorded at the onset of TAEs in discharges with a magnetic divertor during L and H modes. The data shows that for values of $q_{95} < 3.9$ no TAEs with $n \leq 3$ are observed.

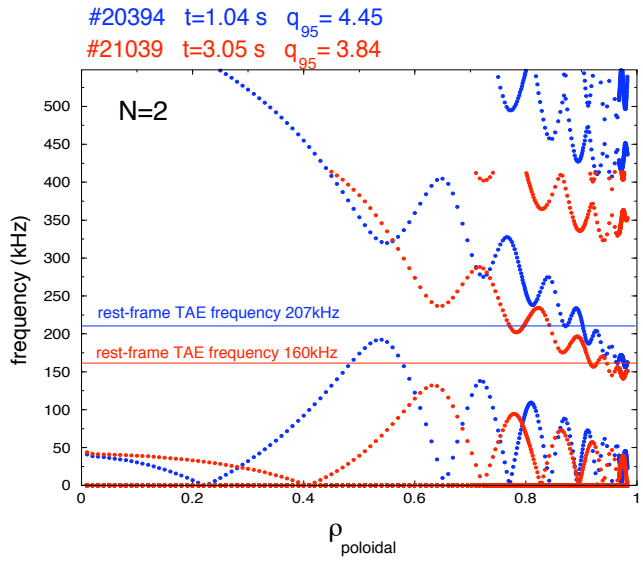

(a) Alfvén Continua with Toroidicity induced gaps

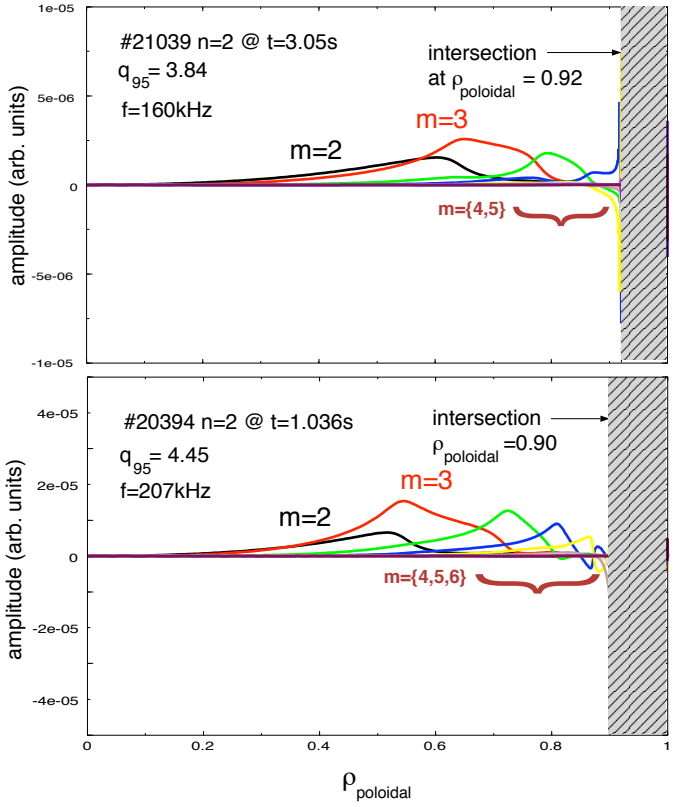

(b) Radial Displacement Eigenfunctions

Figure 5.11: Discharge #20394 : n=2 TAE at 207kHz at 1.04s with parameters B_T=2.4T, I_p=0.83MA, $n_e(0)$= $3.3 \times 10^{19} m^{-3}$, q_0=0.97, q_{95}=4.7. Discharge #21039 : n=2 TAE at 160kHz in discharge at 3.05s with parameters B_T=1.94T, I_p=0.88MA, $n_e(0)$= $3.9 \times 10^{19} m^{-3}$, q_0=0.97, q_{95}=3.9.

In figures 5.11 (a) and (b), the Alfvén continua and eigenfunctions for two similar discharges #20394 with $q_{95} = 4.45$, and #21039 with $q_{95} = 3.8$ are shown. Here one can see that the frequency of the TAE intersects the continuum in both discharges, which results in non-negligible continuum damping. Equivalent to that shown by A. Jaun, the intersection moves radially inwards with increased q_{95} further localising the eigenfunction. It is necessary to point out here that the CASTOR_FLOW code is not capable of simulating the interaction with the continuum, and therefore the shape of the eigenfunctions from the intersection to the plasma edge are not physically correct and have therefore been covered.

5.4 Fast ion losses induced by TAEs

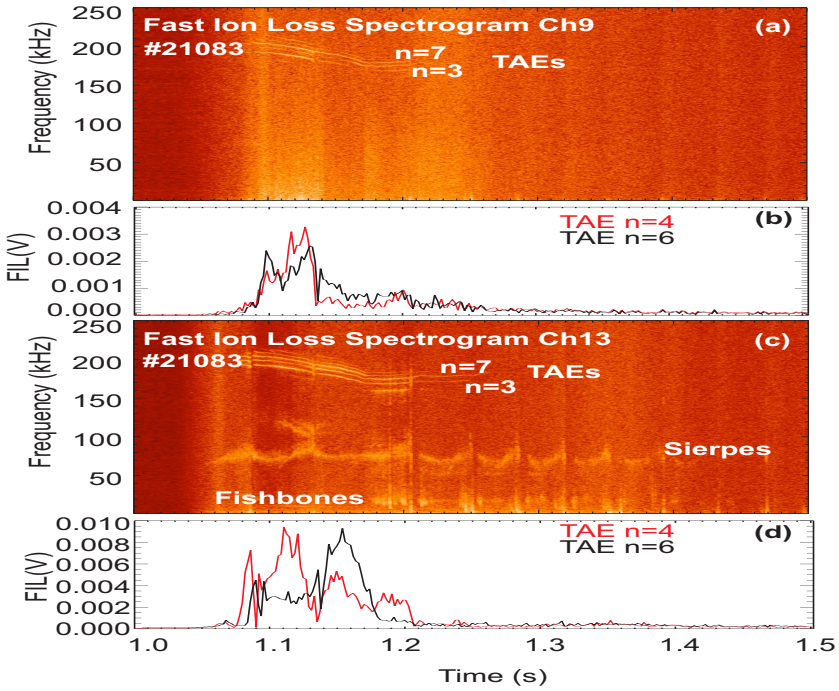

Figure 5.12: Discharge 21083 : a) Spectrogram of FILD channel 7 data, b) fast ion loss amplitudes of the n=4,6 TAEs in channel 7, c) Spectrogram of FILD channel 13 data, and d) fast ion loss amplitudes of the n=4,6 TAEs in channel 13.

Fast ion losses correlated with active TAEs, whose frequencies are between 160kHz and 210kHz, were identified in discharge #21083 in two FILD channels[67]. This is shown in figure 5.12, where the measured losses have energies in the range 0.25MeV-1.6MeV for Hydrogen and pitch angles

($\theta = arccos(v_{\|}/v_{total})$) between 60 and 70 degrees, identifying them as highly energetic deeply trapped particles. This can be seen in data taken from a similar discharge #21011, see figure 5.13. The losses observed were associated with two fast ions groups at energies of 0.3MeV and 1.1MeV (energies thus quoted are the mean energy of each group). Using the HAGIS code[32], solutions of the resonance condition (expression 3.9) were identified, and these solutions demonstrated that an n=4 TAE can be resonant with two ion groups at very different energies. The solutions were at the bounce harmonics (k = 0 and 1) and the precessional harmonic (n=4)[67]. It is important here to remember that this solution represents the effect of the n=4 TAE alone, whereas the observed losses are caused by all unstable TAEs.

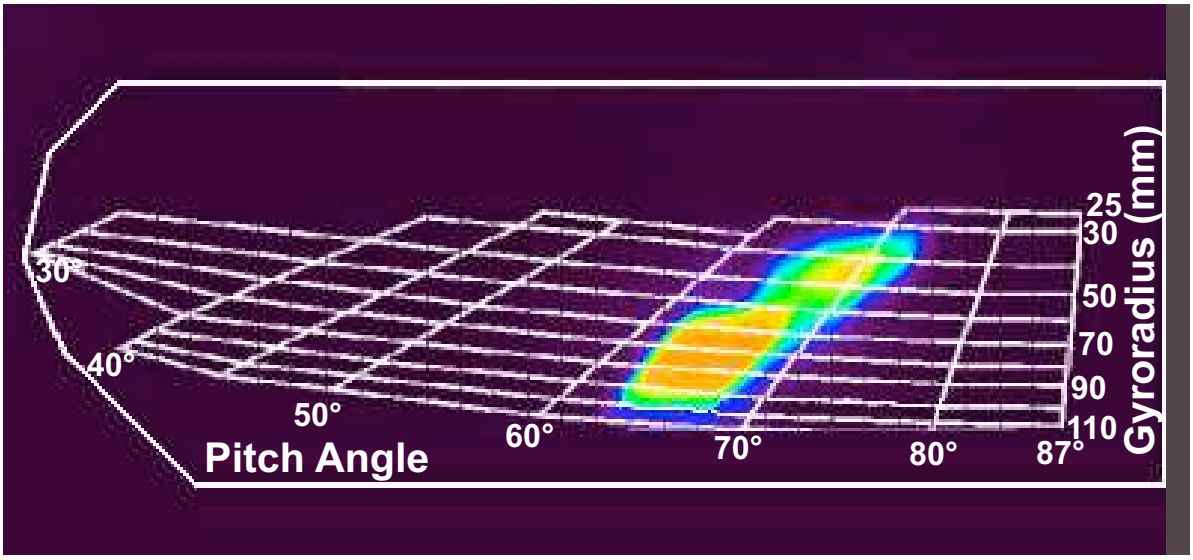

Figure 5.13: Discharge 21011 : Fast ion losses induced by TAEs are found to be deeply trapped fast ions covering a wide range of gyroradii (energies).

Particle loss rates of $3 \times 10^{16} s^{-1} m^{-2}$ and $1 \times 10^{17} s^{-1} m^{-2}$ were measured for the ion groups with energies of 0.3MeV and 1.1MeV respectively. However all of these losses cannot be attributed solely to TAEs as there are other MHD modes present in the plasma expelling fast particles[67].

The FILD is present in one toroidal location at the plasma edge on the magnetic mid-plane low field side. Due to the effects of ICRH and the magnetic mirror, fast ion losses will occur on the low

field side of the torus, and therefore a non-isotropic distribution of fast ion losses is expected. In order to estimate what reduction in heating power these losses represent, it is assumed that the fast ion losses are homogeneously distributed on the low field side of the torus. Using this an upper bound on the power loss caused by all TAEs for each loss rate and corresponding energy are,

$$P_{FILD} \leq (3 \times 10^{16} s^{-1} m^{-2} \times 300 keV) \times (S_{lc}/2) = 0.035 MW \tag{5.2}$$

and

$$P_{FILD} \leq (1 \times 10^{17} s^{-1} m^{-2} \times 1.1 MeV) \times (S_{lc}/2) = 0.43 MW \tag{5.3}$$

respectively. Here S_{lc} is the surface area of the last closed flux surface, and the fraction $S_{lc}/2$ embodies the statement that the fast ion losses occur only on the low-field side of the torus. It is important here to remember that the large upper bound on the power lost is an estimate derived from losses caused by all loss-mechanisms and not just TAEs.

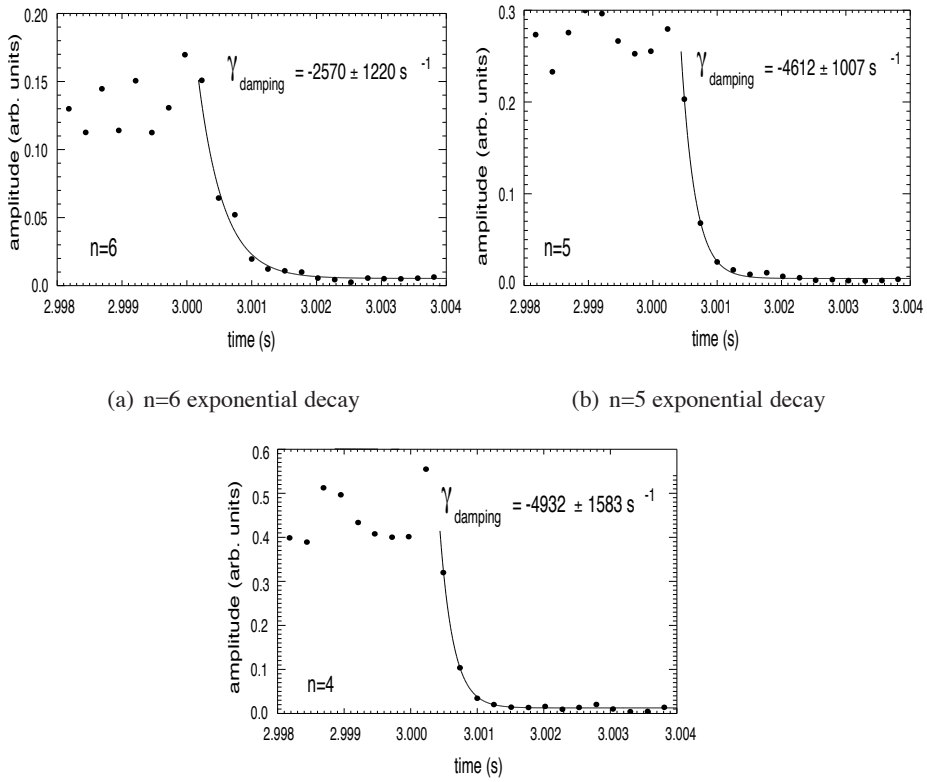

(a) n=6 exponential decay

(b) n=5 exponential decay

(c) n=4 exponential decay

Figure 5.14: Discharge #21067 : Measurement of the n=4,5,6 decay rates by fitting an exponential curve to the modes' amplitudes.

5.5 Decay rate and growth rate measurements

The damping rate experienced by a TAE excited by ICRH-generated fast ions is greater than or equal to the mode's decay rate when the ICRH power is switched off as a result of neglecting the finite slowing down time of the ICRH ions. Experimentally the decay rate R_d is measured by fitting an exponential curve the mode amplitude. An example of this measurement is shown in figures 5.14(a)-5.14(c) corresponding to the n=4,5,6 TAEs in discharge #21067. To be consistent with the representation of growth, drive and damping rates used in equation 3.10, these decay rates are expressed as a percentage of the average frequency of the TAEs in the plasma's rest frame f_{TAE}. The measured decay rates are: $3.0 \pm 1.0\%$, $2.8 \pm 0.6\%$, $1.6 \pm 0.8\%$ of the average frequency ($f_{TAE} = 162$kHz) corresponding to the n=4,5,6 TAEs and are larger than those calculated with the LIGKA code, which are within the range 0.8%-1.1%[30].

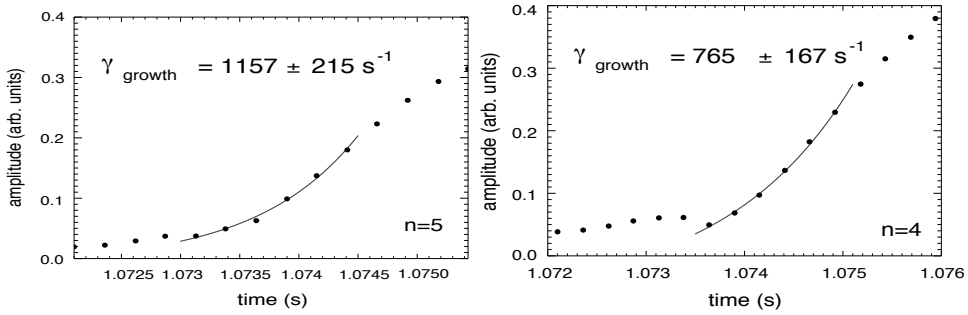

(a) n=5 exponential growth

(b) n=4 exponential growth

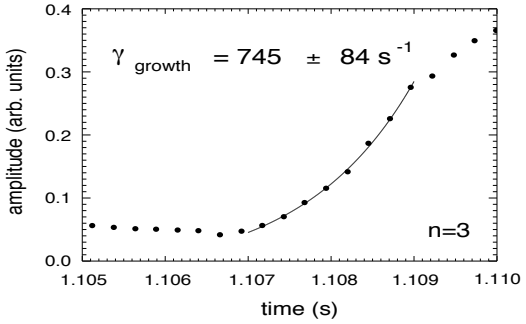

(c) n=3 exponential growth

Figure 5.15: Discharge #21083 : Measurement of the n=3,4,5 growth rates by fitting an exponential curve to the modes' amplitudes.

Growth rate measurements, some of which are shown in figures 5.15(a)-5.15(c), were calculated

using an exponential fit to the amplitudes of TAEs for n=3,4,5,6 in discharge #21083 during the exponential growth phase. Since this method neglects the time needed to build up the fast ion distribution these growth rates are lower limits. The growth rates, expressed as a percentage of the average frequency of the TAEs in the plasma's rest frame ($f_{TAE} = 168$kHz), for n=3,4,5,6 are: $0.44 \pm 0.05\%$, $0.5 \pm 0.1\%$, $0.7 \pm 0.1\%$, and $0.5 \pm 0.2\%$ respectively.

If plasma conditions do not vary significantly then the damping rate at the end of the exponential growth phase can be taken to be equal to the damping rate when ICRH is switched off (measured decay rate). In order to approximate the average drive, it is assumed that in similar discharges that damping rate of individual TAEs is the same. Now taking the average TAE damping rate for the observed TAEs to be 2.5% and the average growth rate to be 0.5%, using equation 3.10, we find an average drive at the end of the growth phase of the TAEs from ICRF accelerated hydrogen ions to be 3.0%.

5.6 Fast ion pressure profiles

The equilibrium pressure profile can be reconstructed accurately by the CLISTE code[49]; if density (from DCN, Lithium Beam, and Reflectometry diagnostics) and temperature (from ECE, Thompson scattering diagnostics) data from the plasma edge, and q profile information from MHD modes and/or MSE data are used to constrain the solution. In such a well diagnosed equilibrium pressure profile, the fast pressure profile is the difference between the equilibrium pressure profile and the thermal pressure profile ([43], see section 7.2). (Apart from the edge region, where the fast pressure contribution is generally negligible, the thermal pressure data, assumed to be available across the full minor radius, is not used to constrain the CLISTE equilibrium solution) In the following discussion the CLISTE fast pressure profile has been calculated from such a reconstruction of the equilibrium pressure profile.

According to equation 3.10, the fast pressure profile has a strong influence on the stability of TAEs and therefore must support the measured growth rates. In figure 5.16, the total fast pressure profiles calculated by the ICRH power deposition codes PION [34][35] and TORIC[33], and the equilibrium code CLISTE; are shown together with the positions of the TAEs and the m=4,5 poloidal fourier harmonics of the n=4 TAE eigenfunction.

The first observation is that the TORIC pressure profile at the positions of the TAEs, provides only a negligible fast pressure and fast pressure gradient, and therefore an insufficient drive, whereas the

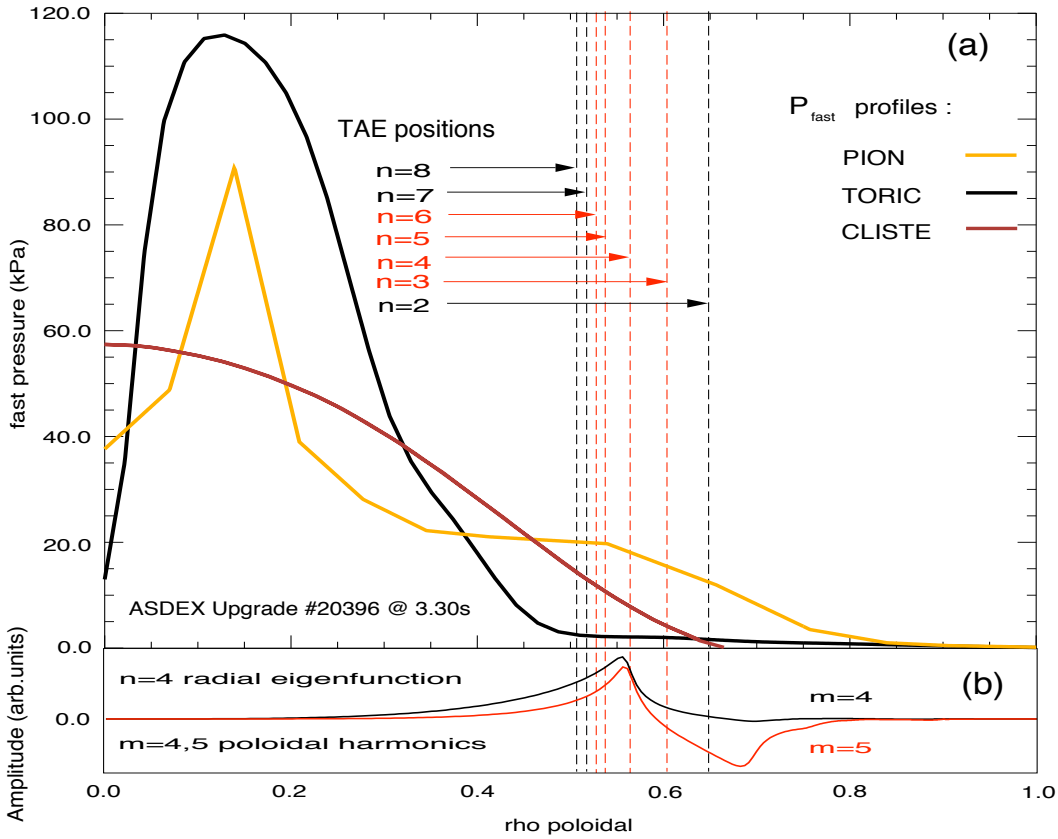

Figure 5.16: (a) Discharge #20396 @ 3.3s : Fast pressure profiles produced by the CLISTE, PION and TORIC codes. The red lines indicate position of the most commonly observed TAEs with the black representing TAEs observed less frequently.

(b) the dominant m=4,5 poloidal harmonics of the observed n=4 TAE.

CLISTE and PION profiles have a much larger fast pressure and fast pressure gradient. It is believed this occurs because the TORIC code assumes a zero banana orbit width ansatz, in contrast to PION which allows for finite banana orbit widths[76]. This results in a radial *broadening* of the PION fast pressure profile when compared to the profile calculated with TORIC. The PION and CLISTE codes do not simulate the interaction of fast ions with MHD instabilities, such as TAEs, and as such, the fast pressure profiles do not contain any information pertaining to these interactions.

From the considerable radial overlap of the CLISTE and PION fast pressure profiles with the n=4 m=4,5 TAE's eigenfunction, it is evident that there is considerable energy available to drive TAEs, which can result in a modest redistribution or loss of fast ions (figure 5.16). In [67], fast ion losses caused by TAEs in ASDEX Upgrade were shown to be deeply trapped and with an average energy of

1.1MeV. Combining this with an average pressure gradient ($(dp/dr)_{avg} = (p_{min} - p_{max})/a$) from each of the fast ion pressure profiles displayed in figure 5.16, and the fast pressure, from the PION and CLISTE profiles, at the position of the n=4 TAE and using the part of equation 3.10 pertaining to the drive, one can estimate the drive these profiles would provide at the position of a TAE's maximum displacement. The drive rates, normalised with respect to the average frequency of the TAEs in the plasma's rest frame f_{TAE}, calculated from the CLISTE and PION profiles for an n=4 TAE are 3% and 12% respectively. Comparing this with the expected TAE drive rate, which for a saturated TAE is the damping rate, one sees that the drive rates estimated using the fast pressure profiles are of the same order of the estimate taken to be equal to the average damping/decay rate, which is $2.5 \pm 0.8\%$. The discrepancy between the calculated and measured values is believed to originate from the pressure gradients, and fast ion velocity derived from the energy of the fast ion losses. In the case of the fast pressure profiles one can see that calculated drive rates span an interval from 3-12%, this demonstrates how sensitive the TAE drive rate is to the pressure profile. In fact one sees from equation 3.10 that the drive rate depends strongly on local pressure and gradient. In addition, when the role of the fast ion velocity ($V_A/V_f \simeq 0.5$) is considered, it is revealed that a decrease of this velocity, with the local value of V_A held constant, can increase the TAE drive rate by as much as a factor of 3. Thus any uncertainty in this value can have an appreciable effect. In spite of these facts, one can see that the estimated drive rates show reasonable agreement with the measured value.

The simple expression for $\langle \beta_{fast} \rangle$ defined by equation 2.82 gives a value of $\langle \beta_{fast} \rangle = 0.005$ which is seen to be larger than the values 0.0024, 0.0030, and 0.0025 calculated from CLISTE, PION and TORIC profiles respectively. Here the difference is believed to be as a result of the form of the Spitzer slowing down time used, and the explicit assumption that all of the heating power is absorbed by the minority species. With respect to the slowing down time, it was assumed that electron velocity v_e was much greater than fast ion velocity v_f. However the energies of observed fast ion losses suggest in reality that $v_f/v_e \simeq 0.30 \rightarrow 0.45$. This implies that the form of the slowing down formula which explicitly uses the test particle's energy would be more accurate. Thus the facts suggest that expression 2.82 gives an upper limit on $\langle \beta_{fast} \rangle$.

Using the equation for the volume averaged β_{fast}, it was determined that a critical stability threshold for TAEs within similar discharges did not exist. The details of which can be found in the appendix.

5.7 Effects of radial and tangential NBI on the stability of TAEs

Due to the injection angle of radial beams, there is a strong particle deposition in the centre of the plasma. This is precisely where the ICRF resonance is chosen to be. The resulting rise in density leads to a reduction in the slowing-down time of fast ions, which can result in weakening of the fast ion drive of the TAEs. And as a result of this, TAEs are observed to be either severely weakened or suppressed entirely.

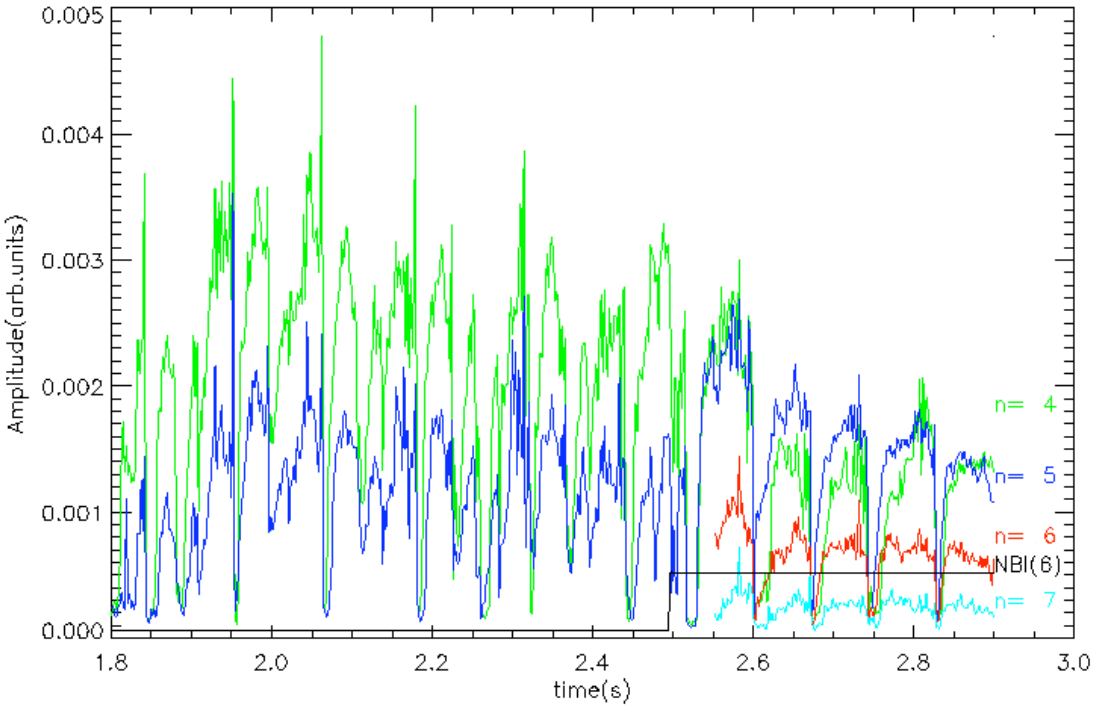

Figure 5.17: Discharge #21140 Amplitude time traces of n=4,5,6,7 TAEs with ICRH only and with both ICRH and continuous tangential NBI source #6 from 2.5s onwards. These amplitudes were measured by tracking frequencies of the TAEs in a Fourier spectrum of the signal from the radial ballooning coil B_r coil "B31-14". NBI power = 2.5MW

Discharge #21140 was designed to study the effect of tangential NBI (source #6) on TAEs (see figure 4.4). In figure 5.17, starting at 1.8s, an n=4 and n=5 TAEs are excited. At the same time a sawtooth instability is present in the plasma, from the temperature time trace in figure 4.4 this instability is seen to have two different periods. This leads to a unstable amplitudes in both TAEs, see figure 5.17. Once the tangential NBI is switched on the sawtooth period increases and a clear modulation of the

TAEs' amplitudes is seen. The amplitude of the n=4 TAE is reduced, whereas the n=5 has slightly grown in amplitude. It is expected that for these discharges a flat central q-profile is present, thus one can have a non-negligible distance between the n=4 and n=5 TAEs. One possible explanation is that the fast ion population in the vicinity of the n=4 has been affected more by the tangential NBI, which deposits more particles off axis. However, the NBI has had the effect that high energy tail of the ICRH distribution has been enhanced by the NBI and destabilised the n=6 and n=7 TAEs. At 2.9s ICRF coupling becomes unstable, shortly after the MSE NBI blip occurs. Up until 3.95s, TAEs reappear only for short periods as the the ICRF power fluctuates. Due to additional NBI power, an m=2/n=1 NTM grows and is able to lock to the vessel causing the plasma rotation to slow, experience a sharp density decrease, and a sharp decrease in radiated power which persists beyond the ICRF recovery. In addition, after 3.95 seconds, the TAEs' amplitudes are significantly increased with the n=3 TAE becoming unstable, all except for the n=7 TAE which disappears (figure 5.18). What seems likely to have occurred is that the density decrease has increased the slowing down time of the fast ions, thereby increasing the TAE drive and destabilising the n=3 TAE. However with the density decrease the lower Alfvén continuum branch f_- is increased, closing the gap in the core which in turn increases the continuum damping experienced by the higher n TAEs such as the n=7 TAE. This increase in damping is too large for the increase in drive to overcome and thus the n=7 TAE is stabilised. Throughout these dynamics, the doppler shift measured increases due to the NBI momentum input, however it differs by 5kHz between phases on either side of the period of unstable ICRF. This difference is attributed to the effect of the locked mode.

Once the ICRH is switched off these TAEs disappear, ruling out the possibility that these were destabilised by passing fast ions through the $v_{fast\ ions} = \frac{v_A}{3}$ resonance, where v_A is the plasma Alfvén velocity. This is not unexpected, because for deuterium, the fastest beams introduce ions with 60% of $\frac{v_A}{3}$; and the conversion of ICRF accelerated fast trapped ions into resonant passing particles through coulomb interactions is considered to be small enough to be neglected.

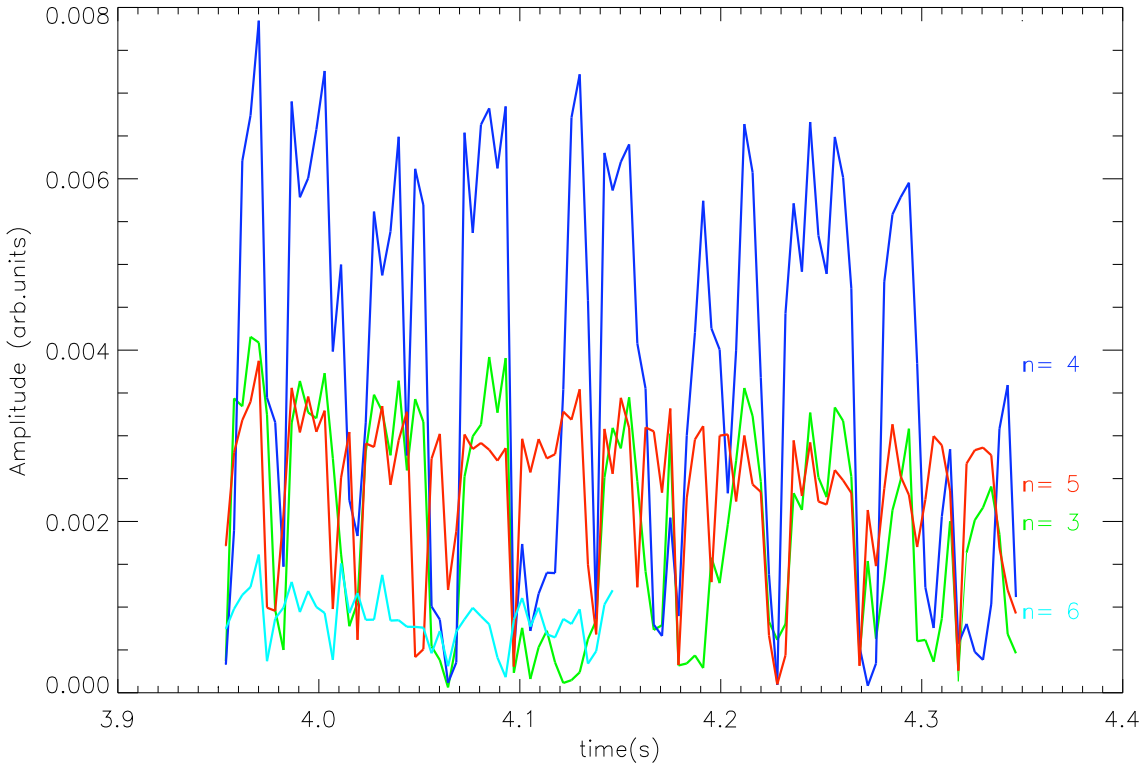

Figure 5.18: Discharge #21140 Amplitude time traces of n=3,4,5,6 TAEs after a radial NBI blip with ICRH and continuous tangential NBI from 2.5s onwards. These amplitudes were measured by tracking the frequencies of the TAEs in a Fourier spectrum of the signal from the radial ballooning coil B_r coil "B31-14".

5.8 Spectral line widths

The spectral line widths (Full Width-Half Maximum) of TAEs were measured during systematic variations in key plasma parameters, B_ϕ, I_p and $\hat{n}_e$ to reveal any dependencies that might exists. The B_r coil "B31-14", positioned at the mid-plane on the low-field side with high frequency response was used for each of these measurements. These values are shown as a percentage of the average frequency of the TAEs in the plasma's rest frame. In tables 5.1, 5.2 and 5.3 these results are given along with the value of the relevant plasma parameter at corresponding time point. In table 5.1, spectral line widths are shown for a 30% variation in density. From the data the line widths do not show a clear trend with increasing density. What one can infer is that density does not play a large role in determining the behaviour of these measurements as a group.

For the toroidal field ramp, table 5.2, line widths were collected for a 5% increase from its initial

n\$n_e(0)[10^{19}m^{-3}]$	4.08	4.19	4.29	4.50	4.64	5.04	5.20	5.34	$\mu \pm \sigma$
4	0.25	0.26	0.41	0.31	0.32	–	0.40	0.34	0.33 ± 0.06
5	0.40	0.20	0.41	0.57	0.37	0.22	0.57	0.23	0.37 ± 0.15
6	0.30	0.31	0.62	0.41	0.53	0.16	–	–	0.39 ± 0.17

Table 5.1: Discharge #20396 : Spectral line widths measured during a ramp in particle density n_e $[10^{19}]$ for n=4,5,6 TAEs. Also presented is the mean damping μ for each toroidal mode number n, along with one standard deviation σ.

n\B_t[T]	2.43	2.43	2.45	2.47	2.49	2.51	2.54	2.56	$\mu \pm \sigma$
4	0.19	0.19	0.30	0.19	0.19	0.19	0.23	0.19	0.21 ± 0.04
5	0.19	0.15	0.30	0.19	0.19	0.14	0.42	0.23	0.23 ± 0.09
6	0.33	0.24	0.20	0.16	0.23	0.14	0.33	0.23	0.23 ± 0.07
7	0.19	0.15	0.34	0.19	0.19	0.14	0.23	–	0.20 ± 0.07

Table 5.2: Discharge #20397 : Spectral line widths measured during a ramp in the toroidal field B_t [T] for n=4,5,6,7 TAEs. Also presented is the mean damping μ for each toroidal mode number n, along with one standard deviation σ.

value. Over this interval no dependence is observed. But, over such a small interval, it is not possible to draw a stronger conclusion.

n\I_p[MA]	0.873	0.890	0.890	0.890	0.915	0.915	0.915	$\mu \pm \sigma$
4	0.23	0.13	0.14	0.19	0.14	0.23	0.23	0.18 ± 0.05
5	0.18	0.13	0.18	0.24	0.14	0.23	0.18	0.18 ± 0.04
6	0.23	0.18	0.23	0.33	0.19	0.37	0.18	0.24 ± 0.08
7	0.14	0.18	0.18	0.28	0.23	0.23	0.14	0.20 ± 0.05

Table 5.3: Discharge #20398 : Spectral line widths measured during a ramp in the plasma current I_p [MA] for n=4,5,6,7 TAEs. Also presented is the mean damping μ for each toroidal mode number n, along with one standard deviation σ.

During the plasma current ramp a 5% increase current was recorded (table 5.3). For each TAE the

line widths measured suggests that here also no trend exists. However a larger ramp would be necessary to conclusively rule out the possible existence of a trend.

Spectral line width measurements for n=4,5 TAEs are compared in table 5.4 for L-mode (limiter configuration, ICRH only), L-mode (divertor configuration, ICRH only), H-mode (divertor configuration, ICRH only) and H-mode (divertor configuration, ICRH and tangential NBI). No significant difference in line widths between these different divertor cases is seen with respect to the average standard deviation $\sigma = 0.08$ seen in the previous parameter scans.

n	L-mode ICRH only		H-mode divertor	
	divertor	Limiter	ICRH	ICRH+TNBI
4	0.20	0.32	0.23	0.15
5	0.20	0.32	0.23	0.20

Table 5.4: Measured Spectral line widths for n=4 & 5 TAEs. In L-mode with ICRH power only for divertor and limiter configurations and during H-mode with a divertor configuration using both, ICRH power only and ICRH plus Tangential NBI power (TNBI).

All spectral line width measurements were taken at the same phase during each sawtooth crash in an attempt to limit the effect of the sawtooth induced fluctuations. What becomes clear is that even with deviations from the mean no clear general dependancies emerged and one would conclude that in general line widths are not very sensitive to changes in these parameters. However it s observed that an increase was seen with respect to discharges with a higher **starting** density. These values are a factor of 3-5 smaller than the measured decay rates. If one considers a forced and damped Lorentz oscillator alone, then this line width is equal to the mode damping[56]. In reality this model is too simple to model TAEs, because the fast ions that drive them also damp them and in turn TAEs cause fast ions to be lost. However, since the line widths being the same order of magnitude as the decay rates and their apparent response to starting density, it is possible that these measurements are related to the actual damping rates.

5.9 Summary

The theoretical background for TAEs is extensive as are the experimental results. This thesis presents the 2005/2006/2007 experimental results for TAEs observed at ASDEX Upgrade. TAEs are very sensitive to both the bulk plasma and the fast ion populations, while at the same time not perturbing plasma performance significantly in present day experiments. Therefore TAEs are a valuable tool with which a tokamak plasma can be diagnosed. However, it remains possible that in future experiments the TAE gap could be open resulting in TAEs that will not be so benign.

TAEs are identified by means of the gap frequency dependence on the bulk mass density, toroidal field and safety factor. Therefore the behaviour of these quantities at the position of the gap can be inferred. The amount of ICRH power required to destabilise TAEs was shown to be dependent on density and toroidal mode number, in particular the consistency of the ICRF power threshold behaviour with respect to the finite orbit effects favouring the n=4,5 TAEs; and independent of q_{95}. However, from the data it was shown that q_{95} indirectly influences the stability of TAEs with $n = 2$. This was further supported by results from experiments performed in a limiter configuration. This implies that high values of q_{95} and by extension high edge shear stabilises low $n \leq 2$ TAEs, whether or not a separatrix is present.

ECE data, and reconstructions of the TAEs' eigenfunctions using Soft X-ray and reflectometry data verified important features, such as the position of maximal displacement, the sign change of the eigenfunction, and the intersection of the mode's frequency with the continuum at the plasma edge in the eigenfunction structure predicted by the CASTOR_FLOW code. This latter feature indicates a closed TAE gap at the plasma edge, which leads to the conclusion that a closed gap is not detrimental to TAEs. The ballooning character of the observed TAEs was demonstrated by the corrected poloidal amplitude distribution. This verified the observed TAEs as even modes and the location of the simulated frequencies below the centre of the 1^{st} gap.

Measured decay rates were found to be larger than damping rates calculated by LIGKA. From the measured growth and decay rates an average drive was calculated and found to be 3.0% of the average frequency of the TAEs in the plasma's rest frame.

Several candidate fast pressure profiles calculated using the CLISTE, PION and TORIC codes were tested for compatibility with TAEs. It was found that the CLISTE and PION fast pressure profiles consistently met the observed requirements and values of the drive derived from these profiles

showed reasonable agreement with the average drive rate estimated from measurements. However the TORIC profile was found to be unable to provide a sufficient fast pressure at the TAEs' positions. This demonstrated the value of TAE drive rate measurements when comparing fast pressure profiles.

The derived expression for volume average β_{fast} was shown to give an upper limit when compared with the corresponding values calculated from the CLISTE, PION and TORIC fast pressure profiles. The difference between the values is believed to come from the form of the Spitzer slowing down time and the assumption that all the ICRH power was absorbed by the minority species.

Tangential NBI was seen to have a noticeable and overall positive effect on TAEs, in contrast to radial NBI which typically has a detrimental effect. This change is manifested by the promotion of additional TAEs, such as the n=5,6,7 over the n=4. When an (m=2,n=1) NTM is seen to lock to the vessel a decrease in: radiation, plasma rotation, and density are observed; which led to the excitation of an n=3 TAE and stabilisation of an n=7 TAE. This suggests that NBI could be used to *select*, in a limited way, which TAEs will be excitable.

The spectral line widths of the TAEs observed were measured and shown to be insensitive to a modest change in density, and small changes in the toroidal field and plasma current within a discharge. However, in the set of discharges studied, observations suggest that a high starting density may be responsible for the observed larger line widths. These line width values were seen to be smaller than measured decay rates by an order of magnitude. This suggests that these measurements may be related to the mode damping, but not in a simple manner.

Chapter 6

Results from the Beatwave Experiments

There were two main milestones which these experiments were designed to achieve. The first was to demonstrate that ICRF beatwaves could be used to drive TAEs from the 1^{st} gap. These TAEs, which are usually destabilised by fast ions have been studied in great detail with results from ASDEX upgrade having been presented in the previous chapter and several publications [30][53][55][63][66][67]. These experiments used the same scenario as that used in discharges with TAEs excited by fast ions, so as to be comparable and thus draw on the experience gained from these studies.

The second milestone was to localise the TAEs excited by ICRF beatwaves and use this information to derive q-profile information, which could then be used to constrain equilibrium reconstructions. To this end, both of these milestones have been achieved and in the following sections and chapter thereafter, these results will be presented.

6.1 Sweeping Frequency ICRF Beatwave

The beatwave experiments were based on the scenario developed for experiments in which TAEs were destabilised by ICRF accelerated fast ions. The focus of these experiments was to excite TAEs using an external antenna independent of the fast ion population. To achieve this density was kept as low as possible to increase the slowing down time of fast ions, while producing conditions which would allow for the best possible coupling of ICRF power to the plasma. An example of the plasma parameters of such a discharge are shown in figure 6.1 (top) along with the externally imposed time dependent frequency difference Δf between the two Antenna-generator groups ICRH[1,2] and ICRH[3,4] (bottom).

The technique adopted was that used in experiments undertaken by M.Maraschek et al. at ASDEX Upgrade[12], which were in turn inspired by the experiments performed by A. Fasoli et al. on the JET experiment in Culham, U.K[54]. This frequency difference Δf is equal to the frequency of the ICRF beatwave f_{bw} produced in the plasma. In figure 6.1 (bottom), Δf is swept continuously at a constant rate within the range $\Delta f^0 \pm \delta f$ for the entire discharge. In this example $\Delta f^0 = 150kHz$ and $\delta f = 100kHz$.

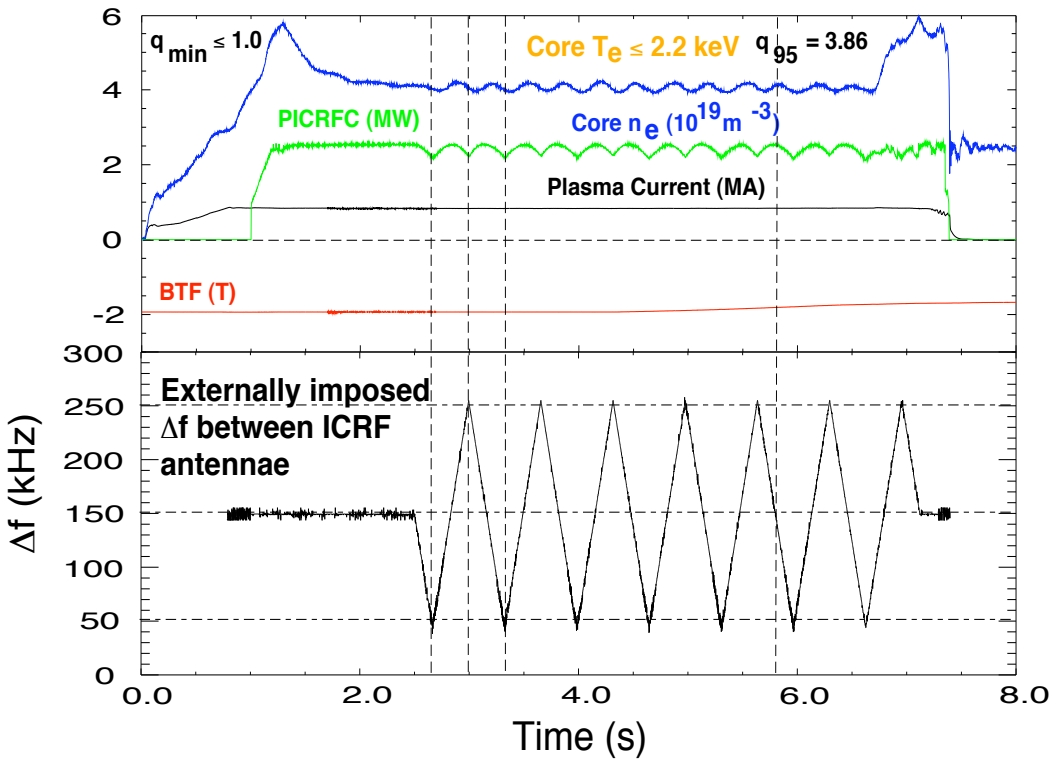

Figure 6.1: Discharge #21039 : Plasma parameters (top), and the tracked beatwave frequency which exactly matches the externally imposed time dependent frequency difference between the two Antenna-generator groups ICRH[1,2] and ICRH[3,4] (bottom). Δf sweeps continuously at a constant rate between 50kHz and 250kHz.

The range was chosen, such that the the resulting beatwave frequency would scan a frequency range which covered the frequency range corresponding to the 1^{st} gap in the Alfvén spectrum and 'safety zone' to cover frequency shifts from doppler corrections and profile uncertainties. This required frequency range was determined a priori from CASTOR_FLOW Alfvén spectrum calculations which incorporated diagnosed density and q profiles from a previous similar discharge.

As a result of varying the frequency of one antenna-generator group relative to the fixed frequency of the other group to produce the beatwave, a variation in the coupled ICRF power of approximatively

0.4MW was observed. This is reflected in the coupled power signal PICRFc in figure 6.1 (top) to decrease as δf increases with the maximum coupled power for $\delta f = 0$.

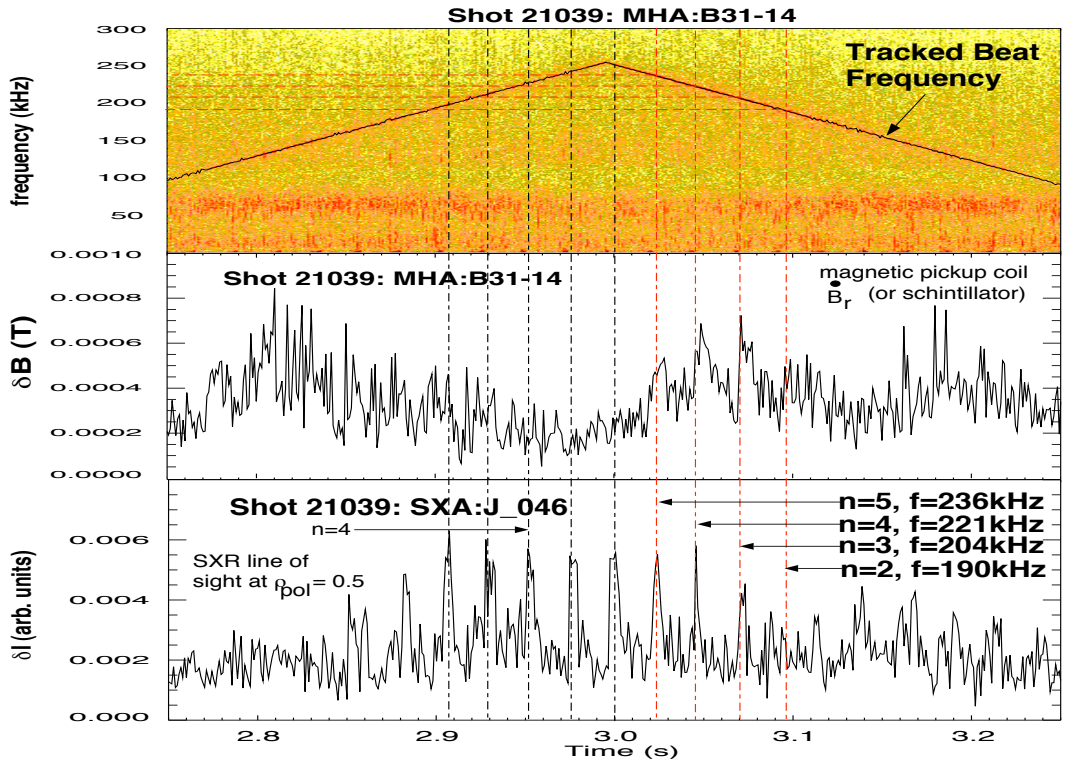

Figure 6.2: Discharge #21039 : (top) spectrogram of the magnetic coil signal MHA B31-14 with tracked beatwave frequency, (middle) excitations seen in magnetic coil signal during frequency seep, and (bottom) corresponding excitations observed in SXR diode SXA J_046 located at $\rho_{poloidal} = 0.5$. *The red dashed line mark the excitations from which toroidal mode numbers could be determined from the high frequency response toroidal ballooning coil array. The peak at* $t \simeq 2.95$ *in the bottom image is believed to be an n=4 TAE from symmetry in the frequency sweep and is highlighted so as to facilitate a comparison with the excitation that has been identified as an n=4.*

Figure 6.2 shows: the tracked beatwave frequency overlaid on the spectrogram of magnetic coil data from the mirnov coil MHA:B31-14 (measuring $\dot{B}_r$), and mode excitations observed in the magnetic coil and soft X-ray signals. In the top part of the image: the amplitude $B_r = \dot{B}_r/(2\pi f)$ of the tracked beatwave frequency is shown. The dashed lines intersecting this tracked frequency indicate the frequencies at which mode excitations occur. These excitations are simultaneously observed in the 2MHz magnetic coil and soft X-ray camera data. The signal from the SXR channel J_046 used for the

spectrogram in figure 6.2 is a line integrated measurement of the soft X-ray emissivity of the plasma along a line of sight which is tangent to the flux surface at $\rho_{poloidal} = 0.5$.

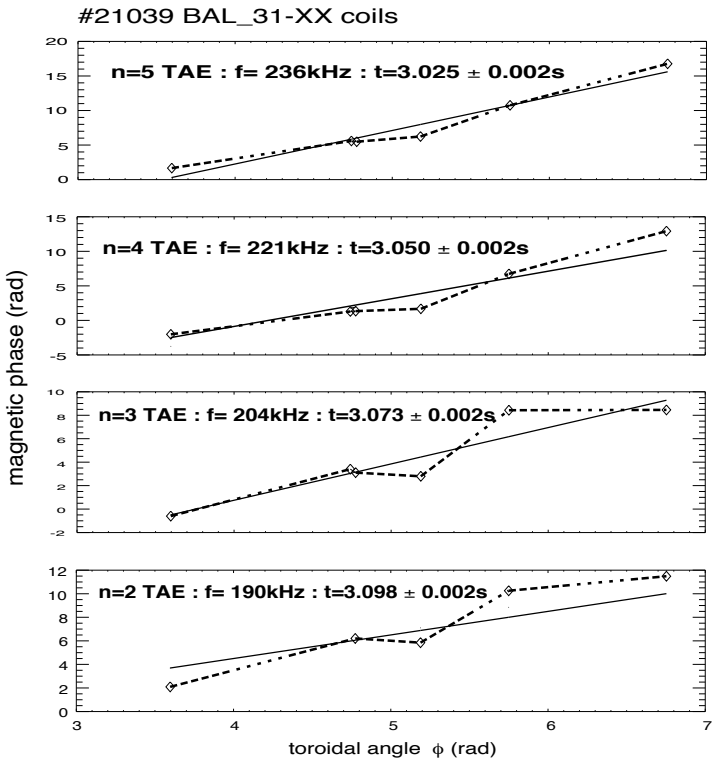

Figure 6.3: Discharge #21039 : Toroidal mode numbers of the observed excitations determined from phase fits made to the toroidal mirnov coil array data.

This measurement is dominated by soft X-ray emissions from that location, which shows that the beatwave is active in the centre of the plasma. In figure 6.2, the dashed red lines indicate the excitations whose toroidal mode numbers could be determined from mirnov coil data. The toroidal mode numbers determined from an analysis of magnetic phase of each excitation are presented in figure 6.3 and show the excitations to be an n=5 mode at 236kHz, an n=4 mode at 221kHz, an n=3 mode at 204kHz and an n=2 mode at 190kHz. These numbers coincide with those commonly observed in discharges used to study fast ion destabilised TAEs (see chapters 4 and 5).

In order to ascertain if these excitations were as a result the fast ion population the same discharge was repeated without a frequency difference between the launched ICRF waves at the same power level (no beatwave). The result was that the fast particle drive alone was insufficient to overcome the mode damping and no unstable TAEs were seen. From frequencies observed in discharge #21039

one immediately sees that there is a similar frequency difference, of approximatively 15kHz, between successive excitations. One can interpret this as all the excited modes experiencing a doppler shift proportional to the toroidal mode number n. This would imply that the modes all see the same plasma rotation and are thus close to one another radially, similar to TAEs excited by fast ions presented in the previous chapter.

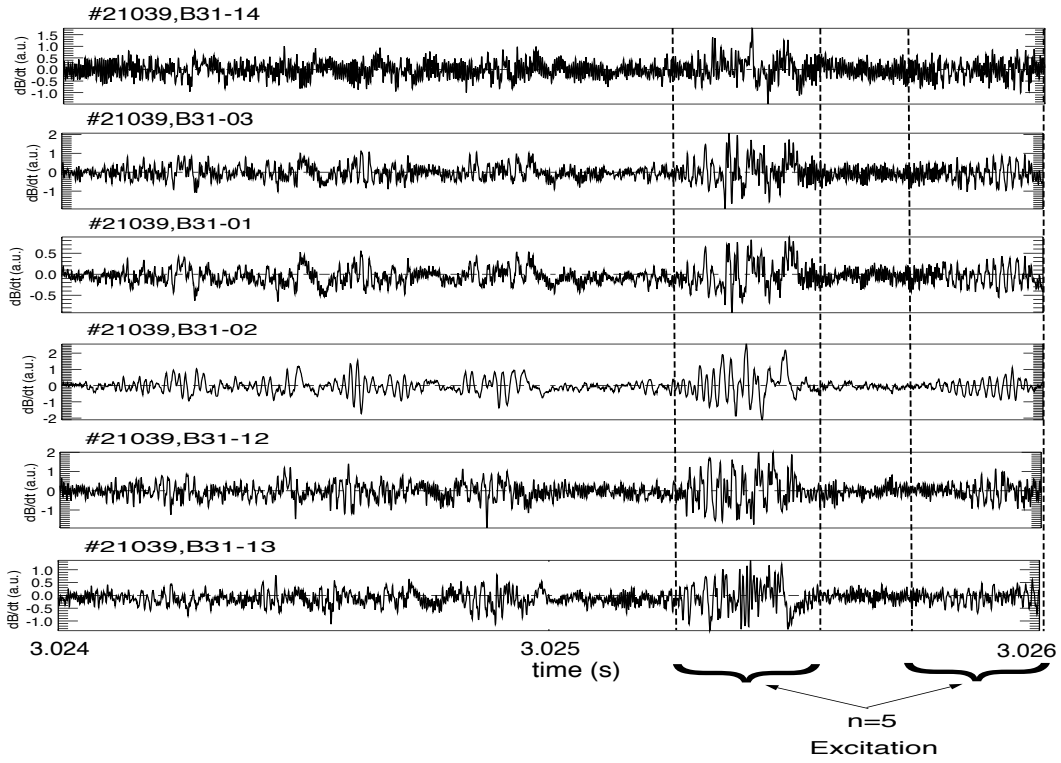

Figure 6.4: Discharge #21039 : Raw signals from the toroidal mirnov coil array showing the fine structure of the the n=5 mode excitation centred at 3.0253s highlighted in each coil.

The presence of individual excitations with well defined toroidal mode numbers decreasing with decreasing frequency, all separated by the same frequency difference, supports the earlier assertion that the matching condition (section 2.8) is between the doppler shifted mode frequency and the beatwave frequency. This occurs because the beatwave is launched from the lab frame and can only match the mode frequency as seen in the lab frame, ie. the doppler shifted frequency. On the other hand, if the beatwave were to match the plasma rest frame frequency then as soon as the resonance was excited, the mode frequency, as seen in the magnetic coil measurements, should separate from the beatwave frequency due to the n-dependant doppler shift. This is not seen in figure 6.2 and therefore can be

discounted.

Additionally the frequencies of the excitations decrease with decreasing toroidal mode number, consistent with a positive doppler shift indicating that these modes are travelling in the direction of the plasma rotation, and therefore in the co-current direction as shown by D.Borba et al.[53].

In figure 6.4, the time window from 3.024s to 3.026s shows that the n=5 mode excitation is composed of a complex sequence of small excitations, which are seen simultaneously in all of the mirnov coils measuring $\dot{B}_r$. Similar behaviour is repeated throughout the time interval 3.02s to 3.03s which corresponds to the full extent of the excitation shown in figure 6.2 at 3.025s and suggests that each large peak (mode excitation) has a fine structure.

In figure 6.2 (bottom), the SXR signal clearly shows the excitations to be symmetric about the maximum beatwave frequency, however the symmetry is not seen in the magnetic coil signal. One possible explanation is hinted at by the SXR signal in the bottom pane of figure 6.2. If one looks at the width of the two peaks labelled "n=4" then the peak on the left hand side of the image appears to have a larger width than the peak on the right hand side. This is also true when one compares corresponding peaks on either side of the maximum frequency and suggests that a reason why we do not see modes in the *up-sweep* is because the mode damping is larger.

An example of the complementary nature of these diagnostics is the excitation seen in the SXR signal at 3.0s, which we conjecture is an n=6 mode from the doppler frequency shift, the symmetry of the excitations, and experience from fast ion excited TAE results in similar discharges. However this mode is not seen in the magnetics, which is believed to be as a result of the radial mode's magnetic field decaying according to $\left(\frac{r_{res}}{r_{coil}}\right)^{m+1}$, being the mode furthest inside radially and having the largest poloidal mode number m.

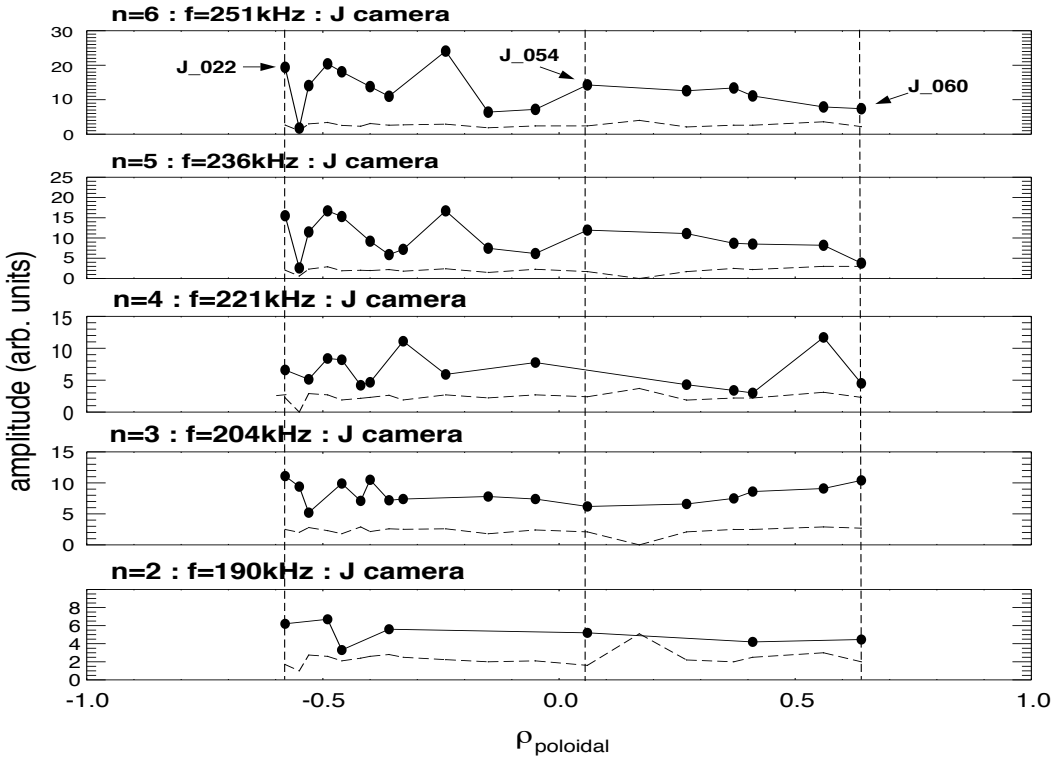

Figure 6.5: Discharge #21039 : Measured SXR fluctuations at the frequencies of the excited n=5,4,3,2 modes from the 2MHz J camera. Also shown is the conjectured n=6 modes. For clarity in the image only, the diodes from the J camera whose lines of sight intersect the plasma above the magnetic axis (or central line of sight) are assigned a negative $\rho_{poloidal}$ value (J_022,..,J_053), whereas those below are assigned a positive value (J_055,..,J_060). An average group position of $\rho_{poloidal} = 0.62$ is inferred from the radial extent of the SXR fluctuations caused by all TAEs observed and knowledge of fast ion excited TAE behaviour.

The global nature of these mode is evident from the amplitudes of the measured fluctuations at the frequencies of the excited n=5,4,3,2 modes from the 2MHz J camera in figure 6.5. For clarity, in figure 6.5, the diodes from the J camera whose lines of sight intersect the plasma above the magnetic axis are assigned a negative $\rho_{poloidal}$ value (J_022,..,J_053), whereas those below are assigned a positive value (J_055,..,J_060). The radial extent of the fluctuations in the SXR data for the n=4,5,6 modes suggest that these modes have a maximum displacement at approximately, but not greater than, $\rho_{poloidal} = 0.60$, while the maximum of the n=3,2 TAEs appears to be further outside and closer to $\rho_{poloidal} = 0.65$. From previous results of the fast ion excited TAE studies[66], one would not expect the position of the maximum displacement to be much further out than $\rho_{poloidal} = 0.65$, and therefore an average of

$\rho_{poloidal} = 0.62$ will be taken as the best estimate of the average position for all of the excited modes, similar to that done for TAEs from the 1^{st} gap in chapter 5. It is important to highlight, that the 2MHz SXR camera J could not see the beatwave or modes for $\rho_{poloidal} \leq -0.6$, and that while it was seen for $\rho_{poloidal} \geq 0.65$ the data was unusable (which is believed to have been caused by over estimated calibration factors), and the positions are best estimates based on the radial extent of the modes and published work[66]. These modes have been shown to have the same character to those excited by fast ions. What remains, is to show that the equilibrium does in fact support TAEs at the plasma rest frame frequency of the the observed modes.

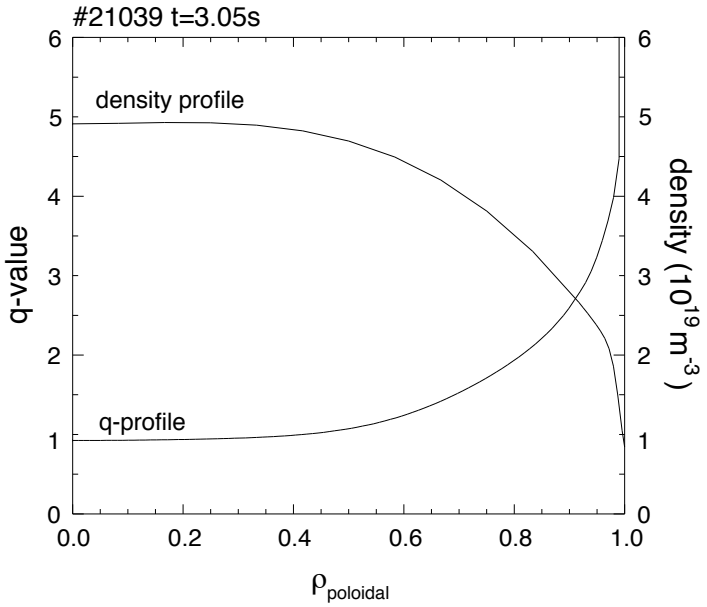

Figure 6.6: Discharge #21039 : Diagnosed density and q profiles used in the CASTOR_FLOW spectrum and eigenfunction calculations for the n=5,4,3,2 TAEs.

Using the measured frequencies and toroidal mode numbers, a linear extrapolations in the toroidal mode number n, back to the plasma rest frame frequency can be made. This gives us an experimental rest frame frequency of 160kHz and a total doppler shift of 15kHz. Figure 6.6 shows the diagnosed density and q profiles (q-profile derived from an MHD-enhanced equilibrium, section 7.1.2) used in the CASTOR_FLOW spectrum and eigenfunction calculations for the n=5,4,3,2 TAEs. The search for solutions which best agree with observations begins with an initial guess of the eigenvalue (frequency), and the toroidal mode number n. The initial eigenvalue is taken to be the experimental rest frame frequency of the modes shown above (160kHz).

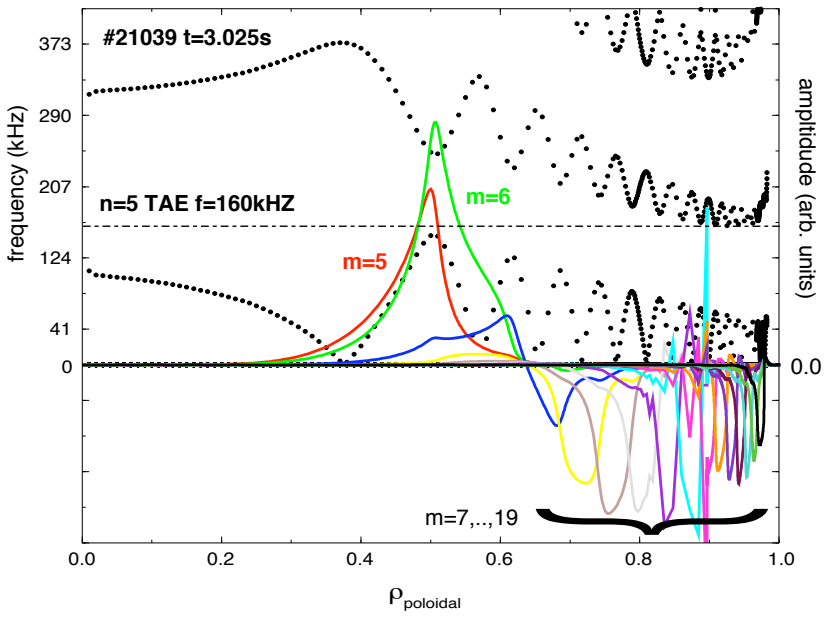

Figure 6.7: Discharge #21039 : n=5 TAE Alfvén spectrum, eigenfunction and eigenfrequency f=160kHz. Note: As CASTOR_FLOW in unable to treat continuum damping correctly, the eigenfunction structure beyond $\rho_{poloidal} \geq 0.9$ *is not correct.*

The best solution for the n=5 which match observations was found to have an eigenfrequency of 160kHz with the dominant poloidal harmonics m=5,m=6. This eigenfunction in displayed in figure 6.7 and is similar to eigenfunction of fast ion excited TAE shown in the previous chapter. This demonstrates that the equilibrium supports an n=5 TAE from the 1^{st} gap at the expected frequency, and identifies the observed n=5 mode excited by the ICRF beatwave as an n=5 TAE. Adopting the same approach, similar eigenfunctions were found for the n=4,3,2 TAEs. The solutions for the n=4,3,2 are shown in figures 6.8, 6.9, and 6.10 respectively, with frequencies 159kHz, 158kHz, and 159kHz. These eigenfunctions also have dominant poloidal harmonics in the 1^{st} gap placing them in the same group as the n=5, similar to those eigenfunctions in the fast ion TAE examples. The frequencies as in the case of the n=5 TAE agree well with the plasma rest frame frequency of the excited modes, which demonstrates that these are n=4,3,2 TAEs.

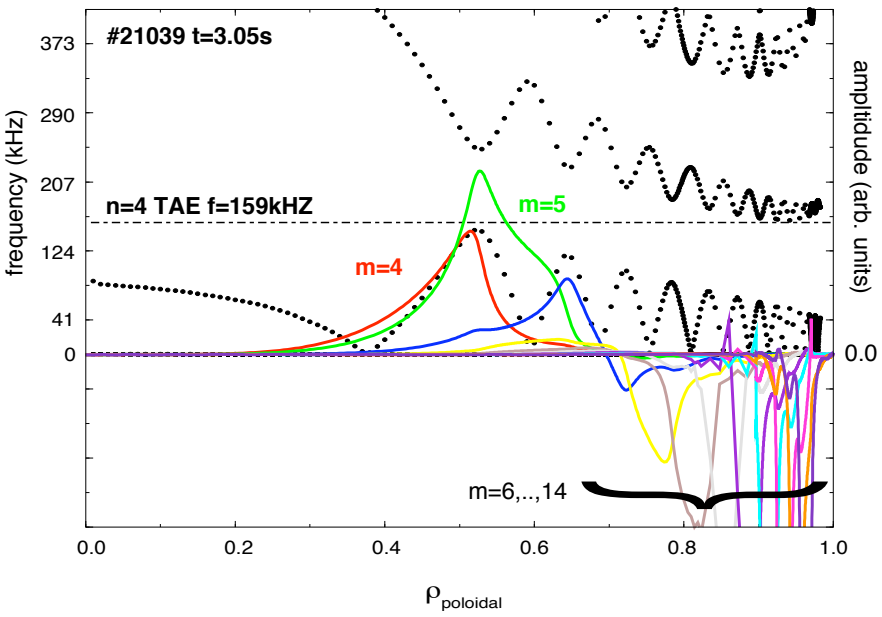

Figure 6.8: Discharge #21039 : n=4 TAE Alfvén spectrum, eigenfunction and eigenfrequency f=159kHz. Note: As CASTOR_FLOW in unable to treat continuum damping correctly, the eigenfunction structure beyond $\rho_{poloidal} \geq 0.9$ *is not correct.*

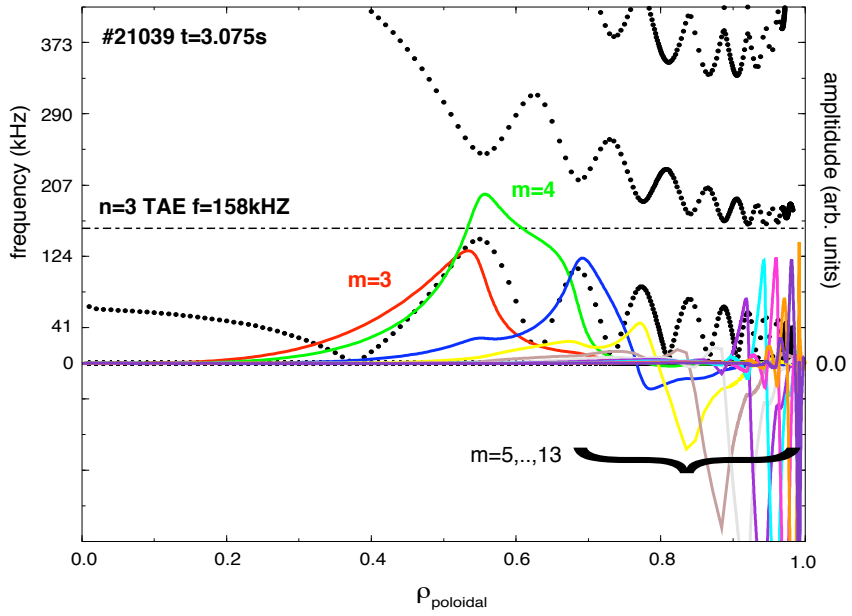

Figure 6.9: Discharge #21039 : n=3 TAE Alfvén spectrum, eigenfunction and eigenfrequency f=158kHz. Note: As CASTOR_FLOW in unable to treat continuum damping correctly, the eigenfunction structure beyond $\rho_{poloidal} \geq 0.9$ *is not correct.*

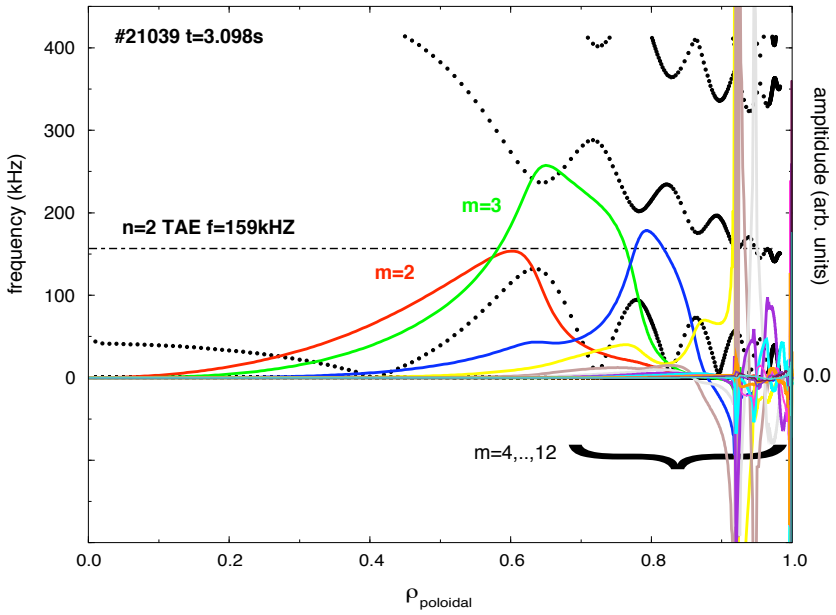

Figure 6.10: Discharge #21039 : n=2 TAE Alfvén spectrum, eigenfunction and eigenfrequency f=159kHz. Note: As CASTOR_FLOW in unable to treat continuum damping correctly, the eigenfunction structure beyond $\rho_{poloidal} \geq 0.9$ *is not correct.*

The main difference between the n=2 mode and the previous examples is the amplitude of the m=4 poloidal harmonic which is comparable to the m=2,3 harmonics. Unfortunately it was not possible to confirm this feature from the diagnostic data and should therefore not be be taken entirely as fact.

In figure 6.11, we have an example of the ICRF beatwave driving MHD activity at a frequency lower (100kHz $\leq f \leq$ 150kHz) than the previous example shown (190kHz $\leq f \leq$ 251kHz). These modes are believed to be the edge TAEs reported by M. Maraschek et al. [41]. The plasma parameters which influence a TAE's frequency, namely the toroidal field B and density, do not change in a manner that would increase the lab frame frequency of the previously presented ICRF beatwave driven TAEs beyond the range of the beatwaves, and so another explanation of why these lower frequency modes have been *selected*, is required. The toroidal field was decrease by 4% (see figure 6.1), which would in turn move the ICRH resonance by as much as a 7cm towards the high-field side of the plasma. This would move the beatwave and fast ion drive outwards decreasing the drive available to the TAEs, while increasing the drive of the edge TAEs.

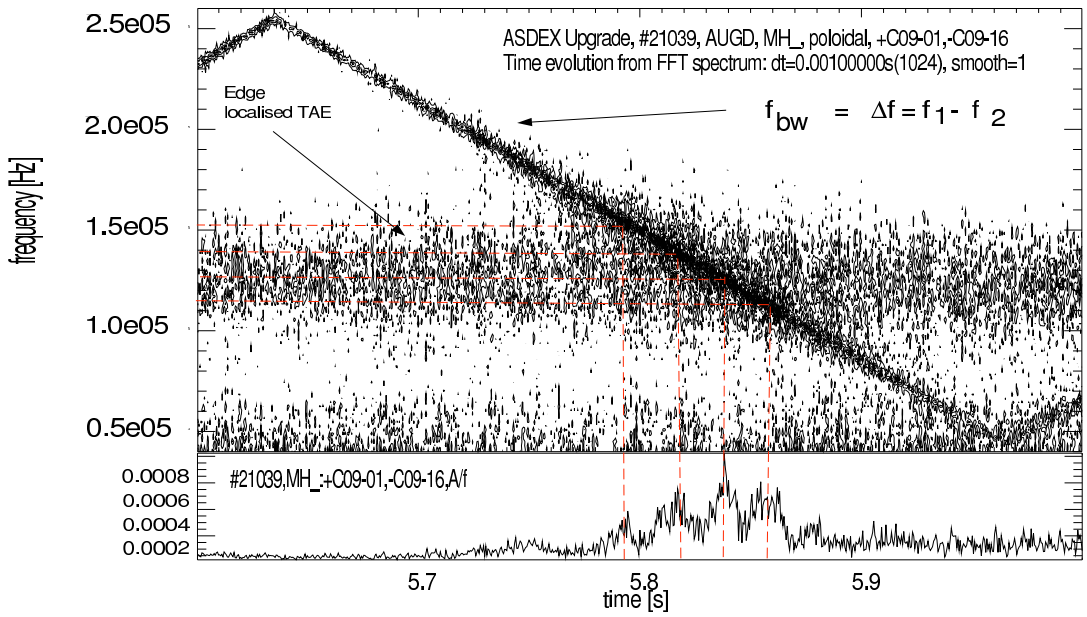

Figure 6.11: Discharge #21039 : Edge Alfvén modes excited at the plasma edge by the ICRF betawave at $t = \simeq 5.8s$.

6.2 Summary

It has been demonstrated through careful analysis of ICRF beatwave driven MHD activity and comparison with fast ion excited TAEs, that these modes can be identified as TAEs from the 1^{st} gap. With the aid of SXR these modes were localised and can therefore be used to provide q-profile information which can be used to constrain a current density profile reconstruction. Additionally, it was shown that the ICRF beatwave was also able to excite MHD modes, at lower frequencies than the centrally localised modes, which are believed to be edge localised TAEs. This result however requires more analysis and dedicated experiments before a definitive identification can be made. In the coming chapter, the quality of this q-profile information along with that gleaned from fast ion excited TAEs will be demonstrated. Since this technique can be used whenever ICRH power is used, it provides a passive q-profile diagnostic across the entire plasma radius. With the improving SXR and reflectometry diagnostics, it will in the future be possible to localise the maxima of individual TAEs, providing multiple q-profile points from q=1 up to q=1.5, which is a region of the q-profile that is poorly diagnosed in the absence of MSE and even with MSE is the least accurately diagnosed due to the diminishing poloidal field strength, and therefore MSE signal strength, with diminishing flux surface radius.

Chapter 7

Equilibrium Current Density and Pressure profile reconstructions

A current density profile reconstruction can be greatly enhanced by including q-profile information derived from active MHD instabilities. The technique of using MHD instabilities to provide q-profile information is often referred to as MHD-Spectroscopy [72]. MHD instabilities have a q-value associated with their resonant surfaces. Therefore once an instability has been identified and localised, the q-value and location of its resonant flux surface can be used to improve the reconstruction. Such MHD-enhanced equilibria are the focus of this chapter and were used in TAE eigenfunction simulations presented in chapters 5 and 6. The manner in which the CLISTE code uses diagnostic, and q-profile information gathered from MHD instabilities was briefly discussed in section 2.3, with more information about the CLISTE algorithm presented in the appendix.

7.1 Extracting q-profile information from MHD instabilities

If an instability has a single poloidal mode number m for a given toroidal mode number n. The q-value of the mode's resonant surface is defined as q=m/n. Therefore once the location of the mode has been determined using either the ECE[78] or SXR[79] (and figure 7.2) diagnostics, this information can be used to constrain the q-profile reconstruction. Common examples of such MHD modes are a Sawtooth, Neoclassical Tearing Modes and Fishbones. Modes formed by the coupling of more than one poloidal harmonic, such as the TAEs, require additional analysis to extract q-profile information.

The dominant m & m+1 poloidal harmonics form the TAE gap and it is the q-value and location of their resonant surface, or equivalently their gap, which provides the required q-profile information. At ASDEX Upgrade TAE originating from the gap formed by the coupling of the m=n and m=n+1 poloidal harmonics are most commonly observed. In this case the m=n and m=n+1 are the dominant poloidal harmonics and the equation for the q-value reduces to $q(n) = 1 + 1/(2n)$. Therefore to extract q-profile information the TAE's toroidal mode number n and the location of the resonant surface of the dominant poloidal harmonics must be identified. To achieve this the mode's radial displacement eigenfunction must be reconstructed from either the measured TAE induced temperature or density fluctuations and compared with simulations. The associated fluctuations are measured by the SXR and ECE, and microwave reflectometry diagnostics respectively. Examples of the procedures involved are given in the following references[66][80] (temperature) and [63] (density). See also section 5.2 for a brief discussion of the SXR and microwave reflectometry techniques.

7.2 Constraining the equilibrium current density profile using MHD instabilities

The resistive current diffusion time over the plasma minor radius is expected to be of the order of seconds, typically between 2s and 3s for ASDEX Upgrade. With this knowledge it would be useful to establish a *rule-of-thumb* to determine the largest set of MHD modes which can contribute q-profile information for an equilibrium reconstruction at a given time point. From experience it was determined that a time interval of 100ms in duration centred on a given time point was short enough to guarantee that the current density profile and therefore the q-profile would remain unchanged over the specified interval. Thus we define this interval to be $[t_r - 50ms, t_r + 50ms]$ within which a mode must be *almost* stationary in amplitude and frequency, as in practice an instability is never truly stationary, in order for it's q-profile information to be used in an equilibrium reconstruction at t_r.

7.2.1 Using the Sawtooth and NTM instabilities

The most common low frequency ($f \leq 50$kHz) MHD instabilities used to improve current profile reconstructions are the Sawtooth, Fishbone, and NTM instabilities. There are other MHD instabilities which do not have a special name and are simply referred to as (m,n)-modes.

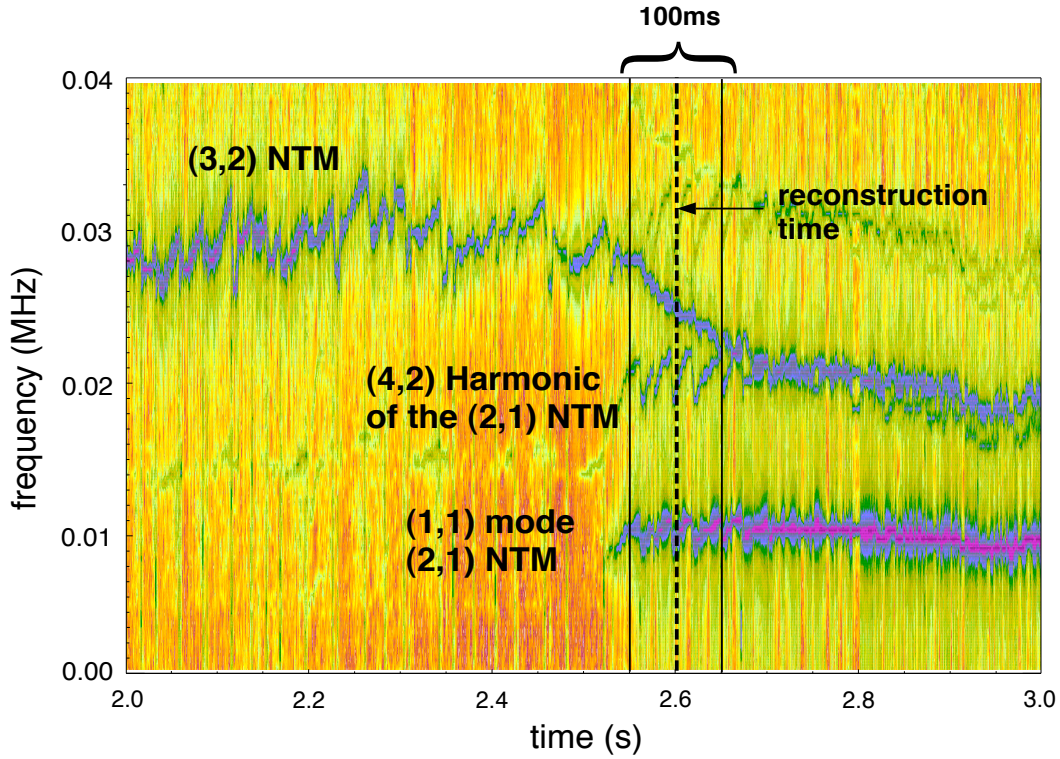

Figure 7.1: Discharge #17066 : At 2.6s there are three modes present in the plasma. A (3,2) and (2,1) NTM, and a continuous (1,1) mode. In the spectrogram the (1,1) is not visible because it is being obscured by the much stronger (2,1) NTM (see figure 7.2). Each of these modes provides a point of q-profile information. To either side of the dashed vertical line at 2.6s, there is a solid vertical line representing the time interval within which a mode has to be active, in order to be admissible in the reconstruction at 2.6s.

In the H-mode discharge #17066 a reconstruction was made at 2.6s using: MHD mode positions and magnetic data[17][18]. A 15-knot parameterisation was used with knots at $\rho_{poloidal} = 0.0, 0.15, 0.3, 0.45, 0.6, 0.65, 0.7, 0.75, 0.8, 0.85, 0.9, 0.93, 0.96, 0.98, 1.0$ on a computational grid of 128×256 cells in (R,z). No Kinetic profiles were used due to poor density data in the pedestal region. The main plasma parameters at the time of the reconstruction were: $I_p = 1.0$MA, $B_{toroidal} = -2.2$T, $\hat{n}_e \simeq 7.7 \times 10^{19}\mathrm{m}^{-3}$ (core line-integrated measurement), $P_{heat} = 12.5$MW (NBI) and $\beta_{poloidal} = 1.27$.

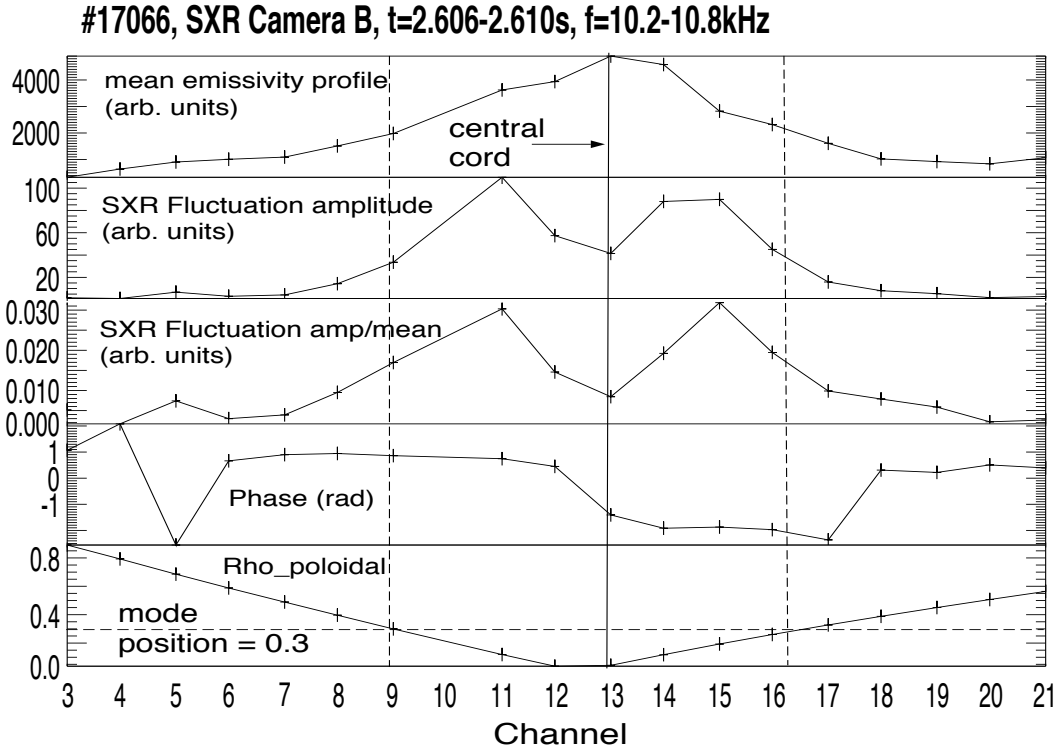

Figure 7.2: Discharge #17066 : At 2.6s there is a continuous (1,1) mode present in the plasma. This image shows the SXR fluctuations caused by the (1,1) mode as a function of channel number. Top: the mean SXR fluctuation amplitude profile; second from the top: the raw SXR fluctuation amplitude caused by the (1,1), middle: the raw SXR fluctuation amplitude caused by the (1,1) mode divided by the mean profile, second from the bottom: the phase of the SXR fluctuations caused by the (1,1) mode, and bottom: the radius, in $\rho_{poloidal}$, of the flux surface tangent to the line of sight of each diode (channel) of the SXR camera B. The solid vertical line represents the central line of sight which looks through the plasma core. The two dashed vertical lines represent the radial position of the mode's resonant surface.

There are three primary MHD modes admissible at the time of the reconstruction. These are shown in figures 7.1 and 7.2, and are: a (3,2) {q=1.5 surface} and a (2,1) {q=2.0 surface} NTM, and a continuous (1,1) {q=1.0 surface} mode. In the spectrogram (magnetics) the (1,1) is obscured by the much stronger (2,1) NTM. In figure 7.2 (middle), the (1,1) mode is clearly identified in the SXR measurements as the structure consisting of one central minimum flanked by two outer maxima[19], at the same frequency as the (2,1) NTM.

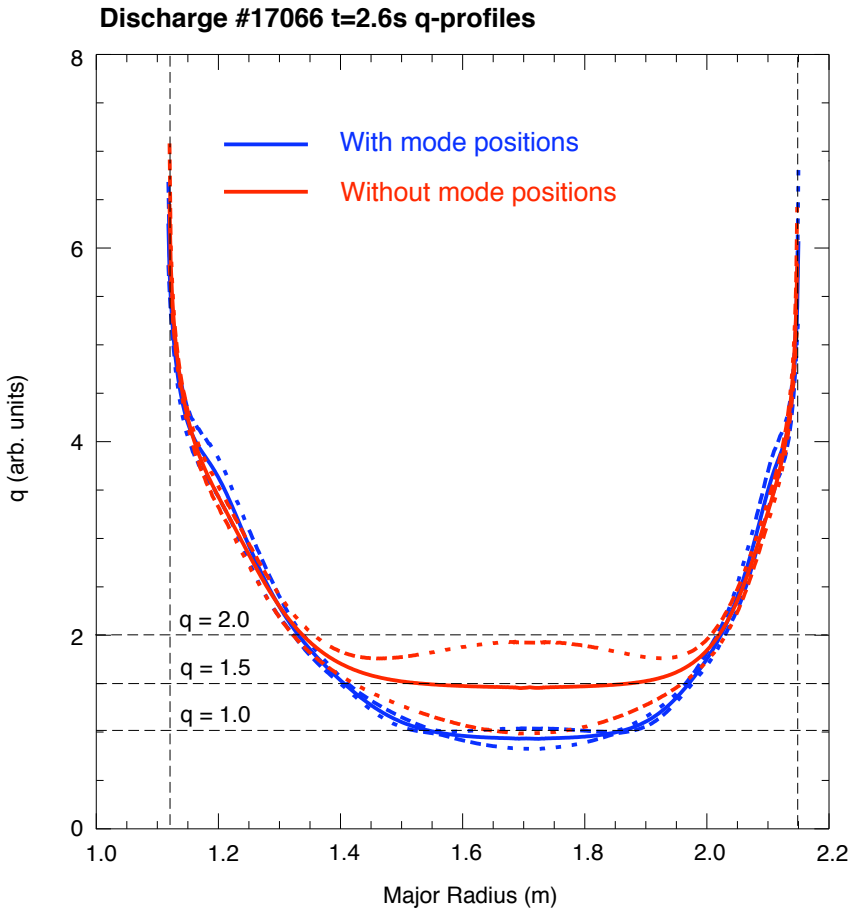

Figure 7.3: Discharge #17066 - The blue curve represents the q-profile reconstructed using additional q-profile information provided by MHD modes (Sawteeth, (3,2) and (2,1)-NTMs) with the associated confidence bands (dashed blue curves). The red curve shows the profile that is reconstructed without the additional information provided by MHD modes with the associated confidence bands (dashed red curves). The horizontal dashed lines highlights the location of the additional q-profile information.

At this time the frequency and therefore magnetic field of the (3,2) NTM is seen to be changing. This would ordinarily make such a mode inadmissible, however in this instance measurements of the mode's position, at the limits of the time range indicated in figure 7.1 by the solid vertical lines, were found to be similar with respect to uncertainties in the measurements. This information together with the observation that this behaviour did not significantly effect the equilibrium reconstruction, as indicated by the small error in magnetics (see $\langle dB \rangle$ below), demonstrates that the q-profile data derived from this mode could be used without corrupting the result.

In figure 7.3, two q-profiles are shown, both are made at 2.6s. The red curve is derived from a reconstruction made with the edge magnetic information alone, and the blue curve shows the q-profile resulting from the inclusion of q information provided by the described MHD modes. Outside q=2.0 both profiles are similar, in contrast to the central region, demonstrating that the edge magnetic measurements can describe the q-profile from the plasma edge up until the radius of the q=2.0 surface with reasonable accuracy. Inside the q=2.0 surface the profiles differ significantly. This difference between the q-profiles is made most obvious by the presence of a q=1 surface as required by the existence of a (1,1) mode in the plasma. Thus a (1,1) mode provides a very important piece of q-profile information, not only from it's position, but by it's existence.

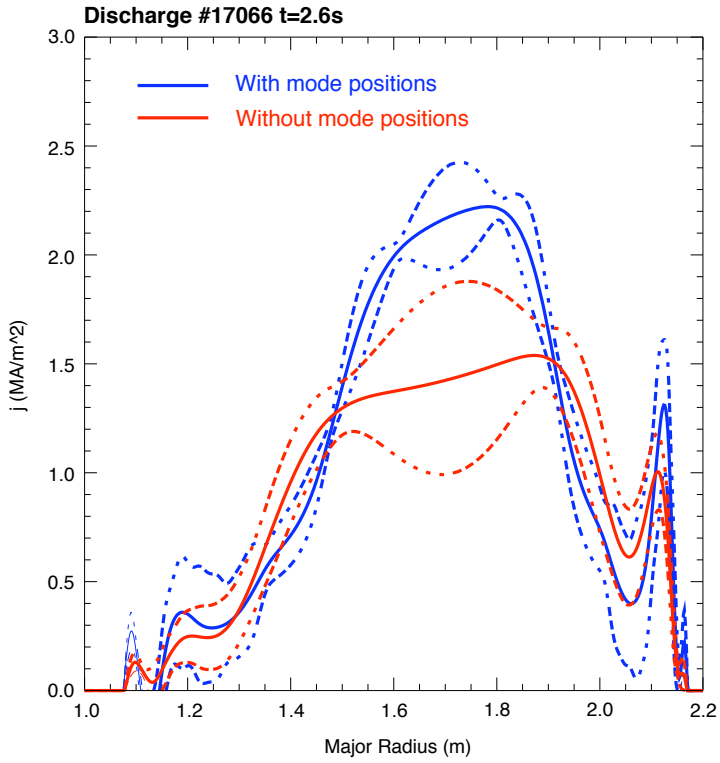

Figure 7.4: Discharge #17066 - The blue curves represent the current density profile and confidence (dashed curves) bands associated with the equilibrium reconstruction performed using additional mode information. The red curves show the current density profile with confidence bands (dashed curves) reconstructed without additional mode information.

#17066	With mode positions	Without mode positions
$\langle dB \rangle$	1.1mT (0.5%)	1.2mT (0.6%)
$\langle dF \rangle$	1.4mT (1.6%)	1.5mT (1.7%)

Table 7.1: Discharge #17066 : $\langle dB \rangle$ and $\langle dF \rangle$ for reconstructions made with and without mode positions. Here $\langle dB \rangle$ and $\langle dF \rangle$are also presented as a percentage of the root mean square poloidal field and root mean square poloidal flux respectively.

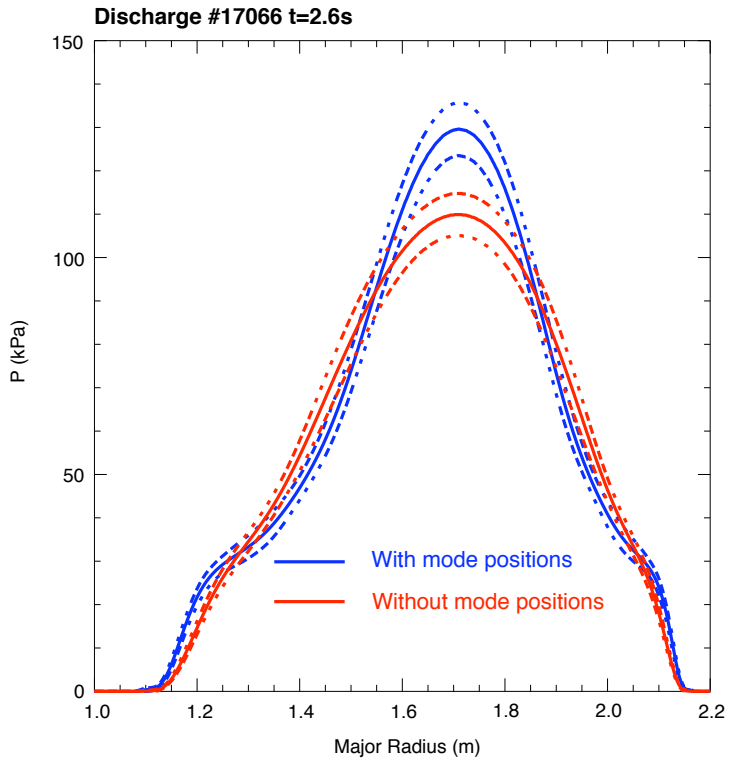

Figure 7.5: Discharge #17066 - The blue curves represent the pressure profile and confidence (dashed curves) bands associated with the equilibrium reconstruction performed using additional mode information. The red curves show the pressure profile with confidence bands (dashed curves) reconstructed without additional mode information.

In order to compare reconstructions with and without MHD mode positions, one must use the root-mean-square error $\langle dB \rangle$ in fitting the magnetic coil data (time-integrated Rogowski coils, and poloidal field measurements) and the root-mean-square error in the poloidal magnetic flux differences involving two flux loops $\langle dF \rangle$. These measures are displayed in table 7.1, and as one can see that the in-

q-value	d_{mid} (cm)	measured	predicted
1	29.9	1.000	1.001
1.5	56.4	1.500	1.499
2	69.2	2.000	2.003

Table 7.2: Discharge #17066 : Measured and predicted (CLISTE) q-values with the corresponding measured flux surface diameters on the magnetic mid-plane d_{mid}.

clusion of mode positions has made little difference demonstrating that the additional MHD information is fully consistent with the external magnetic measurements.

The flux measurements would normally be in Webers = Volt-seconds, however CLISTE converts them to field values by normalising them with respect to the area between the two flux loops. Another valuable measure of the *goodness* of the reconstruction is the difference between the measured and predicted value of q for a given flux surface diameter d_{mid} (see section 2.3.3). These results are shown in table 7.2 along with the corresponding flux surface diameter d_{mid}. From the results, the provided flux surface diameters and q-profile points were fitted to within a difference of 1%. This is an indication of the seamless way in which CLISTE incorporates this directly measurable type of q-profile information. The current density profiles that result from these reconstructions are shown in figure 7.4. The important difference between these two profiles are larger maximal values on the magnetic axis and tighter confidence bands in the reconstruction using MHD mode positions. In fact this larger central current is a direct consequence of having a q=1 surface in the plasma. The strong peak in the edge j-profile is a robust feature of high-$\beta_{poloidal}$ CLISTE equilibria and is consistent with an edge peak in the bootstrap current profile which scales with $\beta_{poloidal}$[17]. The outboard value of the current density peak at $R = 2.12$ was found to be 1.30MAm^{-2}.

A salient feature of both pressure profiles shown in figure 7.5 is a well defined pedestal as a result of the magnetics alone and is seen to be a robust feature showing little change as a result of manipulating the current density profile. This implies that it is a product of the good quality edge magnetic measurements.

7.2.2 Using TAEs in Equilibrium reconstructions

ICRH Fast ion excited TAEs

A commonly observed example of high frequency ($f \geq 50$kHz) MHD are TAEs, which are typically excited in groups (ie. from the 1^{st} gap). Similar to the example shown in the last section these modes also provide q-profile information that can be used in equilibrium reconstructions.

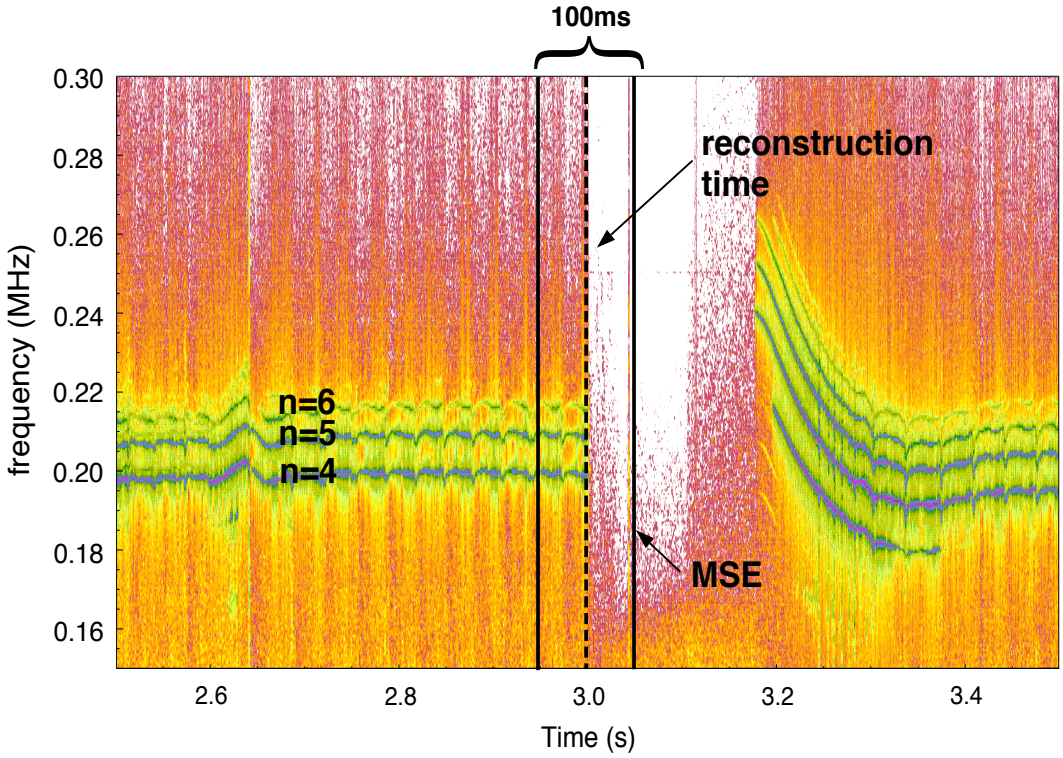

Figure 7.6: Discharge #21067 : n=4,5,6 TAEs used in the equilibrium reconstruction performed at 2.99s. The vertical lines indicate the time-interval indicating MHD admissible for the reconstruction at 2,99s. Additionally at 3.1s MSE data was recorded to provide an independent q-profile reconstruction, to be used in a critique of the reconstruction at 2.99s.

In this example, a current density profile reconstruction was made with q-profile information provided by n=4,5,6 TAEs. These modes are shown in figure 7.6. At the time the reconstruction was made, there was a sawtooth instability (m=1,n=1) active in the plasma. This indicates there is a q=1 flux surface in the plasma. The position of this surface was used in addition to the TAE information in the reconstruction. The equilibrium reconstruction was performed at 2.99s. In addition at 3.1s MSE data was recorded to provide an independent q-profile reconstruction to which the reconstruction made

at 2.99s using MHD alone could be compared.

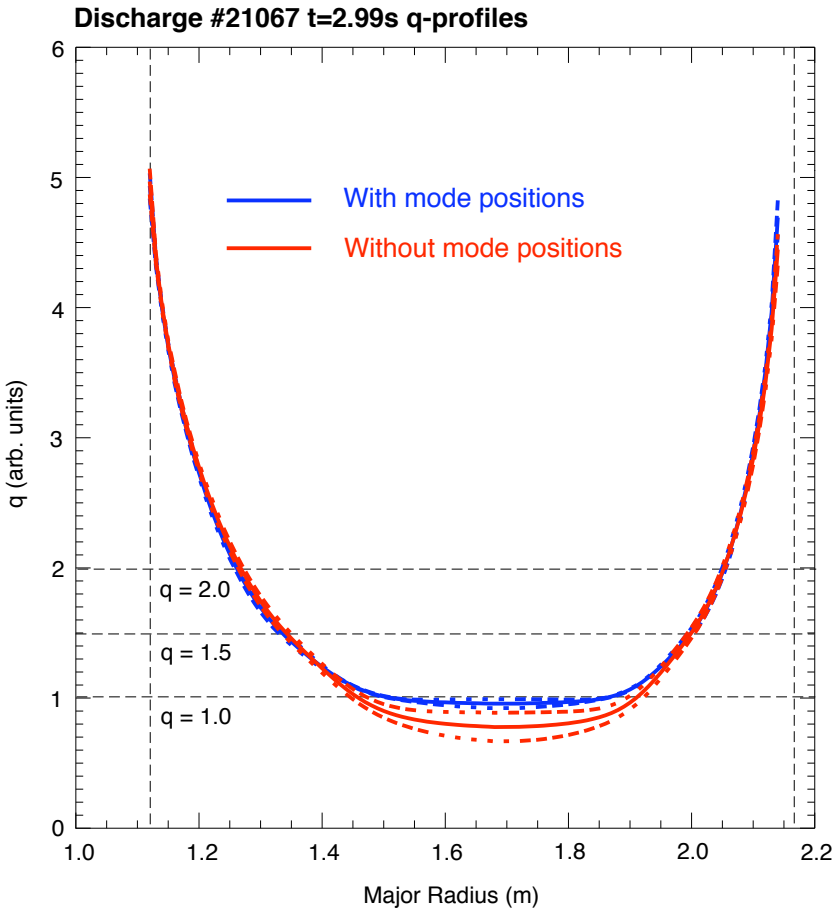

Figure 7.7: Discharge #21067 : reconstructed q profiles done with and without mode positions, and corresponding confidence bands (dashed curves). The plasma boundary is indicated by the vertical dashed lines. Important q surfaces, q=1.0,1.5,2.0 are shown by the horizontal dashed lines.

For the reconstruction the following data was used: MHD mode positions; magnetic coil measurements, temperature, and density data. A 13-knot parameterisation was used with knots at $\rho_{poloidal} = 0.0, 0.1, 0.2, 0.3, 0.4, 0.5, 0.6, 0.7, 0.8, 0.9, 0.95, 0.98, 1.0$ on a computational grid of 128×256 cells in (R,z). Edge kinetic data in the range $1.91 \leq R \leq 2.15$ was used in the reconstruction with the assumption that $T_e = T_i$. The main plasma parameters at the time of the reconstruction were: $I_p = 0.8$MA, $B_{toroidal} = -1.94$T, $\hat{n}_e \simeq 3.7 \times 10^{19}\mathrm{m}^{-3}$, $P_{heat} = 5.0$MW (ICRH) and $\beta_{poloidal} = 0.52$. It was assumed that $Z_{eff} \simeq 2.0$ to allow for impurities[44][43], in fact it was observed that the equilibrium reconstruction remained unchanged when several values of Z_{eff} between 1.0 and 2.0 were used.

#21067	With mode positions	Without mode positions
$\langle dB \rangle$	1.4mT (0.8%)	1.4mT (0.8%)
$\langle dF \rangle$	0.8mT (1.4%)	0.8mT (1.5%)
$\langle dP \rangle$	0.38kPa (3.6%)	0.36kPa (3.3%)
$\langle dJ.B \rangle$	117kATm^{-2} (14%)	84kATm^{-2} (10%)

Table 7.3: Discharge #21067 : $\langle dB \rangle$, $\langle dF \rangle$, $\langle dP \rangle$ and $\langle dJ.B \rangle$ for reconstructions made with and without mode positions. Here $\langle dB \rangle$, $\langle dF \rangle$, $\langle dP \rangle$ and $\langle dJ.B \rangle$ are also presented as a percentage of the root mean square (rms) poloidal field, poloidal flux, edge pressure and edge parallel neo-classical current density respectively.

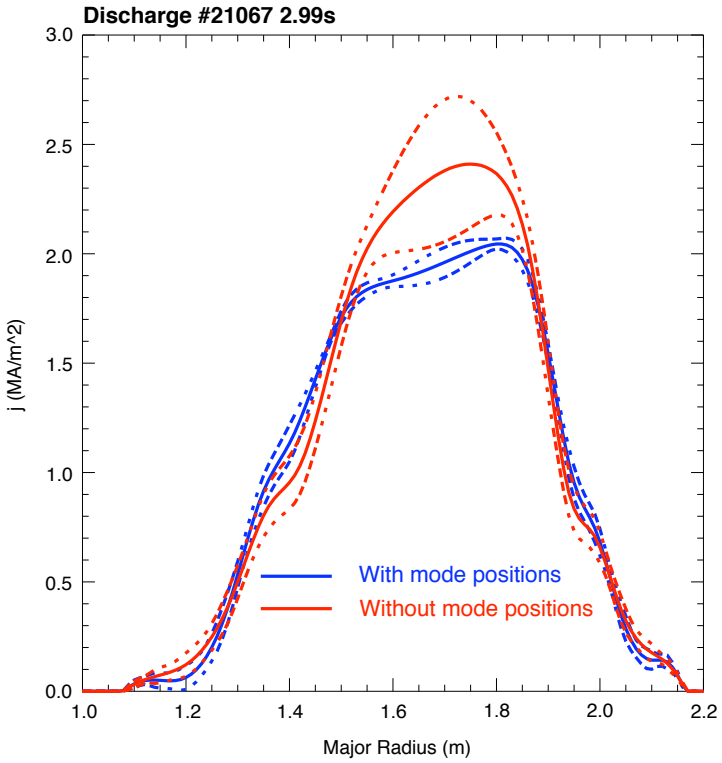

Figure 7.8: Discharge #21067 - The blue curves represent the current density profile and confidence (dashed curves) bands associated with the equilibrium reconstruction performed using additional mode information. The red curves show the current density profile with confidence bands (dashed curves) reconstructed without additional mode information.

The following procedure is used to incorporate q-profile information derived from TAEs in an equilibrium reconstruction. First the TAEs' group position is deduced from diagnostics, such as SXR,

reflectometry, or ECE. This is a necessary step because at ASDEX Upgrade TAEs are observed in groups and are normally very close radially. Therefore they are difficult to localise on their own. Once this position is found, it is used with an average q-value, which is equal to the average value of q_{gap} for the excited TAEs, to constrain the equilibrium reconstruction. In this example we see an n=4,5,6 TAEs. Since $q_{gap} = 1 + 1/(2n)$ for TAEs from the 1^{st} gap (section 3.1.1), we get an average q-value of 1.1.

In figure 7.7, two q-profiles are shown both of which were calculated at 2.99s. The red curve is derived from a reconstruction made with the magnetic coil measurements, density and temperature information, the blue curve shows the q-profile resulting from the inclusion of q information provided by an (m=1, n=1) mode and TAEs. The first observation is that outside the q=1.5 surface the profiles are very similar. This is not unexpected as no q information was provided for this region. The difference between the q-profiles is made most obvious by the change in location of the q=1.0 surface from 1.45m to 1.515m on the high field side and from 1.92m to 1.86m on the low field side, and the increase of q_{min} from 0.80 to 0.95. In the case of the q=1.0 surface, the diameter d_{mid} of the flux surface decreases from 0.47m to 0.345m as a result of MHD mode information.

In addition to the root-mean-square (rms) errors in the poloidal field $\langle dB \rangle$ and poloidal magnetic flux $\langle dF \rangle$, one should also look at the rms errors in the edge parallel neo-classical current density $\langle dJ.B \rangle$ (1.99m $\leq$ R $\leq$ 2.15m) and edge pressure $\langle dP \rangle$ respectively, when kinetic profiles are used. These measures are displayed in table 7.3, and as one can see that the inclusion of mode positions has made little difference to these measures.

q-value	d_{mid} (cm)	measured	predicted
1	34.5	1.000	0.999
$q_{TAE,\,avg} = 1.100$	46.3	1.1	1.097

Table 7.4: Discharge #21067 : Measured and predicted (CLISTE) q-values with the corresponding measured flux surface diameters on the magnetic midplane d_{mid}.

The difference between the measured and predicted value of q for the given flux surface diameters are shown in table 7.4 along with the corresponding flux surface diameter d_{mid}. From the results, the provided flux surface diameters and q-profile points were fitted to within a difference of 1%. This is once more a demonstration of the seamless way in which CLISTE incorporates this directly measurable type of q-profile information.

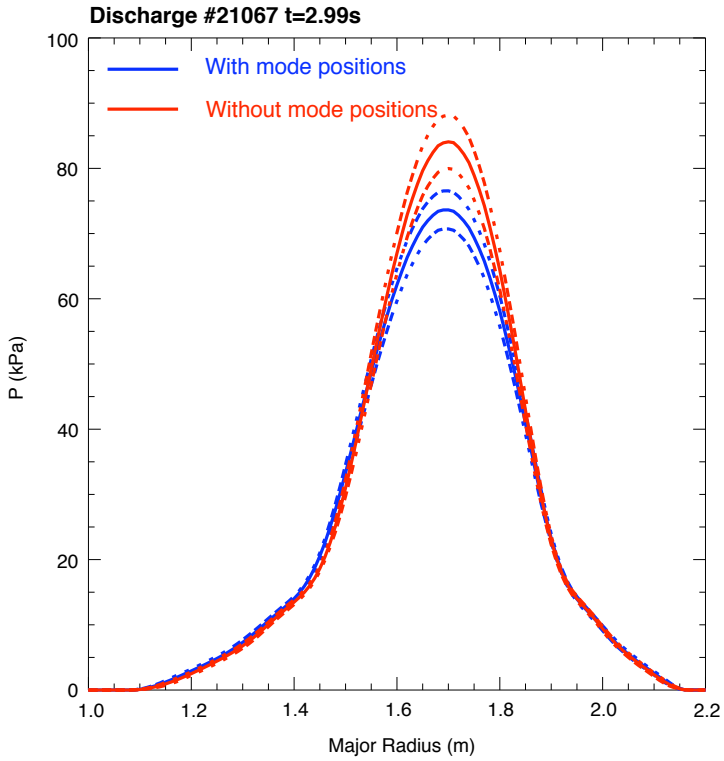

Figure 7.9: Discharge #21067 - The blue curves represent the pressure profile and confidence (dashed curves) bands associated with the equilibrium reconstruction performed using additional mode information. The red curves show the pressure profile with confidence bands (dashed curves) reconstructed without additional mode information.

The current density profiles and pressure profiles reconstructed with and without mode information are shown in figures 7.8 and 7.9 respectively along with the corresponding confidence bands. The current density profile reconstructed using mode positions is seen to have a lower central maximum, reflecting the higher value of q_{min} shown in figure 7.7. The effect of including mode information on the pressure profile has been to reduce the central maximum and a tightening of the confidence bands on both profiles.

A useful comparison can be made between the reconstruction using TAEs' group position (with no MSE), with a reconstruction made using MSE data (with no TAE data), which shows the quality of this approach. Such a comparison is displayed in figure 7.10, where very good agreement is seen between the two profiles. The root-mean-square error in the MSE angles is 0.06^o. The close agreement between the q-profiles in figure 7.10 is an independent confirmation of the quality of q-profile informa-

tion derived from the TAEs. This result in addition to the measures given by the reconstruction using TAEs itself demonstrate the overall quality of the reconstruction made using TAEs and the validity of the technique used to incorporate the data.

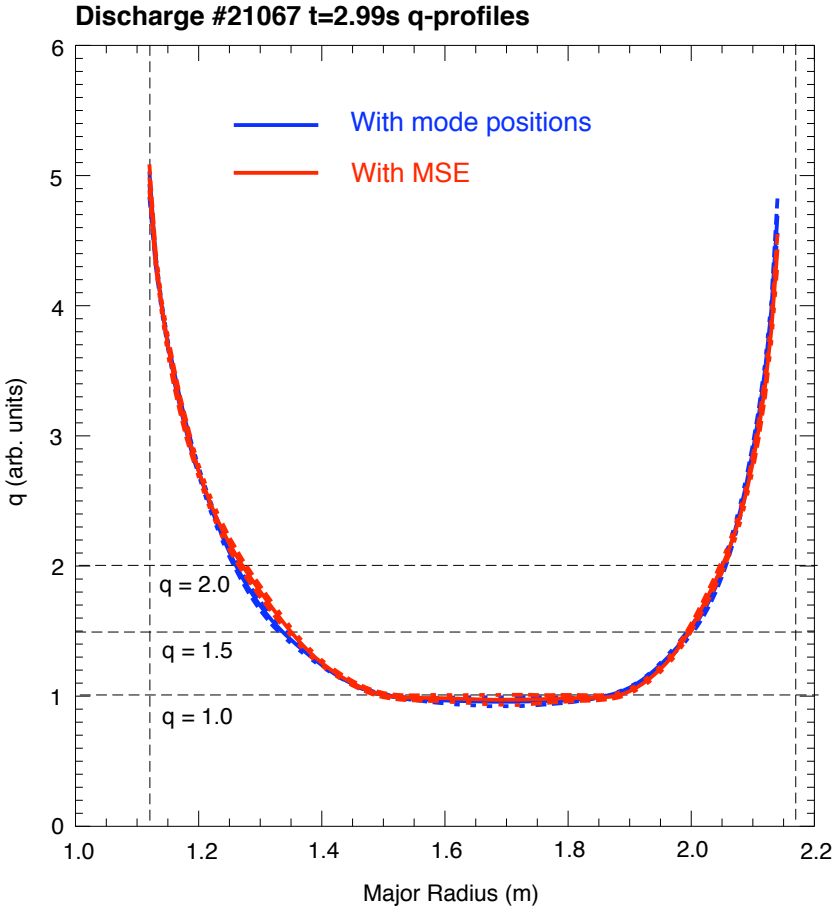

Figure 7.10: Discharge #21067 : Comparison of q profiles reconstructed with mode positions (blue) and MSE (red).

Table 7.5 shows the uncertainties in the q-profile as a result of each individual MSE channel used in reconstruction. In figure 7.10 the confidence bands associated with the reconstruction using MSE data are seen to be very tight on the q-profile with the exception of channel 9. This combined with the smallness of uncertainties in the channels used marks this reconstruction as being a good quality reconstruction.

A final test of the q-profile information derived from TAEs, is to see if the inclusion of TAE information alone leads to an accurate prediction of the position of the q=1 surface, as determined from

experimental measurements. Using this information alone, the following predictions, as to the location of the q=1 surface were made: $R_{min} = 1.515$m and $R_{max} = 1.860$m (and $d_{mid} = 0.345$m). Comparing this with measurements of the position of the q=1 surface from the experiment, we find $R_{min} = 1.510$m and $R_{max} = 1.865$m (and $d_{mid} = 0.355$m) leading to a discrepancy of 0.5cm in the radius (or position) of the q=1 flux surface.

Channel	R	Used	error	q_{min}	q_{max}	$dq_{MSE} = (q_{min} + q_{max})/2$
1	2.07m	yes	0.06^o	2.24	2.33	0.05
2	2.02m	yes	0.06^o	1.70	1.74	0.02
3	1.97m	yes	0.06^o	1.32	1.35	0.02
4	1.93m	yes	0.07^o	1.11	1.13	0.02
5	1.88m	yes	0.04^o	0.99	1.02	0.02
6	1.84m	yes	0.05^o	0.96	1.00	0.02
7	1.80m	yes	0.07^o	0.94	1.01	0.03
8	1.76m	yes	0.05^o	0.85	0.95	0.05
9	1.72m	yes	0.04^o	0.65	0.90	0.13
10	1.68m	no	0.72^o	-	-	-

Table 7.5: Discharge #21067 : Minimum and maximum q-values predicted by CLISTE as a result of a given MSE channel. The uncertainty in the q-profile as a result of using that channel $dq_{MSE} = (q_{max} - q_{min})/2$. These uncertainties are measure of the goodness of the q-profile as a result of the MSE data specifically, in addition to the confidence bands.

This is within the uncertainty of experimental measurements and thus constitutes a very good result. This demonstrates that, in the absence of information pertaining to the q=1 surface, or even in the absence of a q=1 flux surface in the plasma; q-profile information derived from TAEs is very valuable.

ICRF Beatwave driven TAEs

It was shown in the previous chapter on ICRF beatwaves, that it was possible to force otherwise stable TAEs to oscillate. As in the case of fast ion excited TAEs, these TAEs provide q-profile information. Therefore one can employ the technique outlined in the previous subsection to include this data in an

equilibrium reconstruction. In this example, the reconstruction uses the TAEs' group TAE (n=6,5,4,3,2) position and average $q_{gap} \simeq 1.16$. At the time the reconstruction was made, there was a sawtooth instability (m=1, n=1) active in the plasma. This indicates there is a q=1 flux surface in the plasma. The position of q=1 surface was used in addition to the TAE information in the reconstruction.

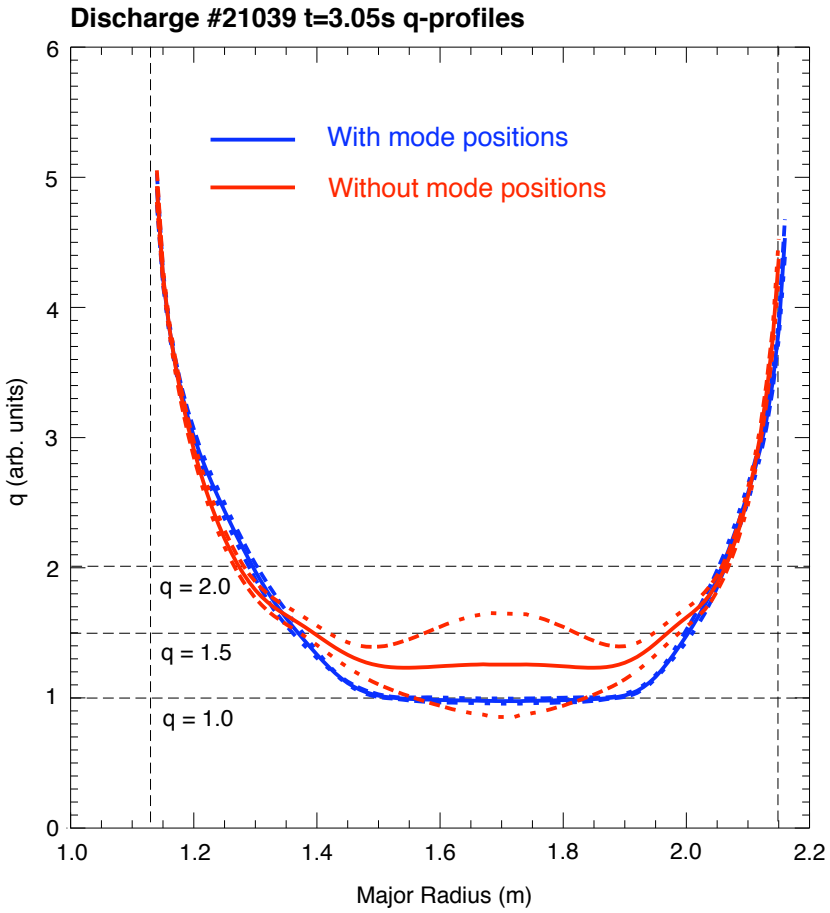

Figure 7.11: Discharge #21039 : reconstructed q profiles done with and without mode positions, and corresponding error bands. The plasma boundary is indicated by the vertical dashed lines. Important q surfaces, q=1.0,1.5,2.0 are shown by the horizontal dashed lines.

In this example the reconstruction was made for the L-mode discharge #21039 at 3.05s using: MHD mode positions; edge magnetic, temperature, and density data. A 13-knot parameterisation was used with knots at $\rho_{poloidal} = 0.0, 0.1, 0.2, 0.3, 0.4, 0.5, 0.6, 0.7, 0.8, 0.9, 0.95, 0.98, 1.0$ on a computational grid of 128×256 cells in (R,z). Edge kinetic data in the range $1.91 \leq R \leq 2.15$ was used in the reconstruction, with the assumption that $T_e = T_i$ (a necessary assumption because T_i was not available).

q-value	d_{mid} (cm)	measured	predicted
1	35.1	1.000	0.999
$q_{TAE,\,avg} = 1.16$	51.4	1.160	1.163

Table 7.6: Discharge #21039 : Measured and predicted q-values with corresponding final flux surface diameters on the magnetic midplane dmid $= R_{right} - R_{left}$.

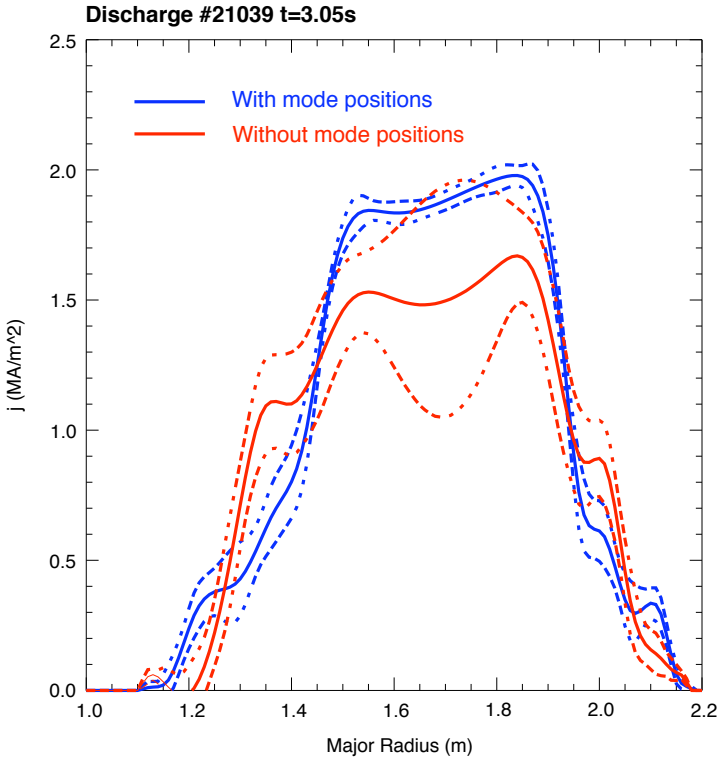

Figure 7.12: Discharge #21039 - The blue curves represent the current density profile and confidence (dashed curves) bands associated with the equilibrium reconstruction performed using additional mode information. The red curves show the current density profile with confidence bands (dashed curves) reconstructed without additional mode information.

The main plasma parameters at the time of the reconstruction were: $I_p = 0.83$MA, $B_{toroidal} = -1.92$T, $\hat{n}_e \simeq 4.0 \times 10^{19}\mathrm{m}^{-3}$, $P_{heat} = 2.5$MW (ICRH), $\beta_{poloidal} = 0.43$, and $Z_{eff} \simeq 2.0$. In figure 7.11 the q-profiles corresponding to reconstructions performed with and without mode positions ((1,1) mode

#21039	With mode positions	Without mode positions
$\langle dB \rangle$	1.2mT (0.7%)	1.2mT (0.7%)
$\langle dF \rangle$	1.5mT (2.3%)	1.3mT (2.2%)
$\langle dP \rangle$	0.47kPa (11%)	0.38kPa (9%)
$\langle dJ.B \rangle$	17kATm^{-2} (8%)	41kATm^{-2} (19%)

Table 7.7: Discharge #21039 : $\langle dB \rangle$, $\langle dF \rangle$, $\langle dP \rangle$ and $\langle dJ.B \rangle$ for reconstructions made with and without mode positions. Here $\langle dB \rangle$, $\langle dF \rangle$, $\langle dP \rangle$ and $\langle dJ.B \rangle$ are also presented as a percentage of the root mean square (rms) poloidal field, poloidal flux, edge pressure and edge parallel neo-classical current density respectively.

and beatwave driven TAEs) are displayed. When the two q-profiles are compared, one can conclude that they are similar in shape for R$<$ 1.3m and R$>$ 2.05m, however this is where the similarity ends. The q-profile derived from the reconstruction using mode positions is shown to be deeper and having a q=1 surface in the plasma. Here q_{min} is seen to go from 1.26 to 0.97. The *flatness* of the profile constructed using mode information, is believed to be accurate as the plasma rest frame TAEs' frequencies are typically found to be very close to the lower Alfvén continuum (f_-), and therefore one would expect low magnetic shear at the position of the gap. Looking at the measured and predicted q-values in table 7.6, one sees that the q-values predicted by CLISTE corresponding to the given radii agree within 1% of the measurements. This demonstrates that the beatwave driven TAEs, like their fast ion driven counterparts, are valuable sources of q-profile information, providing the basis of q-profile diagnostic which requires a relatively small amount of ICRH power.

The rms errors in $\langle dB \rangle$, $\langle dF \rangle$, $\langle dp \rangle$ and $\langle dJ.B \rangle$ (2.13m $\leq$ R $\leq$ 2.19m) for the reconstructions with and without mode positions are displayed in table 7.7 and there one sees that the inclusion of mode positions has made little difference to these measures with the exception of the edge neo-classical parallel current density. When a comparison is made between the values of $\langle dB \rangle$ and $\langle dF \rangle$ in discharges #21067 (table 7.3) and #21039 (table 7.7) one can see that these values are larger in discharge #21039, after an in depth review it was concluded that uncertainties in the kinetic profiles were responsible for the discrepancies.

The reconstructed current density and pressure profiles are shown in figures 7.12 and 7.13, where the current density profiles reconstructed with and without mode information are seen to significantly different. The current profile reconstructed using mode positions is smoother inside the radial positions

1.4m and 2.0m, and has a larger maximum as required by a q=1 surface. This smoothing was found to be a direct result of the inclusion of mode information.

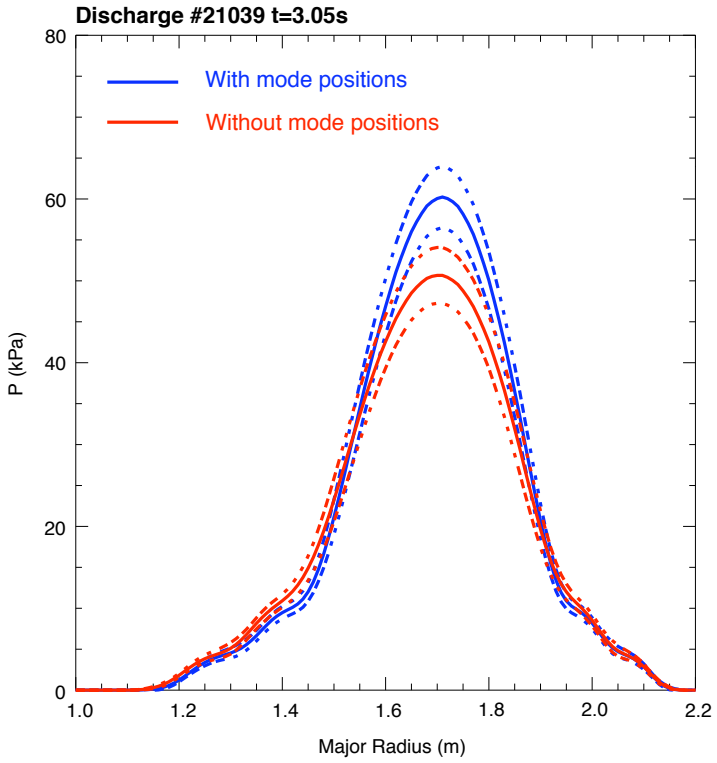

Figure 7.13: Discharge #21039 - The blue curves represent the pressure profile and confidence (dashed curves) bands associated with the equilibrium reconstruction performed using additional mode information. The red curves show the pressure profile with confidence bands (dashed curves) reconstructed without additional mode information.

Using this well diagnosed equilibrium, CASTOR_FLOW solutions for the n=2,3,4,5 TAEs were checked for consistency with the plasma rest frame frequency. The eigenfrequencies found using this new q-profile for the n=2,3,4,5 TAEs were 157.0kHz, 158kHz, 158kHz and 161kHz respectively. This agrees well rest average frequency of 160kHz in the plasma's rest frame and demonstrates that the q-profile information was good and the technique used to include the information was sound.

Here also one would like to know if the inclusion of q-profile information from beatwave driven TAEs leads to an accurate prediction of the position of the q=1 surface (see the previous subsection). Using TAE information alone, the following predictions, as to the location of the q=1 surface were made: $R_{min} = 1.52$m and $R_{max} = 1.87$m (and $d_{mid} = 0.35$m). Comparing this with measurements of

the position of the q=1 surface from the experiment, we find $R_{min} = 1.52$m and $R_{max} = 1.88$m (and $d_{mid} = 0.36$m) leading to a discrepancy of 0.5cm in the radius (or position) of the q=1 flux surface. This again, is within the uncertainty of experimental measurements and constitutes a good result.

7.3 Constraining the equilibrium pressure profile

The CLISTE code is capable of solving the Grad-Shafranov equation 2.56 using a wide variety of diagnostic data. If the q profile is well constrained and edge pressure information is supplied, then CLISTE is capable of reconstructing an accurate equilibrium pressure profile, and from it a reliable fast pressure profile. For discharge #20396, such a reconstruction was made, so as to be compared with simulated fast pressure profiles generated by the TORIC and PION codes. The results of this comparison was shown in chapter 4, figure 5.16. Here the reconstructed CLISTE current density and pressure profiles and associated *goodness-of-fit* measures are shown to highlight the quality of a well diagnosed CLISTE fast pressure profile.

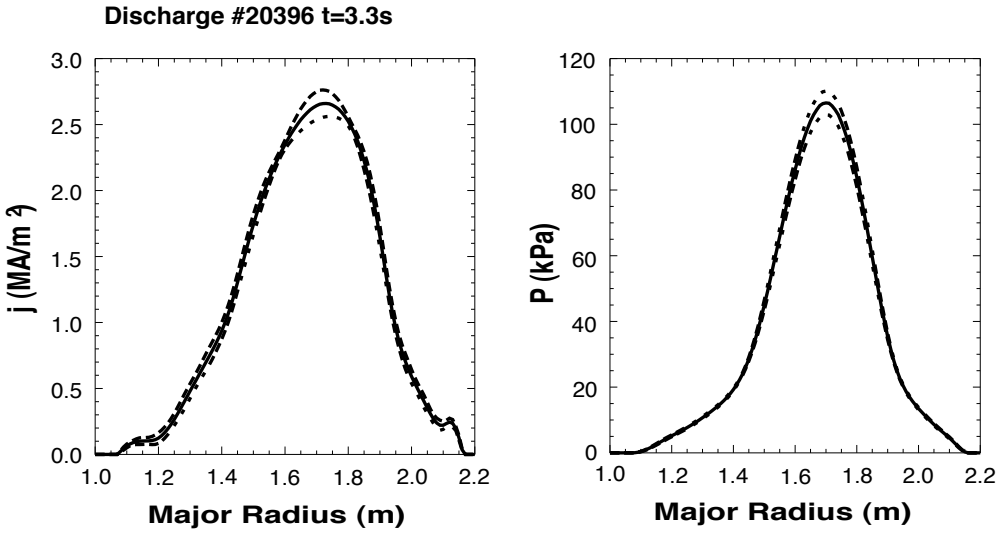

Figure 7.14: Discharge #20396 : Reconstructed equilibrium pressure and current density profiles with associated error bands.

In this example the reconstruction was made for the L-mode discharge #20396 at 3.3s using: the q=1 position from a (m=1,n=1 mode); edge magnetic measurements, temperature, and density data. During this discharge no positions information was available for the TAEs, and so they do

q-value	d_{mid} (cm)	measured	predicted
1	31.9	1.000	0.999

Table 7.8: Discharge #20396 : Measured and predicted q-values with corresponding final flux surface diameters on the magnetic midplane d_{mid}.

#20396	With mode positions	Without mode positions
$\langle dB \rangle$	1.2mT (0.7%)	1.2mT (0.7%)
$\langle dF \rangle$	0.8mT (1.2%)	0.8mT (1.2%)
$\langle dP \rangle$	0.84kPa (6%)	0.93kPa (6%)
$\langle dJ.B \rangle$	169kATm^{-2} (17%)	167kATm^{-2} (17%)

Table 7.9: Discharge #20396 : $\langle dB \rangle$, $\langle dF \rangle$, $\langle dP \rangle$ and $\langle dJ.B \rangle$ for reconstructions made with and without mode positions. Here $\langle dB \rangle$, $\langle dF \rangle$, $\langle dP \rangle$ and $\langle dJ.B \rangle$ are also presented as a percentage of the root mean square (rms) poloidal field, poloidal flux, edge pressure and edge parallel neo-classical current density respectively.

not contribute to this reconstruction. A 13-knot parameterisation was used with knots at $\rho_{poloidal} = 0.0, 0.1, 0.2, 0.3, 0.4, 0.5, 0.6, 0.7, 0.8, 0.9, 0.95, 0.98, 1.0$ on a computational grid of 128×256 cells in (R,z). Edge kinetic data in the range $1.92 \leq R \leq 2.31$ was used in the reconstruction, with the assumption that $T_e = T_i$ (a necessary assumption because T_i was not available). The main plasma parameters at the time of the reconstruction were: $I_p = 0.88$MA, $B_{toroidal} = -2.43$T, $\hat{n}_e \simeq 4.0 \times 10^{19}$m^{-3}, $P_{heat} = 5.1$MW (ICRH), $\beta_{poloidal} = 0.72$, and $Z_{eff} \simeq 2.0$.

The reconstructed current density and pressure profiles are shown in figure 7.14. In table 7.8, the measured and predicted q=1 values are seen to agree well with one another. The rms errors in the poloidal field $\langle dB \rangle$, poloidal magnetic flux $\langle dF \rangle$, edge parallel neoclassical current density $\langle dJ.B \rangle$ (1.99m $\leq$ R $\leq 2.15m$), and edge pressure $\langle dp \rangle$ for the reconstructions made with and without mode information are displayed in table 7.9 and show a negligible discrepancy. By subtracting the thermal pressure profile (red curve in figure 7.15) from the total equilibrium pressure (blue curve in figure 7.15), one arrives at the fast pressure profile (green curve in figure 7.15). This fast pressure profile shows that the fast ion energy is distributed throughout a significant proportion of the plasma.

7.4 Summary

The examples shown demonstrate the technique used to incorporate MHD mode information into CLISTE equilibrium reconstructions, and the resulting quality of the reconstructions made with mode information. In particular the ease in which q-profile information from MHD instabilities can be incorporated, and the effect such information has on the reconstruction.

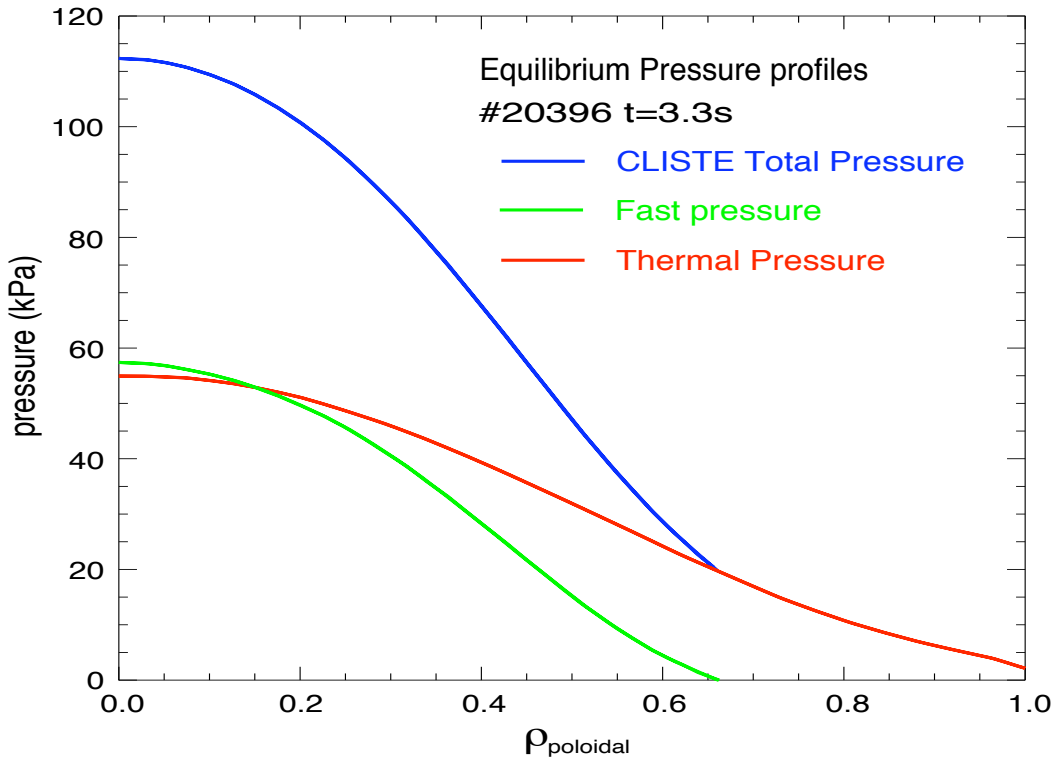

Figure 7.15: Discharge #20396 : Total reconstructed equilibrium pressure (blue) decomposed in constituent fast pressure (green) and thermal pressure profiles (red).

In the case of the H-mode discharge, the combination of mode information and magnetic measurements, not only improved the q-profile, made it possible for a good H-mode pedestal to be recovered without including kinetic data. For the L-mode discharges, it was shown that TAEs excited by fast ions or driven by ICRF beatwaves provided very valuable q-profile information that could be used effectively with edge kinetic data to improve the equilibrium current density and pressure profiles. In addition, it was shown that using q-profile information provided by TAEs could accurately predict the position of the q=1 flux surface.

Chapter 8

Conclusions

The theoretical background for TAEs is extensive as are the experimental results. This thesis presented the 2005/2006/2007 experimental results for TAEs observed at ASDEX Upgrade. TAEs depend on the thermal and fast ion populations to define their character, and so can be identified by means of the gap frequency's dependence on the bulk mass density, toroidal field and q-profile. This in turn means that the behaviour of these quantities at the position of a particular gap can be inferred from the behaviour of TAEs. The amount of ICRH power required to destabilise TAEs was shown to increase with increasing particle density and toroidal mode number, this demonstrated increasing density reduces the fast ion drive, and suggests that finite orbit width effects can increase this effect with increasing toroidal mode number n. The TAE threshold was found to be independent of q_{95}, however it was shown that q_{95} indirectly influences the stability of the $n = 2$ TAE by leading to an increase in continuum damping. In addition to this, results from experiments performed in a limiter configuration demonstrated that high values of q_{95} and by extension high edge shear stabilises low $n \leq 2$ TAEs, whether or not a separatrix is present.

From ECE data and reconstructions of a TAE's eigenfunction using Soft X-ray and reflectometry data, important features such as: the position of the maximal displacement, the sign change of the eigenfunction predicted by the CASTOR_FLOW code, and a *closed* TAE gap at the plasma edge were confirmed. The ballooning character of the observed TAEs was demonstrated by the corrected poloidal amplitude distribution, from magnetics. This verified the observed TAEs as even modes and the location of the simulated frequencies below the centre of the 1^{st} gap. Measured decay rates were found to be larger than damping rates calculated by LIGKA. From the measured growth and decay rates it was

possible to calculate an average drive. From these results one sees that TAE models are capable of accurately describing the behaviour and character of TAEs, demonstrating that theory and experiments are converging smoothly towards each other. It was observed that tangential NBI not only increased the amplitude of particular TAEs, it changed the nature of drive itself. This change is manifested by the promotion of additional TAEs such as the n=5,6,7 over the n=4. It was also observed that the effects of locked mode changed the environment, such that an n=3 TAE was destabilised, and the n=7 TAE was stabilised.

Fast ion excited TAE spectral line widths were measured and shown to be insensitive to parameter changes within a discharge. However a high starting density is believed to be responsible for the observed increase in line widths. These line width values were also seen to be smaller, but of the same order of magnitude as measured decay rates. When one considers this information and the Lorentz oscillator damping model together, it suggests that there may be a relationship between these line widths and decay rates (damping rates).

Several candidate fast pressure profiles calculated using the CLISTE, PION and TORIC codes were tested for compatibility with TAE requirements. It was found that the values of the drive for the n=4 TAE derived from these profiles showed reasonable agreement with the average drive taken as been equal to the average measured decay rate.

The derived expression for volume average β_{fast} was shown to be an upper limit when compared with the corresponding value calculated from the CLISTE, PION and TORIC fast pressure profiles. The remaining difference between the values is believed to come from the form of the Spitzer slowing down time and the assumption that all of the ICRH power is absorbed by the minority species. In spite of assumptions made, the compared values show reasonable agreement.

It has been demonstrated by comparison of fast ion excited TAEs with ICRF beatwave driven TAEs, that ICRF beatwaves can be used to drive TAEs from the 1^{st} gap. With the aid of the Soft X-ray diagnostic these modes were localised and used to provide q-profile information. Additionally, it was shown that the ICRF beatwave was also able to excite MHD modes at lower frequencies than the centrally localised modes, which are believed to be edge localised TAEs.

The equilibrium reconstruction examples shown demonstrate the technique used to incorporate MHD mode information into CLISTE equilibrium reconstructions, and the resulting good quality of the reconstructions made with mode information. In particular the ease in which mode q-profile information

can be incorporated and effect such information has on the reconstruction. In the case of the H-mode discharge, the combination of mode information and magnetic measurements, not only improved the q-profile, but made it possible for a good H-mode pedestal to be recovered with out including edge kinetic data. For the L-mode discharges, it was shown that TAEs excited by fast ions or driven by ICRF beatwaves provided good q-profile information which could be used effectively with edge kinetic data to improve the equilibrium current density and pressure profiles, and to predict the position of the q=1 flux surface. Since this technique can be used whenever ICRH power is used, it provides the basis for a new passive q-profile diagnostic. With the ever improving SXR, ECE and reflectometry diagnostics, it will in the future be possible to localise the maxima of individual TAEs, providing multiple q-profile points from q=1 up to q=1.5, which is the least diagnosed region of the q-profile, in the absence of MSE. This would therefore provide an invaluable tool, which would add to and complement MSE, with particular value in discharges where NBI could not be used.

When all observations are considered, TAEs are seen to be a valuable tool with which a tokamak plasma can be diagnosed, while at the same time not perturbing plasma performance significantly in present day experiments. However, it remains possible that in future experiments the TAE gap could be open resulting in TAEs that will not be so benign.

8.1 Outlook

Even TAEs from the 1^{st} gap have been well studied in L-mode and compared with TAEs observed in H-mode, which are believed to be the same modes as observed in L-mode. Throughout the previous experimental campaigns, several types of Alfvén modes have also been observed. Such examples include, TAE splitting, TAEs from the outer gaps, TAEs in improved H-mode and TAEs observed in the new full-tungsten ASDEX Upgrade. It would be enriching to study these modes and ascertain, if existing models can adequately explain these occurrences. Once these modes have been characterised, they could be exploited to provide more information about the q-profile and fast ion pressure profile across the entire plasma radius. The next logical step would be to refine the ICRF beatwave technique to excite these modes on demand in order to flesh out the concept of a passive MHD-q profile diagnostic. However for this technique to fully realise its potential, there needs to be a close collaboration with diagnosticians such as SXR, reflectometry and especially the new 2MHz ECE, to enhance these diagnostics so as to be capable of resolving the position of maximal displacement of individual TAEs. This

is in essence the final milestone that once achieved will truly unleash the potential of this diagnostic.

One final remark remains to be made. The observations made concerning the line widths of TAEs excited by fast ions; and the effect of tangential NBI on these TAEs deserves more study. In particular, it would be very interesting to understand fully, the observed behaviour of TAEs resulting from the tangential NBI, as this would provide an insight into the fast ion drive available to TAEs and a means to tailor TAEs, in a limited way, to one's own preference.

Chapter 9

Appendix

9.1 CLISTE Interpretive Equilibrium

This following appendix is reproduced from [73] and is meant to serve as a brief introduction to the CLISTE code.

CLISTE Algorithm: During each iteration cycle, a linear optimisation of the free parameters in the $p'(\Psi)$ and $FF'(\Psi)$ (see the related information pertaining to the Grad-Shafranov equation in section 2.3.1) profiles is carried out. The linear parameterisation of the source profiles is given by

$$p'(\Psi) = \sum_{i=1}^{m_p} c_i \pi_i(\Psi) \tag{9.1}$$

$$FF'(\Psi) = \sum_{j=1}^{m_{FF}} d_j \varphi_i(\Psi) \tag{9.2}$$

where $\pi_i(\Psi)$ and $\varphi_j(\Psi)$ are arbitrary functions of Ψ with fixed coefficients and c_i, d_j are the free parameters in the problem. Thus $\pi_i(\Psi)$ and $\varphi_j(\Psi)$ constitute the basis functions of the plasma current distribution where Ψ is the full equilibrium flux function from the previous iteration cycle. New poloidal flux functions $\Psi_{p,i}^{new}$ and $\Psi_{FF,j}^{new}$ are found from the updated equilibrium flux function after solving the 'Poisson problem'

$$-\left(\frac{\delta^2\Psi_{p,i}^{new}}{\delta R^2} - \frac{1}{R}\frac{\delta\Psi_{p,i}^{new}}{\delta R} + \frac{\delta^2\Psi_{p,i}^{new}}{\delta Z^2}\right) = \mu_0 R^2 \pi_i(\Psi) \tag{9.3}$$

$$-\left(\frac{\delta^2\Psi_{FF,j}^{new}}{\delta R^2} - \frac{1}{R}\frac{\delta\Psi_{FF,j}^{new}}{\delta R} + \frac{\delta^2\Psi_{FF,j}^{new}}{\delta Z^2}\right) = \varphi_j(\Psi) \tag{9.4}$$

separately for each $\Psi^{new}_{p,i}$ and $\Psi^{new}_{FF,j}$. Note that equations 9.3 and 9.4 only take care of that part of the updated equilibrium flux generated by the i^{th} component of the $p'(\Psi)$ and j^{th} component of the $FF'(\Psi)$ related plasma current distributions respectively. In addition, the full equilibrium flux includes the contribution from the external measured currents, which are held constant. In terms of the coefficients c_i and d_j, yet to be determined, the updated full equilibrium flux is given by

$$\Psi^{new} = \sum_{i=1}^{m_p} c_i \Psi^{new}_{p,i} + \sum_{j=1}^{m_{FF}} d_j \Psi^{new}_{FF,i} + \Psi^{ext} \tag{9.5}$$

The solution grids for $\Psi^{new}_{p,i}$ and $\Psi^{new}_{FF,j}$ yielded by equations 9.3 and 9.4 are passed individually to the routine which calculates the predicted measurements from the flux function. In this way, a matrix of $m_p + m_{FF}$ columns of *basis values* $b_{n,k}$, $((n = 1,\ldots,N),(k = 1,\ldots,m_p + m_{FF}))$ is constructed for the N measurements. The values of $b_{n,k}$ is the contribution to the n^{th} measurement prediction per **unit strength** of the k^{th} basis function. An extra column catering for the vertical shift parameter is added to the matrix by calculating the change in each measurement when its Z position is shifted by -1cm. This gives the sensitivity per +1cm shift in the plasma position. Another row is added to the matrix for each regularisation condition on the free parameters. If $\vec{\vec{B}}$ is the data matrix and $\vec{y}$ is the vector of measurements less all the contributions from the measured external currents, then the optimisation problem reduces to the solving of the linear regression problem

$$\vec{y} = \vec{\vec{B}}\vec{x} \tag{9.6}$$

where $\vec{x}$ is the solution vector of the optimised free parameters for the current iteration cycle. The equation for y_n in the over-determined system of linear equations which constitutes the linear regression problem is thus

$$y_n = \sum_{k=1}^{m_p+m_{FF}+1} x_k b_{n,k} \tag{9.7}$$

Once $\vec{x}$ has been determined, the full equilibrium flux grid is constructed. The plasma flux function Ψ_{plasma} is computed by once more solving equations 9.3 and 9.4, where the *right-hand-side* now is the full $\mu_0 j_\phi$ profile constructed from the first $m_p + m_{FF}$ elements of the newly obtained vector $\vec{x}$:

$$-\left(\frac{\delta^2\Psi_{plasma}}{\delta R^2} - \frac{1}{R}\frac{\delta\Psi_{plasma}}{\delta R} + \frac{\delta^2\Psi_{plasma}}{\delta Z^2}\right) = \mu_0 R^2 \sum_{i=1}^{m_p} c_i \pi_i(\Psi) + \sum_{j=1}^{m_{FF}} d_j \varphi_j(\Psi) \tag{9.8}$$

Finally, the external flux contribution Ψ_{ext} is restored to yield

$$\Psi_{new} = \Psi_{plasma} + \Psi_{ext} \tag{9.9}$$

The procedure is iterated until a user specified convergence criterion is satisfied. For more information on that which has been discussed here, please see reference [73].

In the description given above, the CLISTE code is seen to construct a matrix, from the contributions to the n^{th} measurement prediction per unit strength of the k^{th} basis function, which are then directly used in the optimisation process. In the following discussion it will be shown how the contribution, made by each new basis function using the MHD derived q-profile information, is calculated by CLISTE.

The poloidal flux Ψ and the rotational transform ι are related through the following equation,

$$\iota = \frac{d\Psi}{d\Phi}, \tag{9.10}$$

here Φ is the toroidal flux function. On the magnetic mid-plane, $\frac{\partial\Psi}{\partial z} = 0$, and therefore by the *chain-rule*

$$\iota = \frac{d\Psi}{dR}\frac{dR}{d\Phi}. \tag{9.11}$$

For a fixed radial position, or equivalently the input flux surface diameter d_{mid} of the target q value from the SXR or ECE diagnostics, $\frac{d\Phi}{dR}$ will vary little from one cycle to the next, as $\Phi = \left\langle B_\phi \right\rangle \times Area$, and so at $R_{q-target}$ we have,

$$\frac{d\Psi}{dR} = \frac{\iota_{latest}}{\left(\frac{d\Psi}{dR}\right)_{latest}} \equiv \frac{\iota_{target}}{\left(\frac{d\Psi}{dR}\right)_{target}}, \tag{9.12}$$

which implies that

$$\left(\frac{d\Psi}{dR}\right)_{target} = \left(\frac{d\Psi}{dR}\right)_{latest}\frac{\iota_{target}}{\iota_{latest}}. \tag{9.13}$$

where the latest values of each quantity is that value which was available at the end of the previous iteration cycle. Since $\iota = 1/q$, this means that the the target value of $\frac{d\Psi}{dR}$ is proportional to its latest value at the MHD mode's position, the specified d_{mid}, where the constant of proportionality is the ratio of the latest q-value to the target q-value.

$$\left(\frac{d\Psi}{dR}\right)_{target} = \frac{q_{latest}}{q_{target}}\left(\frac{d\Psi}{dR}\right)_{latest} \tag{9.14}$$

Now using a new label k, with the range $k = 1, \ \ldots \ , m_p + m_{FF}$, for the entire set of basis functions $\{\Psi_k\} = \{\{\Psi_{p,i}\}_{i=1}^{m_p}, \{\Psi_{FF,j}\}_{j=1}^{m_{FF}}\}$ and free parameters $\{\beta_k\}$, we can express the derivative of the full *target* equilibrium flux function, minus the vacuum solution, using a single summation:

$$\Psi'_{target} = \sum_{k=1}^{m_p+m_{FF}} \beta_k \Psi'^{new}_k, \tag{9.15}$$

where $\Psi' = \frac{d\Psi}{dR}$. Since the Ψ'_k from each basis function super-imposes, the contribution to ι_{target} from the kth basis function is

$$\Delta_k \iota = \iota_{target} \frac{\beta_k \Psi'^{new}_k}{\Psi'_{target}} = \frac{\beta_k \Psi'^{new}_k}{q_{target} \Psi'_{target}}. \tag{9.16}$$

Now using equation 9.14 we can express the kth contribution to the *latest* full flux function and q-value as

$$\Delta_k \iota = \frac{\beta_k \Psi'^{new}_k}{q_{latest} \Psi'_{latest}}. \tag{9.17}$$

Here we see that this gives a constraint on the reconstruction, which is **linear** in the free parameters incorporating the user supplied value of q_{target}. This allows the addition of a new row to the contribution matrix $\vec{\vec{B}}$ for each user supplied $\{$q-value, $d_{mid}\}$ pair as shown in equation 9.19 (all quantities are evaluated at d_{mid}).

An example of regularisation is a curvature penalty $C \simeq 1.0001$ placed on the p' and ff' profiles at each of the p knots in the cubic-spline representation of these profiles. Here the π_i and φ_j basis functions are cubic-splines (see [73] for more information). This is incorporated into the optimisation problem as shown in equation 9.19, where each new *curvature*-row in the matrix corresponds to one of the p *null-pseudo-measurements*. This is equivalent to the minimisation of

$$\|\vec{y} - \vec{\vec{B}}\vec{x}\|^2 + C|\vec{x}|^2. \tag{9.18}$$

$$\begin{bmatrix} y_0 \\ \vdots \\ \vdots \\ \vdots \\ y_N \\ \vdots \\ \frac{1}{q_{target}} \\ \vdots \\ 0 \\ \vdots \\ 0 \\ \vdots \\ 0 \end{bmatrix} = \begin{bmatrix} b_{0,0} & \dots & \dots & \dots & b_{0,m_p+m_{FF}} \\ \vdots & \ddots & \vdots & \dots & \vdots \\ \dots & \dots & b_{n,k} & \dots & \dots \\ \vdots & \dots & \vdots & \ddots & \vdots \\ b_{N,0} & \dots & \dots & \dots & b_{N,m_p+m_{FF}} \\ \vdots & \vdots & \vdots & \vdots & \vdots \\ \vdots & \vdots & \frac{\Psi_k'^{new}}{q_{latest}\Psi'_{latest}} & \vdots & \vdots \\ \vdots & \vdots & \vdots & \vdots & \vdots \\ C & \dots & 0 & \dots & 0 \\ 0 & \ddots & 0 & \dots & 0 \\ 0 & \dots & C & \dots & 0 \\ \vdots & \dots & \vdots & \ddots & \vdots \\ 0 & \dots & 0 & \dots & C \end{bmatrix} \begin{bmatrix} \beta_0 \\ \vdots \\ \beta_k \\ \vdots \\ \beta_{m_p+m_{FF}} \end{bmatrix} \tag{9.19}$$

9.2 The stability of TAEs - β_{fast} dependence

9.2.1 The stability threshold of TAEs

If the shape of the fast pressure profile is assumed to remain the same as the fast pressure increases during an ICRH power ramp, then one would expect that the radial fast pressure gradient to be proportional to fast pressure ($dp_f/dr = kp_f$) at each radial location in the plasma. Here k would be that constant of proportionality. In a well conditioned machine the hydrogen concentration is not expected to change significantly and will therefore not effect the driving term in equation 3.10. Using this and the assumption that $dp_f/dr = kp_f$, we can reduce the driving-term at $\rho^{gap}_{poloidal}$ to a form reflecting its dependency on the fast pressure and density alone, namely,

$$\frac{\gamma_{drive}}{f_{TAE}} = \frac{9}{4}\beta_f \left(\frac{f_{*,f}}{f_{TAE}} - \frac{1}{2}\right) H\left(\frac{v_A}{v_f}\right) \quad \propto \quad c_1 p_f \left(c_2 \frac{p_f}{\sqrt{n_e}} - \frac{1}{2}\right) H\left(\frac{c_3}{\sqrt{n_e}}\right). \tag{9.20}$$

In order to focus on the dynamic quantities, $c_1 = \frac{9\mu_0}{2B^2}$, $c_2 = \frac{-2mkqR_0\sqrt{(\delta+2(1-\delta))\mu_0}}{re_f B^2 \delta\sqrt{m_h}}$ and $c_3 = \frac{B}{4\pi qR_0\sqrt{2E_f\mu_0(\delta+2(1-\delta))}}$ are used to represent quantities which do not change. Here δ is the hydrogen concentration in the plasma, m_h is the mass of a hydrogen atom and E_f is the energy of the fast ions,

where E_f, for the purpose of calculations, was assumed to be the average energy of the losses and approximately constant.

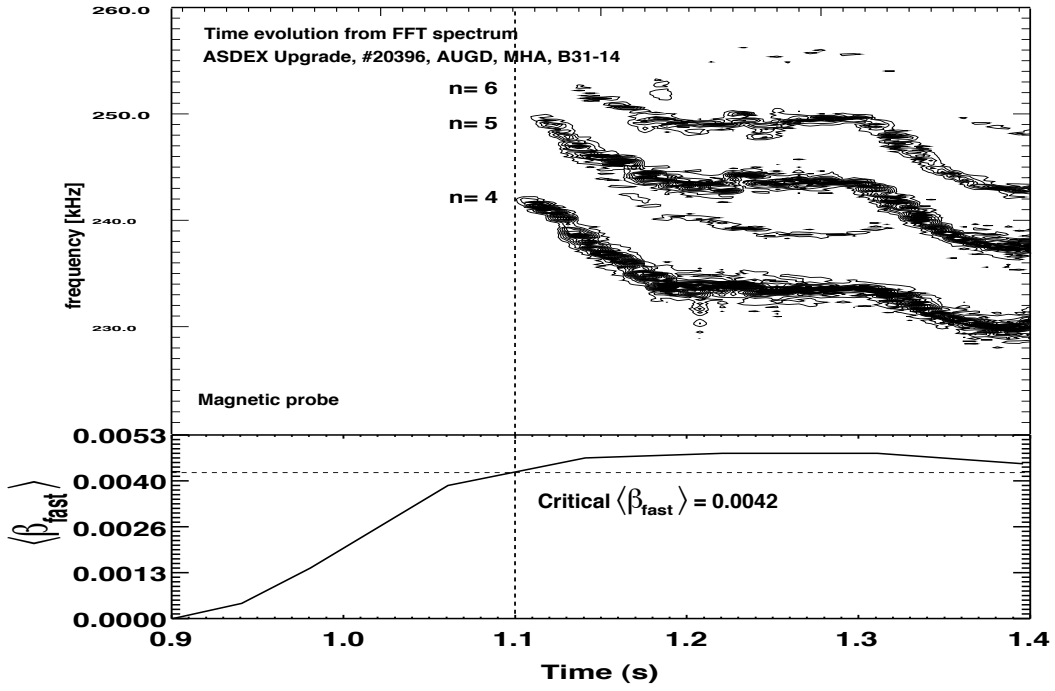

Figure 9.1: Discharge #20396 Identification of $\langle \beta_{fast} \rangle$ (equation 2.82) threshold at the onset of TAEs. Critical $\langle \beta_{fast} \rangle = 0.0042$.

Since $\sqrt{n_e}$ is the relevant term, a moderate change in n_e will have smaller influence than p_f during the power increase because of the term proportional to p_f^2, the rightmost expression in (9.20) becomes

$$\frac{\gamma_{drive}}{f_{TAE}} \propto c_4 p_f^2 - c_5 p_f. \tag{9.21}$$

Here the contribution of n_e is contained within the quantities $c_4 = \frac{c_1 c_2}{\sqrt{n_e}} H\left(\frac{c_3}{\sqrt{n_e}}\right)$ and $c_5 = -\frac{c_1}{2} H\left(\frac{c_3}{\sqrt{n_e}}\right)$ for clarity.

Now if we can take the shape of the fast pressure to remain constant during an ICRH power increase, then p_f and by extension $\langle \beta_{fast} \rangle$ can be used to identify the onset threshold of TAEs in that discharge.

The critical value of the $\langle \beta_{fast} \rangle$ required to excite TAEs in a discharge is taken as the value of $\langle \beta_{fast} \rangle$ (equation 2.82) at the onset of the TAEs. For discharge #20396 this threshold was found to be

0.0042, see figure 9.1.

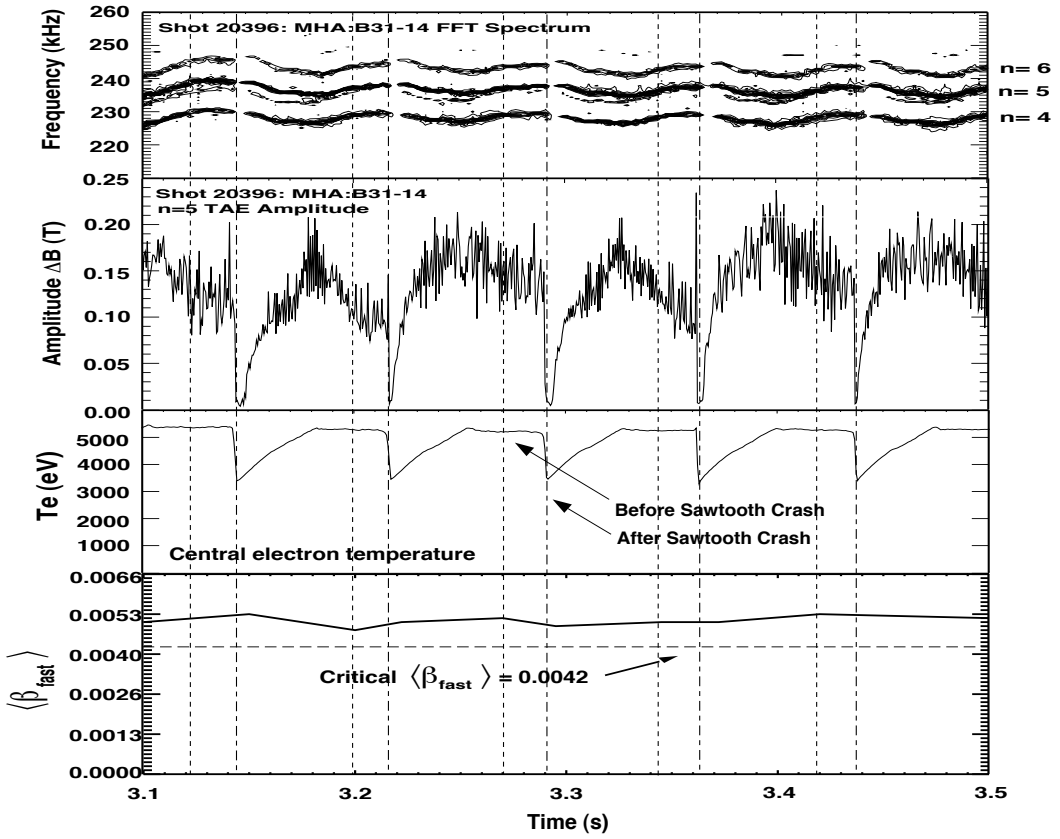

Figure 9.2: In discharge #20396 the sawtooth instability is seen to have an important stabilising effect on TAEs. The value of $\langle\beta_{fast}\rangle$ stays well above the critical value of 0.0042.

Looking past the onset of TAEs, the $\langle\beta_{fast}\rangle$ is shown in figures 9.1 and 9.2 to remain above the threshold while TAEs are present. This suggests that the assumption made about the shape of the fast pressure profile as being reasonable and therefore that the $\langle\beta_{fast}\rangle$ threshold exists. However figure 9.2 also shows the limits to the application of this threshold because the active TAEs are seen to cease every time there is a sawtooth crash while the $\langle\beta_{fast}\rangle$ remains above the threshold. This occurs because the volume averaged slowing down time used to calculate $\langle\beta_{fast}\rangle$ is not sensitive to the sawtooth crash.

To extend this result to the existence of a unique critical $\langle\beta_{fast}\rangle$ for similar discharges it would be necessary for the initial shape of fast pressure profile to be the same. It is also expected that for similar discharges the mode damping is the same. To test this the critical $\langle\beta_{fast}\rangle$ in several similar discharges were identified (see table 9.1). The resulting mean and uncertainty (standard deviation) of

Discharge #	19077	19117	19141	19142	19153	19155	19156
$\langle \beta_{fast} \rangle$	0.0046	0.0095	0.0054	0.0046	0.0032	0.0061	0.0061
Discharge #	19161	20203	20396	20399	20487	21067	
$\langle \beta_{fast} \rangle$	0.0098	0.0042	0.0042	0.0055	0.0029	0.0037	

Table 9.1: $\langle \beta_{fast} \rangle$ values at the onset of TAEs calculated using equation 2.82 for a set of 13 similar discharges.

these measurements was found to be 0.0054 ± 0.0032. Given the large uncertainty it was evident that a unique critical $\langle \beta_{fast} \rangle$ did not exist. This leads us to conclude that in similar discharges, the initial shape of the fast pressure gradient profile can not be taken as being the same.

9.3 Article - Stability of Toroidicity induced shear Alfvén Eigenmodes in ASDEX Upgrade

K.Sassenberg[1,2], M.Maraschek[2], P.J.Mc Carthy[1,2], H.Zohm[2], R.Bilato[2], W.Bobkov[2], S.Da Graça[3], A.Flaws[2], M.García-Muñoz[2], S.Günter[2], V.Igochine[2], P.Lauber[2], M.J.Mantsinen[2,4], P.Piovesan[5], and the ASDEX Upgrade Team[2].

[1] Department of Physics, University College Cork, Association EURATOM DCU, Cork, Ireland.

[2] Max-Planck-Institut für Plasmaphysik, Garching, Euratom Association, Germany.

[3] Centro de Fusao Nuclear, Associac cao EURATOM / IST, Instituto Superior Tecnico, Av. Rovisco Pais, P-1049-001 Lisboa, Portugal.

[4] Helsinki University of Technology, Association EURATOM-TEKES, P.O. Box 4100, FIN-02015 HUT, Finland.

[5] Consorzio RFX - Associazone EURATOM-ENEA sulla fusione, Padova, Italy.

Abstract In a tokamak plasma, Toroidicity induced Alfvén Eigenmodes (**TAE**s) are excited by and alter the orbits of resonant fast ions with the character of these modes defined by both the thermal and supra-thermal fast ion populations. To explore the stability of TAEs in ASDEX Upgrade, the effects of magnetic shear and density on TAEs, the decay and growth rate of individual TAEs, and fast ion drive rates have been studied. In particular, the mode structure of TAEs, the dependance of the ICRF power-density threshold on the toroidal mode number n, the effect of magnetic shear at the plasma edge on low-n TAEs ($n \leq 2$), and a comparison of measured decay rates of TAEs with predictions made by the LIGKA code are discussed. In addition, fast ion pressure profiles generated by the ICRF power deposition codes PION and TORIC, and the equilibrium code CLISTE have been examined to see if they lead to a sufficient fast ion drive rate for the observed TAEs, and to benchmark a formula for volume averaged β_{fast} using measurable quantities in ICRH-only plasmas.

Reference K. Sassenberg et al., Plasma Physics Contr. Fusion, **51**, 065003, (2009).

Plasma Phys. Control. Fusion **51** (2009) 065003 (14pp) doi:10.1088/0741-3335/51/6/065003

Stability of toroidicity induced shear Alfvén eigenmodes in ASDEX Upgrade

K Sassenberg[1,2], M Maraschek[2], P J Mc Carthy[1,2], H Zohm[2], R Bilato[2], W Bobkov[2], S Da Graça[3], A Flaws[2], M García-Muñoz[2], S Günter[2], V Igochine[2], P Lauber[2], M J Mantsinen[2,4], P Piovesan[5] and the ASDEX Upgrade Team[2]

[1] Department of Physics, University College Cork, Association EURATOM DCU, Cork, Ireland
[2] Max-Planck-Institut für Plasmaphysik, Garching, Euratom Association, Germany
[3] Centro de Fusao Nuclear, Associac cao EURATOM / IST, Instituto Superior Tecnico, Av. Rovisco Pais, P-1049-001 Lisboa, Portugal
[4] Helsinki University of Technology, Association EURATOM-TEKES, PO Box 4100, FIN-02015 HUT, Finland
[5] Consorzio RFX–Associazone EURATOM-ENEA sulla fusione, Padova, Italy

Received 15 November 2008, in final form 3 March 2009
Published 16 April 2009
Online at stacks.iop.org/PPCF/51/065003

Abstract

In a tokamak plasma, toroidicity induced Alfvén eigenmodes (TAEs) are excited by and alter the orbits of resonant fast ions with the character of these modes defined by both thermal and supra-thermal fast ion populations. To explore the stability of TAEs in ASDEX Upgrade, the effects of magnetic shear and density on TAEs, the decay and growth rate of individual TAEs and fast ion drive rates have been studied. In particular, the mode structure of TAEs, the dependence of the ICRF power-density threshold on the toroidal mode number n, the effect of magnetic shear at the plasma edge on low-n TAEs ($n \leqslant 2$) and a comparison of measured decay rates of TAEs with predictions made by the LIGKA code are discussed. In addition, fast ion pressure profiles generated by the ICRF power deposition codes PION and TORIC and the equilibrium code CLISTE have been examined to see if they lead to a sufficient fast ion drive rate for the observed TAEs, and to benchmark a formula for volume averaged β_{fast} using measurable quantities in ICRH-only plasmas.

(Some figures in this article are in colour only in the electronic version)

1. Overview

A readily excitable and sensitive class of MHD instability are weakly damped global toroidicity induced Alfvén eigenmodes (TAEs). These modes have the ability to extract energy from resonant fast ions through wave–particle interactions; and as these modes grow they alter the orbits of resonant fast ions, leading to a premature loss and increased transport of fast ions [1].

This leads to a reduction in heating efficiency, a degradation of plasma confinement, and potentially, damage to the plasma facing components. This is of special interest to ITER [2] and DEMO, as α-particles are the dominant fast ion species and the main source of energy to maintain a burning plasma.

In order to understand what effect TAEs destabilized by fast α-particles could be expected to have, the stability of TAEs in ASDEX Upgrade excited by ion cyclotron resonance heating (ICRH) generated fast hydrogen ions in a majority deuterium plasma was studied. Accordingly the findings are organized into the following sections, the effect of magnetic shear and density on the stability of TAEs, measured decay and growth rates of TAEs and an analysis of simulated and reconstructed fast pressure profiles with respect to TAE stability. In particular, fast ion pressure profiles generated by the ICRF power deposition codes PION [3, 4] and TORIC [5] and the equilibrium code CLISTE [6] have been tested to see if they can produce a TAE drive that is comparable in magnitude to the measured values, and to benchmark a formula for the volume averaged β_{fast} in terms of simple observables for ICRH-only plasmas.

2. Toroidicity induced shear Alfvén eigenmodes (TAEs)

2.1. Introduction

In a tokamak toroidicity leads to a modification of the Alfvén continuum, which causes cylindrical shear Alfvén waves with the same toroidal mode number n and adjacent poloidal mode numbers $(m, m+1)$ to couple resulting in the formation of gaps in the shear cylindrical Alfvén spectrum at the point where these continua cross. It is within these gaps that the weakly damped TAEs can be excited [7, 8]. At ASDEX Upgrade TAEs are most commonly observed from the 1st-*gap* which is formed as a result of the coupling of the $m = n$ and $m = n+1$ poloidal harmonics for a given n. These poloidal harmonics determine the shape of the global mode structure and are referred to as the dominant poloidal harmonics [9]. These gaps have a unique frequency $f_{\mathrm{gap}} = v_{\mathrm{A}}(r_{\mathrm{gap}})/(4\pi q(r_{\mathrm{gap}})R_0)$ associated with them, where $v_{\mathrm{A}}(r_{\mathrm{gap}}) = B_0/(\sqrt{\mu_0\rho_{\mathrm{m}}})$ and $q(r_{\mathrm{gap}})$ are the values of the Alfvén velocity and safety factor at the position of the gap, respectively, R_0 is the major radius, B_0 is the magnetic field at the magnetic axis and ρ_{m} is the mass density profile. The gap frequency f_{gap} can be used as a 0th approximation to the TAEs frequency f_{TAE} in the plasma rest frame, but the effect of magnetic shear $s = (r/q)(\mathrm{d}q/\mathrm{d}r)$ has to be taken into account to recover the TAEs frequency fully. The effect of magnetic shear (magnetic shear values used are calculated with the CLISTE equilibrium code [6]) on the TAEs frequency is to move it away from the gap frequency f_{gap} [9, 10]. TAEs typically come in two different types, either even or odd. The former arises from the dominant harmonics having the same sign (ballooning structure) and have a frequency less than f_{gap}, the latter occurs when they have opposite sign(anti-ballooning structure) and have frequencies larger than f_{gap} [11, 12]. When TAEs from the 1st-*gap* are observed each is seen to have a distinct lab frame frequency. This distinction in frequency is dominated by the doppler shift between the plasma rest frame and the lab frame. In order to extrapolate from the measured frequencies back to rest frame frequencies the equation $f_{\mathrm{lab}} = f_{\mathrm{TAE}} + nf_{\mathrm{tor}} + nq_{\mathrm{gap}}f_{\mathrm{i}}^{*}$ is used [13, 14]. Here f_{tor} is the toroidal rotation frequency of the plasma and f_{i}^{*} is the ion diamagnetic frequency.

In the discharges studied, ICRH was the primary heating and as such it is expected that the fast ion drive for TAEs should predominantly come from trapped supra-thermal ions. In addition, the drive is modified by finite ion orbit widths [15] causing the drive to reach a maximum at moderate n, typically $n = 3$–5 at ASDEX Upgrade. Experimentally, a method exists to measure the total damping a TAE would experience. This involves forcing, an

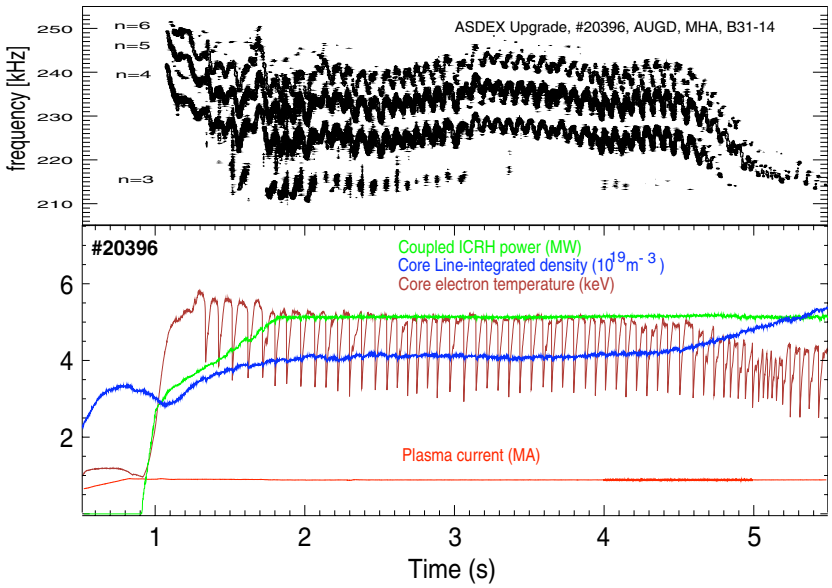

Figure 1. L-mode discharge with ICRH only: #20396—parameter evolution and spectrogram (magnetic coil B31-14) displaying unstable TAEs. $\beta_N = 1.3$, $B_{tor} = -2.4\,T$, $q_{min} \leqslant 1.0$, $q_{95} \simeq 4.9$.

otherwise stable, TAE to oscillate using an external antenna [16]. In the case of fast ion excited TAEs, when ICRH power is switched off during a discharge, effectively removing the fast ion drive, the TAEs decay rate R_d is approximately equal to the damping rate of the mode. These measured damping rates will be compared with the values calculated using the gyro-kinetic code LIGKA [17].

3. Experimental scenarios

3.1. ICRH discharge

Majority deuterium discharges were operated in a lower single null divertor configuration. The primary heating scheme used was hydrogen minority ICRH. In this environment the behaviour of typically observed TAEs [18] $n = 2, \ldots, 7$ in response to variations in parameters such as toroidal magnetic field, density and plasma current were studied. The approach used to study the effects on the stability of TAEs was to vary the relevant parameter smoothly. If stationary plasma conditions were required, a sequence of discharges with systematic variations in the relevant parameter was made.

Figure 1 shows the prototypical ICRH L-mode discharge upon which all other discharges were based. This discharge starts with an Ohmic current ramp followed by an ICRH power increase, leading to a steady phase during which a sawtooth instability is excited indicating a $q_{min} \leqslant 1.0$. Two such discharges are taken to have a similar Alfvén continuum structure, if they have the same toroidal field, core line-integrated density, density peaking (‘core line-integrated density’/‘edge line-integrated density’), plasma current, heating power and shape.

In all discharges analysed bulk parameters were within the following ranges, plasma current [0.8,1.0] MA, toroidal magnetic field [2.0,2.5] T, density n_e [3.0, 7.0] $\times 10^{19}$ m^{-3}, total ICRH power [4.0,5.0] MW, major radius $\simeq$1.70 m, minor plasma radius [0.45,0.5] m, plasma

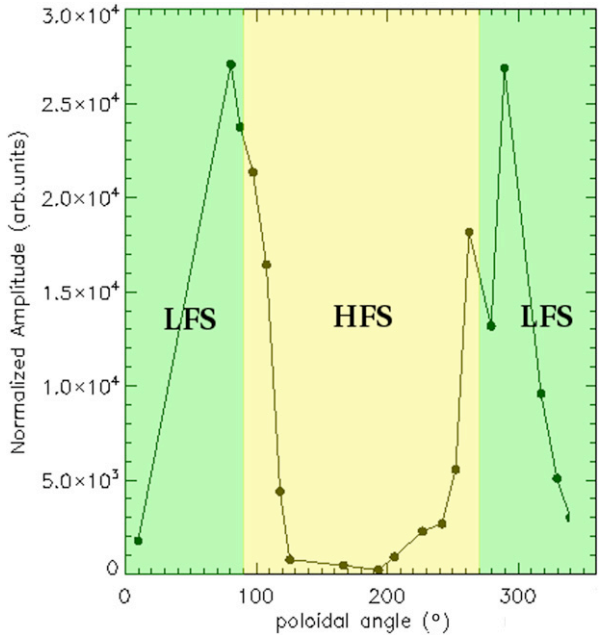

Figure 2. Poloidal amplitude distribution from a poloidal array of Mirnov coils of the $n = 4$ TAE in discharge #21067 at 2.99 s corrected for the radial decay of the magnetic perturbation field. Here the TAE has a much lower amplitude on the high field side (HFS) than on the low field side (LFS).

elongation $\kappa \approx 1.6$, upper plasma triangularity $\delta^{u} \approx 0.0$ and lower plasma triangularity $\delta^{l} \approx 0.3$. During selected discharges 2.5 MW of radial NBI power was injected at the end of the discharge after the observed TAEs. This was to acquire MSE data for current profile reconstructions and charge exchange data for rotation and ion temperature measurements. The operational ICRF frequencies used to provide central heating were 30.0 MHz and 36.5 MHz for a 2 T and 2.5 T magnetic field, respectively. To complement the divertor discharges, a set of discharges were operated in a limiter configuration (only the $n = 4$,5 TAEs are observed). This made it possible to compare TAEs observed in different flux surface topologies.

Discharges with a small content of low-Z impurities following a boronization made the transition to H-mode with ICRH alone. This provided the opportunity to compare TAEs destabilized by ICRH fast ions alone in L-mode and H-mode.

4. TAEs—effects of magnetic shear on a mode's frequency

At ASDEX Upgrade TAEs from the 1st-*gap* are most commonly observed to have frequencies that rest just above the bottom of the gap and less than f_{gap}, identifying these modes as even TAEs. This occurs as a result of low central magnetic shear $s < \epsilon = a/R_0 \simeq 0.3$, which is consistent with equilibrium reconstructions made for several similar discharges. Here a is the minor radius of the plasma. Therefore, the eigenfunction of such TAEs should have a larger amplitude on the low field side (LFS) of the torus [9]. In figure 2 the $n = 4$ TAE poloidal amplitude distribution derived from a poloidal array of Mirnov coil measurements is shown. These coils measure the time derivative of the poloidal magnetic field $\dot{B}_\theta(t)$ at the plasma edge. In order to calculate a mode's amplitude at the plasma edge from a particular coil signal, the frequency and corresponding Fourier amplitude of the mode must be identified. From this the

mode's magnetic field amplitude $B_\theta(t)$ is recovered by dividing the tracked mode's fourier amplitude by the mode's frequency. Figure 2 shows that the TAE does indeed have a larger amplitude on the LFS of the torus between 0°–90° and 270°–360° poloidally confirming them as even TAE. In figure 2 the amplitude measured for the given TAE from each Mirnov coil had to be corrected for radial decay because all Mirnov coils are not the same distance from the resonant flux surface. To do this it is assumed that the poloidal magnetic field of a TAE decays according to the following approximate formula (cylindrical vacuum approximation for $\lambda_{\mathrm{tor}} \gg \lambda_{\mathrm{pol}}$) [20]:

$$B_{\mathrm{coil}}^{\mathrm{edge}} \sim B_\theta^{\mathrm{res}} \left(\frac{r_{\mathrm{res}}}{r_{\mathrm{coil}}} \right)^{m+1} . \tag{1}$$

Here $B_{\mathrm{coil}}^{\mathrm{edge}}$ is the poloidal magnetic field at the Mirnov coil, B_θ^{res} is the value of the poloidal magnetic field at the resonant surface, r_{coil} is the distance from the Mirnov coil to the magnetic axis, r_{res} is the distance from the resonant surface to the magnetic axis at the same poloidal angle and $m = nq_{\mathrm{gap}}$.

5. Coupled ICRF power vs density and q_{95} at the onset of TAEs

When considering the stability of TAEs, the ICRH power $P_{\mathrm{ICRH}}^{\mathrm{onset}}$(MW) required to excite a TAE with toroidal mode number n versus core line-integrated (CLI) density $\hat{n}_{\mathrm{e}}$ (10^{19} m^{-3}) reveals several facts about the drive and that type of TAE.

An increase in density with other parameters held constant increases collisionality, thereby reducing the slowing down time of the fast ion population, which in turn decreases β_{f}, leading to a reduction in the available drive [7]. Therefore, one would expect a TAE's onset threshold to increase with increasing density. In figures 3 (L-mode) and 5 (H-mode) this is demonstrated by the positive slope A_1 of the linear least squares fit $P_{\mathrm{ICRH}}^{\mathrm{onset}} = A_1\hat{n}_{\mathrm{e}} + A_0$ to the data. The fitted slopes A_1 of the L-mode data set (figure 3) are plotted in figure 4, where the strength of the dependence of the threshold on density for individual TAEs suggests an overall increasing trend with increasing n (highlighted by the dashed line). The deviations from an increasing trend in figure 4 would appear to contradict this interpretation; however, they are not believed to be fatal as a result of the large uncertainties in the fitted slopes. If one considers finite orbit width effects [15] together with a density increase, then one could expect to observe an increasing trend in the strength of the threshold dependence on density for increasing n. This occurs as the fast ion drive is believed to be at its maximum at low to moderate n (n = 3–5 for ASDEX Upgrade) and then decreases with increasing n, which would amplify the detrimental effect that an increase in density has on the fast ion β as n increases. Upon comparison of the value of A_1 in L and H modes for the $n = 4$ and 5 TAEs, respectively, no statistically significant difference was observed (figure 4). The absolute coupled ICRF power required to excite TAEs was found to be independent of q_{95}. However, it was seen that if $q_{95} > 3.9$ (figure 6), an $n = 2$ TAE was not observed while $n \geqslant 3$ TAEs were. In addition, discharges operated in limiter configuration showed no $n = 2$ TAE activity. In these discharges, the value of q_{95} remained above 3.9. These results suggest that $q_{95} > 3.9$, and by extension that edge magnetic shear above a certain value is the important stabilizing factor for TAEs with $n < 3$ and not necessarily a separatrix. This position is supported by the work done by Jaun *et al* [21], in which it was shown that a high value of q_{95} and by extension edge magnetic shear resulted in a localization of the wave radial electric field, and increased continuum damping [22, 23] rates. The Alfvén continua and TAE eigenfunctions for two similar discharges #20394 with $q_{95} = 4.45$ and #21039 with $q_{95} = 3.8$ are shown in figures 7(*a*) and (*b*), respectively. The large radial extent of the observed TAEs and closed TAE gap at ASDEX Upgrade were demonstrated by [19, 24]. Here one can see that the

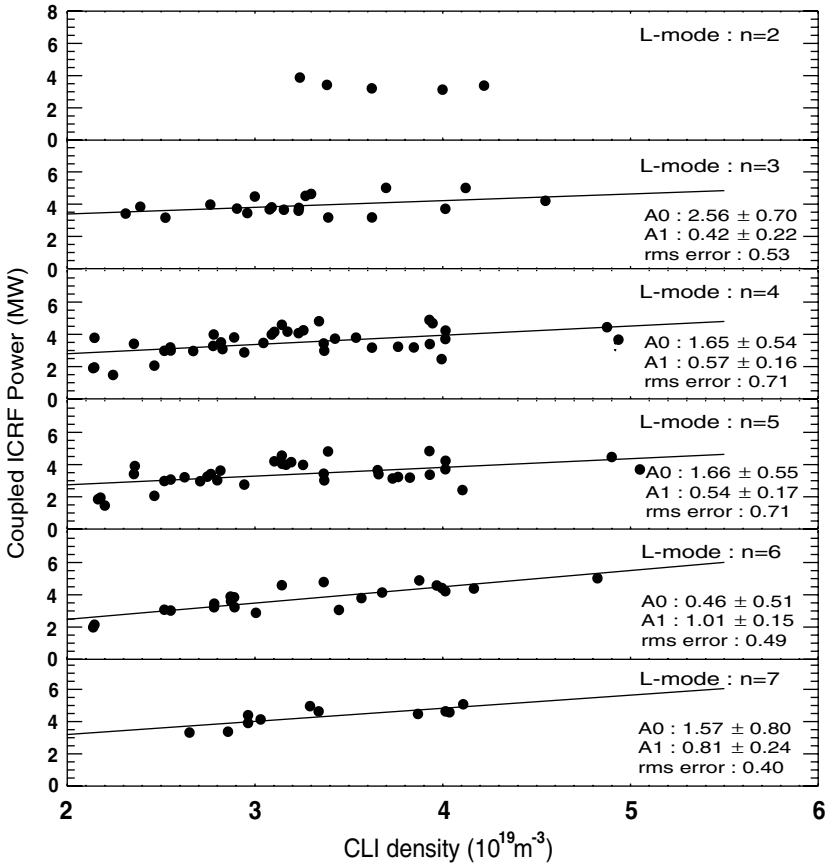

Figure 3. TAEs: ICRF power threshold versus CLI density during L-mode. Linear fit $P_{\mathrm{ICRH}}^{\mathrm{onset}} = A_1\hat{n}_e + A_0$ performed on data. RMS-error and coefficients A_0, A_1 with the corresponding standard deviations are presented.

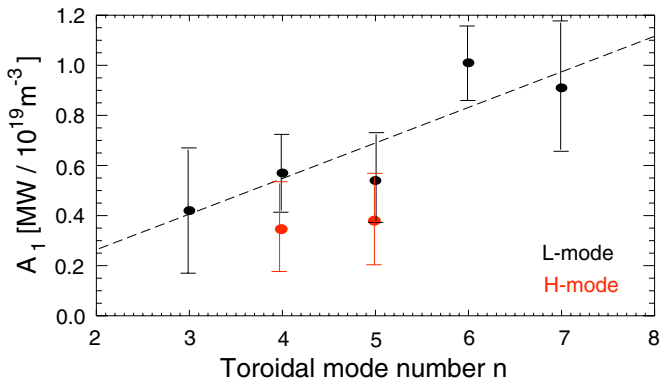

Figure 4. TAEs: fitted slopes A_1 shown in figures 3 and 5, from the linear fit of the ICRF power threshold versus CLI density during L-mode and H-mode, versus toroidal mode number n. The dashed line is a visual guide to the increasing trend from moderate to high n.

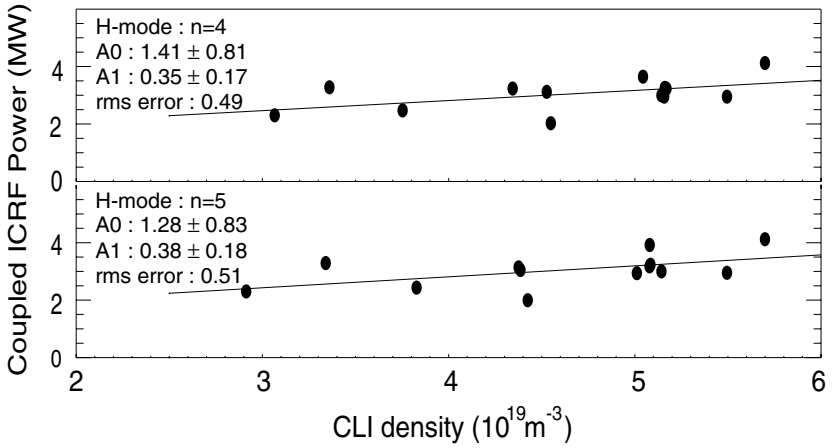

Figure 5. TAEs: ICRF power threshold versus CLI density during H-mode. Linear fit $P_{\mathrm{ICRH}}^{\mathrm{onset}} = A_1\hat{n}_e + A_0$ performed on data. RMS error and coefficients A_0, A_1 with the corresponding standard deviations are presented.

TAE's frequency intersects the continuum in both discharges, which results in non-negligible continuum damping. Equivalent to that shown by Jaun, the intersection moves radially inwards with increased q_{95} further localizing the eigenfunction. It is necessary to point out here that the CASTOR_FLOW code is not capable of simulating the interaction with the continuum, and therefore the shapes of the eigenfunctions from the intersection to the plasma edge are not physically correct and have therefore been covered.

6. TAEs: decay and growth rate measurements

The damping rate experienced by a TAE excited by ICRH-generated fast ions is greater than or equal to the mode's decay rate when the ICRH power is switched off as a result of neglecting the finite slowing down time of the ICRH ions and the time required for the mode to flatten the fast ion distribution function. Here the reduction in the effective collisionality as a result of the ICRH switching off leaves the distribution function un-replenished destroying the drive [25]. Experimentally the decay rate R_{d} is measured by fitting an exponential curve to the tracked Fourier amplitude of the mode determined using the same procedure outlined in section 4 with one difference. Here the time derivative of the mode's radial magnetic field $\dot{B}_r(t)$ taken from ballooning coils measuring $\dot{B}_r$ is used instead of the poloidal coils. These are used as they have a better response to higher frequencies, such as TAE frequencies, and are closer to the plasma than the poloidal Mirnov coils. An example of this measurement is shown in figures 8(*a*)–(*c*) corresponding to the $n = 4,5,6$ TAEs in discharge #21067. In choosing a consistent representation of growth, drive and damping rates in this paper, all rates are expressed as a percentage of the average frequency of the TAEs in the plasma's rest frame f_{TAE}. The measured decay rates were found to be $3.0 \pm 1.0\%$, $2.8 \pm 0.6\%$, $1.6 \pm 0.8\%$ of $f_{\mathrm{TAE}} = 162\,\mathrm{kHz}$, for the $n = 4,5,6$ TAEs and are larger than those calculated with the LIGKA code, which are within the range 0.8–1.1% [17]. Measurement of the growth rate of individual TAEs, some which are shown in figures 9(*a*)–(*c*), was acquired by applying an exponential fit to the tracked Fourier amplitude of an $n = 3,4,5,6$ TAE in discharge #21083 during the exponential growth phase. Since this method neglects the time needed to build up the fast ion distribution these growth rates are lower limits. The duration of this phase

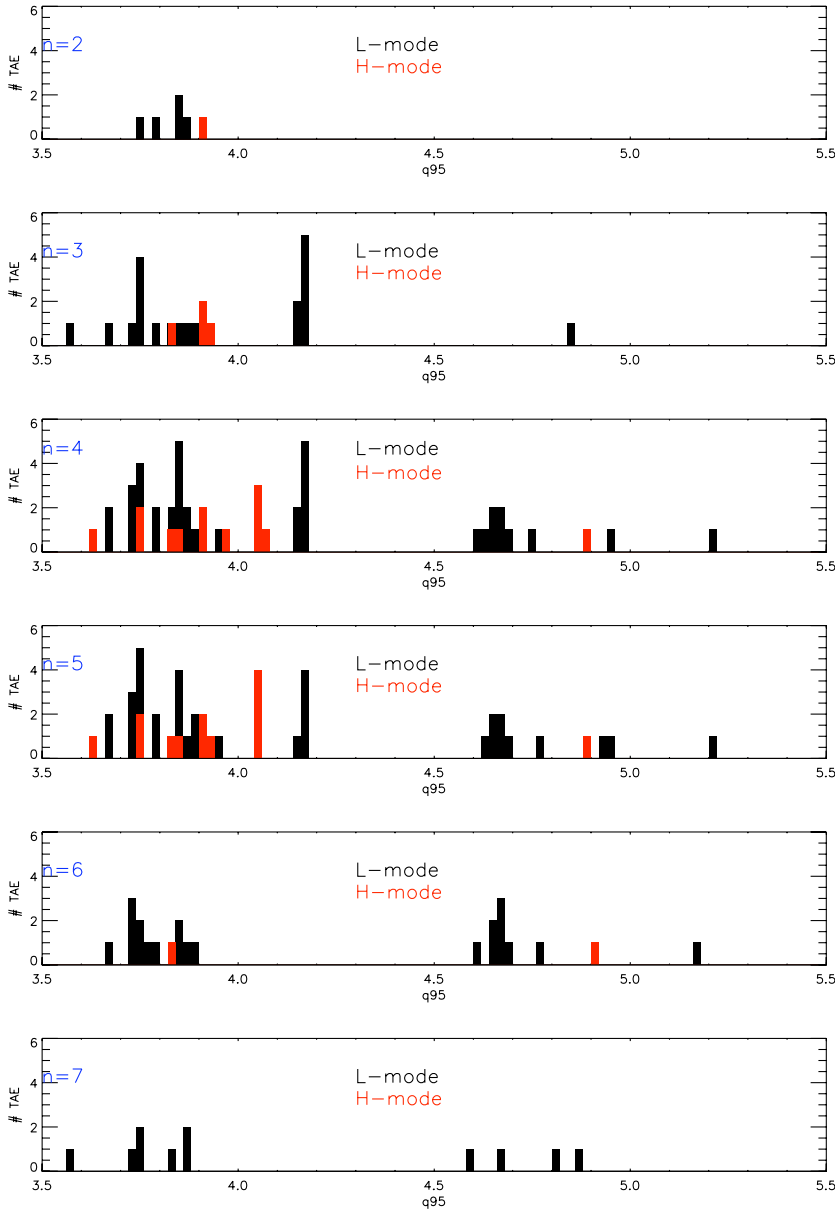

Figure 6. q_{95} values recorded at the onset of TAEs in discharges with a magnetic divertor during L and H modes. The data show that for values of $q_{95} > 3.9$ no TAEs with $n < 3$ are observed.

lasts less than 5 ms, but with a sampling rate of 2 MHz it was clearly resolved. The growth rates, expressed as a percentage of the average frequency of the TAEs in the plasma's rest frame ($f_{\mathrm{TAE}} = 168$ kHz), for the $n = 3$,4,5,6 are $0.44\pm0.05\%$, $0.5\pm0.1\%$, $0.7\pm0.1\%$ and $0.5\pm0.2\%$, respectively.

If plasma conditions do not vary significantly then the damping rate at the end of the exponential growth phase can be taken to be equal to the damping rate when ICRH is switched off (measured decay rate). In order to estimate the drive of a TAE, it is assumed that in similar

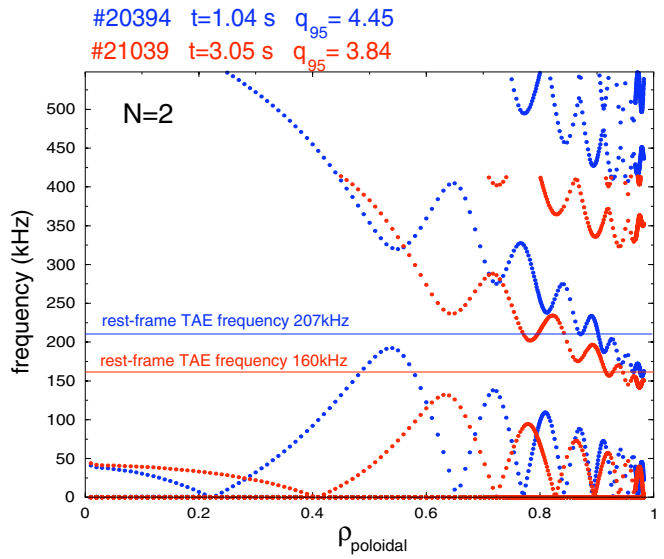

(a) Alfvèn Continua with Toroidicity induced gaps

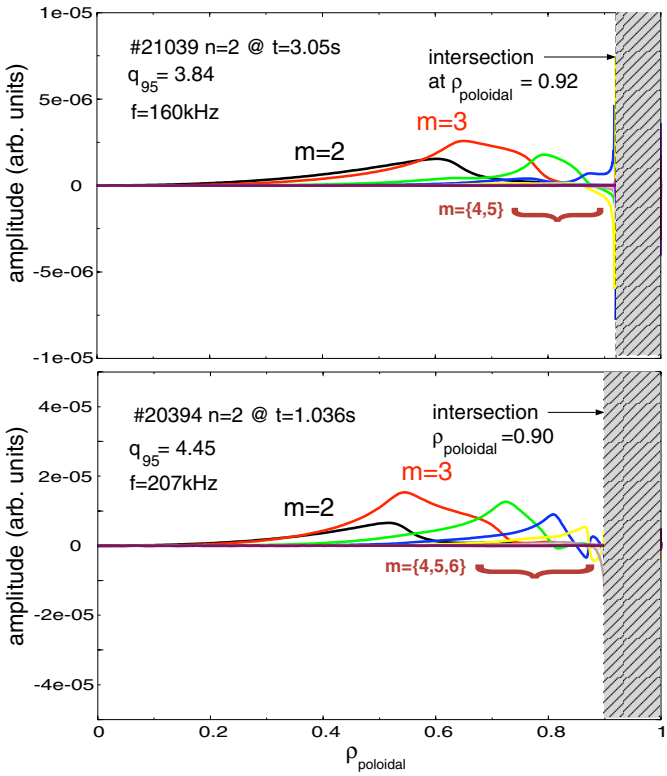

(b) Radial Displacement Eigenfunctions

Figure 7. Discharge #20394: $n = 2$ TAE at 207 kHz at 1.04 s with parameters $B_T = 2.4$ T, $I_p = 0.83$ MA, $n_e(0) = 3.3 \times 10^{19}$ m^{-3}, $q_0 = 0.97$, $q_{95} = 4.7$. Discharge #21039: $n = 2$ TAE at 160 kHz in discharge at 3.05 s with parameters $B_T = 1.94$ T, $I_p = 0.88$ MA, $n_e(0) = 3.9 \times 10^{19}$ m^{-3}, $q_0 = 0.97$, $q_{95} = 3.9$.

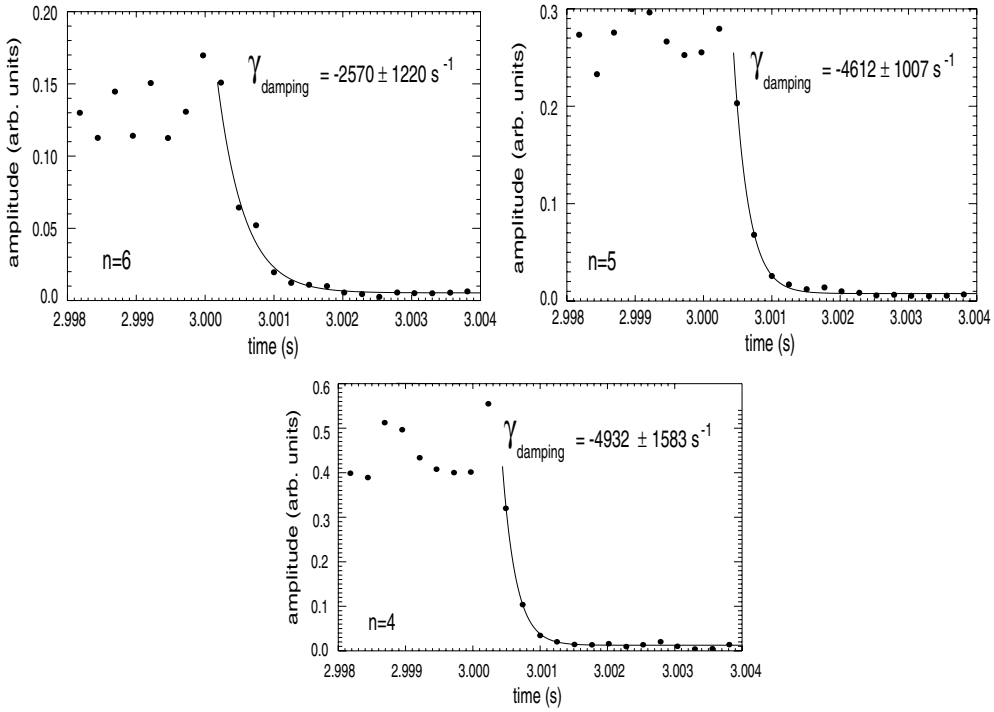

Figure 8. Discharge #21067: measurement of the $n = 4,5,6$ decay rates by fitting an exponential curve to the modes' amplitudes.

discharges the damping rate of a particular TAE is the same. Taking the average damping rate for the observed TAEs to be 2.5% and the average growth rate to be 0.5%, we find the average drive at the end of the growth phase of the TAEs from ICRF accelerated hydrogen ions to be 3.0%, where the growth rate is the difference between the drive and damping rates.

7. Fast ion pressure profiles

The equilibrium pressure profile can be reconstructed accurately by the CLISTE code if density and temperature data from the plasma edge, and q profile information from MHD modes and/or MSE data are used to constrain the solution. In such a well diagnosed equilibrium pressure profile, the fast pressure profile is the difference between the equilibrium pressure profile and the thermal pressure profile. (Apart from the edge region, where the fast pressure contribution is generally negligible, the thermal pressure data, assumed to be available across the full minor radius, are not used to constrain the CLISTE equilibrium solution.) In the following discussion the CLISTE fast pressure profile has been calculated from such a reconstruction of the equilibrium pressure profile. According to the drive equation derived by Fu and Van Dam for passing α-particles [7] the fast pressure profile has a strong influence on the stability of TAEs. Therefore, to predict instability from a given fast pressure profile, the drive rates derived from that profile must be positive and of the same order of magnitude as the measured drive rates. In figure 10, the total fast pressure profiles calculated by the ICRH power deposition codes PION [3, 4] and TORIC [5] and the equilibrium code CLISTE are shown together with

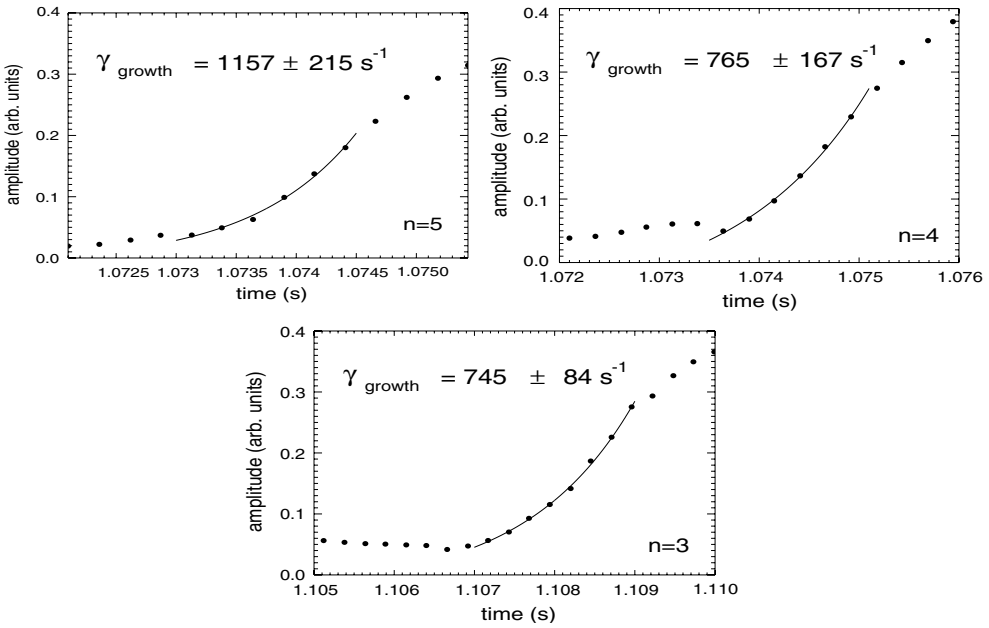

Figure 9. Discharge #21083: measurement of the $n = 3,4,5$ growth rates by fitting an exponential curve to the modes' amplitudes.

the position of individual TAEs and the $m = 4,5$ poloidal Fourier harmonics of the $n = 4$ TAE's eigenfunction.

The first observation is that the TORIC pressure profile at the positions of the TAEs provides only a negligible fast pressure and fast pressure gradient, and therefore would predict stability, whereas the CLISTE and PION profiles have a significantly larger fast pressure and fast pressure gradient. It is believed that this occurs because the TORIC code assumes a zero banana orbit width ansatz, in contrast to PION which allows for finite banana orbit widths [26]. This results in a radial *broadening* of the PION fast pressure profile when compared with the profile calculated with TORIC. It should be noted that the PION and CLISTE codes do not simulate the interaction of fast ions with MHD instabilities, and the fast pressure profiles do not contain any information pertaining to finite orbit width effects.

From the considerable radial overlap of the CLISTE and PION fast pressure profiles with the $n = 4\, m = 4,5$ TAE's eigenfunction, it is evident that there is considerable energy available to drive TAEs, which can result in a modest redistribution or loss of fast ions (figure 10). In order to test whether these profiles would predict instability, the Fu–Van Dam drive equation [7] is used in conjunction with an average pressure gradient ($(\mathrm{d}p/\mathrm{d}r)_{\mathrm{avg}} = (p_{\mathrm{min}} - p_{\mathrm{max}})/a$) and fast pressure from the CLISTE and PION profiles at the position of the $n = 4$ TAE, and an average fast ion velocity. A rigorous calculation of the trapped fast ion drive would require a full kinetic simulation, which would itself require further assumptions to be made concerning the energy and pitch angle distribution of the ICRH fast ions. This last point remains an open question and therefore cannot currently be resolved. In [27], fast ion losses caused by TAEs in ASDEX Upgrade were shown to be deeply trapped and with an average energy of 1.1 MeV. The average fast ion velocity is calculated from this energy. The drive rate, for a saturated TAE, is equal to the damping rate which in this case is $2.5 \pm 0.8\%$. The drive rates, normalized with respect to the average frequency of the TAEs in the plasma's rest frame f_{TAE}, calculated

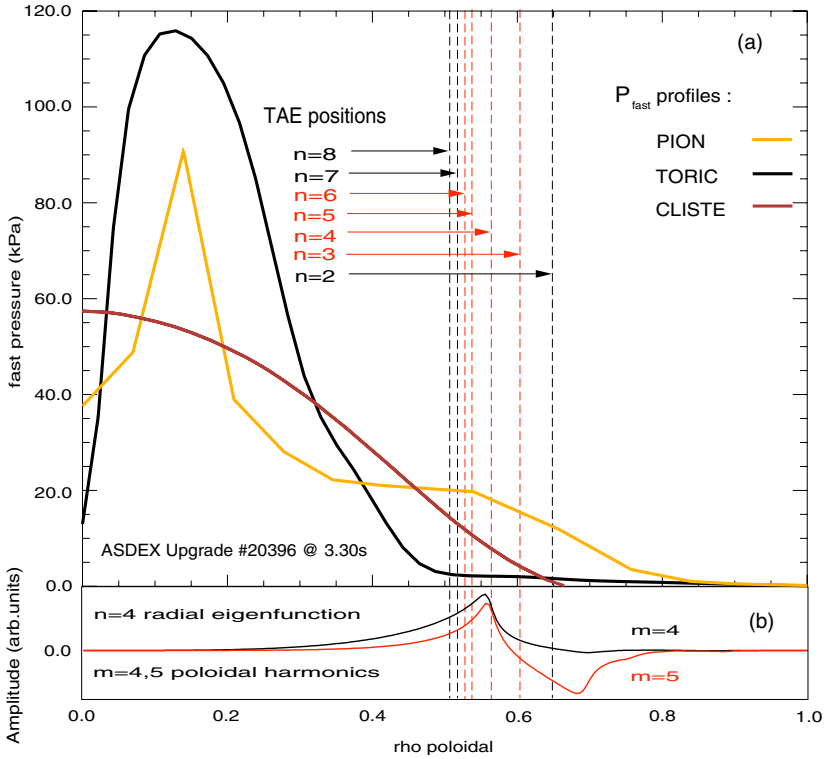

Figure 10. (a) Discharge #20396 at 3.3 s: fast pressure profiles produced by the CLISTE, PION and TORIC codes. The black lines indicate positions of the most commonly observed TAEs with the gray representing TAEs less frequently observed. (b) The dominant $m = 4,5$ poloidal harmonics of the observed $n = 4$ TAE.

from the CLISTE and PION profiles for an $n = 4$ TAE are in the range 3–12%. Therefore, from these profiles one would predict instability.

The evolution of the fast ion energy content arising from ICRH was discussed by Ramos *et al* in [28]. From this an approximate expression for the volume averaged β_{fast} can be obtained, which is

$$\langle\beta_{\text{fast}}\rangle = (4\mu_0\langle\tau_{\text{sd}}\rangle P_{\text{ICRH}})/(3B_0^2 V), \tag{2}$$

where V is the plasma volume and $\langle\tau_{\text{sd}}\rangle$ is the volume averaged slowing down time [29]. Here it is assumed that the fast ion velocity v_{f} is much less than thermal electron velocity v_{e} and $\langle\tau_{\text{sd}}\rangle$ is calculated from the measured electron density and temperature profiles. Typical slowing down times in the discharges studied were found to be 230 ms in the core, 90 ms at the TAE gap, down to 15 ms at the plasma edge. Using expression (2) a value of $\langle\beta_{\text{fast}}\rangle = 0.005$ is found at the same time as the profiles displayed in figure 10. The value of $\langle\beta_{\text{fast}}\rangle$ calculated from the CLISTE, PION and TORIC profiles are 0.0024, 0.0030 and 0.0025, respectively. From this the profile-derived values are seen to be similar but less than the estimate given by expression (2). The difference between the values calculated from the profiles and from expression (2) is believed to result from the form of the Spitzer slowing down time used, and the explicit assumption that all of the heating power is absorbed by the minority species. From the latter point, the derived expression would therefore be expected to give an upper limit on $\langle\beta_{\text{fast}}\rangle$. With respect to the slowing down time, it was assumed that $v_{\text{e}} \gg v_{\text{f}}$. However, the

energies of observed fast ion losses suggest in reality that $v_f/v_e \simeq 0.30 \rightarrow 0.45$. This implies that the form of the slowing down formula which explicitly uses the test particle's energy would be more accurate.

8. Summary

The theoretical background for TAEs is extensive as are the experimental results. This publication presents results from the analysis of observed TAEs in the 2005/2006/2007 experimental campaign at ASDEX Upgrade. The TAEs observed were shown to be even modes when the poloidal amplitude distribution was corrected for radial decay. This verified the low central shear q-profiles that had previously been predicted by equilibrium reconstructions. The amount of ICRH power required to destabilize TAEs was shown to be dependent on density and toroidal mode number, in particular, the consistency of the ICRF power threshold behaviour with respect to the finite orbit effects favouring the $n = 4{,}5$ TAEs; and independent of q_{95}. However, it was shown that q_{95} indirectly influences the stability of TAEs with $n = 2$. This was further supported by results from experiments performed in a limiter configuration, which led us to conclude that high values of q_{95} and by extension high edge shear stabilizes low-n TAEs, whether or not a separatrix is present. The measured decay rates were found to be larger than the corresponding damping rates calculated by LIGKA; however, only by a factor of 2–3. Several candidate fast pressure profiles calculated using the CLISTE, PION and TORIC codes were tested for compatibility with the requirements of TAEs. It was found that the CLISTE and PION fast pressure profiles consistently met the observed requirements in terms of a sufficient TAE drive. In addition, the approximate expression for volume average β_{fast} was shown to give an upper limit on the corresponding values calculated from the fast pressure profiles.

Acknowledgments

This work was supported by a research agreement between the Max-Planck-Institut für Plasmaphysik, Garching, Germany; University College Cork, Ireland, and EURATOM.

References

[1] Heidbrink W W 2008 *Phys. Plasmas* **15** 5
[2] Ikeda K 2007 Progress in the ITER Physics Basis *Nucl. Fusion* **47** S1–S414
[3] Eriksson L-G *et al* 1993 *Nucl. Fusion* **33** 1037
[4] Eriksson L-G *et al* 1995 *Phys. Scr.* **55** 70
[5] Brambilla M 1999 *Plasma Phys. Control. Fusion* **41** 1
[6] Mc Carthy P 1999 *Phys. Plasmas* **6** 3554–60
[7] Fu G Y and Van Dam J W 1989 *Phys. Fluids* B **1** 10
[8] Cheng C Z and Chance M S 1986 *Phys. Fluids* **29** 11
[9] Breizmann B N *et al* 1995 *Plasma Phys. Control. Fusion* **37** 1057
[10] Candy J 1994 *Phys. Plasmas* **1** 356–72
[11] Berk H L *et al* 1995 *Phys. Plasmas* **2** 9
[12] Krammer G J *et al* 2004 *Phys. Rev. Lett.* **92** 1
[13] Nazikian R *et al* 2006 *Phys. Rev. Lett.* **96** 105006
[14] Strait E J *et al* 1994 *Plasma Phys. Control. Fusion* **36** 1211–26
[15] Gorelenkov N N 2003 *Nucl. Fusion* **43** 594–606
[16] Fasoli A *et al* 1995 *Phys. Rev. Lett.* **75** 4
[17] Lauber P *et al* 2007 *J. Comput. Phys.* **226** 447–65
[18] Borba D *et al* 2004 *Plasma Phys. Control. Fusion* **46** 809–33
[19] Da Graça S *et al* 2007 *Plasma Phys. Control. Fusion* **49** 1849–72

[20] Zohm H 1990 Untersuchung magnetischer Moden am Tokamak ASDEX *IPP Report* 1/292 IPP Garching, Universität Heidelberg
[21] Jaun A *et al* 1998 *Phys. Plasmas* **5** 8
[22] Zonca F *et al* 1992 *Phys. Rev. Lett.* **68** 592
[23] Rosenbluth M N *et al* 1992 *Phys. Rev. Lett.* **68** 596
[24] Piovesan P *et al* 2008 *Nucl. Fusion* **48** 065001
[25] Wong K L *et al* 1997 *Phys. Plasmas* **4** 393
[26] Eriksson L-G, Willén U and Hellsten T 1990 *Proc. Joint Varenna-Lausanne International Workshop on 'Theory of Fusion Plasmas' (Varenna, Italy, 27–31 August)* p 421
[27] García-Muñoz M *et al* 2008 *Phys. Rev. Lett.* **100** 055005
[28] Ramos de Andrade M C *et al* 1994 *Plasma Phys. Control. Fusion* **36** 1171
[29] Stix T H 1972 *Plasma Phys.* **14** 367

Bibliography

[1] F. L. Hinton, R. D. Hazeltine, Rev. Mod. Phys. 48 239, (1976).

[2] M. Scittenhelm et al., Nuclear Fusion, 37, 1255-1270, (1997).

[3] S. Goeler et al., Physical Review Letters, 33, 1201, (1974).

[4] V. Igochine et al., Nuclear Fusion 47, 23-32A (2007).

[5] M. Sokoll, MHD-Instabilitäten in magnetisch eingeschlossenen Plasmen und ihre tomographische Rekonstruktion im Röntgenlicht. Report IPP 1/309 (Ph.D Dissertation), Max-Planck-Institut für Plasmaphysik, Garching bei München, April (1997).

[6] A. Flaws et al., to be published.

[7] M. Bessenrodt-Weberpals et al., Plasma Phys. Control. Fusion, 38, 1543-1559, (1996).

[8] M. Bornatici et al., Nuclear Fusion, 23, 1153, (1983).

[9] Summer University manual for Plasma Physics, Max-Planck-Institut für plasmaphysik, Greifswald, (2002).

[10] J.Wesson, Tokamak, Third Edition, (2004).

[11] R. Dendy, Plasma Physics : An Introductory Course, Cambridge University press, (1996).

[12] M. Maraschek, Ph.D Dissertation, Technische Universität München, Munich, Germany,(1997).

[13] Report No 1/308, IPP, Garching, Germany, (1997).

[14] P.J. Mc Carthy, Ph.D. thesis, University College Cork, (1992).

[15] H. J. De Blank, Fusion Science and Technology; Journal Volume: 45; Journal Issue: 2T, (2006).

[16] W. Schneider et al., ASDEX Upgrade MHD Equilibria Reconstruction on Distributed workstations. Fusion Engineering and Design, 48, 127-134, (2000).

[17] P. J. Mc Carthy et al., Current profile identification on ASDEX Upgrade via motional stark effect and the CLISTE interpretive equilibrium code. In 27^{th} EPS conference, Budapest, Europhysics Abstract, volume 24B, 440-443, $12^{th} - 16^{th}$ June (2000).

[18] P. J. Mc Carthy et al., 28^{th} EPS Conference on Contr. Fusion and Plasma Phys., Funchal, 18-22 June (2001).

[19] V. Igochine, IPP-Report 5/101 (Ph.D dissertation), Ludwig-Maximillian-Universität, Munich, Germany, (2002).

[20] L .L. Lao et al., Nuclear Fusion, 30, 1035 (1990).

[21] A.Fasoli et al., Nuclear Fusion, Vol. 36, No. 2, (1996).

[22] K. McGuire, Phys. Rev. Letters, 50, 891, (1983).

[23] S. Günter, Nuclear Fusion, 39, 1535, (1999).

[24] T.Kass et al., Nulcear Fusion, Vol. 38, No. 6 (1998).

[25] L. Chen, Phys. Rev. Letters, 52, 1122, (1984).

[26] B. Coppi, Phys. Rev. Letters, 57, 2272, (1986).

[27] MC Ramos de Andrade et al, Plasma Phys. Contr. Fusion 36, 1171, (1994).

[28] E. Strumberger et al., Nucl. Fusion 45 (2005) 1156.

[29] G. Huijsmans, External Resistive Modes in Tokamaks, Utrecht (1991).

[30] P. Lauber et al., Journal of Computational Phys., 226, 447-465 (2007).

[31] H. Qin , PhD Thesis, Princeton University, (1998).

[32] S.D.Pinches et al., Comp. Phys. Comm. 111, 133 (1998).

[33] M.Brambilla, Plasma Phys. and Contr. Fus. 41 (1999) 1.

[34] L.-G Eriksson et al., Nuclear Fusion 33, 1037 (1993).

[35] L.-G Eriksson et al., Phys. Scripta 55 70 (1995).

[36] R. J. LaHaye, Phys. Plasmas 13, 055501, (2006).

[37] L. Urso, M. Maraschek, H. Zohm, Institute of Physics Publishing, Journal of Physics: Conference Series,25, 266-273, (2005).

[38] Private Communication with Dr. M. G. Munoz.

[39] S. Günter et al., Plasma Phys. Contr. Fusion, 41, 767-774, (1999).

[40] O. Sauter et al., Phys. Plasmas, 4, 1654, 64, (1997).

[41] M. Maraschek et al., Physical Review Letters 79(21), 4186-4189, doi: 10.1103/Phys-RevLett.79.4186 (1997).

[42] H. Zohm, Plasma Physics and Controlled Fusion 38, 105-128, (1996).

[43] Private Communication with Dr. L. D. Horton.

[44] Private Communications with Dr. P. Mc Carthy.

[45] G. Y. Fu and J. W. Van Dam, Phys.Fluids B1 10, October 1989.

[46] B. N. Breizmann et al., Plasma Phys. and Contr. Fus. 37, 1057, (1996).

[47] J. Candy et al., Phys. Plasma, 1 (2), (1994).

[48] C. Z. Cheng, M.S. Chance, Phys. Fluids 29, 11 (1986).

[49] P. Mc Carthy, Physics of Plasmas Vol. 6 (1999) 3554-3560.

[50] M. S. Chance et al., Plasma Phys. Control. Fusion, 41, (1999) 1379-1392.

[51] H. L. Berk et al., Phys. plasmas 2, 9 (1995).

[52] G. J. Krammer et al., Phys. Review Lett. 92, 1, (2004).

[53] D. Borba et al., Plasma Phys. Control. Fusion 46, 809-833 (2004).

[54] A. Fasoli et al., Phys. Review Lett. 75, 4, (1995).

[55] J. Schirmer et al. 34th EPS conference on Contr. Fusion and Plasma Phys., Warsaw, Poland, (2007).

[56] T.L.Chow, Classical Mechanics, ISBN 0-471-04365-6, (1995).

[57] N.N.Gorelenkov, Nulcear Fusion 43, 594-606, (2003).

[58] M.N Rosenbluth et al., Phys. Rev. Lett., 68, 596, (1992).

[59] F. Zonca et al., Phys., Rev. Lett., 68, 592, (1992).

[60] R. R. Mett et al., Phys. Plasmas 1, 3277, (1994).

[61] T.H. Stix, Plasma Physics 14, 367 (1972).

[62] E. J. Strait et al., Nuclear Fusion, 33, 1849, (1993).

[63] S. DaGraça et al., Plasma Phys. Control. Fusion, 49 No.11 1849-1872 (2007).

[64] A. Jaun et al., Phys. plasmas **5**, 8, (1998).

[65] H.L. Berk et al., Phys. Fluids B 4 **7** (1992).

[66] P. Piovesan et al., Nuclear Fusion, 48 (2008) 065001.

[67] M. Garcia-Munoz et al., Physical Review Letters, 100, 055005, (2008).

[68] H.L.Berk et al., Phys.Lett. A , 234, 213 (1997).

[69] E.J.Strait et al., Plasma Phys.Control.Fusion, 36, 1211-1226 (1994).

[70] R.B.White. Phys.Fluids, 26, (10) 2958, 1983.

[71] D.Testa et al., 28th EPS conference on Contr. Fusion and Plasma Phys. Funchal (2001).

[72] A. Fasoli et al., Plasma Phys. Control. Fusion 44 B159-B172 (2002).

[73] P. J. Mc Carthy et al., IPP-Report : The CLISTE Interpretive code, IPP 5/85, May 1999.

[74] Progress in the ITER physics basis, volume 47, number 6, June (2007).

[75] H. Zohm, Untersuchung magnetischer Moden am Tokamak ASDEX, IPP Report (Ph.D Dissertation), 1/292, IPP Garching, Universität Heidelberg, (1990).

[76] L. -G. Eriksson, U. Willén, T. Hellsten, Proceedings of the Joint Vareena-Lausanne International Workshop on "Theory of Fusion Plasmas", Varenna, Italy, p421, August 27-31, (1990).

[77] C. S. Chang et al., Phys. Fluids B 3, 3429, (1991).

[78] J. P. Meskat et al., Plasma Phys. Control. Fusion, **43**, 13251332, (2001).

[79] M. Sokoll, MHD Instabilitäten in magnetisch eingeschlossenen Plasmen und ihre tomographische Rekonstruktion im Röntgenlicht, PhD Thesis, IPP Rep. 1/309, Max-Planck-Institut für Plasmaphysik Garching, (1997).

[80] M.A. Van Zeeland et al., Phys. Review Letters, **97**, 135001, (2006).